

# **Prediction of railway induced vibration by means of numerical, empirical, and hybrid methods**

**Hans VERBRAKEN**

Supervisory Committee:  
Prof. dr. ir. P. Wollants, chair  
Prof. dr. ir. G. Degrande, promotor  
Prof. dr. ir. G. Lombaert, promotor  
Prof. dr. ir. W. Desmet  
Prof. dr. ir. G. Vermeir  
Prof. dr. ir. D. Thompson  
(University of Southampton, UK)  
Prof. dr. ir. P. Galvín Barrera  
(University of Seville, Spain)  
dr. ir. P. Vanhonacker  
(D2S International, Belgium)

Dissertation presented in partial fulfillment of the requirements for the degree of Doctor of Engineering

© KU Leuven – Faculty of Engineering Science  
Kasteelpark Arenberg 40 box 2448, B-3001 Leuven (Belgium)

Alle rechten voorbehouden. Niets uit deze uitgave mag worden vermenigvuldigd en/of openbaar gemaakt worden door middel van druk, fotocopie, microfilm, elektronisch of op welke andere wijze ook zonder voorafgaande schriftelijke toestemming van de uitgever.

All rights reserved. No part of the publication may be reproduced in any form by print, photoprint, microfilm or any other means without written permission from the publisher.

D/2013/7515/147  
ISBN 978-94-6018-762-9

# Dankwoord

Een doctoraat is een werk van lange adem. Ik wil vandaag een aantal mensen bedanken die me geholpen hebben het tot een goed einde te brengen.

Mijn dank gaat in de eerste plaats naar mijn beide promotoren, Geert Degrande en Geert Lombaert. Ze gaven me de kans om als doctoraatsstudent aan de slag te gaan. Ik wil hen bedanken voor de steun, het sturen van het onderzoek en de vele inspanningen om de kwaliteit van mijn werk te verbeteren. Verder denk ik bijvoorbeeld met plezier terug aan het IWRN congres in Japan waar we met drie aan deelnamen en waar ik met hen zowel de wereld van ‘railway induced vibration’ als de Japanse cultuur beter leerde kennen.

Verder dank ik Wim Desmet en Gerrit Vermeir voor het begeleiden van dit doctoraatsproject en David Thompson, Pedro Galvín en Patrick Vanhonacker voor het zetelen in mijn jury. Hun opmerkingen en interesse in het werk betekenden een waardevolle bijdrage. Patrick Wollants bedank ik voor het vervullen van de voorzitterstaak.

Ik heb inhoudelijk ook kunnen rekenen op andere collega’s binnen de afdeling. Ik wens in het bijzonder Stijn François te bedanken bij wie ik altijd snel terecht kon voor uitleg en oplossingen voor allerhande probleempjes en Pieter Coulier die, hoewel twee jaar later gestart, een grote steun betekende in mijn onderzoek.

Ik kan niet anders dan Miche, Pieter C., Ellen, Pieter F., Geert L., Bui, Mattias en Eliz-Mari bedanken voor het helpen uitvoeren van de experimenten in Lincent, de ruggengraat van mijn thesis. Vooral Pieter C. en Miche bedank ik voor de koude, nachtelijke proeven en Ellen voor het ’s ochtends vroeg te hulp schieten. Verder wil ik ook de mensen van Infrabel bedanken, in het bijzonder Raymond Demaret, voor de aangename samenwerking.

Omdat niet alleen de inhoud telt, maar ook de verpakking wil ik Jeroen en Stijn bedanken voor de hulp bij het maken van de cover.

Ik kijk met een tevreden gevoel terug op mijn tijd aan de afdeling Bouwmechanica. Zonder verdere namen te noemen wil ik de vele medewerkers en bezoekers van de afdeling tijdens mijn verblijf bedanken voor de aangename sfeer tijdens de werkuren en erbuiten, voor de nodige babbels en voor de fijne momenten tijdens geplande uitstapjes of minder geplande activiteiten. Speciale vermeldingen zijn er voor de meetcampagnes die een fijne afwisseling boden met het bureauwerk, het Eurodyn congres waar ik met veel plezier aan meewerkte en, hoewel met een negatief winstsaldo, de hevig bevochten pingpongmatches. Een speciaal woord van dank gaat ook naar Guido, ons afdelingshoofd, en naar Danielle en Ann voor de administratieve ondersteuning.

Ik dank het Fonds Wetenschappelijk Onderzoek – Vlaanderen dat me een beurs toekende en me gedurende vier jaar financierde voor mijn onderzoek.

Ik ben zeker ook een woord van dank verschuldigd aan familie en vrienden die onrechtstreeks hebben bijgedragen. Ik dank mijn huis(jes)genoten van de voorbije jaren, de vrienden van de scouts en van het alma-groepje. Thomas wil ik bedanken voor de vele gezellige lunches. Ook Filip, Pieter en Barbara zorgden voor de nodige afleiding. Walter en Chris wil ik bedanken voor de steun en interesse die ze steeds toonden.

Een bijzonder woord van dank gaat naar mijn ouders. Ik voelde jullie interesse en meelevens op de fijne maar ook de moeilijker momenten. Ik dank jullie voor de wijze raad, de onvoorwaardelijke steun en het geloof in een goed einde.

Het grootste woord van dank is voor Severien. Je hebt me leren kennen in de laatste fase van mijn doctoraat en hebt daardoor de laatste loodjes mee moeten helpen dragen. Niet in het minst dank zij jouw hulp is dat gelukt. Het is een heerlijk gevoel met jou te kunnen uitkijken naar de toekomst!

# Summary

Ground vibration induced by railway traffic is a problem with a large environmental impact. Vibration generated at the wheel/rail contact is transferred through the soil and excites the foundation of nearby buildings where it causes disturbance of sensitive equipment, hindrance to inhabitants, or structural damage. An accurate prediction of expected vibration levels is required when designing new tracks or when changes are made to existing tracks. The study of possible vibration mitigation measures also requires accurate models.

This work addresses the numerical, empirical, and hybrid prediction of railway induced vibration. For the assessment of these methods, an elaborate measurement campaign has been carried out at a site in Lincet, Belgium.

First, a numerical model is presented that allows for a detailed representation of the track geometry. The influence of commonly made simplifying assumptions regarding the track and soil geometry is investigated for the site in Lincet. The dynamic track and soil characteristics are identified based on preliminary tests at the site. The predictions are compared to measured results of the transfer functions and during train pass-bys and show a reasonable agreement.

Second, empirical prediction methods are discussed with a focus on the procedure presented by the U.S. Federal Railroad Administration (FRA), where the source and the propagation path are characterized experimentally. The experimental determination of these terms is critically assessed. Furthermore, the limitations of the FRA procedure are investigated by means of numerical simulations.

Third, a hybrid model is presented according to the empirical FRA procedure by replacing the experimental result of either the source term or the propagation path term by a numerical prediction. The hybrid model is applied at the site in Lincet and compared to the experimental and numerical results.



# Samenvatting

Trillingen ten gevolge van treinverkeer hebben een grote omgevingsimpact. Ze worden veroorzaakt aan het contact tussen wiel en rail, planten zich voort door de grond en exciteren de funderingen van nabijgelegen gebouwen waar ze zorgen voor storing van gevoelige apparatuur, hinder voor inwoners en structurele schade. Een nauwkeurige voorspelling van de verwachte trillingsniveaus is nodig bij het ontwerp van nieuwe sporen of bij aanpassingen aan bestaande sporen. Nauwkeurige modellen zijn ook nodig voor de studie van trillingsreducerende maatregelen.

Dit werk bestudeert de numerieke, empirische en hybride voorspelling van trillingen ten gevolge van treinverkeer. Voor de beoordeling van deze modellen werd een uitgebreide meetcampagne uitgevoerd op een site in Lincet, België.

Ten eerste wordt een numeriek model voorgesteld dat een gedetailleerde modellering van het probleem toelaat. De invloed van vaak gemaakte aannames met betrekking tot de geometrie van het spoor en de grond wordt onderzocht voor de site in Lincet. De voorspelling op basis van vooraf geïdentificeerde parameters wordt vergeleken met experimentele resultaten en tonen een behoorlijke overeenkomst.

Ten tweede worden empirische modellen besproken waar de bron en het transmissiepad afzonderlijk worden gekarakteriseerd. De focus ligt op de procedure voorgesteld door de Federal Railroad Administration (FRA), waarvan de experimentele uitvoering kritisch wordt geëvalueerd. De beperkingen van de FRA procedure worden onderzocht door middel van numerieke simulaties.

Ten derde wordt een hybride model voorgesteld dat is gebaseerd op de empirische FRA procedure door het experimentele resultaat van ofwel de bron of het transmissiepad te vervangen door een numerieke voorspelling. Het hybride model wordt gebruikt op de site in Lincet en vergeleken met de experimentele en numerieke resultaten.





# List of symbols

The following list provides an overview of symbols used throughout the text. The physical meaning of the symbols is explained in the text. Vectors, matrices, and tensors are denoted by bold characters. In the text, variables in the space-frequency domain are denoted by a hat, and variables in the wavenumber-frequency domain are denoted by a tilde. No hats or tildes are used in the following list, however.

## Abbreviations

BE	Boundary Element
FE	Finite Element
BSI	British Standards Institution
DIN	Deutsches Institut für Normung
FRA	Federal Railroad Administration
FTA	Federal Transit Administration
ISO	International Standards Organization
SBR	Stichting BouwResearch
RMS	Root Mean Square
PSD	Power Spectral Density
HST	High Speed Train
IC	InterCity [train]
SASW	Seismic Analysis of Surface Waves
SCPT	Seismic Cone Penetration Test

**General symbols and conventions**

$(x, y, z)$	Cartesian coordinates
$(r, \theta, z)$	Cylindrical coordinates
$\mathbf{e}_i$	Unit vector along the axis $i$
$t$	Time
$f$	Frequency
$\omega$	Circular frequency
$k_y$	Wavenumber in the longitudinal direction $\mathbf{e}_y$
$\bar{k}_y$	Dimensionless wavenumber in the longitudinal direction $\mathbf{e}_y$
$n_y$	Circumferential wavenumber in the longitudinal direction $\mathbf{e}_y$
$C_y$	Phase velocity in the longitudinal direction $\mathbf{e}_y$
$k_r$	Wavenumber in the radial direction
$C_r$	Phase velocity in the radial direction
$\square_{\text{RMS}}$	(Running) RMS value of the variable $\square$
$\square_{\text{RMS}m}$	One-third octave band RMS value of the variable $\square$ in the $m$ -th frequency band
$\langle \square \rangle_m$	One-third octave band representation of the variable $\square$ in the $m$ -th frequency band
$S_{\square}$	PSD of the variable $\square$
$\delta(\square)$	Dirac Delta function
$\mathbf{I}$	Unity matrix
$\square^{-1}$	Inverse of a matrix $\square$
$\square^T$	Transpose of a matrix $\square$
$\square^H$	Hermitian (or conjugate transpose) of a matrix $\square$

**Response to moving loads**

$\mathbf{x}$	Source location
$\mathbf{x}'$	Receiver location
$\mathbf{u}$	Displacement vector
$\mathbf{v}$	Velocity vector
$\rho\mathbf{b}$	Body forces
$\mathbf{g}$	Axle load vector
$\mathbf{H}$	Force–displacement transfer matrix
$\mathbf{H}_v$	Force–velocity transfer matrix
$\mathbf{u}_{w/r}$	Wheel/rail unevenness vector
$\mathbf{C}^t$	Track compliance matrix
$\mathbf{C}^v$	Vehicle compliance matrix

**Track–soil interaction model**

$\Omega_t$	Track domain
$\Omega_s$	Soil domain
$\Sigma_{ts}$	Track–soil interface
$\Sigma_{s0}$	Free boundary
$\mathbf{u}_t$	Track displacement vector
$\mathbf{f}_t$	Load vector
$\mathbf{u}_s$	Soil displacement vector
$\mathbf{t}_s$	Soil traction vector
$\square$	Discretized vector
$\mathbf{K}_{tt}$	FE stiffness matrix
$\mathbf{M}_{tt}$	FE mass matrix
$\mathbf{K}_{tt}^s$	FE soil stiffness matrix
$\mathbf{U}$	Displacement BE system matrix
$\mathbf{T}$	Traction BE system matrix
$\mathbf{U}_r$	Displacement BE transfer matrix
$\mathbf{T}_r$	Traction BE transfer matrix

**Elastodynamics**

$\lambda$	First Lamé constant
$\mu$	Second Lamé constant, shear modulus
$\nu$	Poisson’s ratio
$\rho$	Density
$C_s$	Shear wave velocity
$C_p$	Longitudinal wave velocity
$\beta_s$	Material damping ratio for shear waves
$\beta_p$	Material damping ratio for longitudinal waves
$C_R$	Rayleigh wave velocity

**Track–soil model parameters**

$E_r I_r$	Rail flexural stiffness
$\rho_r A_r$	Rail mass per length
$x_r$	Position of the rail
$\bar{k}_{rp}$	Equivalent rail pad stiffness
$\bar{c}_{rp}$	Equivalent rail pad viscous damping
$\bar{m}_{sl}$	Equivalent sleeper mass
$\rho_{sl} \bar{I}_{t\ sl}$	Equivalent sleeper mass moment of inertia
$l_{sl}$	Sleeper length

$h_b$	Ballast height
$w_{bu}$	Ballast upper width
$w_{bl}$	Ballast lower width
$h_s$	Subgrade height
$w_s$	Subgrade width
$h_e$	Excavation height
$w_{eu}$	Excavation upper width
$w_{el}$	Excavation lower width

### Train model parameters

$L_t$	Train length
$L_c$	Car length
$L_b$	Bogie distance
$L_a$	Axle distance
$M_t$	Total axle mass
$M_s$	Sprung axle mass
$M_u$	Unsprung axle mass
$n_a$	Number of axles

### Signal processing

$H_{ij}$	Transfer function between channels $i$ and $j$
$\sigma_{H_{ij}}$	Standard deviation of the transfer function $H_{ij}$
$\gamma_{ij}$	Coherence between channels $i$ and $j$
$R_{ij}$	(Cross-)correlation between channels $i$ and $j$
$S_{ij}$	(Cross-)PSD between channels $i$ and $j$

### Empirical methods

$L_v$	Vibration velocity level
$L_{v0}$	Reference velocity level
$L_F$	Force density
$TM_L$	Line source transfer mobility
$TM_P$	Point source transfer mobility

### Hybrid methods

$\square^{EXP}$	Experimental result of the variable $\square$
$\square^{NUM}$	Numerical prediction of the variable $\square$
$\square^{HYB}$	Hybrid prediction of the variable $\square$

# Contents

<b>Dankwoord</b>	<b>i</b>
<b>Summary</b>	<b>iii</b>
<b>Samenvatting</b>	<b>v</b>
<b>List of symbols</b>	<b>vii</b>
<b>Contents</b>	<b>xi</b>
<b>List of Figures</b>	<b>xv</b>
<b>List of Tables</b>	<b>xxxiii</b>
<b>1 Introduction</b>	<b>1</b>
1.1 Problem outline . . . . .	1
1.2 State of the art and further needs . . . . .	3
1.3 Objectives and contributions of the thesis . . . . .	11
1.4 Organization of the text . . . . .	13
<b>2 Numerical methods</b>	<b>15</b>
2.1 Introduction . . . . .	15

2.2	The response to moving loads . . . . .	16
2.2.1	General formulation . . . . .	16
2.2.2	Quasi-static contribution . . . . .	19
2.2.3	Dynamic contribution . . . . .	19
2.3	The dynamic axle loads . . . . .	20
2.3.1	Excitation mechanisms . . . . .	20
2.3.2	Train-track interaction . . . . .	22
2.4	The track-soil interaction problem . . . . .	25
2.4.1	The track model . . . . .	26
2.4.2	The soil model . . . . .	29
2.5	Numerical example . . . . .	32
2.5.1	Free field transfer functions . . . . .	32
2.5.2	Track-soil interaction . . . . .	40
2.5.3	Train-track interaction . . . . .	45
2.5.4	Response due to a train passage . . . . .	49
2.6	Free field response for fixed and incoherent axle loads . . . . .	59
2.6.1	Assumption of fixed axle loads . . . . .	59
2.6.2	Assumption of incoherent axle loads . . . . .	63
2.7	Conclusion . . . . .	65
<b>3</b>	<b>Experimental validation</b>	<b>67</b>
3.1	Introduction . . . . .	67
3.2	The site in Lincent . . . . .	67
3.3	The free field mobility . . . . .	70
3.3.1	The identification of dynamic soil characteristics . . . . .	70
3.3.2	Influence of the excavation on the free field mobility . . . . .	74
3.3.3	Validation of the free field mobility . . . . .	77

3.4	The track receptance . . . . .	87
3.4.1	The dynamic track characteristics . . . . .	87
3.4.2	Influence of the excavation on the track receptance . . . . .	91
3.4.3	Influence of the track subgrade on the track receptance . . . . .	93
3.4.4	Updating of the track parameters . . . . .	95
3.5	The track – free field mobility . . . . .	101
3.5.1	Influence of the excavation on the track – free field mobility . . . . .	102
3.5.2	Influence of the track subgrade on the track – free field mobility . . . . .	103
3.5.3	Validation of the track – free field mobility . . . . .	104
3.6	Train passages . . . . .	108
3.6.1	The dynamic train characteristics . . . . .	108
3.6.2	The track unevenness . . . . .	110
3.6.3	Validation of the response due to train passages . . . . .	112
3.7	Conclusion . . . . .	129
<b>4</b>	<b>Empirical methods</b> . . . . .	<b>131</b>
4.1	Introduction . . . . .	131
4.2	The FRA procedure . . . . .	133
4.3	Analytical expressions for the empirical model . . . . .	137
4.4	Determination of the line source transfer mobility level . . . . .	141
4.4.1	Numerical assessment . . . . .	142
4.4.2	Experimental assessment . . . . .	152
4.5	Determination of the force density level . . . . .	155
4.5.1	Numerical assessment . . . . .	155
4.5.2	Experimental assessment . . . . .	160
4.6	Influence of the track and soil characteristics on the force density level . . . . .	164

4.6.1	Influence of the soil characteristics . . . . .	165
4.6.2	Influence of the track characteristics . . . . .	171
4.7	Conclusion . . . . .	174
<b>5</b>	<b>Hybrid methods</b>	<b>177</b>
5.1	Introduction . . . . .	177
5.2	Numerical prediction of the force density level . . . . .	178
5.2.1	Direct prediction of the force density level . . . . .	179
5.2.2	Indirect prediction of the force density level . . . . .	183
5.3	Numerical prediction of the line source transfer mobility level . . . . .	190
5.4	Numerical correction for the position of the source point . . . . .	197
5.5	Conclusion . . . . .	199
<b>6</b>	<b>Conclusions and recommendations for further research</b>	<b>201</b>
6.1	Conclusions . . . . .	201
6.2	Recommendations for further research . . . . .	205
	<b>Bibliography</b>	<b>209</b>
	<b>Curriculum vitae</b>	<b>225</b>



# List of Figures

1.1	Problem outline. . . . .	2
2.1	A longitudinally invariant track–soil domain. . . . .	17
2.2	2D multi-body model of a single carriage. . . . .	24
2.3	Vehicle model used in the present work. . . . .	25
2.4	Cross section of a classical ballasted track. . . . .	26
2.5	Cross section of the track model used in the present work. . . . .	27
2.6	Cross section of the soil model used in the present work. . . . .	29
2.7	Modulus of the free field mobility $\tilde{h}_{vzz}(k_r, z = 0, \omega)$ as a function of the frequency $\omega$ and the phase velocity $C_r$ for the homogeneous halfspace. The dispersion curve of the Rayleigh wave in the homogeneous halfspace is superimposed (black line). . . . .	33
2.8	Real (solid line) and imaginary (dotted line) part of the dimensionless (a) horizontal and (b) vertical displacement of the Rayleigh wave at 20 Hz as a function of the depth $z$ for the homogeneous halfspace. . . . .	34
2.9	Real (solid line) and imaginary (dotted line) part of the dimensionless (a) horizontal and (b) vertical displacement of the Rayleigh wave at 40 Hz as a function of the depth $z$ for the homogeneous halfspace. . . . .	34
2.10	Level of the free field mobility $\hat{h}_{vzz}(r, z = 0, \omega)$ as a function of the frequency $\omega$ at (a) $r = 6$ m, (b) $r = 12$ m, (c) $r = 24$ m, and (d) $r = 48$ m for the homogeneous halfspace. . . . .	35

2.11	Level of the one-third octave band free field mobility $\langle h_{vzz}(r, z = 0) \rangle_m$ at (a) $r = 6$ m, (b) $r = 12$ m, (c) $r = 24$ m, and (d) $r = 48$ m for the homogeneous halfspace. . . . .	36
2.12	Modulus of the free field mobility $\tilde{h}_{vzz}(k_r, z = 0, \omega)$ as a function of the frequency $\omega$ and the phase velocity $C_r$ for the layered halfspace. The dispersion curves of the first three Rayleigh waves are superimposed (black lines). . . . .	37
2.13	Real (solid line) and imaginary (dotted line) part of the dimensionless (a) horizontal and (b) vertical displacement of the Rayleigh wave at 20 Hz as a function of the depth $z$ for the layered halfspace. . . . .	37
2.14	Real (solid line) and imaginary (dotted line) part of the dimensionless (a) horizontal and (b) vertical displacement of the Rayleigh wave at 40 Hz as a function of the depth $z$ for the layered halfspace. . . . .	38
2.15	Level of the free field mobility $\hat{h}_{vzz}(r, z = 0, \omega)$ as a function of the frequency $\omega$ at (a) $r = 6$ m, (b) $r = 12$ m, (c) $r = 24$ m, and (d) $r = 48$ m for the layered halfspace. . . . .	39
2.16	Level of the one-third octave band free field mobility $\langle h_{vzz}(r, z = 0) \rangle_m$ at (a) $r = 6$ m, (b) $r = 12$ m, (c) $r = 24$ m, and (d) $r = 48$ m for the layered halfspace. . . . .	39
2.17	(a) Modulus and (b) phase of the rail receptance of the ballasted track on the homogeneous (black line) and the layered (grey line) halfspace. . . . .	41
2.18	Level of the track – free field mobility $\hat{h}_{vzz}(x, y, z, \omega)$ (solid line) at the surface of the homogeneous halfspace as a function of the frequency $\omega$ for (a) $r = 6$ m, (b) $r = 12$ m, (c) $r = 24$ m, and (d) $r = 48$ m. The corresponding free field mobility is superimposed (dotted line). . . . .	43
2.19	Level of the one-third octave band track – free field mobility $\langle h_{vzz}(r, z) \rangle_m$ (solid line) at the surface of the homogeneous halfspace as a function of the frequency $\omega$ for (a) $r = 6$ m, (b) $r = 12$ m, (c) $r = 24$ m, and (d) $r = 48$ m. The corresponding free field mobility is superimposed (dotted line). . . . .	43
2.20	Level of the track – free field mobility $\hat{h}_{vzz}(r, z, \omega)$ at the surface of the layered halfspace as a function of the frequency $\omega$ for (a) $r = 6$ m, (b) $r = 12$ m, (c) $r = 24$ m, and (d) $r = 48$ m. . . . .	44

2.21	Level of the one-third octave band track – free field mobility $\langle h_{vzz}(r, z) \rangle_m$ at the surface of the layered halfspace as a function of the frequency $\omega$ for (a) $r = 6$ m, (b) $r = 12$ m, (c) $r = 24$ m, and (d) $r = 48$ m. . . . .	44
2.22	(a) PSD $\tilde{S}_{u_w/rz}(k_y)$ of the vertical unevenness according to FRA class 1 (dark grey line), class 3 (black line), and class 6 (light grey line) [56] and (b) modulus of an unevenness profile $\hat{u}_{w/rz}(\omega)$ generated from FRA class 3 for a train speed of 200 km/h. . . . .	46
2.23	Real (solid line) and imaginary (dotted line) part of the vertical track compliance $\hat{C}^t(\omega)$ for a train speed (a) $v = 0$ km/h and (b) $v = 200$ km/h. . . . .	47
2.24	Real (solid line) and imaginary (dotted line) part of the vertical vehicle compliance $\hat{C}^v(\omega)$ of a single axle. . . . .	47
2.25	Real (solid line) and imaginary (dotted line) part of the vertical combined compliance $\hat{C}^t(\omega) + \hat{C}^v(\omega)$ for a single axle (200 km/h) running on the track. . . . .	48
2.26	Modulus of the vertical track compliance $\hat{C}^t(\omega)$ (dark grey line), vehicle compliance $\hat{C}^v(\omega)$ (light grey line), and combined compliance $\hat{C}^t(\omega) + \hat{C}^v(\omega)$ (black line) for a single axle (200 km/h) running on the track. . . . .	48
2.27	(a) PSD $\hat{S}_{g_z}(\omega)$ and (b) narrow band spectrum $\hat{g}_z(\omega)$ of the vertical dynamic load of a single axle (200 km/h) on the track on the layered halfspace. . . . .	49
2.28	(a) Time history and (b) frequency content of the vertical quasi-static rail velocity during the passage of a single axle (200 km/h). . . . .	50
2.29	Signature of the Thalys train (200 km/h). . . . .	50
2.30	(a) Time history and (b) frequency content of the vertical quasi-static rail velocity during the passage of a Thalys train (200 km/h). . . . .	50
2.31	(a) Time history and (b) frequency content of the vertical quasi-static free field velocity at 6 m, 12 m, 24 m, and 48 m during the passage of a Thalys train (200 km/h). . . . .	52
2.32	(a) Time history and (b) frequency content of the vertical dynamic rail velocity during the passage of a Thalys train (200 km/h). . . . .	53

2.33 (a) Time history and (b) frequency content of the vertical dynamic free field velocity at 6 m, 12 m, 24 m, and 48 m during the passage of a Thalys train (200 km/h). . . . .	54
2.34 (a) Time history and (b) running RMS value of the vertical free field velocity at 12 m from the track during the passage of a Thalys train (200 km/h) indicating the time periods $T_1$ (black line), $T_2$ (dark grey line), and $T_3$ (light grey line). . . . .	55
2.35 (a) Running RMS value and (b) and one-third octave band RMS level of the vertical total rail velocity during the passage of a Thalys train (200 km/h). The quasi-static (dashdotted line) and dynamic (dotted line) one-third octave band RMS value are superimposed. . . . .	56
2.36 (a) Running RMS value and (b) and one-third octave band RMS level of the vertical total free field velocity at 6 m, 12 m, 24 m, and 48 m during the passage of a Thalys train (200 km/h) for 10 unevenness samples based on FRA class 3 (black to grey lines). . . . .	58
2.37 (a) Time history and (b) running RMS value of the vertical free field velocity at 6 m, 12 m, 24 m, and 48 m during the passage of a Thalys train (200 km/h) computed with moving (black line) and fixed (grey line) axle loads. . . . .	61
2.38 One-third octave band RMS level of the vertical free field velocity at (a) 6 m, (b) 12 m, (c) 24 m, and (d) 48 m during the passage of a Thalys train (200 km/h) computed with moving (black line) and fixed (grey line) axle loads. . . . .	62
2.39 Modulus of the PSD of the vertical loads of a Thalys train for 26 coupled axles (grey lines) and a single uncoupled axle (black line). . . . .	63
2.40 PSD of the vertical free field velocity at (a) 6 m, (b) 12 m, (c) 24 m, and (d) 48 m during the passage of a Thalys train (200 km/h) computed with coherent (black line) and incoherent (grey line) axle loads. . . . .	64
2.41 One-third octave band RMS level of the vertical free field velocity at (a) 6 m, (b) 12 m, (c) 24 m, and (d) 48 m during the passage of a Thalys train (200 km/h) computed with coherent (black line) and incoherent (grey line) axle loads. . . . .	65
3.1 Plan of the site in Lincent [132]. . . . .	68

3.2	Cross section of the site in Lincent [132]. . . . .	68
3.3	View of (a) the measurement site and (b) the track in Lincent. . . . .	69
3.4	Local geology at the site in Lincent [69]. . . . .	71
3.5	Location of the SCPT and SASW tests at the site in Lincent. . . . .	72
3.6	(a) Shear wave velocity and (b) material damping ratio obtained from SCPT1, SCPT2, SASW1, and SASW2 at the site in Lincent. . . . .	73
3.7	Longitudinal wave velocity obtained from SR1 and SR2 at the site in Lincent . . . . .	74
3.8	Assumed geometry of the excavation at the site in Lincent. . . . .	75
3.9	Cross section of the 2.5D soil model for excitation (a) at the surface and (b) in the excavation. . . . .	76
3.10	Predicted mobility level at line C ( $y = 0$ m) at (a) 6 m, (b) 12 m, (c) 24 m, and (d) 48 m from the track center line for a source point at the surface (grey line) and in the excavation (black line) at $x = 5.05$ m and $y = 0$ m. . . . .	77
3.11	Measurement setup in the free field at the site in Lincent, indicating the receiver points (♣) and the source points at the track (■) and at the soil's surface adjacent to the track (■). . . . .	78
3.12	(a) Time history and (b) frequency content of the measured force during the first hammer impact at the soil's surface at $x = 5.05$ m and $y = 0$ m. . . . .	79
3.13	Measured vertical acceleration at line C ( $y = 0$ m) at (a) 6 m, (b) 12 m, (c) 24 m, and (d) 48 m from the track center line due to the first hammer impact at the soil's surface at $x = 5.05$ m and $y = 0$ m. . . . .	81
3.14	Measured vertical acceleration at line C ( $y = 0$ m) at (a) 6 m, (b) 12 m, (c) 24 m, and (d) 48 m from the track center line stacked for 100 hammer impacts at the soil's surface at $x = 5.05$ m and $y = 0$ m. . . . .	81
3.15	Predicted (grey line) and measured (black line) free field mobility level and confidence interval (grey region) at line C ( $y = 0$ m) at (a) 6 m, (b) 12 m, (c) 24 m, and (d) 48 m from the track center line for a source point at the soil's surface at $x = 5.05$ m and $y = 0$ m. . . . .	83

3.16	Predicted (grey line) and measured (black line) one-third octave band free field mobility level and confidence interval (grey region) at line C ( $y = 0$ m) at (a) 6 m, (b) 12 m, (c) 24 m, and (d) 48 m from the track center line for a source point at the soil's surface at $x = 5.05$ m and $y = 0$ m. . . . .	84
3.17	Predicted (grey line) and measured (black line) free field mobility level and confidence interval (grey region) at line C ( $y = 0$ m) at (a) 6 m, (b) 12 m, (c) 24 m, and (d) 48 m from the track center line for a source point at the soil's surface at $x = 5.05$ m and $y = 40$ m. . . . .	86
3.18	Predicted (grey line) and measured (black line) one-third octave band free field mobility level and confidence interval (grey region) at line C ( $y = 0$ m) at (a) 6 m, (b) 12 m, (c) 24 m, and (d) 48 m from the track center line for a source point at the soil's surface at $x = 5.05$ m and $y = 40$ m. . . . .	86
3.19	One-third octave band free field mobility level measured at five different measurement lines (grey to black lines) at (a) 12 m and (b) 24 m from the track center line for source points at the soil's surface at $x = 5.05$ m and at the corresponding measurement line.	87
3.20	Cross section of the 2.5D track model used by Lombaert et al. [98].	88
3.21	Cross section of the 2.5D track-soil model for (a) model A, (b) model B, (c) model C, (d) model D, (e) model E, and (f) model F, where $h_e$ indicates the depth of the excavation and $h_s$ indicates the depth of the track subgrade. . . . .	92
3.22	(a) Modulus and (b) phase of the vertical rail receptance predicted with model A (grey line) and model B (black line). .	93
3.23	(a) Modulus and (b) phase of the vertical rail receptance predicted with model B (grey line) and model C (black line). .	93
3.24	(a) Modulus and (b) phase of the vertical rail receptance predicted with model B (grey line) and model D (black line). .	94
3.25	(a) Modulus and (b) phase of the vertical rail receptance predicted with model D (light grey line), model E (dark grey line), and model F (black line). . . . .	95
3.26	Position of the accelerometers and impact points used for the determination of the track receptance [78]. . . . .	96

3.27	View of the measurement setup for the determination of the track receptance in loaded conditions. The impact location F1 is indicated by the red arrow. . . . .	97
3.28	(a) Modulus and (b) phase of the measured vertical rail receptance in unloaded condition (grey lines) and loaded condition (black line). . . . .	98
3.29	(a) Modulus and (b) phase of the predicted (grey line) and measured (black line) vertical rail receptance at the site in Lincent before updating of the track parameters. . . . .	98
3.30	(a) Modulus and (b) phase of the predicted (grey line) and measured (black line) vertical rail receptance at the site in Lincent after updating the track parameters. . . . .	99
3.31	Predicted track – free field mobility level at line C ( $y = 0$ m) at (a) 6 m, (b) 12 m, (c) 24 m, and (d) 48 m from the track center line for a source point at the edge of the sleeper at $x = 1.10$ m and $y = 0$ m for model A (grey line) and model B (black line). .	102
3.32	Predicted track – free field mobility level at line C ( $y = 0$ m) at (a) 6 m, (b) 12 m, (c) 24 m, and (d) 48 m from the track center line for a source point at the edge of the sleeper at $x = 1.10$ m and $y = 0$ m with model B (grey line) and model D (black line). .	103
3.33	Predicted (grey line) and measured (black line) track – free field mobility level and confidence interval (grey region) at line C ( $y = 0$ m) at (a) 6 m, (b) 12 m, (c) 24 m, and (d) 48 m from the track center line for a source point at the edge of the sleeper at $x = 1.10$ m and $y = 0$ m. . . . .	106
3.34	Predicted (grey line) and measured (black line) one-third octave band track – free field mobility level and confidence interval (grey region) at line C ( $y = 0$ m) at (a) 6 m, (b) 12 m, (c) 24 m, and (d) 48 m from the track center line for a source point at the edge of the sleeper at $x = 1.10$ m and $y = 0$ m. . . . .	106
3.35	Predicted (grey line) and measured (black line) track – free field mobility level and confidence interval (grey region) at line C ( $y = 0$ m) at (a) 6 m, (b) 12 m, (c) 24 m, and (d) 48 m from the track center line for a source point at the edge of the sleeper at $x = 1.10$ m and $y = 40$ m. . . . .	107

3.36	Predicted (grey line) and measured (black line) one-third octave band track – free field mobility level and confidence interval (grey region) at line C ( $y = 0$ m) at (a) 6 m, (b) 12 m, (c) 24 m, and (d) 48 m from the track center line for a source point at the edge of the sleeper at $x = 1.10$ m and $y = 40$ m. . . . .	107
3.37	One-third octave band track – free field mobility level measured at five different measurement lines (grey to black lines) at (a) 12 m and (b) 24 m from the track center line for source points at the edge of the sleeper at $x = 1.10$ m and at the corresponding measurement line. . . . .	108
3.38	View of (a) an IC train and (b) a Thalys HST passing at the site in Lincent. . . . .	109
3.39	Configuration of the Thalys HST. . . . .	110
3.40	Measured (a) vertical and (b) horizontal unevenness of the right rail (grey line) and the left rail (black line) of track 1 at the site in Lincent. . . . .	111
3.41	Measured (solid black line) and fitted (dashed black line) PSD of the vertical rail unevenness at the site in Lincent and according to FRA class 1 (dark grey line) and class 6 (light grey line). The fitted PSD based on measurements in 2002 (dotted black line) is added as a reference [98]. . . . .	112
3.42	Modulus of a sample of vertical track unevenness generated for a train speed of 198 km/h (black line) and 300 km/h (grey line). . . . .	112
3.43	Measurement setup on the track indicating the position of the accelerometers at the rail (TR) and at the edge of the sleeper (TS). . . . .	113
3.44	Modulus of the (a) first and (b) fifth diagonal element of the vertical track compliance (dark grey line), vehicle compliance (light grey line), and combined compliance (black line) for an IC train (198 km/h). . . . .	115
3.45	Vertical dynamic load at the first axle of (a) the locomotive and (b) the first carriage of an IC train (198 km/h). . . . .	116
3.46	(a) Time history and (b) frequency content of the measured (black line) and predicted (1 unevenness sample, grey line) vertical rail velocity at line C during the passage of an IC train (198 km/h). . . . .	116



3.47 (a) Running RMS value and (b) one-third octave band RMS level of the measured (black line) and predicted (10 unevenness samples, grey lines) vertical rail velocity at line C during the passage of an IC train (198 km/h). . . . .	116
3.48 (a) Time history and (b) frequency content of the measured (black line) and predicted (1 unevenness sample, grey line) vertical free field velocity at line C ( $y = 0$ m) at (a) 6 m, (b) 12 m, (c) 24 m, and (d) 48 m from the track center line during the passage of an IC train (198 km/h). . . . .	119
3.49 (a) Running RMS value and (b) one-third octave band RMS level of the measured (black line) and predicted (10 unevenness samples, grey lines) vertical free field velocity at line C ( $y = 0$ m) at (a) 6 m, (b) 12 m, (c) 24 m, and (d) 48 m from the track center line during the passage of an IC train (198 km/h). . . . .	120
3.50 One-third octave band RMS level of the measured vertical free field velocity at line C ( $y = 0$ m) at (a) 6 m, (b) 12 m, (c) 24 m, and (d) 48 m from the track center line during the passage of 17 IC trains (193 – 203 km/h). . . . .	121
3.51 One-third octave band RMS level of the measured vertical free field velocity at five different measurement lines (grey to black lines) at (a) 12 m and (b) 24 m from the track center line during the passage of an IC train (198 km/h). . . . .	121
3.52 Modulus of the first diagonal element of the vertical track compliance (dark grey line), vehicle compliance (light grey line), and combined compliance (black line) for a Thalys train (300 km/h). . . . .	122
3.53 Vertical dynamic load at the first axle of the Thalys train (300 km/h). . . . .	122
3.54 (a) Time history and (b) frequency content of the measured (black line) and predicted (1 unevenness sample, grey line) vertical rail velocity at line C during the passage of a Thalys train (300 km/h). . . . .	123
3.55 (a) Running RMS value and (b) one-third octave band RMS level of the measured (black line) and predicted (10 unevenness samples, grey lines) vertical rail velocity at line C during the passage of a Thalys train (300 km/h). . . . .	123

3.56	(a) Time history and (b) frequency content of the measured (black line) and predicted (1 unevenness sample, grey line) vertical free field velocity at line C ( $y = 0$ m) at (a) 6 m, (b) 12 m, (c) 24 m, and (d) 48 m from the track center line during the passage of a Thalys train (300 km/h). . . . .	125
3.57	(a) Running RMS value and (b) one-third octave band RMS level of the measured (black line) and predicted (10 unevenness samples, grey lines) vertical free field velocity at line C ( $y = 0$ m) at (a) 6 m, (b) 12 m, (c) 24 m, and (d) 48 m from the track center line during the passage of a Thalys train (300 km/h). . . . .	126
3.58	One-third octave band RMS level of the measured vertical free field velocity at line C ( $y = 0$ m) at (a) 6 m, (b) 12 m, (c) 24 m, and (d) 48 m from the track center line during the passage of 5 Thalys trains (290 – 300 km/h). . . . .	127
3.59	One-third octave band RMS level of the measured vertical free field velocity at five different measurement lines (grey to black lines) at (a) 12 m and (b) 24 m from the track center line during the passage of a Thalys train (300 km/h). . . . .	127
3.60	Average one-third octave band RMS level of the measured vertical free field velocity at line C ( $y = 0$ m) at (a) 6 m, (b) 12 m, (c) 24 m, and (d) 48 m from the track center line during the passage of an IC train (198 km/h, black line) and a Thalys train (300 km/h, grey line). . . . .	128
4.1	Position of the source and receiver points at (a) the assessment site and (b) the measurement site for the case where a track is present at the assessment site. . . . .	136
4.2	Position of the source and receiver points at (a) the assessment site and (b) the measurement site for the case where no track is present at the assessment site. . . . .	137
4.3	Location of the source points for the determination of the line source transfer mobility level with (a) $n_a$ source points corresponding to the axle locations, (b) $n_b$ source points corresponding to the bogie locations, (c) $n_a$ equidistant source points, (d) $n$ equidistant source points with spacing $h$ , and (e) $n$ equidistant source points with spacing $h'$ including two edge points. . . . .	140

4.4	Predicted line source transfer mobility level at (a) 6 m, (b) 12 m, (c) 24 m, and (d) 48 m determined with source points corresponding to the axle locations of a Thalys train (grey line) and with equidistant points with a source length of 202 m and a source point spacing of 7.76 m (black line).	143
4.5	Predicted line source transfer mobility level at (a) 6 m, (b) 12 m, (c) 24 m, and (d) 48 m for a source length of 200 m and a source point spacing of 40 m, 20 m, 10 m, 6 m, and 3 m (grey to black lines).	144
4.6	Predicted line source transfer mobility level at (a) 6 m, (b) 12 m, (c) 24 m, and (d) 48 m for a source length of 100 m, 120 m, 140 m, 160 m, 180 m, and 200 m (grey to black lines) and a source point spacing of 10 m.	145
4.7	Position of the source point at the head of the right rail (RR) and the left rail (RL), at the edge of the sleeper (SE), and at the center of the sleeper (SC).	146
4.8	Position of the source point at a foundation installed at the soil's surface at the center line of the future track (FC) or adjacent to the track (FA).	147
4.9	Predicted line source transfer mobility level at (a) 6 m, (b) 12 m, (c) 24 m, and (d) 48 m determined with source points $\mathbf{X}_{RR}$ at the right rail (black line) and $\mathbf{X}_{RB}$ at both rails (grey line).	148
4.10	Predicted line source transfer mobility level at (a) 6 m, (b) 12 m, (c) 24 m, and (d) 48 m determined with source points $\mathbf{X}_{RB}$ at both rails (black line) and $\mathbf{X}_{SC}$ at the center of the sleeper (grey line).	149
4.11	Predicted line source transfer mobility level at (a) 6 m, (b) 12 m, (c) 24 m, and (d) 48 m determined with source points $\mathbf{X}_{RB}$ at both rails (grey line) and $\mathbf{X}_{SE}$ at the edge of the sleeper (black line).	150
4.12	Predicted line source transfer mobility level at (a) 6 m, (b) 12 m, (c) 24 m, and (d) 48 m determined with source points $\mathbf{X}_{RB}$ at both rails (black line) and $\mathbf{X}_{FC}$ at the soil's surface at the track center line (grey line).	150

- 4.13 Predicted line source transfer mobility level at (a) 6 m, (b) 12 m, (c) 24 m, and (d) 48 m determined with source points  $\mathbf{X}_{FC}$  at the soil's surface at the track center line (black line) and  $\mathbf{X}_{FA}$  at the soil's surface adjacent to the track (grey line). . . . . 151
- 4.14 Measured line source transfer mobility level at (a) 6 m, (b) 12 m, (c) 24 m, and (d) 48 m determined with source points  $\mathbf{X}_{SE}$  at the edge of the sleeper for a source length of 200 m and a source point spacing of 40 m, 20 m, and 10 m (grey to black lines). . . 152
- 4.15 Measured line source transfer mobility level at (a) 6 m, (b) 12 m, (c) 24 m, and (d) 48 m determined with source points  $\mathbf{X}_{SE}$  at the edge of the sleeper for a source length of 100 m, 120 m, 140 m, 160 m, 180 m, and 200 m (grey to black lines) and a source point spacing of 10 m. . . . . 153
- 4.16 Measured line source transfer mobility level at (a) 6 m, (b) 12 m, (c) 24 m, and (d) 48 m determined with source points  $\mathbf{X}_{SE}$  at the edge of the sleeper (black line) and  $\mathbf{X}_{FA}$  at the soil's surface adjacent to the track (grey line). . . . . 154
- 4.17 Predicted force density level based on the total response (black line) and the dynamic contribution (grey line) at (a) 6 m, (b) 12 m, (c) 24 m, and (d) 48 m for an IC train (198 km/h). . . . . 156
- 4.18 Predicted force density level based on the response at (a) 6 m, (b) 12 m, (c) 24 m, and (d) 48 m for an IC train (198 km/h) determined with source points  $\mathbf{X}_{RB}$  at both rails (black line),  $\mathbf{X}_{FC}$  at the soil's surface at the track center line (dark grey line) and  $\mathbf{X}_{FA}$  at the soil's surface adjacent to the track (light grey line). 157
- 4.19 Predicted force density level based on the response at 6 m to 64 m (grey to black lines) for an IC train (198 km/h) determined with source points (a)  $\mathbf{X}_{RB}$  at both rails and (b)  $\mathbf{X}_{RR}$  at the right rail. . . . . 159
- 4.20 Predicted force density level based on the response at 6 m to 64 m (grey to black lines) for an IC train (198 km/h) determined with source points (a)  $\mathbf{X}_{FC}$  at the soil's surface at the track center line and (b)  $\mathbf{X}_{FA}$  at the soil's surface adjacent to the track. . . . 159
- 4.21 Measured force density level based on the response at five different measurement lines (grey to black lines) at (a) 12 m and (b) 24 m from the track for an IC train (198 km/h). . . . . 160

4.22	Measured force density level based on the response at (a) 6 m, (b) 12 m, (c) 24 m, and (d) 48 m for 12 IC trains (192–200 km/h) (grey to black lines).	161
4.23	Measured force density level based on the response at (a) 6 m, (b) 12 m, (c) 24 m, and (d) 48 m for an IC train (198 km/h) determined with source points $\mathbf{X}_{SE}$ at the edge of the sleeper (black line) and $\mathbf{X}_{FA}$ at the soil's surface adjacent to the track (grey line).	162
4.24	Measured force density level based on the response at 6 m to 64 m (grey to black lines) for an IC train (198 km/h) determined with source points (a) $\mathbf{X}_{SE}$ at the edge of the sleeper and (b) $\mathbf{X}_{FA}$ at the soil's surface adjacent to the track.	164
4.25	Predicted vibration velocity level at (a) 6 m, (b) 12 m, (c) 24 m, and (d) 48 m for an IC train (200 km/h) at a site with soft, medium, and stiff soil (grey to black lines).	166
4.26	Predicted line source transfer mobility level at (a) 6 m, (b) 12 m, (c) 24 m, and (d) 48 m at a site with soft, medium, and stiff soil (grey to black lines) determined with source points $\mathbf{X}_{RB}$ at both rails.	167
4.27	Predicted line source transfer mobility level at (a) 6 m, (b) 12 m, (c) 24 m, and (d) 48 m at a site with soft, medium, and stiff soil (grey to black lines) determined with source points $\mathbf{X}_{FC}$ at the soil's surface at the track center line.	168
4.28	Predicted force density level based on the response at (a) 6 m, (b) 12 m, (c) 24 m, and (d) 48 m for an IC train (200 km/h) at a site with soft, medium, and stiff soil (grey to black lines) determined with source points $\mathbf{X}_{RB}$ at both rails.	169
4.29	Predicted force density level based on the response at (a) 6 m, (b) 12 m, (c) 24 m, and (d) 48 m for an IC train (200 km/h) at a site with soft, medium, and stiff soil (grey to black lines) determined with source points $\mathbf{X}_{FC}$ at the soil's surface at the track center line.	170
4.30	Predicted force density level based on the response at (a) 6 m, (b) 12 m, (c) 24 m, and (d) 48 m for an IC train (200 km/h) at a site with soft, medium, and stiff soil (grey to black lines) determined with source points $\mathbf{X}_{RB}$ at both rails for a track with subgrade.	171

4.31	Predicted vibration velocity level at (a) 6 m, (b) 12 m, (c) 24 m, and (d) 48 m for an IC train (200 km/h) at a track with soft, medium, and stiff rail pad (grey to black lines). . . . .	172
4.32	Predicted line source transfer mobility level at (a) 6 m, (b) 12 m, (c) 24 m, and (d) 48 m for a track with soft, medium, and stiff rail pad (grey to black lines) determined with source points $\mathbf{X}_{RB}$ at both rails. . . . .	173
4.33	Predicted force density level based on the response at (a) 6 m, (b) 12 m, (c) 24 m, and (d) 48 m for an IC train (200 km/h) at a track with soft, medium, and stiff rail pad (grey to black lines) determined with source points $\mathbf{X}_{RB}$ at both rails. . . . .	174
5.1	Directly predicted force density level for (a) an IC train (198 km/h) and (b) a Thalys train (300 km/h). . . . .	180
5.2	Measured line source transfer mobility level at 6 m, 12 m, 24 m, and 48 m (black to grey lines) for source points (a) $\mathbf{X}_{SE}$ at the edge of the sleeper and (b) $\mathbf{X}_{FA}$ at the soil's surface adjacent to the track. . . . .	180
5.3	Hybrid prediction based on a directly predicted force density level (light grey line), numerical prediction (dark grey line), and measured result (black line) of the vibration velocity level at (a) 6 m, (b) 12 m, (c) 24 m, and (d) 48 m for an IC train (198 km/h). . . . .	181
5.4	Hybrid prediction based on a directly predicted force density level (light grey line), numerical prediction (dark grey line), and measured result (black line) of the vibration velocity level at (a) 6 m, (b) 12 m, (c) 24 m, and (d) 48 m for a Thalys train (300 km/h). . . . .	182
5.5	Hybrid prediction based on a directly predicted force density level with correction for the source position (light grey line), numerical prediction (dark grey line), and measured result (black line) of the vibration velocity level at (a) 6 m, (b) 12 m, (c) 24 m, and (d) 48 m for an IC train (198 km/h). . . . .	183
5.6	Hybrid prediction based on a directly predicted force density level with correction for the source position (light grey line), numerical prediction (dark grey line), and measured result (black line) of the vibration velocity level at (a) 6 m, (b) 12 m, (c) 24 m, and (d) 48 m for a Thalys train (300 km/h). . . . .	184

5.7	Indirectly predicted force density level based on the response at 6 m, 12 m, 24 m, and 48 m (black to grey lines) for (a) an IC train (198 km/h) and (b) a Thalys train (300 km/h) determined with source points $\mathbf{X}_{SE}$ at the edge of the sleeper. . . . .	185
5.8	Indirectly predicted force density level based on the response at 6 m, 12 m, 24 m, and 48 m (black to grey lines) for (a) an IC train (198 km/h) and (b) a Thalys train (300 km/h) determined with source points $\mathbf{X}_{FA}$ at the soil's surface adjacent to the track. . .	185
5.9	Hybrid prediction based on an indirectly predicted force density level determined with source points $\mathbf{X}_{SE}$ at the edge of the sleeper (light grey line), numerical prediction (dark grey line), and measured result (black line) of the vibration velocity level at (a) 6 m, (b) 12 m, (c) 24 m, and (d) 48 m for an IC train (198 km/h). . . . .	187
5.10	Hybrid prediction based on an indirectly predicted force density level determined with source points $\mathbf{X}_{SE}$ at the edge of the sleeper (light grey line), numerical prediction (dark grey line), and measured result (black line) of the vibration velocity level at (a) 6 m, (b) 12 m, (c) 24 m, and (d) 48 m for a Thalys train (300 km/h). . . . .	187
5.11	Hybrid prediction based on an indirectly predicted force density level determined with source points $\mathbf{X}_{FA}$ at the soil's surface adjacent to the track (light grey line), numerical prediction (dark grey line), and measured result (black line) of the vibration velocity level at (a) 6 m, (b) 12 m, (c) 24 m, and (d) 48 m for an IC train (198 km/h). . . . .	188
5.12	Hybrid prediction based on an indirectly predicted force density level determined with source points $\mathbf{X}_{FA}$ at the soil's surface adjacent to the track (light grey line), numerical prediction (dark grey line), and measured result (black line) of the vibration velocity level at (a) 6 m, (b) 12 m, (c) 24 m, and (d) 48 m for a Thalys train (300 km/h). . . . .	188
5.13	Average measured force density level determined with source points $\mathbf{X}_{SE}$ at the edge of the sleeper for (a) IC trains (193 – 202 km/h) and (b) Thalys trains (291 – 300 km/h) based on the response at 6 m, 12 m, 24 m, and 48 m (black to grey lines). . . .	191

5.14	Average measured force density level determined with source points $\mathbf{X}_{FA}$ at the soil's surface adjacent to the track for (a) IC trains (193 – 202 km/h) and (b) Thalys trains (291 – 300 km/h) based on the response at 6 m, 12 m, 24 m, and 48 m (black to grey lines). . . . .	192
5.15	Predicted line source transfer mobility level determined with source points (a) $\mathbf{X}_{SE}$ at the edge of the sleeper and (b) $\mathbf{X}_{FA}$ at the soil's surface adjacent to the track at 6 m, 12 m, 24 m, and 48 m (black to grey lines). . . . .	192
5.16	Hybrid prediction based on a predicted line source transfer mobility level determined with source points $\mathbf{X}_{SE}$ at the edge of the sleeper (light grey line), numerical prediction (dark grey line), and measured result (black line) of the vibration velocity level at (a) 6 m, (b) 12 m, (c) 24 m, and (d) 48 m for an IC train (198 km/h). . . . .	194
5.17	Hybrid prediction based on a predicted line source transfer mobility level determined with source points $\mathbf{X}_{SE}$ at the edge of the sleeper (light grey line), numerical prediction (dark grey line), and measured result (black line) of the vibration velocity level at (a) 6 m, (b) 12 m, (c) 24 m, and (d) 48 m for a Thalys train (300 km/h). . . . .	194
5.18	Hybrid prediction based on a predicted line source transfer mobility level determined with source points $\mathbf{X}_{FA}$ at the soil's surface adjacent to the track (light grey line), numerical prediction (dark grey line), and measured result (black line) of the vibration velocity level at (a) 6 m, (b) 12 m, (c) 24 m, and (d) 48 m for an IC train (198 km/h). . . . .	196
5.19	Hybrid prediction based on a predicted line source transfer mobility level determined with source points $\mathbf{X}_{FA}$ at the soil's surface adjacent to the track (light grey line), numerical prediction (dark grey line), and measured result (black line) of the vibration velocity level at (a) 6 m, (b) 12 m, (c) 24 m, and (d) 48 m for a Thalys train (300 km/h). . . . .	196
5.20	Hybrid prediction with a numerical correction for the position of the source point (light grey line), numerical prediction (dark grey line), and measured result (black line) of the vibration velocity level at (a) 6 m, (b) 12 m, (c) 24 m, and (d) 48 m for an IC train (198 km/h). . . . .	198



5.21 Hybrid prediction with a numerical correction for the position of the source point (light grey line), numerical prediction (dark grey line), and measured result (black line) of the vibration velocity level at (a) 6 m, (b) 12 m, (c) 24 m, and (d) 48 m for a Thalys train (300 km/h). . . . . 199



# List of Tables

2.1	Dynamic soil characteristics of the homogeneous halfspace. . . . .	32
2.2	Dynamic soil characteristics of the layered halfspace. . . . .	36
2.3	Dynamic characteristics of the ballasted track. . . . .	40
2.4	Track quality parameters according to the FRA database [56]. . . . .	45
3.1	Dynamic soil characteristics at the site in Lincent obtained from SASW1 [10]. . . . .	75
3.2	Computational requirements for the track–soil models. . . . .	95
3.3	Results of the optimization process of the dynamic track parameters. . . . .	100
3.4	Dynamic characteristics of the ballasted track at the site in Lincent after updating the track receptance. . . . .	101
3.5	Geometrical and mass characteristics of the IC train. . . . .	109
3.6	Geometrical and mass characteristics of the Thalys HST. . . . .	110
4.1	Dynamic characteristics of the three soil types. . . . .	165
4.2	Dynamic characteristics of the track subgrade. . . . .	170
4.3	Dynamic characteristics of the three rail pads. . . . .	172



# Chapter 1

## Introduction

### 1.1 Problem outline

Railway induced vibration is an environmental problem with a large impact. The need for public transport has stimulated the construction of railways in densely populated urban areas, such as light rail systems and subway lines. Furthermore, the development of high speed train (HST) networks has significantly increased the speed of passenger trains, while the (desired) shift of freight transport to railway traffic leads to a larger loading and an increased number of freight trains. Due to these developments, the problem of railway induced vibration has gained considerable attention.

The problem of railway induced vibration is outlined in figure 1.1. At the source side, vibration is generated at the wheel/rail contact due to several excitation mechanisms, including moving static loads (quasi-static excitation), wheel/rail unevenness, variations in track stiffness, wheel/rail defects, and track discontinuities [66]. The vibration is transferred along the propagation path and is modified depending on the track and soil characteristics. At the receiver side, railway induced vibration excites the foundation of nearby buildings and results in structural vibration, also referred to as ground-borne vibration.

The assessment of ground-borne vibration in buildings is described in many (inter)national standards, including those of the British Standards Institution (BSI) [17], Deutsches Institut für Normung (DIN) [34, 35], International Standards Organization (ISO) [65], and Stichting Bouwresearch (SBR) [140–142].

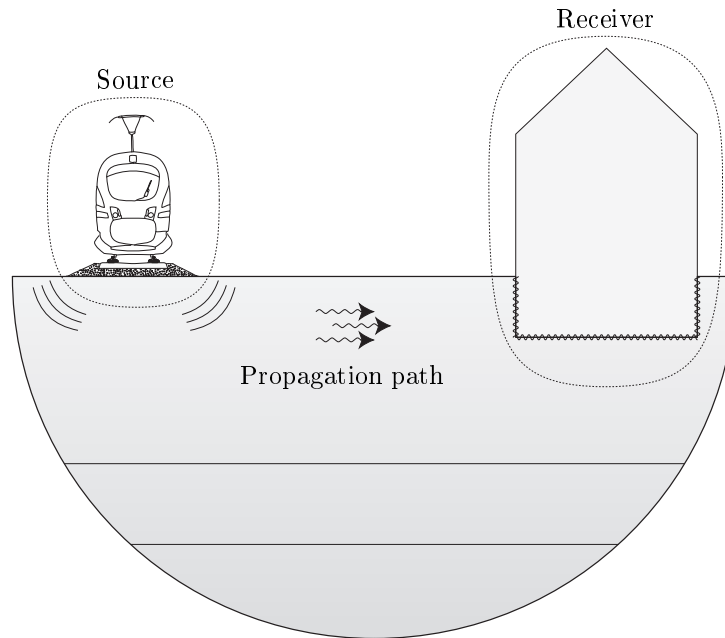


Figure 1.1: Problem outline.

At low amplitudes, ground-borne vibration may result in the malfunctioning of sensitive equipment or affect vibration-sensitive tasks such as microprocessor manufacturing and some forms of medical surgery [53, 66, 142]. Vibration criteria are typically described in terms of one-third octave band spectra and are in the order of magnitude of  $1 \mu\text{m/s}$ .

At higher amplitudes, railway induced vibration may cause hindrance to inhabitants of surrounding buildings [17, 34, 65, 141]. Ground-borne vibration is perceived as mechanical vibration of the human body in the frequency range from 1 to 80 Hz or as re-radiated noise by structural elements of a building such as walls, floors, and ceilings in the frequency range from 16 to 250 Hz [66]. The latter is also referred to as ground-borne noise as to distinguish from direct air-borne noise and typically causes problems in cases where air-borne noise is eliminated, e.g. in tunnels or by means of noise reducing measures. The amplitude at which vibration is perceived by humans and is in the order of magnitude of  $0.1 \text{ mm/s}$ . The perception of ground-borne noise strongly depends on the frequency.

At very high amplitudes, ground-borne vibration may even cause damage to buildings [35, 140]. Stress caused by extremely high vibration amplitudes can

cause direct damage to building components, while a large number of high amplitude vibration cycles can cause indirect damage through settlement of soils [66]. Vibration criteria are described in terms of maximum velocities and are in the order of magnitude of 10 mm/s [140].

Problems concerning ground-borne vibration arise due to the construction of new buildings close to railway tracks, due to the construction of new railway tracks in urban areas, or due to changes of the traffic (increase of the speed, load, or traffic volume) or the track condition (deterioration of the track quality). In order to reduce (expected) vibration amplitudes, vibration mitigation measures are taken at the source (e.g. soft rail pads, under sleeper pads, ballast mats), the propagation path (e.g. trenches, subgrade stiffening, wave impeding blocks), or the receiver (e.g. base isolation).

In order to prevent economical losses due to railway induced vibration, accurate prediction models are required during the design stage of new railways or buildings to identify areas where excessive vibration amplitudes are expected. Furthermore, the development and assessment of effective vibration mitigation measures requires accurate prediction models as well.

## 1.2 State of the art and further needs

The ISO standard 14873-1 [66] provides general guidance on the prediction of railway induced vibration and distinguishes between parametric, empirical, and hybrid models. Parametric models are derived from first principles and include analytical and numerical models. Empirical models are defined as models that are fully derived from measured data. Hybrid models are a combination of parametric and empirical models. This standard further indicates that the complexity of the model should reflect the design stage of new rail systems, where a distinction is made between scoping models (earliest stage), environmental assessment models (planning process), and detailed design models (part of construction and design).

In the following, a brief overview is presented of the state of the art regarding the numerical, empirical, and hybrid prediction of railway induced vibration and a number of needs is identified for these methods.

### Numerical models

Parametric models, including analytical and numerical models, offer a useful tool for the prediction of absolute levels of railway induced vibration when

sufficient data is available concerning the dynamic characteristics of the train-track-soil system. They are particularly convenient to study the efficiency of vibration mitigation measures, as they allow to gain physical insight in the mechanisms governing railway induced vibration.

Parametric models in an analytical form are well suited for the theoretical study of railway induced vibration, but their use is limited to relatively simple problems. The focus is therefore on numerical models that represent the problem domain in an approximate way, allowing to model more complex geometries. They have a wide range of application in the field of railway induced vibration. The numerical prediction of railway induced vibration (and noise) is comprehensively treated by Thompson [144] and an overview of existing methods is presented by Lombaert et al. [96].

As railway induced vibration leads to small strains and stresses in the track and the soil, it is generally studied by linear models allowing for a solution in the frequency domain. The study of non-linear effects requires a solution in the time domain. Recent examples are presented by Kouroussis et al. [81] and Connolly et al. [25].

The prediction of the response due to a moving train requires the prediction of the source and the vibration transfer. The source consists of the axle loads, where a distinction is generally made between static and dynamic loads. The vibration transfer is characterized by the track – free field transfer functions.

The contribution of the static axle loads of the moving train is referred to as the quasi-static response. Krylov and Ferguson [84] and Krylov [85] present a model where only the static load of axles moving on the track are taken into account. This model has been used and validated by Degrande and Lombaert [32] and Galvín and Domínguez [48]. A good agreement is found for receivers close to the track, while the agreement at larger distances is not good, as the quasi-static response quickly decreases with distance and only contributes to the response of the track and in the free field close to the track for train speeds well below the phase velocity of surface waves in the soil [60].

When the train speed is close to or exceeds the phase velocity of the surface waves, propagating waves are generated by the quasi-static excitation and a severe amplification of the free field response is observed. The critical velocities of constant moving loads are studied by Krylov [85] and Dieterman and Metrikine [36,37]. Supercritical train speeds are, for instance, obtained for HSTs on soft soils. High vibration levels have been measured for the passage of a X2000 train at the site in Ledsgård (Sweden) along the West Coast Line between Göteborg and Malmö [2]. These measurements have been used by Madshus and Kaynia [103] and Takemiya [143] to validate their numerical



models. For conventional tracks and HST tracks on common soil types, however, the train speeds are well below the phase velocities of surface waves in the soil and this problem is not encountered.

The contribution of the dynamic axle loads is referred to as the dynamic response. Dynamic axle loads are determined by different excitation mechanisms: parametric excitation due to spatial variation of the support stiffness, such as the discrete support of the rails or the change of stiffness in the track subgrade in transition zones, unevenness excitation due to wheel and rail unevenness, and impact excitation due to rail joints and wheel flats [60]. The computation of the dynamic response requires two steps: first, the dynamic axle loads are determined based on the train–track interaction and second, the axle loads are multiplied with the transfer functions [96].

The prediction of the dynamic axle loads is performed based on the dynamic interaction between the train and the track. For the problem of railway induced vibration, the dynamic behavior of the train can be approximated in the frequency range of interest by means of a relatively simple multi-body vehicle model. The prediction of the dynamic behavior of the track requires a much larger modeling effort [96], however. As the effect of the soil on the train–track interaction is significant, the dynamic track–soil interaction should be taken into account in the latter model [60].

A large number of numerical models has been developed to model the dynamic train–track–soil interaction and predict the dynamic axle loads and the track – free field transfer function. Models that only take into account quasi-static excitation lead to a good prediction of the track response and the free field response close to the track [32, 85]. In order to obtain a good prediction of the free field response at a larger distance from the track, however, dynamic excitation should be taken into account as well [7, 49, 94, 137].

A distinction between different models can be made based on the assumed geometry of the track–soil system. The most detailed models are fully 3D finite element (FE) models, offering the flexibility to model complex geometries. In this case, the infinite dimensions of the soil should be accounted for, e.g. by means of absorbing boundary conditions [39, 40] or infinite elements [80, 81]. Alternatively, the infinite dimensions of the unbounded soil are inherently taken into account by coupling the FE model of the track to a boundary element (BE) model [48, 50] of the soil. The BE method improves the efficiency of the model at the expense of a reduced flexibility, as it relies on simplifying assumptions such as a horizontal soil layering in order to employ fundamental solutions of the soil domain. These models can be used to analyze local discontinuities, underpasses, and coupling with nearby structures that break the uniformity of the geometry along the track line [50]. The main disadvantage of 3D models

is that they require the modeling of a large part of the track–soil domain and are therefore computationally demanding.

When the geometry of the track and soil is assumed invariant in the longitudinal direction of the track, an efficient computational model is obtained by a Fourier transformation with respect to the longitudinal coordinate and the problem is solved in the wavenumber–frequency domain [6, 20]. These so-called 2.5D approaches only require the solution of a 2D problem for each frequency and wavenumber. Due to their computational efficiency, they are used by a large number of researchers [96], e.g. the research groups at ISVR [134–137], BAM [7], TU Delft [36, 106], TU Munich [55], NGI [73, 103], KU Leuven [94, 98], and University of Seville [49].

Due to the assumption of longitudinal invariance, 2.5D models do not allow to account for periodic rail support, e.g. as in conventional ballasted tracks, or for parametric excitation, unless represented as an equivalent geometric unevenness [7]. This problem is avoided by assuming a periodic instead of an invariant geometry, by using a Floquet transform instead of a Fourier transform [21, 22, 24, 31].

Of particular interest in the previously discussed track–soil interaction models is the distribution of the load at the track–soil interface, which is often modeled in a simplified way. In early models, the track is modeled as a simple beam supported by a Winkler foundation [47, 54, 75]. Dieterman and Metrikine [36] and Metrikine and Popp [107] present a simple beam model for the track supported by an elastic halfspace where the soil’s impedance is calculated analytically. The track–soil interaction problem is simplified, assuming a smooth contact between the track and the soil and a uniform stress distribution along the cross section of the track. The assumption of a smooth contact corresponds to the application of relaxed boundary conditions in a BE model. Furthermore, the continuity of displacements is only enforced at the beam’s axis. Similar assumptions are made by Lieb and Sudret [93] and by Sheng et al. [134, 135].

Kaynia et al. [73] and Madshus and Kaynia [103] model the track by coupled beam elements, assuming a smooth contact between the track and the soil. The coupling of the track to the soil is enforced at the nodes of the beam elements. The calculation of the soil’s impedance is based on the Green’s functions for disk loads on a horizontally layered elastic halfspace.

With the increase of computing power, more detailed track models have been presented that more accurately represent the distribution of the load from the rails to the soil. Lombaert et al. [98] present a multi degree-of-freedom FE model for the track including the rails, rail pads, sleeper, and the ballast layer.

The ballast layer is modeled as a spring–damper connection, simplifying the load distribution from the sleeper to the soil. No simplifying assumptions are made regarding the contact conditions between the track and the halfspace. Similar track models are presented by Galvín et al. [49], Auersch [7], Knothe and Wu [76], Kouroussis et al. [82], and Sheng et al. [134]. Hildebrand [61] presents a model where the ballast is taken into account as a layer of the supporting halfspace, disregarding its finite lateral dimensions. The dynamic behavior of different track models is compared by Auersch [9].

In the previously discussed track models, the track subgrade is often disregarded, while it has a considerable influence in the frequency range below 200 Hz [76]. Knothe and Wu [76] and Hildebrand [61] take into account the track subgrade as a layer of the supporting soil, disregarding its finite lateral dimensions. Recently, more detailed track models have been presented that additionally include a sub-ballast and subgrade [25] or an embankment [25,49].

Numerical models provide a valuable approach for the prediction of railway induced vibration and have contributed to a better understanding of the governing physical mechanisms. They have some important limitations as well, however.

First, simplifying assumptions that are introduced to improve the efficiency of numerical models may be too restrictive. For instance, deviations up to 10 dB are found by assuming a horizontal soil stratification [68]. Furthermore, the load distribution from the rails to the soil is often modeled in a simplified way. The increase of computing power has led to more complex models that allow for a detailed modeling of different track components. The impact of commonly made simplifications to increase the efficiency is not fully understood, however.

Second, even when numerical models adequately represent the track and soil, they crucially depend on accurate input parameters that are subject to significant uncertainty. Soil parameters are generally identified from preliminary site investigation. Track parameters for existing tracks are identified based on measurements, whereas they are based on experience or design values in case of new-build situations. Preliminary measurements do not allow to completely eliminate the uncertainty in the predicted transfer functions [133] or track response [94], however. Deviations due to parameter uncertainty are expected to be of the same order of magnitude as those arising from model uncertainty [64]. Model and parameter uncertainty can be eliminated when direct use is made of experimental data, e.g. measured transfer functions, as in empirical models.

The most important research needs that follow from the previous discussion are the following: (1) simplifying assumptions that are commonly made to

improve the efficiency of numerical models should be assessed by means of a detailed numerical model; (2) the direct incorporation of experimental data in numerical predictions needs to be investigated, as to eliminate model and parameter uncertainty where possible.

### Empirical models

Although a large number of numerical models has recently been developed, they are still mainly used for research and are only slowly finding their way to engineering practice where empirical models are widely used. The ISO standard [66] defines empirical models as models that are fully derived from measured data by extrapolation from, or interpolation within, the measured data sets. Elementary models provide a simple formula based on a large database of measurements and are used in earlier design stages. More detailed models offer a prediction of the vibration amplitude  $A(f)$  as a function of the frequency  $f$  based on the following fundamental expression [66]:

$$A(f) = S(f)P(f)R(f) \quad (1.1)$$

where the source term  $S(f)$ , the propagation term  $P(f)$ , and the receiver term  $R(f)$  are determined experimentally. The receiver term  $R(f)$  represents the modification of the ground-borne vibration amplitude due to the coupling between the soil and a receiver, e.g. a building. In the present work, the focus is on the prediction of the free field vibration amplitude and the receiver term  $R(f)$  is not considered.

In equation (1.1), the response at a certain frequency  $f$  is predicted as the product of different terms at the same frequency. This expression is therefore strictly speaking only valid for fixed sources. This is the fundamental assumption of empirical models that are based on equation (1.1).

A number of empirical models has been developed for the prediction of ground-borne vibration for railway traffic at grade. These methods mainly originate from earlier models, dating back to the 1970s, for the prediction of ground-borne noise due to railway traffic in tunnels, as ground-borne noise and vibration is generally overshadowed by directly generated air-borne noise for tracks at grade. These models are based on a reference vibration level, providing corrections for the train, track, and soil [88, 147] and for the distance from the source [87, 91]. A more detailed model is based on a chain of transmission losses within the source–path–receiver system [105]. An overview of mainly empirical methods used at the time is given by Manning et al. [104]

and Nelson and Saurenman [109]. The prediction and control of railway induced noise and vibration is comprehensively treated by Saurenman et al. [125].

Most of the previous methods are so-called multiple site models and formulate a relationship between the governing parameters and the resulting (noise and) vibration levels based on a large set of measurements. In particular circumstances, not covered by the range of measurements, deviations will occur from this relationship, as indicated by Bovey [15]. Motivated by this observation, Bovey [15] introduces the impact method to determine the vibration transfer characteristics of railway systems by directly measuring the vibration transfer from the railway to the free field or a building [113]. This results in a so-called single site model where the vibration transfer is measured at a single site.

The impact method of Bovey [15] is further elaborated by Nelson and Saurenman [110] into a prediction procedure for ground-borne noise and vibration, introducing the concept of a force density to represent particular vehicle and track systems. This method has been developed with the support of the U.S. Department of Transportation (DOT) and has been adopted as a standard prediction procedure for vibration induced by railway traffic at grade or in tunnels. More recently, the introduction of HST networks has stimulated the extension of the U.S. DOT prediction method, which has been assessed for several HSTs in Europe [57, 123]. This method is called the Detailed Vibration Assessment and is contained as a detailed design model in the manuals of the U.S. DOT Federal Railroad Administration (FRA) [58] and Federal Transit Administration (FTA) [59]. These manuals additionally present the Screening Procedure and the Generalized Vibration Assessment as prediction models suited for earlier design stages.

Recently, more empirical prediction models for railway induced vibration have been presented. Kuppelwieser and Ziegler [86] and Ziegler [161] present a two-level empirical prediction method VIBRA-1-2 with increasing complexity for different design stages and a database program VIBRA-3, developed for the Swiss Federal Railways (SBB). Madshus et al. [102] propose a detailed design method based on measurements in Norway and Sweden and additionally consider the issue of prediction uncertainty. A similar method has been developed by Hood et al. [63] within the frame of the Channel Tunnel Rail Link in the United Kingdom. Bahrekazemi [11] presents the semi-empirical models ENVIB-1 and ENVIB-2, serving as early design stage models, which are validated with measurements in Sweden [155].

In a single site model, the empirical prediction of the free field vibration level is based on the extrapolation of a measured source term  $S(f)$  that allows for a prediction at sites where the propagation term  $P(f)$  has been determined.

Compared to numerical models, the experimental characterization of the source and the propagation path offers the advantage that the train, track, and soil characteristics are inherently taken into account, avoiding the identification of model parameters and the introduction of simplifying assumptions, e.g. concerning the problem geometry. The application of empirical models is limited, however, to cases where the extrapolation of the measured source term  $S(f)$  is valid.

Empirical methods are used to predict absolute vibration levels as well as relative levels, e.g. to assess the efficiency of mitigation measures. Their application is widespread and they have proven their practical value to provide a correct assessment of ground-borne vibration. Most empirical methods are still based on the assumptions originally made [124], however, and there is a lack of clear physical understanding of these underlying assumptions. For instance, empirical models are subject to uncertainty arising during the experimental characterization of the source and the propagation path. Furthermore, the extrapolation of a measured source term  $S(f)$  is expected to have a significant influence on the prediction accuracy. It is therefore not very clear what the limitations of empirical methods are.

The main research need is to provide a critical assessment of empirical models in order to provide a better theoretical background and define their limitations.

### Hybrid models

Hybrid or semi-empirical models combine data obtained from measurements and numerical simulations [66]. This approach can be used to extend the application area of empirical models, e.g. by modifying the source term to include the presence of a mitigation measure.

Some empirical models are partially based on theoretical principles, e.g. when a measured source characterization is combined with an analytical attenuation law for the characterization of the propagation path [86,102,161]. These models can to some extent be regarded as hybrid models. The present state of the art in the numerical prediction of railway induced vibration allows for more elaborate hybrid models, however.

Whereas numerical models offer the flexibility to cover a great variety in train, track, and soil characteristics, they crucially depend on accurate input parameters for the prediction of vibration. Empirical models offer the advantage that the local characteristics are inherently taken into account in measured data, but the application of empirical predictions is limited by

the availability of accurate experimental input data. In hybrid models, the advantages of both approaches are combined.

As little information is available concerning hybrid methods, the main research need is the development of a hybrid model in order to improve the accuracy or extend the applicability of numerical and empirical predictions. These models should be assessed in terms of their accuracy and their added value in comparison with numerical and empirical models.

### 1.3 Objectives and contributions of the thesis

In this work, the numerical, empirical, and hybrid prediction of railway induced vibration is investigated.

Due to the increase of computing power, numerical models have recently been developed that represent the track–soil system with large detail. As these models are computationally very demanding, simplified models are still advantageous, provided that they offer sufficient accuracy. A first objective of this thesis is to investigate the influence of commonly made assumptions to simplify numerical models and improve their efficiency. For this purpose, a numerical model is used that represents the track–soil system in detail.

The numerical model is validated in different steps. An elaborate measurement campaign is therefore carried out at a site in Lincent (Belgium), measuring transfer functions and the response during train passages. The dynamic soil characteristics are identified from preliminary site investigation, while the track parameters are calibrated based on a measured track stiffness. The aim is to obtain a better fit between measured and predicted results.

The empirical prediction of railway induced vibration generally relies on a separate characterization of the source and the propagation path, as shown in equation (1.1). In the FRA procedure, their levels are represented by the force density level and the line source transfer mobility level, respectively. The vibration velocity level is predicted as the sum of both levels. This is strictly speaking not valid for moving sources such as a train. One of the objectives of this work is therefore to provide a better understanding of the underlying assumptions made in empirical methods.

At the same time, this work aims to critically assess empirical models and therefore uses numerical simulations as well as measurement results. This investigation is carried out for the site in Lincent, for which a calibrated numerical model as well as extensive experimental data are available.

Hybrid methods are a combination of numerical and empirical methods. Little information is available about the accuracy obtained with hybrid models. One of the objectives of the present work is the development of a hybrid model. Therefore, the previously discussed numerical and empirical models are combined. The numerical model and experimental data available for the site in Lincent allow for hybrid predictions at this site and a comparison with the other models.

The original contributions of the present work are the following:

- A detailed track–soil interaction model is used to assess the influence of some commonly made simplifying assumptions to improve the efficiency of numerical models. This study is based on the results for the site in Lincent, where a track in excavation is present. It is shown that the excavation and the track subgrade have a significant influence on the track stiffness, while their influence on the (track –) free field transfer functions remains limited. The track stiffness is mainly determined by the track and soil characteristics underneath the track. This observation justifies the introduction of simplifying assumptions and allows to use equivalent models that require a smaller computational effort to calculate the track stiffness.
- An elaborate measurement campaign has been carried out, measuring transfer functions and the response during train passages. Compared to previous measurements, an increased number of source points is used for the determination of the transfer functions, allowing to characterize the transfer due to a line load. Furthermore, the free field transfer functions as well as the track – free field transfer functions are determined in order to assess the influence of the track–soil interaction on the vibration transfer. The precision of the transfer functions is assessed by means of uncertainty quantification on the measured data. The experimental results allow for the validation of the numerical model, as well as for the assessment of the empirical and hybrid models.
- It is shown that the stationary part of the free field response is well approximated by introducing the assumptions of fixed and incoherent axle loads. This observation allows to derive analytical expressions for the force density and the line source transfer mobility that are directly related to the axle loads and the transfer functions and provides a better insight in empirical models. Furthermore, they allow for a numerical prediction of these terms that can be used in a hybrid model.
- The empirical FRA procedure is comprehensively analyzed by means of numerical simulations and experimental data. This analysis allows to



formulate (1) recommendations for a correct experimental application and (2) explore limitations of the empirical model.

- A hybrid model is presented that is more detailed than existing hybrid or semi-empirical models. Different hybrid approaches are used to predict the vibration at the site in Lincent and the results are compared with numerical predictions and measured results.

## 1.4 Organization of the text

**Chapter 1** introduces the problem of railway induced vibration. The state of the art of numerical, empirical, and hybrid models is discussed, highlighting further research needs that lead to the objectives of this thesis.

**Chapter 2** presents a numerical model, consisting of different submodels. The model is illustrated by means of a numerical example, elucidating some particular aspects of railway induced vibration. Furthermore, it is shown that the stationary part of the free field response is well approximated by considering the response due to fixed and incoherent axle loads.

**Chapter 3** treats the experimental validation of the numerical model at the site in Lincent in different steps. First, the relevant dynamic characteristics are identified for each submodel. Next, the influence of commonly made simplifying assumptions is investigated. Finally, the predictions of each submodel are validated based on the presented measurement results.

**Chapter 4** discusses empirical prediction models for railway induced vibration, highlighting the FRA procedure. An analytical expression is derived that relates the FRA procedure to the governing equations of railway induced vibration and provides a theoretical interpretation. Furthermore, the FRA procedure is comprehensively analyzed by means of numerical simulations and experimental data allowing to formulate recommendations for a correct application of the empirical model and to highlight its limitations.

**Chapter 5** presents a number of hybrid approaches for the prediction of railway induced vibration based on the empirical FRA procedure. In these approaches, either the source term or the propagation term is predicted numerically or a numerical correction of the empirical data is made. The hybrid prediction is validated at the site in Lincent where it is compared with the numerical prediction and the experimental results.

**Chapter 6** finally summarizes the most important conclusions of this work and discusses some recommendations for further research.



## Chapter 2

# Numerical methods

### 2.1 Introduction

This chapter discusses the numerical prediction of railway induced vibration based on different submodels. An existing model is introduced and is applied to specific cases within the present work. The model is a 2.5D coupled FE-BE model [46] that is based on the model of Lombaert et al. [98].

First, the response to moving loads is considered in section 2.2, distinguishing between quasi-static and dynamic excitation. The computation of the dynamic axle loads is based on a compliance formulation of the vehicle and the track and is treated in section 2.3.

In section 2.4, the track–soil interaction model of a ballasted track is introduced. Compared to the model of Lombaert et al. [98], the ballast is modeled as an elastic continuum and additional layers can be taken into account to model the track subgrade or an embankment. Furthermore, the model allows to represent a track in excavation by modeling the free surface of the excavation.

The numerical prediction is illustrated in different steps by means of a numerical example, elucidating some particular aspects of railway induced vibration. In particular, it reveals that the response due to a train passage is characterized by an approximately stationary vibration amplitude during the passage. It is shown in section 2.6 that this quasi-stationary part is well approximated by considering the response due to fixed and incoherent axle loads.

The conclusion is presented in section 2.7.

## 2.2 The response to moving loads

The response of the coupled track-soil system due to multiple moving loads is calculated based on the axle loads and the track – free field transfer functions. The transfer functions are calculated by means of the numerical track–soil interaction model presented in section 2.4. For the axle loads, a distinction is made between static (constant) and dynamic axle loads. The calculation of the dynamic axle loads is treated in section 2.3. The analytical derivation presented in these sections is derived from the work of Lombaert and Degrande [94].

### 2.2.1 General formulation

The response of the coupled track–soil system, shown in figure 2.1, due to multiple moving loads is calculated from the  $3 \times 3$  transfer matrix  $\mathbf{H}(\mathbf{x}', \mathbf{x}, t)$  of the coupled track-soil system. Each element  $h_{ij}(\mathbf{x}', \mathbf{x}, t)$  of this matrix represents the displacement at a point  $\mathbf{x}$  in the direction  $\mathbf{e}_j$  at a time  $t$  due to an impulsive load at a point  $\mathbf{x}'$  in the direction  $\mathbf{e}_i$  at the time  $t = 0$ . The displacement  $\mathbf{u}(\mathbf{x}', t)$  due to an arbitrary body load  $\rho\mathbf{b}(\mathbf{x}, t)$  is calculated as follows [23, 94]:

$$\mathbf{u}(\mathbf{x}', t) = \int_{-\infty}^t \int_{\Omega} \mathbf{H}(\mathbf{x}', \mathbf{x}, t - \tau) \rho\mathbf{b}(\mathbf{x}, \tau) \, d\mathbf{x} \, d\tau \quad (2.1)$$

where  $\Omega$  is the domain of the coupled track-soil system. In the following, dynamic reciprocity is used to replace the matrix  $\mathbf{H}(\mathbf{x}', \mathbf{x}, t)$  by  $\mathbf{H}^T(\mathbf{x}, \mathbf{x}', t)$ .

For  $n_a$  axle loads  $\mathbf{g}_k(t)$  moving at a constant speed  $v$  in the direction  $\mathbf{e}_y$  (figure 2.1), the body force  $\rho\mathbf{b}(\mathbf{x}, t)$  is equal to:

$$\rho\mathbf{b}(\mathbf{x}, t) = \sum_{k=1}^{n_a} \delta(\mathbf{x} - \mathbf{x}_k(t)) \mathbf{g}_k(t) \quad (2.2)$$

where  $\mathbf{x}_k(t) = \mathbf{x}_{k0} + vt\mathbf{e}_y$  is the time dependent position of the  $k$ -th axle load,  $\mathbf{x}_{k0}$  is the position at the time  $t = 0$  and  $\mathbf{g}_k(t)$  is a vector that contains the time histories of the  $k$ -th axle load in each direction. The axle loads are assumed to be positive when their action on the track is in the positive coordinate direction (figure 2.1).

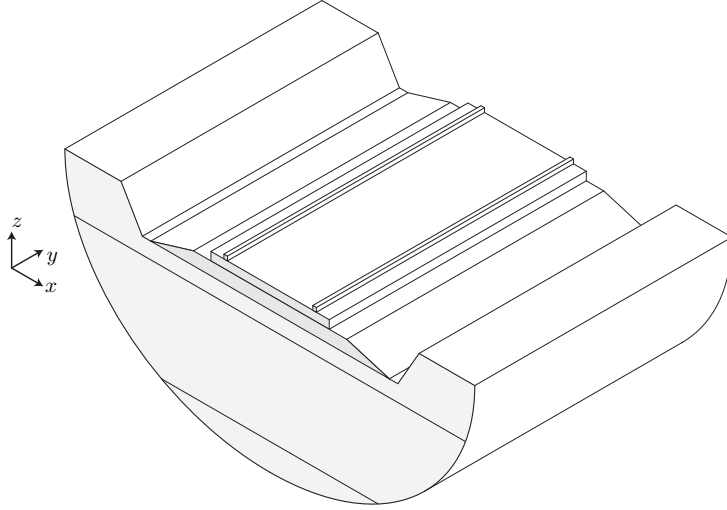


Figure 2.1: A longitudinally invariant track–soil domain.

Introducing equation (2.2) in equation (2.1), the response due to the moving loads is calculated as follows:

$$\mathbf{u}(\mathbf{x}', t) = \sum_{k=1}^{n_a} \int_{-\infty}^t \mathbf{H}^T(\mathbf{x}_k(\tau), \mathbf{x}', t - \tau) \mathbf{g}_k(\tau) d\tau \quad (2.3)$$

In the particular case where the track–soil domain  $\Omega$  is invariant in the longitudinal direction  $\mathbf{e}_y$  (figure 2.1), the transfer function is unaffected by an arbitrary translation  $l\mathbf{e}_y$  of the source and the receiver position. If  $l$  equals  $-(y_{k0} + v\tau)$ , the source position  $\mathbf{x}_k(\tau) + l\mathbf{e}_y = \{x_{k0}, 0, z_{k0}\}^T$  no longer depends on the time  $\tau$  and can be omitted in the argument of the transfer function. Furthermore, the coordinates  $x'$  and  $z'$  of the receiver position  $\mathbf{x}' = \{x', y', z'\}^T$  are assumed to be fixed and are omitted, so that equation (2.3) is rewritten as follows:

$$\mathbf{u}(y', t) = \sum_{k=1}^{n_a} \int_{-\infty}^t \mathbf{H}^T(y' - y_{k0} - v\tau, t - \tau) \mathbf{g}_k(\tau) d\tau \quad (2.4)$$

In the following, the prime denoting the receiver point is omitted.

The invariance in the longitudinal direction  $\mathbf{e}_y$  allows for a double forward Fourier transform from the space–time domain  $(y, t)$  to the wavenumber–

frequency domain  $(k_y, \omega)$ . For an arbitrary function  $f(y, t)$  in the space–time domain, the Fourier transform pair used for the transformation between the time domain and the frequency domain is defined as:

$$\hat{f}(y, \omega) = \int_{-\infty}^{+\infty} f(y, t) \exp(-i\omega t) dt \quad (2.5)$$

$$f(y, t) = \frac{1}{2\pi} \int_{-\infty}^{+\infty} \hat{f}(y, \omega) \exp(+i\omega t) d\omega \quad (2.6)$$

where  $\hat{f}(y, \omega)$  is the Fourier transform in the space–frequency domain, denoted by a hat.

The Fourier transform pair used for the transformation between the spatial domain and the wavenumber domain is defined as:

$$\tilde{f}(k_y, \omega) = \int_{-\infty}^{+\infty} \hat{f}(y, \omega) \exp(+ik_y y) dy \quad (2.7)$$

$$\hat{f}(y, \omega) = \frac{1}{2\pi} \int_{-\infty}^{+\infty} \tilde{f}(k_y, \omega) \exp(-ik_y y) dk_y \quad (2.8)$$

where  $\tilde{f}(k_y, \omega)$  is the Fourier transform in the wavenumber–frequency domain, denoted by a tilde.

The double forward Fourier transform of equation (2.4) leads to the following expression [23]:

$$\tilde{\mathbf{u}}(k_y, \omega) = \sum_{k=1}^{n_a} \tilde{\mathbf{H}}^T(k_y, \omega) \hat{\mathbf{g}}_k(\omega - k_y v) \exp(+ik_y y_{k0}) \quad (2.9)$$

An inverse wavenumber transform gives the frequency content of the response:

$$\hat{\mathbf{u}}(y, \omega) = \sum_{k=1}^{n_a} \frac{1}{2\pi} \int_{-\infty}^{+\infty} \tilde{\mathbf{H}}^T(k_y, \omega) \hat{\mathbf{g}}_k(\omega - k_y v) \times \exp[-ik_y(y - y_{k0})] dk_y \quad (2.10)$$

In equation (2.10), the transfer function  $\tilde{\mathbf{H}}^T(k_y, \omega)$  is calculated in the wavenumber–frequency domain and the axle loads  $\hat{\mathbf{g}}_k(\omega)$  are calculated in the frequency domain. In the following subsections, the axle loads are decomposed and the quasi-static contribution and the dynamic contribution to the response are discussed.

### 2.2.2 Quasi-static contribution

Due to the motion of the train, the response due to the static axle loads is time dependent. For train speeds well below the wave velocities in the soil, the quasi-static response is determined by the time dependent deflection of a fixed point due to the traveling axles of the train.

The quasi-static contribution to the track and free field response is found from the static component  $\mathbf{g}_{sk} = w_k \mathbf{e}_z$  of the axle loads, where  $w_k$  is the total weight carried by the  $k$ -th axle. Introducing the Fourier transform  $\hat{\mathbf{g}}_{sk}(\omega) = w_k \mathbf{e}_z 2\pi \delta(\omega)$  in equation (2.10) gives the quasi-static response [94]:

$$\hat{\mathbf{u}}(y, \omega) = \left[ \frac{w_l}{v} \tilde{\mathbf{H}}^T \left( \frac{\omega}{v}, \omega \right) \mathbf{e}_z \exp \left( -i \frac{\omega}{v} y \right) \right] \left[ \sum_{k=1}^{n_a} \frac{w_k}{w_l} \exp \left( +i \frac{\omega}{v} y_{k0} \right) \right] \quad (2.11)$$

The first bracketed term on the right hand side of equation (2.11) is the response due to a single axle with total weight  $w_l$ . The second bracketed term on the right hand side of equation (2.11) represents a modification of the response, resulting in the characteristic peaks and troughs, and is determined by the ratio of the axle weights  $w_k/w_l$ , the distribution of the axles, and the train speed  $v$  [7, 8, 32]. This term is sometimes referred to as the signature of the train.

### 2.2.3 Dynamic contribution

The dynamic contribution to the track and free field response is found by introducing the dynamic axle loads  $\hat{\mathbf{g}}_{dk}(\omega)$  in equation (2.10):

$$\hat{\mathbf{u}}(y, \omega) = \sum_{k=1}^{n_a} \frac{1}{2\pi} \int_{-\infty}^{+\infty} \tilde{\mathbf{H}}^T(k_y, \omega) \hat{\mathbf{g}}_{dk}(\omega - k_y v) \times \exp[-ik_y(y - y_{k0})] dk_y \quad (2.12)$$

The speed of the train results in a phase shift  $k_y v$  in the axle load spectrum. The response at a certain frequency is therefore not related to an excitation at the same frequency. A change of variables  $\tilde{\omega} = \omega - k_y v$  in equation (2.12) results in the following expression:

$$\hat{\mathbf{u}}(y, \omega) = \sum_{k=1}^{n_a} \frac{1}{2\pi v} \int_{-\infty}^{+\infty} \tilde{\mathbf{H}}^T \left( \frac{\omega - \tilde{\omega}}{v}, \omega \right) \hat{\mathbf{g}}_{dk}(\tilde{\omega}) \times \exp \left[ -i \left( \frac{\omega - \tilde{\omega}}{v} \right) (y - y_{k0}) \right] dk_y \quad (2.13)$$

The relations  $k_y = (\omega - \tilde{\omega})/v$  and  $C_y = \omega/k_y$ , with  $C_y$  the phase velocity in the direction  $\mathbf{e}_y$ , are used to write the circular frequency  $\omega$  at the receiver as  $\omega = \tilde{\omega}/(1 - v/C_y)$ . When the source approaches, the waves between the source and the receiver travel in the positive direction  $\mathbf{e}_y$  and have a positive phase velocity  $C_y$ . The circular frequency  $\tilde{\omega}$  emitted at the source results in higher frequencies  $\tilde{\omega}/(1 - v/C_y)$  at the receiver. When the source recedes, the waves between the source and the receiver travel in the negative direction  $\mathbf{e}_y$  and have a negative phase velocity  $C_y$ . The circular frequency  $\tilde{\omega}$  emitted at the source results in lower frequencies  $\tilde{\omega}/(1 + v/C_y)$  at the receiver. This phenomenon is known as the Doppler effect [95]. Due to the Doppler effect, a source at a fixed frequency  $\tilde{\omega}$  contributes to the response in a frequency range  $[\tilde{\omega}/(1 + v/C_y), \tilde{\omega}/(1 - v/C_y)]$ , determined by the smallest phase velocity  $C_y$  of interest [94].

## 2.3 The dynamic axle loads

The dynamic axle loads  $\hat{\mathbf{g}}_{dk}(\omega)$  in equation (2.12) are determined by the dynamic interaction between the train and the track and are generated by several excitation mechanisms. In the following, these excitation mechanisms are discussed first and the train–track interaction model is discussed next.

### 2.3.1 Excitation mechanisms

A distinction is generally made between unevenness excitation, such as wheel and track unevenness, and parametric excitation due to the spatial variation of the support stiffness [60, 75, 112, 144].



Unevenness excitation is due to geometrical imperfections in the wheels and the track as perceived by the moving axles. Track unevenness is mainly due to geometrical irregularities of the rail, the sleeper position on the ballast, and the substructure. At a train speed of 100 km/h, dynamic excitation in the frequency range of interest (1 – 100 Hz) is caused by wavelengths between 0.28 and 28 m. At a train speed of 300 km/h, it is caused by wavelengths between 0.83 and 83 m .

The unevenness profile of the track is measured by means of specially designed track recording cars in order to monitor the track quality. The measuring bandwidth of track recording cars is generally restricted to wavelengths ranging from a few meters to 20 or 30 m [41]. The measurement of the track unevenness at shorter wavelengths requires other measurement devices such as trolleys. Furthermore, the unevenness measured by a track recording car is based on the measured axle loads and does not only account for track unevenness but for parametric excitation as well.

Wheel unevenness is due to wheel flats and out-of-roundness and depends on the quality of each separate wheel. Differences in the unevenness of wheels within the same train or from different trains may therefore cause different vibration levels during a single passage or between the passage of different trains (of the same type). Recent measurements have shown that the ground velocity has a much more irregular character during the passage of different freight trains than during the passage of different passenger trains [97]. This suggests that wheel unevenness is more irregular in the case of freight traffic.

Parametric excitation is caused by the discrete nature of the track system. Sources of parametric excitation include the discrete support by sleepers, transition zones, and changes in stiffness of the track subgrade [14]. The discrete support by sleepers causes an excitation at the sleeper passage frequency  $f_{sl} = v/d_{sl}$  [157], where  $d_{sl}$  is the sleeper spacing. It is not straightforward to quantify the contribution of parametric excitation to the dynamic axle loads.

As the unevenness measured by track recording cars is determined indirectly based on the measured dynamic axle loads, it accounts for both wheel/rail unevenness and parametric excitation. These measured unevenness profiles can therefore be used to predict absolute vibration levels due to trains with similar characteristics. In the following, the response is predicted based on a measured wheel/rail unevenness profile that is assumed to account for parametric excitation as well.

The vertical wheel/rail unevenness  $u_{w/rz}(y)$  varies with respect to the longitudinal coordinate  $y$  along the track (figure 2.1). It is often modeled as

a stationary Gaussian random process characterized by its one-sided Power Spectral Density (PSD)  $\tilde{S}_{u_{w/rz}}(k_y)$  [ $\text{m}^2/(\text{rad}/\text{m})$ ] [115]. Typical PSDs for railway tracks have been defined based on large databases, e.g. by Hamid and Yang [56] and Braun and Hellenbroich [16].

The PSD of the unevenness can be used to generate samples of the vertical rail unevenness  $u_{w/rz}(y)$  and predict the time history of the dynamic axle loads. Based on the spectral representation theorem [138, 139], these samples  $u_{w/rz}(y)$  are generated as a superposition of harmonic functions with random phase angles:

$$u_{w/rz}(y) = \sum_{m=1}^n \sqrt{2\tilde{S}_{u_{w/rz}}(k_{ym})\Delta k_y} \cos(k_{ym}y - \theta_m) \quad (2.14)$$

where  $k_{ym} = m\Delta k_y$  is the wavenumber sampling,  $\Delta k_y$  is the wavenumber bin, and  $\theta_m$  are independent random phase angles distributed uniformly in the interval  $[0, 2\pi]$ . The samples have a period  $Y = 2\pi/\Delta k_y$  and are asymptotically Gaussian as  $n$  tends to infinity and  $\Delta k_y$  tends to zero for a fixed value of  $k_y^{\text{max}} = n\Delta k_y$ .

The frequency content  $\hat{u}_{w/rz}(\omega)$  of the vertical rail unevenness depends on the train speed  $v$  and is obtained by a Fourier transform from the spatial coordinate  $y$  to the wavenumber  $k_y$  and performing the substitution  $k_y = -\omega/v$ :

$$\begin{aligned} \hat{u}_{w/rz}(\omega) &= \frac{1}{v} \tilde{u}_{w/rz}\left(-\frac{\omega}{v}\right) \\ &= \sum_{m=1}^n \frac{-1}{\sqrt{v}} \sqrt{2\tilde{S}_{u_{w/rz}}\left(\frac{|\omega_m|}{v}\right)} \Delta\omega \\ &\quad \times [\pi\delta(\omega - \omega_m)e^{+i\theta_m} + \pi\delta(\omega + \omega_m)e^{-i\theta_m}] \end{aligned} \quad (2.15)$$

where  $\omega_m = -vk_{ym}$  and  $\Delta\omega = v\Delta k_y$ .

### 2.3.2 Train-track interaction

The calculation of the dynamic component  $\mathbf{g}_{dk}(t)$  of the axle loads is based on the assumption of a perfect contact between the train and the track. For each axle  $k$ , this requires the continuity of displacements at the contact point between the wheel and the track:

$$\hat{\mathbf{u}}_{ak}(\omega) = \hat{\mathbf{u}}_{tk}(\omega) + \hat{\mathbf{u}}_{w/rk}(\omega) \quad (2.16)$$

where  $\hat{\mathbf{u}}_{ak}(\omega)$  is the displacement of the  $k$ -th axle,  $\hat{\mathbf{u}}_{tk}(\omega)$  is the track displacement at the  $k$ -th axle position, and  $\hat{\mathbf{u}}_{w/rk}(\omega)$  is the combined wheel/rail unevenness perceived by the  $k$ -th axle.

When vertical rail unevenness dominates, the unevenness  $\hat{\mathbf{u}}_{w/rk}(\omega)$  can be written as:

$$\hat{\mathbf{u}}_{w/rk}(\omega) = \left\{ 0, 0, \exp\left(\frac{i\omega y_{k0}}{v}\right) \right\}^T \hat{u}_{w/rz}(\omega) \quad (2.17)$$

as all axles of the train perceive the same unevenness  $\hat{u}_{w/rz}(\omega)$  except for a phase shift determined by the axle position  $y_{k0}$ . The unevenness profile at all axles is collected in the  $3n_a \times 1$  vector  $\hat{\mathbf{u}}_{w/r}(\omega)$  [94]:

$$\hat{\mathbf{u}}_{w/r}(\omega) = \hat{\mathbf{T}}(\omega) \hat{u}_{w/rz}(\omega) \quad (2.18)$$

where the matrix  $\hat{\mathbf{T}}(\omega)$  collects the phase shift for all axles:

$$\hat{\mathbf{T}}(\omega) = \left\{ \dots, 0, 0, \exp\left(\frac{i\omega y_{k0}}{v}\right), \dots \right\}^T \quad (2.19)$$

The track displacement vector  $\hat{\mathbf{u}}_t(\omega)$  that collects the track displacements in 3 directions for all  $n_a$  axles is related to the dynamic axle loads  $\hat{\mathbf{g}}_d(\omega)$  by means of the  $3n_a \times 3n_a$  track compliance matrix  $\hat{\mathbf{C}}^t(\omega)$  [m/N]:

$$\hat{\mathbf{u}}_t(\omega) = \hat{\mathbf{C}}^t(\omega) \hat{\mathbf{g}}_d(\omega) \quad (2.20)$$

The track compliance matrix  $\hat{\mathbf{C}}^t(\omega)$  is calculated from the response of the coupled track–soil system in a frame of reference that moves with the train [23]. Based on equation (2.10), Lombaert and Degrande [94] derive the  $3 \times 3$  matrix  $\hat{\mathbf{C}}_{kl}^t(\omega)$  that relates the track displacement at axle  $k$  to the dynamic load at axle  $l$ :

$$\hat{\mathbf{C}}_{kl}^t(\omega) = \frac{1}{2\pi} \int_{-\infty}^{+\infty} \tilde{\mathbf{H}}^T(k_y, \omega + k_y v) \exp[-ik_y(y_{k0} - y_{l0})] dk_y \quad (2.21)$$

The  $3n_a \times 3n_a$  track compliance matrix  $\hat{\mathbf{C}}^t(\omega)$  defined in equation (2.20) is composed by the matrices  $\hat{\mathbf{C}}_{kl}^t(\omega)$  in equation (2.21).

In a similar way, a mechanical model of the train is used to relate the axle displacements  $\hat{\mathbf{u}}_a(\omega)$  at all axles to the axle loads  $\hat{\mathbf{g}}_d(\omega)$  by means of the  $3n_a \times 3n_a$  vehicle compliance matrix  $\hat{\mathbf{C}}^v(\omega)$  [m/N]:

$$\hat{\mathbf{u}}_a(\omega) = -\hat{\mathbf{C}}^v(\omega)\hat{\mathbf{g}}_d(\omega) \quad (2.22)$$

Figure 2.2 shows a 2D multi-body model of a single carriage consisting of the wheel sets, bogies, and the car body. The primary ( $1^\circ$ ) suspension connects the wheel sets with the bogies and the secondary ( $2^\circ$ ) suspension connects the bogies with the car body. In such 2D models the axle load of the train is assumed to be equally distributed over both rails requiring an identical response of both rails and hence a symmetric track–soil model.

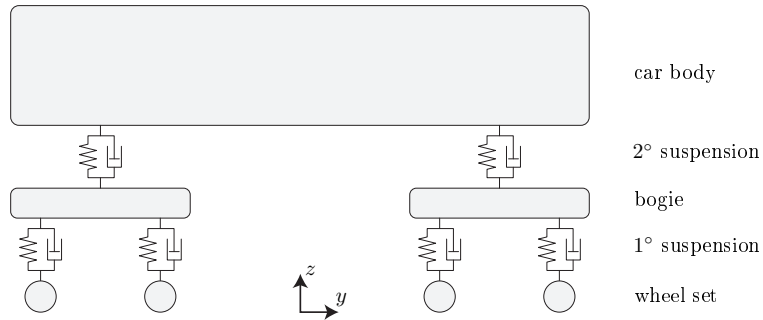


Figure 2.2: 2D multi-body model of a single carriage.

As the primary suspension generally has a relatively low stiffness, it isolates the car body and the bogie from the wheel set at frequencies of more than a few Hertz [75] so that the dynamic vehicle behavior can be represented by means of a simplified model. Figure 2.3 shows such a simplified vehicle model that only takes into account the unsprung mass  $m_u$  of the wheel set. The contact between the wheel set and both rails is modeled based on the Hertz contact theory by means of a Hertzian spring with very high stiffness  $k_H$  [144].

Introducing equations (2.20) and (2.22) in equation (2.16) leads to the following system of equations for the dynamic axle loads  $\hat{\mathbf{g}}_d(\omega)$ :

$$[\hat{\mathbf{C}}^t(\omega) + \hat{\mathbf{C}}^v(\omega)]\hat{\mathbf{g}}_d(\omega) = -\hat{\mathbf{u}}_{w/r}(\omega) \quad (2.23)$$

The inverse of the combined compliance  $\hat{\mathbf{C}}^t(\omega) + \hat{\mathbf{C}}^v(\omega)$  can be considered as the dynamic stiffness of the coupled vehicle–track system. Similar expressions are given by Auersch [7], Sheng et al. [136], and Thompson [144].

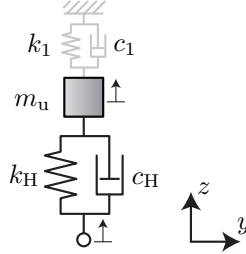


Figure 2.3: Vehicle model used in the present work.

Equation (2.23) allows to compute the dynamic axle loads of a moving train based on the frequency content of the track unevenness. The frequency spectrum  $\hat{\mathbf{u}}_{w/r}(\omega)$  is obtained from a measured unevenness profile or an unevenness sample is generated from the PSD  $\tilde{S}_{u_w/rz}(k_y)$  of the track unevenness according to equation (2.15).

Alternatively, the statistical properties of the dynamic axle loads are calculated directly based on the PSD  $\tilde{S}_{u_w/rz}(k_y)$  of the unevenness. The cross-PSD matrix  $\hat{\mathbf{S}}_{\mathbf{g}}(\omega)$  is a  $3n_a \times 3n_a$  matrix that collects the (cross-)PSDs of all axles. According to random vibration theory [111], it is computed from equations (2.23) and (2.18) as:

$$\hat{\mathbf{S}}_{\mathbf{g}}(\omega) = [\hat{\mathbf{C}}^t(\omega) + \hat{\mathbf{C}}^t(\omega)]^{-1} \hat{\mathbf{T}}(\omega) \frac{1}{v} \tilde{S}_{u_w/rz} \left( -\frac{\omega}{v} \right) \times \hat{\mathbf{T}}^H(\omega) [\hat{\mathbf{C}}^t(\omega) + \hat{\mathbf{C}}^t(\omega)]^{-1H} \quad (2.24)$$

where the superscript H denotes the Hermitian or conjugate transpose of a matrix.

## 2.4 The track–soil interaction problem

The calculation of the transfer functions in equation (2.10) and the track compliance in equation (2.21) requires the solution of the track–soil interaction problem. In the present work, a 2.5D coupled FE-BE approach is used that is a modified version of the track–soil model of Lombaert et al. [98] and is based on the 2.5D methodology proposed by Clouteau [20] and Aubry et al. [6]. In the 2.5D methodology, the track–soil model only includes the cross section of the problem domain, indicated by the grey area in figure 2.1.

A model of a ballasted track is considered. Figure 2.4 shows the cross section of a classical ballasted track, that is composed of the track superstructure, i.e. the rail, fastening system, and sleeper, and the track substructure, i.e. the ballast, sub-ballast, and subgrade.

The rails guide the wheels of the train in a lateral direction and distribute the load over the sleepers [41]. The sleepers provide support and fixing possibilities for the rails and preserve the track gauge [41]. The rails are connected to the sleepers by means of a fastening system that includes the rail pad and the actual mechanical fastening. The function of the rail pads is to transfer the load to the sleeper, while filtering out high frequency components [41].

The ballast distributes the load of the sleeper uniformly towards the subgrade and provides draining possibilities. A sub-ballast is often installed to prevent contamination of the coarse grain ballast material with fine sand and improve the load distribution. The track subgrade is the soil upon which the track is constructed and is often improved to prevent excessive settlements or consolidation.

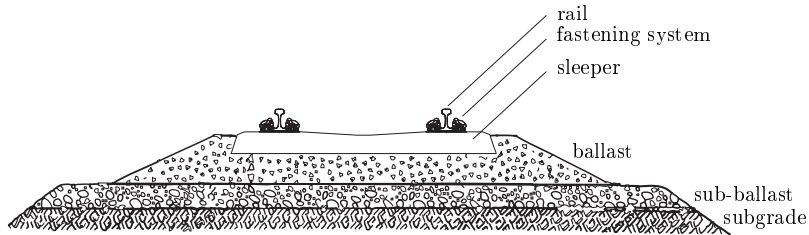


Figure 2.4: Cross section of a classical ballasted track.

### 2.4.1 The track model

The track is modeled by means of a FE model and includes the rails, the rail pads, the sleepers, and the ballast. The model also allows to include possible embankment layers or a track subgrade. This track model has been applied to study the efficiency of vibration mitigation measures [28].

In the 2.5D methodology, an invariant track is assumed which is obtained by replacing the periodic support by sleepers and rail pads by an equivalent continuous support. This does not significantly affect the track dynamics at frequencies sufficiently lower than the pinned–pinned frequency of the track [76, 144]. It is not possible to take into account parametric excitation in 2.5D models, as the track–soil system is assumed to be longitudinally invariant,

unless it is taken into account approximately as an equivalent geometric unevenness [7].

Figure 2.5 shows the cross section of the model for a track with ballast and subgrade. Additional layers can be included to model a sub-ballast or an embankment. The parameters of the track model are discussed in the following.

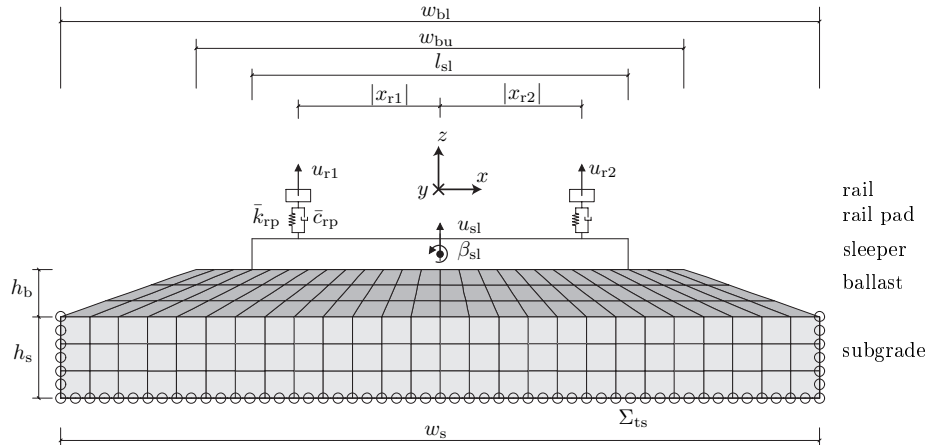


Figure 2.5: Cross section of the track model used in the present work.

The rails are modeled as Euler–Bernoulli beams by means of 2.5D beam elements, accurately representing the dynamic behavior in the frequency range of interest where the wavelength is large compared to the height of the beam [75]. At high frequencies, the shear deformation in the rails should be accounted for and the Timoshenko beam theory is required [145]. The rails have a single degree of freedom in the plane of the cross section, corresponding to the vertical translations  $u_{r1}$  and  $u_{r2}$  (figure 2.5). The rails are characterized by the flexural stiffness (per rail)  $E_r I_r$  [Nm<sup>2</sup>], the mass per length (per rail)  $\rho_r A_r$  [kg/m], and the coordinates of the left and right rail  $x_{r1}$  and  $x_{r2}$ , respectively.

The rail pads are modeled as continuous spring–damper connections. The stiffness  $k_{rp}$  [N/m] and damping coefficient  $c_{rp}$  [Ns/m] of a single rail pad are used to calculate an equivalent stiffness  $\bar{k}_{rp} = k_{rp}/d_{sl}$  [N/m<sup>2</sup>] and damping coefficient  $\bar{c}_{rp} = c_{rp}/d_{sl}$  [Ns/m<sup>2</sup>] in the continuous model, where  $d_{sl}$  is the sleeper distance [98]. Equivalent properties of the longitudinally invariant track model are indicated by a bar.

The sleepers are modeled as a uniformly distributed mass, rigid in the plane of the cross section, with two degrees of freedom: the vertical translation  $u_{sl}$  and the rotation  $\beta_{sl}$  in the plane of the cross section (figure 2.5). The sleeper

is assumed to be in perfect contact with the ballast, with a contact width equal to the sleeper length  $l_{sl}$ . The sleeper is further characterized by an equivalent mass per length  $\bar{m}_{sl} = m_{sl}/d_{sl}$  [kg/m] and a mass moment of inertia  $\rho_{sl}\bar{I}_{t\,sl} = \rho_{sl}I_{t\,sl}w_{sl}/d_{sl}$  [kgm].

The model in figure 2.5 includes a ballast layer with upper width  $w_{bu}$ , lower width  $w_{bl}$ , and height  $h_b$  and a track subgrade with upper and lower width  $w_s$  and height  $h_s$ . The ballast, track subgrade and, if needed, additional layers are modeled as elastic media by means of 2.5D finite volume elements and are characterized by the Young's modulus  $E$ , Poisson's ratio  $\nu$ , and the mass density  $\rho$ . The track model is coupled to the soil model at the track–soil interface  $\Sigma_{ts}$  (figure 2.5).

The FE model of the track is constructed using the 2.5D methodology, interpolating the displacement field with respect to the coordinates  $x$  and  $z$  (figure 2.5). The mesh size for the 2.5D volume elements is adapted for each frequency so that at least 10 elements are used per corresponding wavelength in the track or soil [92]. The discretized displacement vector  $\tilde{\mathbf{u}}_t(k_y, \omega)$  and the external load vector  $\tilde{\mathbf{f}}_t(k_y, \omega)$  of the FE model are related by means of the FE equation, accounting for the equilibrium of stresses on the interface  $\Sigma_{ts}$  [46]:

$$\begin{aligned} & [-\omega^2\mathbf{M}_{tt} + \mathbf{K}_{tt}^0 - ik_y\mathbf{K}_{tt}^1 - k_y^2\mathbf{K}_{tt}^2 \\ & + ik_y^3\mathbf{K}_{tt}^3 + k_y^4\mathbf{K}_{tt}^4 + \tilde{\mathbf{K}}_{tt}^s(k_y, \omega)] \tilde{\mathbf{u}}_t(k_y, \omega) = \tilde{\mathbf{f}}_t(k_y, \omega) \end{aligned} \quad (2.25)$$

where  $\mathbf{K}_{tt}^0$ ,  $\mathbf{K}_{tt}^1$ ,  $\mathbf{K}_{tt}^2$ ,  $\mathbf{K}_{tt}^3$  and  $\mathbf{K}_{tt}^4$  are the stiffness matrices and  $\mathbf{M}_{tt}$  is the mass matrix. These FE matrices are independent of the wavenumber  $k_y$  and the frequency  $\omega$  and are only assembled once. They are calculated by means of the MATLAB toolbox TRAFFIC [100] that has been developed for the prediction of railway induced vibration.

The matrix  $\tilde{\mathbf{K}}_{tt}^s(k_y, \omega)$  represents the dynamic stiffness matrix of the soil and is determined based on the vertical equilibrium at the track–soil interface  $\Sigma_{ts}$ :

$$[\tilde{\mathbf{K}}_{tt}^s(k_y, \omega)]_{ij} = \int_{\Sigma_{ts}} \phi_{ti} \tilde{t}_{sz}(\phi_{tj}) \, d\Gamma \quad (2.26)$$

where  $\phi_{ti}$  is an imposed modal displacement at the track–soil interface  $\Sigma_{ts}$  and  $\tilde{t}_{sz}(\phi_{ti})$  is the vertical component of the corresponding modal soil tractions on the boundary  $\Sigma_{ts}$ . The soil stiffness matrix  $\tilde{\mathbf{K}}_{tt}^s(k_y, \omega)$  is assembled for each wavenumber  $k_y$  and frequency  $\omega$  with the 2.5D BE method, discussed in the following subsection.



### 2.4.2 The soil model

The soil is modeled by means of the BE method by modeling the interface  $\Sigma_s$  that consists of the track–soil interface  $\Sigma_{ts}$  and the free boundary  $\Sigma_{s0}$ , as shown in figure 2.6.

In the 2.5D methodology, an invariant (track–)soil domain is assumed in the longitudinal direction  $\mathbf{e}_y$  of the track (figure 2.6). Natural soils often have a horizontal stratification due to the fact that their formation is governed by phenomena affecting large areas of land, such as erosion, sediment transport, and weathering processes [43]. In this case, the soil can be considered to be a horizontally layered halfspace with material properties varying in the vertical direction  $\mathbf{e}_z$  only and hence invariant in the direction  $\mathbf{e}_y$ .

Furthermore, the longitudinal invariance of the track–soil system requires an invariant geometry of the (track–)soil domain. The cross section in figure 2.6 is therefore assumed to be invariant in the longitudinal direction.

The excavation has an upper width  $w_{eu}$ , lower width  $w_{el}$ , and height  $h_e$  (figure 2.6). In the particular case where no excavation is present, the BE model reduces to the track–soil interface  $\Sigma_{ts}$ . In the following, the BE approach is briefly outlined based on the work of François et al. [46].

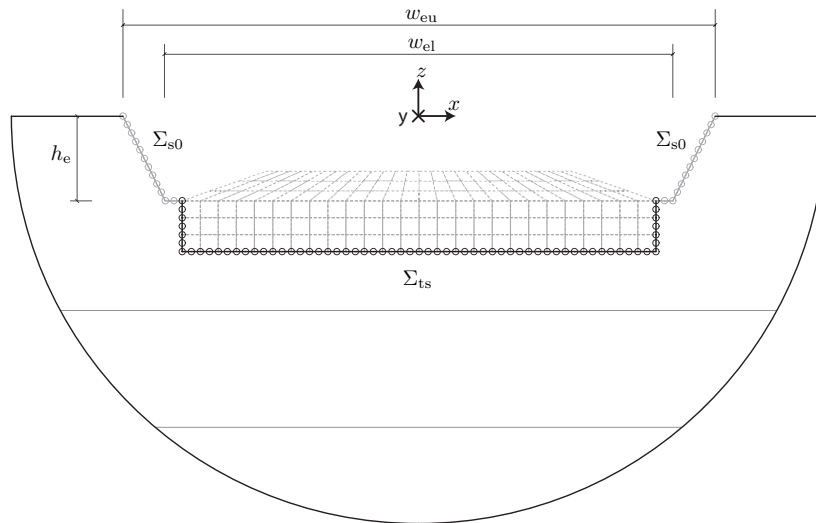


Figure 2.6: Cross section of the soil model used in the present work.

The 2.5D BE method allows to relate the displacements  $\tilde{\mathbf{u}}_s(k_y, \omega)$  and corresponding tractions  $\tilde{\mathbf{t}}_s(k_y, \omega)$  on the boundary  $\Sigma_s$  in the wavenumber–

frequency domain [46]:

$$[\tilde{\mathbf{T}}(k_y, \omega) + \mathbf{I}] \tilde{\mathbf{u}}_s(k_y, \omega) = \tilde{\mathbf{U}}(k_y, \omega) \tilde{\mathbf{t}}_s(k_y, \omega) \quad (2.27)$$

where  $\tilde{\mathbf{T}}(k_y, \omega)$  and  $\tilde{\mathbf{U}}(k_y, \omega)$  are the 2.5D BE system matrices and  $\mathbf{I}$  is the unity matrix.

Equation (2.27) is used to determine the modal tractions  $\tilde{\mathbf{t}}_{sz}(\phi_{ti})$  due to an imposed displacement  $\phi_{ti}$  on the boundary  $\Sigma_{ts}$  and calculate the soil stiffness matrix according to equation (2.26).

The coupled FE-BE equation (2.25) is now solved to calculate the displacements  $\tilde{\mathbf{u}}_t(k_y, \omega)$  of the track. The radiated wave field  $\tilde{\mathbf{u}}_r(k_y, \omega)$  in the soil is calculated based on the displacements  $\tilde{\mathbf{u}}_s(k_y, \omega)$  and tractions  $\tilde{\mathbf{t}}_s(k_y, \omega)$  on the boundary  $\Sigma_s$  [46]:

$$\tilde{\mathbf{u}}_r(k_y, \omega) = \tilde{\mathbf{U}}_r(k_y, \omega) \tilde{\mathbf{t}}_s(k_y, \omega) - \tilde{\mathbf{T}}_r(k_y, \omega) \tilde{\mathbf{u}}_s(k_y, \omega) \quad (2.28)$$

where  $\tilde{\mathbf{U}}_r(k_y, \omega)$  and  $\tilde{\mathbf{T}}_r(k_y, \omega)$  are the BE transfer matrices.

The calculation of the BE system matrices  $\tilde{\mathbf{U}}(k_y, \omega)$  and  $\tilde{\mathbf{T}}(k_y, \omega)$  and the BE transfer matrices  $\tilde{\mathbf{U}}_r(k_y, \omega)$  and  $\tilde{\mathbf{T}}_r(k_y, \omega)$  is implemented in the MATLAB toolbox BEMFUN [45] and requires the fundamental solutions of the (layered) halfspace. A comprehensive overview of the BE method is given by François [44].

The fundamental solutions are provided by means of the Green's functions [4, 101] that represent the displacement in the soil domain due to an impulsive load. Using the Green's functions of a (layered) halfspace offers the advantage that no discretization of the free surface is required and only the boundary  $\Sigma_s$  needs to be discretized.

The Green's functions of the layered halfspace are calculated by means of the direct stiffness method proposed by Kausel and Roësset [72], which is comprehensively treated by Kausel [71] and Schevenels [126] and is implemented in the MATLAB toolbox EDT [127, 128, 130]. In the direct stiffness method, the exact solutions of the Navier equation are obtained for each homogeneous layer or halfspace element and used to formulate element stiffness matrices and determine the Green's functions of the layered halfspace.

The limited shear strain generated by railway induced vibration (below  $10^{-5}$ ) and the strong viscous coupling that prevents the relative motion between the solid and the liquid phase in the frequency range of interest allow to model the soil as a dry elastic medium, characterized by the Young's modulus  $E$ , Poisson's ratio  $\nu$ , and mass density  $\rho$ .

Wave propagation in a homogeneous elastic medium is governed by shear waves (or S-waves), where the motion of the particles is perpendicular to the wave propagation, and longitudinal waves (or P-waves), where the motion of the soil particles is parallel to the wave propagation. The corresponding wave velocities are defined as:

$$C_s = \sqrt{\frac{\mu}{\rho}} \quad (2.29)$$

$$C_p = \sqrt{\frac{\lambda + 2\mu}{\rho}} \quad (2.30)$$

where  $\lambda$  and  $\mu$  are the Lamé constants describing the soil's constitutive behavior. They are related to the Young's modulus  $E$  and Poisson's ratio  $\nu$  as follows:

$$\lambda = \frac{E\nu}{(1 + \nu)(1 - 2\nu)} \quad (2.31)$$

$$\mu = \frac{E}{2(1 + \nu)} \quad (2.32)$$

Waves traveling through the medium are attenuated due to geometrical damping and material damping. Geometrical damping or radiation damping is due to the expansion of the wave fronts, resulting in the spreading of energy over an increasing area, and is not directly related to the material properties of the medium. Material damping is related to the dissipation of energy. In elastodynamics, material damping is usually assumed to be rate independent in the low frequency range [83, 89], referred to as hysteretic material damping, and is modeled in the frequency domain using complex Lamé constants:

$$\mu^* = \mu(1 + 2\beta_s i) \quad (2.33)$$

$$(\lambda + 2\mu)^* = (\lambda + 2\mu)(1 + 2\beta_p i) \quad (2.34)$$

where  $\beta_s$  and  $\beta_p$  represent the hysteretic material damping ratio for the shear waves and the longitudinal waves, respectively.

## 2.5 Numerical example

In the present section, a numerical example of the previously presented prediction model is presented in different steps. First, a homogeneous and a layered halfspace are considered to illustrate the wave propagation in the soil and the track–soil interaction. Next, the train–track interaction and the response are shown for the passage of a Thalys train at the arbitrarily chosen speed of 200 km/h running on the track on the layered halfspace.

### 2.5.1 Free field transfer functions

The wave propagation in the soil is described by means of transfer functions. The transfer function  $h_{vij}(x, y, z, t)$  represents the velocity in a point  $(x, y, z)$  at time  $t$  in the direction  $\mathbf{e}_j$  due to an impulsive load in the origin of the frame of reference at time  $t = 0$  in the direction  $\mathbf{e}_i$  and is obtained as the time derivative of the transfer function  $h_{ij}(x, y, z, t)$ . The transfer function  $h_{vij}(x, y, z, t)$  is also referred to as the free field mobility [m/s/N].

In the particular case of horizontally layered soils, the parameters describing the wave propagation in the soil vary in the vertical direction only. The problem domain of the (layered) halfspace is axisymmetric, so that the transfer functions can be expressed in cylindrical coordinates  $(r, z, t)$ . A Hankel transform from the radial coordinate  $r$  to the radial wavenumber  $k_r$  and a Fourier transform from the time  $t$  to the frequency  $\omega$  allows for a representation in the wavenumber–frequency domain  $(k_r, z, \omega)$ .

In the following, the free field transfer functions are discussed for the case of a homogeneous and a layered halfspace.

#### Homogeneous halfspace

First, a homogeneous halfspace is considered with soil properties as summarized in table 2.1.

Layer	$h$ [m]	$C_s$ [m/s]	$C_p$ [m/s]	$\beta_s$ [-]	$\beta_p$ [-]	$\rho$ [kg/m <sup>3</sup> ]
1	$\infty$	200	400	0.03	0.03	1800

Table 2.1: Dynamic soil characteristics of the homogeneous halfspace.

Figure 2.7 shows the modulus of the free field mobility  $\tilde{h}_{vzz}(k_r, z, \omega)$  at the surface of the homogeneous halfspace ( $z = 0$ ) as a function of the phase velocity  $C_r = \omega/k_r$  and the frequency  $\omega$ .

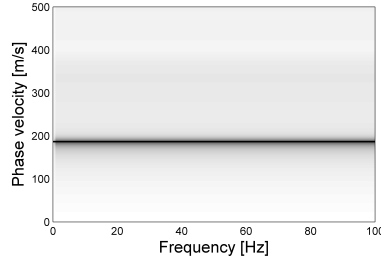


Figure 2.7: Modulus of the free field mobility  $\tilde{h}_{vzz}(k_r, z = 0, \omega)$  as a function of the frequency  $\omega$  and the phase velocity  $C_r$  for the homogeneous halfspace. The dispersion curve of the Rayleigh wave in the homogeneous halfspace is superimposed (black line).

For  $C_r \approx 186$  m/s, a peak appears at all frequencies, corresponding to the Rayleigh wave which is due to the interaction between longitudinal and shear waves at the free surface of the halfspace [118]. The dispersion curve describes the phase velocity of the Rayleigh wave in function of the frequency. In the case of a homogeneous halfspace, the Rayleigh wave is non-dispersive and has a phase velocity  $C_R$  that does not depend on the frequency, approximately equal to [1]:

$$C_R \approx \frac{0.862 + 1.14\nu}{1 + \nu} C_s \tag{2.35}$$

The dispersion curve of the homogeneous halfspace is superimposed in figure 2.7 and corresponds to a Rayleigh wave velocity  $C_R \approx 0.9315 C_s = 186.3$  m/s.

The horizontal and vertical displacement modes of the Rayleigh wave are given by the transfer functions  $\tilde{h}_{zr}(k_r, z, \omega)$  and  $\tilde{h}_{zz}(k_r, z, \omega)$ , respectively, at a certain frequency  $\omega$  and the corresponding wavenumber  $k_r$ .

Figure 2.8 shows the dimensionless horizontal and vertical displacement for the Rayleigh wave as a function of the depth  $z$  at a frequency of 20 Hz. Both displacement components are made dimensionless using the vertical displacement at  $z = 0$ . The displacements decrease with depth, showing a small vertical component at depths below about 1.5 times the Rayleigh wavelength  $\lambda_R = C_R/f$ , which equals 9.32 m at a frequency of 20 Hz. The horizontal displacement changes sign at a depth of about  $0.2\lambda_R$ .

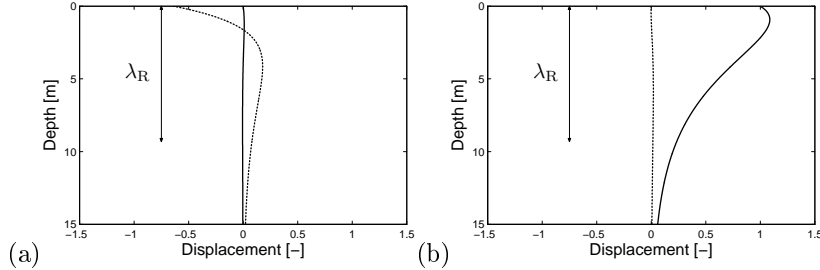


Figure 2.8: Real (solid line) and imaginary (dotted line) part of the dimensionless (a) horizontal and (b) vertical displacement of the Rayleigh wave at 20 Hz as a function of the depth  $z$  for the homogeneous halfspace.

Figure 2.9 shows the dimensionless horizontal and vertical displacement for the Rayleigh wave as a function of the depth  $z$  at a frequency of 40 Hz. The Rayleigh wavelength  $\lambda_R$  has decreased to 4.66 m, resulting in a smaller depth of the displacement modes.

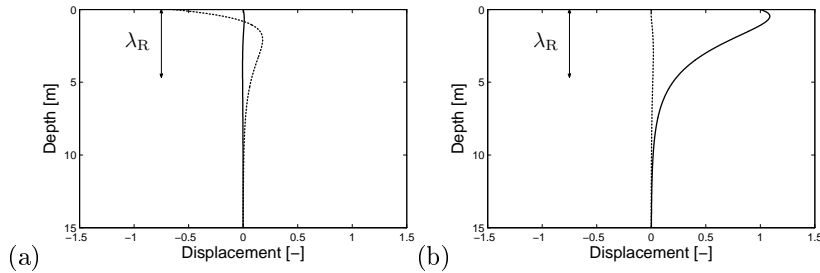


Figure 2.9: Real (solid line) and imaginary (dotted line) part of the dimensionless (a) horizontal and (b) vertical displacement of the Rayleigh wave at 40 Hz as a function of the depth  $z$  for the homogeneous halfspace.

At both frequencies, the horizontal displacement is almost purely imaginary, while the vertical displacement is almost purely real. This implies that both displacement components are  $90^\circ$  out of phase and that the particles move in an elliptic path.

Figure 2.10 shows the free field mobility  $\hat{h}_{vzz}(r, z, \omega)$  at the surface of the homogeneous halfspace ( $z = 0$ ) at a distance  $r = 6$  m,  $r = 12$  m,  $r = 24$  m, and  $r = 48$  m. For  $f = 0$  Hz, the mobility tends to  $-\infty$  on a dB scale, as the velocity is zero in the static case. The mobilities show a clear attenuation with distance, which is governed by geometrical and material damping. At low frequencies, the attenuation with distance is approximately proportional to  $1/r$  due to geometrical damping. At higher frequencies, the mobility is additionally

attenuated due to material damping. The effect of material damping increases with the number of cycles between the source and the receiver and is therefore stronger for higher frequencies, corresponding to a shorter wavelength, and for larger distances.

The problem of railway induced vibration is often studied in frequency bands. The transfer function is represented in one-third octave bands as the average value of the square of the modulus of the mobility within the  $m$ -th frequency band  $[\omega_{1m}, \omega_{2m}]$ :

$$\langle h_{vij}(r, z) \rangle_m = \sqrt{\frac{1}{\omega_{2m} - \omega_{1m}} \int_{\omega_{1m}}^{\omega_{2m}} |\hat{h}_{vij}(r, z, \omega)|^2 d\omega} \quad (2.36)$$

Figure 2.11 shows the one-third octave band free field mobility  $\langle h_{vzz}(r, z) \rangle_m$  at the surface of the homogeneous halfspace ( $z = 0$ ) at a distance  $r = 6$  m,  $r = 12$  m,  $r = 24$  m, and  $r = 48$  m, also showing an increasing attenuation with increasing distance and frequency. Small oscillations are observed in the mobility that are caused by interference between different types of waves.

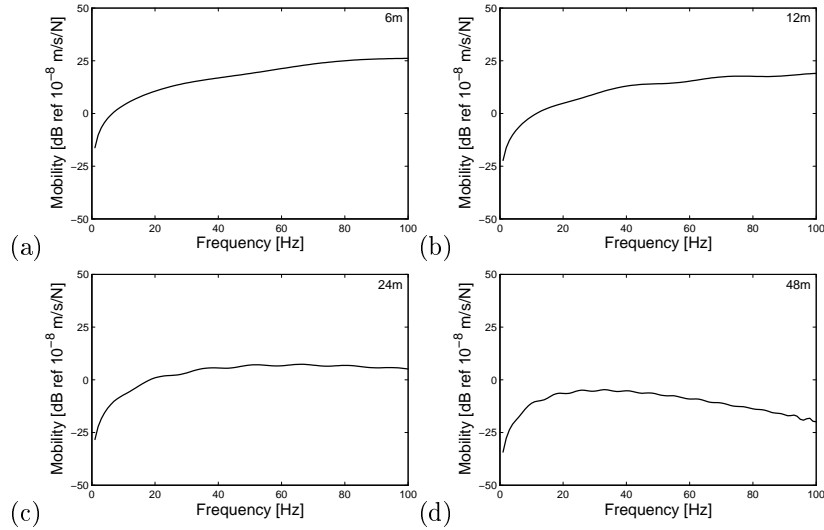


Figure 2.10: Level of the free field mobility  $\hat{h}_{vzz}(r, z = 0, \omega)$  as a function of the frequency  $\omega$  at (a)  $r = 6$  m, (b)  $r = 12$  m, (c)  $r = 24$  m, and (d)  $r = 48$  m for the homogeneous halfspace.

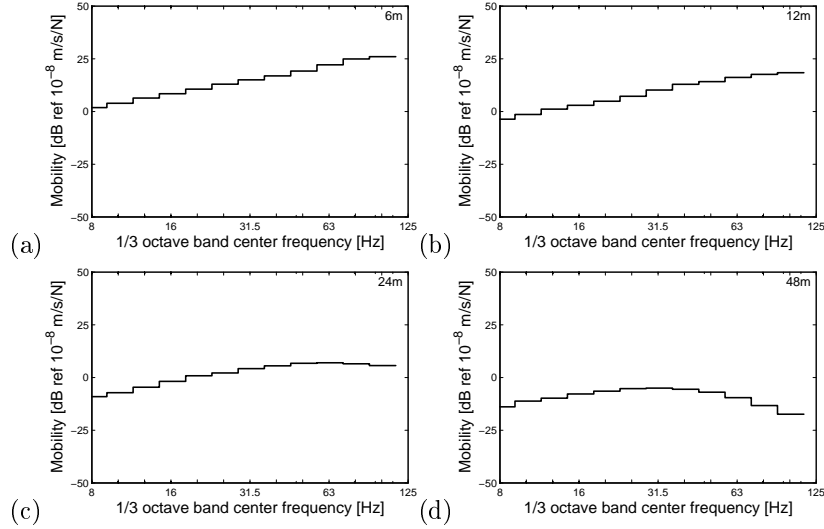


Figure 2.11: Level of the one-third octave band free field mobility  $\langle h_{vzz}(r, z = 0) \rangle_m$  at (a)  $r = 6$  m, (b)  $r = 12$  m, (c)  $r = 24$  m, and (d)  $r = 48$  m for the homogeneous halfspace.

### Layered halfspace

Next, a layered halfspace is considered with a layer of 2 m overlying a halfspace. The soil properties are summarized in table 2.2.

Layer	$h$ [m]	$C_s$ [m/s]	$C_p$ [m/s]	$\beta_s$ [-]	$\beta_p$ [-]	$\rho$ [kg/m <sup>3</sup> ]
1	2	150	300	0.03	0.03	1800
2	$\infty$	300	600	0.03	0.03	1800

Table 2.2: Dynamic soil characteristics of the layered halfspace.

Figure 2.12 shows the modulus of the free field mobility  $\tilde{h}_{vzz}(k_r, z, \omega)$  at the surface of the layered halfspace ( $z = 0$ ) as a function of the phase velocity  $C_r$  and the frequency  $\omega$ .

Whereas a single peak is observed for the homogeneous halfspace (figure 2.7), multiple peaks occur for the layered halfspace (figure 2.12). These peaks correspond to the Rayleigh wave modes in the layered halfspace, which are dispersive due to the variation with depth of the dynamic soil characteristics.



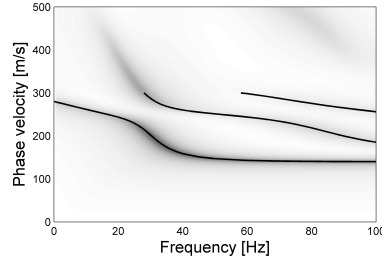


Figure 2.12: Modulus of the free field mobility  $\tilde{h}_{vzz}(k_r, z = 0, \omega)$  as a function of the frequency  $\omega$  and the phase velocity  $C_r$  for the layered halfspace. The dispersion curves of the first three Rayleigh waves are superimposed (black lines).

The dispersion curves of the first three Rayleigh wave modes are superimposed in figure 2.12.

At the cut-on frequency of a mode, the Rayleigh wavelength is large and the surface wave reaches the stiffer halfspace, resulting in a phase velocity  $C_R \approx 279.45$  m/s that corresponds to the phase velocity of Rayleigh waves in the halfspace. As the frequency increases, the Rayleigh wavelength decreases and the Rayleigh wave is concentrated in the top layer, resulting in a phase velocity  $C_R \approx 139.73$  m/s that corresponds to the Rayleigh wave velocity in the top layer.

This is illustrated by the displacement modes of the Rayleigh wave. Figure 2.13 shows the dimensionless horizontal and vertical displacement for the fundamental Rayleigh wave at 20 Hz. The Rayleigh wave reaches the stiffer halfspace and is therefore affected by the characteristics of the halfspace.

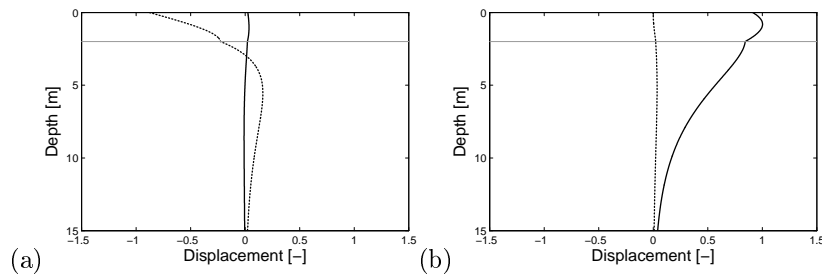


Figure 2.13: Real (solid line) and imaginary (dotted line) part of the dimensionless (a) horizontal and (b) vertical displacement of the Rayleigh wave at 20 Hz as a function of the depth  $z$  for the layered halfspace.

Figure 2.14 shows the dimensionless horizontal and vertical displacement for the fundamental Rayleigh wave at 40 Hz, which is now concentrated in the top layer. The Rayleigh wave velocity is therefore dominated by the characteristics of the top layer.

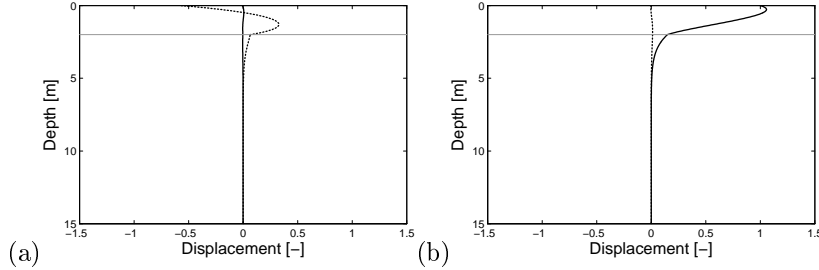


Figure 2.14: Real (solid line) and imaginary (dotted line) part of the dimensionless (a) horizontal and (b) vertical displacement of the Rayleigh wave at 40 Hz as a function of the depth  $z$  for the layered halfspace.

Figure 2.15 shows the free field mobility  $\hat{h}_{vzz}(r, z, \omega)$  at the surface of the layered halfspace ( $z = 0$ ) at a distance  $r = 6$  m,  $r = 12$  m,  $r = 24$  m, and  $r = 48$  m. The velocity is zero in the static case and increases up to 40 Hz. The response is attenuated with increasing distance from the source due to geometrical and material damping. As the effect of material damping is stronger for higher frequencies, the peak of the response moves to lower frequencies with increasing distance. The mobility is furthermore characterized by a number of peaks and troughs, in particular at larger distances, due to interference between different types of waves [129]. Due to interference between waves that predominantly travel in the top layer and waves that travel predominantly in the halfspace, this effect is more pronounced for the layered halfspace (figure 2.15) than for the homogeneous halfspace (figure 2.10).

Figure 2.16 shows the one-third octave band free field mobility  $\langle h_{vzz}(r, z) \rangle_m$  at the surface of the layered halfspace ( $z = 0$ ) at a distance  $r = 6$  m,  $r = 12$  m,  $r = 24$  m, and  $r = 48$  m. Due to averaging within each frequency band, the peaks and troughs observed in the narrow band spectrum are no longer observed in the one-third octave band spectrum. A similar behavior is found as for the narrow band spectrum, showing an increasing attenuation at a larger distance and at a higher frequency.

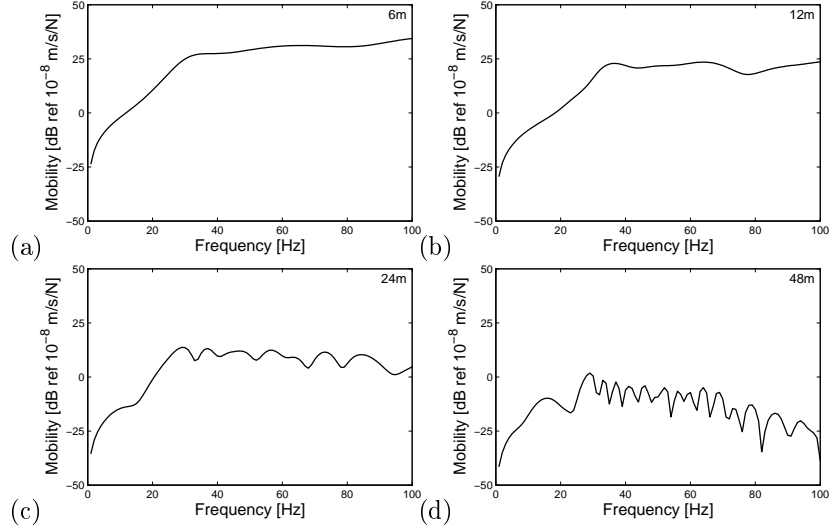


Figure 2.15: Level of the free field mobility  $\hat{h}_{vzz}(r, z = 0, \omega)$  as a function of the frequency  $\omega$  at (a)  $r = 6$  m, (b)  $r = 12$  m, (c)  $r = 24$  m, and (d)  $r = 48$  m for the layered halfspace.

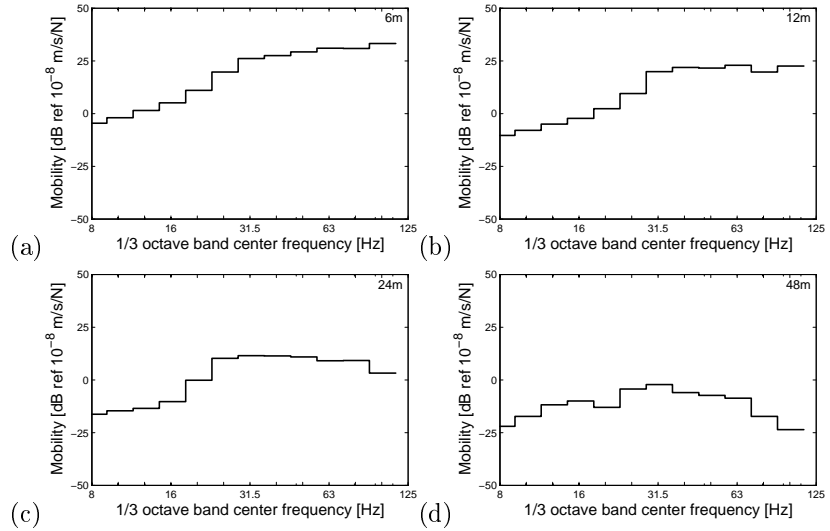


Figure 2.16: Level of the one-third octave band free field mobility  $\langle h_{vzz}(r, z = 0) \rangle_m$  at (a)  $r = 6$  m, (b)  $r = 12$  m, (c)  $r = 24$  m, and (d)  $r = 48$  m for the layered halfspace.

### 2.5.2 Track–soil interaction

The dynamic track–soil interaction is discussed for the case of a classical ballasted track, consisting of UIC 60 rails, medium stiff rail pads, concrete monoblock sleepers, and a ballast layer. The track–soil interaction is solved by means of the 2.5D track–soil model introduced in section 2.4. The parameters of the equivalent track model are summarized in table 2.3. In order to illustrate the effect of the soil properties on the dynamic track behavior, two soil types are considered corresponding to the homogeneous halfspace (table 2.1) and the layered halfspace (table 2.2).

Rail	Flexural stiffness (per rail)	$E_r I_r = 6.45 \times 10^6 \text{ Nm}^2$
	Mass per length (per rail)	$\rho_r A_r = 60.3 \text{ kg/m}$
	Position of left rail	$x_{r1} = -0.7175 \text{ m}$
	Position of right rail	$x_{r2} = +0.7175 \text{ m}$
Rail pad	Stiffness	$k_{rp} = 250 \times 10^6 \text{ N/m}^2$
	Viscous damping	$\bar{c}_{rp} = 20 \times 10^3 \text{ Ns/m}^2$
Sleeper	Mass	$\bar{m}_{sl} = 500 \text{ kg/m}$
	Mass moment of inertia	$\rho_{sl} \bar{I}_{t\,sl} = 262.17 \text{ kgm}$
	Length	$l_{sl} = 2.50 \text{ m}$
Ballast	Height	$h_b = 0.35 \text{ m}$
	Upper width	$w_{bu} = 3.60 \text{ m}$
	Lower width	$w_{bl} = 5.60 \text{ m}$
	Shear wave velocity	$C_s = 150 \text{ m/s}$
	Longitudinal wave velocity	$C_p = 300 \text{ m/s}$
	Shear damping ratio	$\beta_s = 0.03$
	Longitudinal damping ratio	$\beta_p = 0.03$
	Mass density	$\rho_b = 1700 \text{ kg/m}^3$

Table 2.3: Dynamic characteristics of the ballasted track.

The 2D track–soil model is solved for each frequency and wavenumber. Within the present research, a fixed sampling is used for the dimensionless wavenumber  $\bar{k}_y = k_y C_s / \omega$ , with  $C_s$  the smallest shear wave velocity in the track or the soil. A good sampling of the Rayleigh waves is ensured by using a dense sampling for low wavenumbers (121 linearly spaced samples between  $\bar{k}_y = 0$  and  $\bar{k}_y = 1.2$ ) and a coarse sampling for higher wavenumbers (50 logarithmically spaced samples between  $\bar{k}_y = 1.2$  and  $\bar{k}_y = 100$ ). In this way, the sampling of the wavenumber  $k_y$  is adapted for each frequency.

### Rail receptance

The rail receptance [m/N] is defined as the transfer function between the force applied to the rail and the displacement of the rail. The direct rail receptance represents the displacement of the rail due to a unit load at the rail head at the same location. When the displacement is considered in a different point than the load point, it is referred to as the cross rail receptance. In the following, the direct rail receptance is calculated by means of equation (2.25).

Figure 2.17 shows the modulus and the phase of the rail receptance of the ballasted track on a homogeneous and a layered halfspace. The soil affects the track receptance mainly in the low frequency range. Around 25 Hz, a peak is observed for the track on the layered halfspace. This peak is due to the resonance of the top layer on the halfspace and is therefore not observed for the track on a homogeneous halfspace. The dominating wavelength decreases with increasing frequency, so that at higher frequencies the motion is concentrated in the track structure and is no longer determined by the soil properties. The values of the receptance for both soil types therefore converge with increasing frequency.

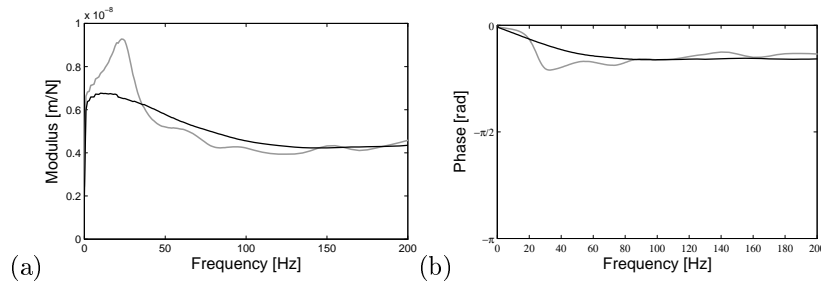


Figure 2.17: (a) Modulus and (b) phase of the rail receptance of the ballasted track on the homogeneous (black line) and the layered (grey line) halfspace.

### Track – free field transfer function

Once the track–soil interaction problem is solved and the track response is determined, the free field response is computed based on equation (2.28) that relates the displacements and tractions at the track–soil interface to the response in the free field. In the following, the track – free field mobility  $\hat{h}_{vij}(x, y, z, \omega)$  is defined as the velocity in a receiver  $(x, y, z)$  in a direction  $\mathbf{e}_j$  due to a harmonic unit load at both rails of the track in a direction  $\mathbf{e}_i$ .

Figure 2.18 shows the track – free field mobility  $\hat{h}_{vzz}(x, y, z, \omega)$  at different distances from the track for a track on the homogeneous halfspace. The vibration transfer is affected by the track–soil interaction, generating waves of the coupled system that propagate along the track. The resulting load transfer could be compared with a combined filtering in the time and the space domain [96]. In order to illustrate the effect of the dynamic track–soil interaction, the free field mobility (figure 2.10) is superimposed in figure 2.18.

At frequencies below 20 Hz, the force is transmitted quasi-statically to the soil and the influence of the track is relatively small, resulting in a small effect of track–soil interaction. Furthermore, the dominating wavelength is large compared to the width of the track so that the effect of the load distribution by the track is very small. Around 20 Hz, the wavelength is of the same order of magnitude as the dimensions of the track and the distribution of the load by the track system results in a reduced mobility. As the track – free field mobility shows a similar attenuation with increasing distance as the free field mobility, the reduction is similar at all distances. As this track filtering effect is determined by the ratio of the wavelength and the dimensions of the track, it is influenced by the soil properties.

The corresponding one-third octave band track – free field mobility  $\langle h_{vzz}(x, y, z) \rangle_m$  is shown in figure 2.19 and allows to study the track filtering effect in frequency bands. As the effect of interference of different waves is limited for the homogeneous halfspace, a similar observation is made in one-third octave band spectrum as for the narrow band spectrum.

Figure 2.20 shows the track – free field mobility  $\hat{h}_{vzz}(x, y, z, \omega)$  at different distances from the track for a track on the layered halfspace. The dynamic track–soil interaction has a similar effect as for the track on the homogeneous halfspace. A difference up to 15 dB is observed between the free field and the track – free field mobility. At a larger distance from the track, the track–soil interaction results in a shift of the characteristic peaks and troughs observed in the mobility for the layered halfspace and the track filtering is observed less clearly.

Figure 2.21 shows the corresponding one-third octave band track – free field mobility  $\langle h_{vzz}(x, y, z) \rangle_m$  where characteristic peaks and troughs are averaged within each frequency band. Due to this averaging, the track filtering effect decreases at a larger distance from the track compared to track on the homogeneous halfspace (figure 2.19).

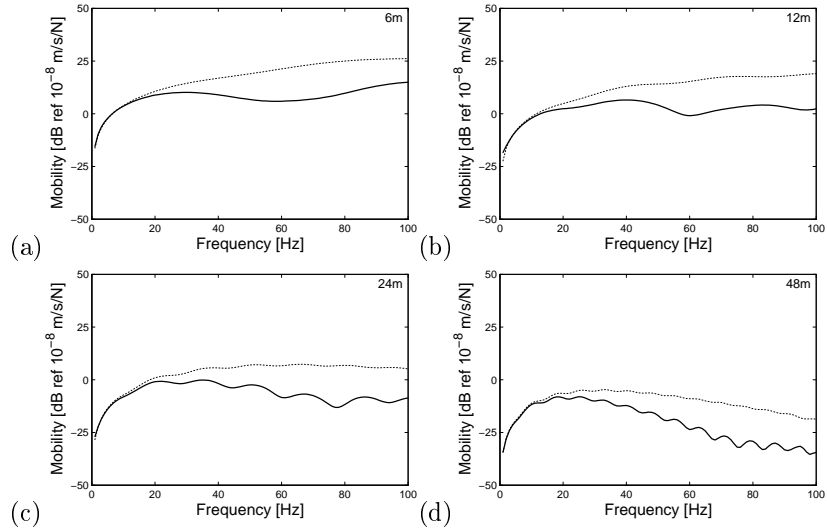


Figure 2.18: Level of the track – free field mobility  $\hat{h}_{vzz}(x, y, z, \omega)$  (solid line) at the surface of the homogeneous halfspace as a function of the frequency  $\omega$  for (a)  $r = 6$  m, (b)  $r = 12$  m, (c)  $r = 24$  m, and (d)  $r = 48$  m. The corresponding free field mobility is superimposed (dotted line).

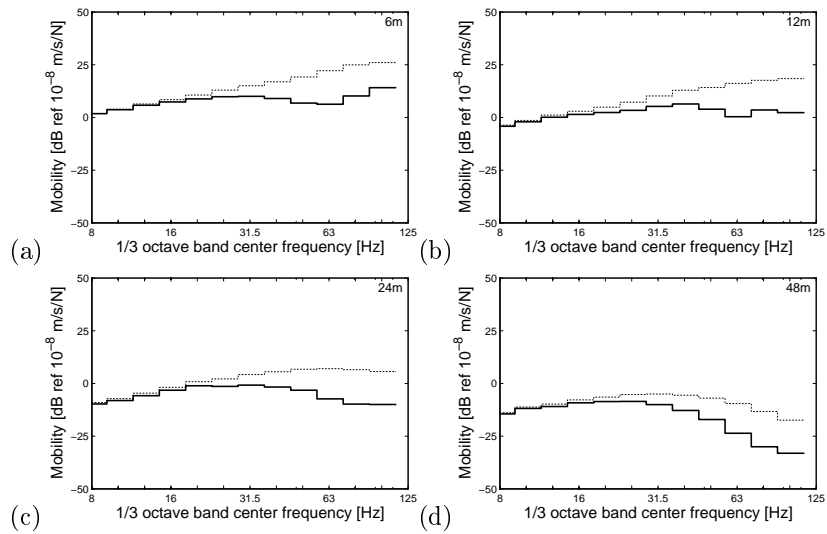


Figure 2.19: Level of the one-third octave band track – free field mobility  $\langle h_{vzz}(r, z) \rangle_m$  (solid line) at the surface of the homogeneous halfspace as a function of the frequency  $\omega$  for (a)  $r = 6$  m, (b)  $r = 12$  m, (c)  $r = 24$  m, and (d)  $r = 48$  m. The corresponding free field mobility is superimposed (dotted line).

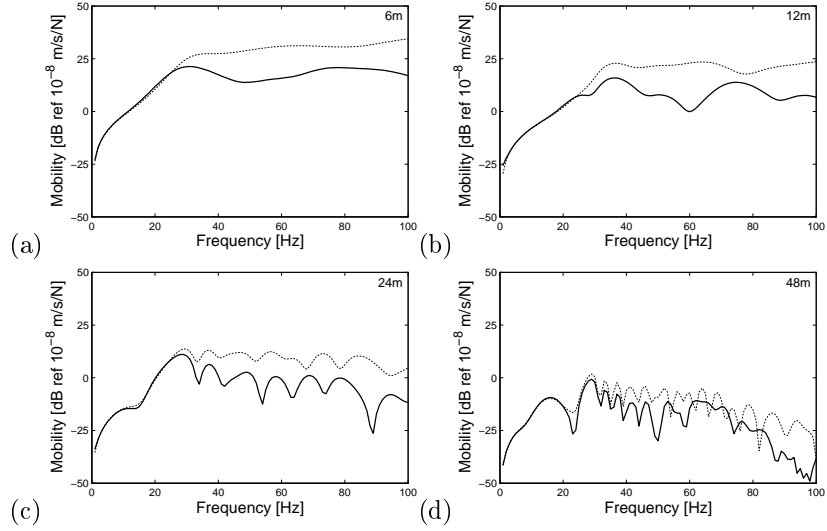


Figure 2.20: Level of the track – free field mobility  $\hat{h}_{vzz}(r, z, \omega)$  at the surface of the layered halfspace as a function of the frequency  $\omega$  for (a)  $r = 6$  m, (b)  $r = 12$  m, (c)  $r = 24$  m, and (d)  $r = 48$  m.

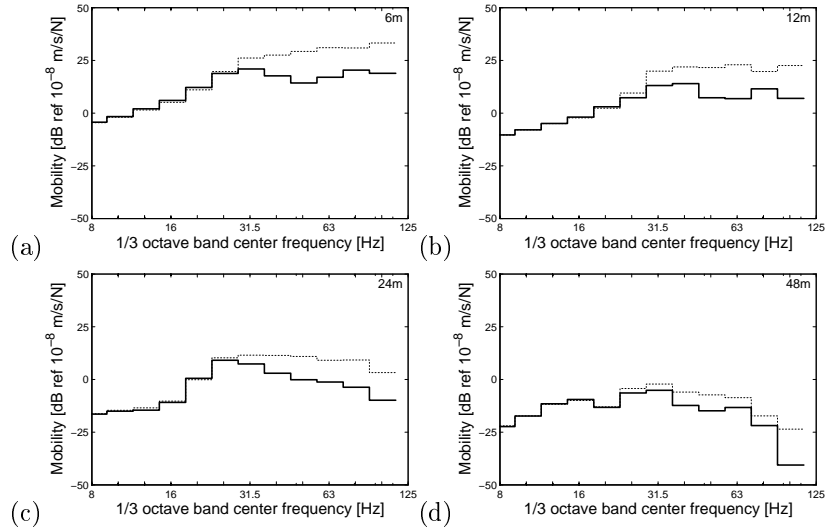


Figure 2.21: Level of the one-third octave band track – free field mobility  $\langle h_{vzz}(r, z) \rangle_m$  at the surface of the layered halfspace as a function of the frequency  $\omega$  for (a)  $r = 6$  m, (b)  $r = 12$  m, (c)  $r = 24$  m, and (d)  $r = 48$  m.



### 2.5.3 Train–track interaction

According to equation (2.23), the dynamic axle loads are determined by the track unevenness and the track and vehicle compliance. The dynamic train–track interaction is illustrated for the case of a single axle of a Thalys train running at a speed of 200 km/h on the ballasted track (table 2.3). Whereas a homogeneous and a layered halfspace are considered to illustrate the effect of the soil properties on the wave propagation, the response due to train passages is only discussed for the layered halfspace (table 2.2). The axle is modeled with the simplified vehicle model shown in figure 2.3 with an unsprung mass  $m_u = 2027$  kg and a Hertzian spring stiffness  $k_H = 2.8 \times 10^9$  N/m [67, 144]. Only vertical track unevenness and vertical axle loads are considered.

#### Rail unevenness

As discussed in subsection 2.3.1, the statistical properties of typical rail unevenness profiles have been defined based on large databases. The FRA has defined the following PSD  $\tilde{S}_{u_w/rz}(k_y)$  [m<sup>3</sup>/rad] based on the database of Hamid and Yang [56]:

$$\tilde{S}_{u_w/rz}(k_y) = \frac{1}{2\pi} A \frac{n_{y2}^2(n_y^2 + n_{y2}^2)}{n_y^4(n_y^2 + n_{y1}^2)} \quad (2.37)$$

where  $n_y = k_y/2\pi$  is the circumferential wavenumber and the constants  $n_{y1} = 0.0233$  m<sup>-1</sup> and  $n_{y2} = 0.13$  m<sup>-1</sup> are determined based on the database. The parameter  $A$  indicates the quality of the track and is defined for six classes of unevenness, ranging from class 1 corresponding to a bad track quality to class 6 corresponding to a good track quality [51, 56]. Table 2.4 gives the value of  $A$  for each class. In the following simulation, the vertical rail unevenness corresponding to FRA class 3 is used.

Class	1	2	3	4	5	6
$A$ [10 <sup>-7</sup> m]	16.72	9.53	5.29	2.96	1.67	0.96

Table 2.4: Track quality parameters according to the FRA database [56].

Figure 2.22a shows the PSD  $\tilde{S}_{u_w/rz}(k_y)$  of the vertical track unevenness corresponding to FRA class 1, class 3, and class 6.

Based on the PSD, an unevenness profile  $\hat{u}_{w/rz}(\omega)$  is generated according to equation (2.15). Figure 2.22b shows the modulus of the frequency spectrum

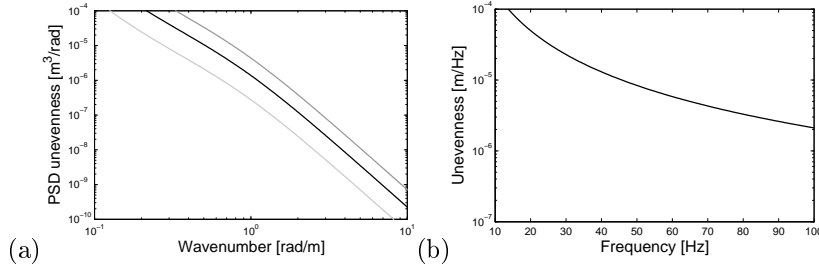


Figure 2.22: (a) PSD  $\tilde{S}_{\hat{u}_{w/rz}}(k_y)$  of the vertical unevenness according to FRA class 1 (dark grey line), class 3 (black line), and class 6 (light grey line) [56] and (b) modulus of an unevenness profile  $\hat{u}_{w/rz}(\omega)$  generated from FRA class 3 for a train speed of 200 km/h.

$\hat{u}_{w/rz}(\omega)$  of the unevenness profile according to FRA class 3 evaluated for a train speed of 200 km/h. Different samples of unevenness generated according to equation (2.15) have a different random phase angle but have the same modulus.

### Track and vehicle compliance

The track dynamics are described by means of the track compliance matrix  $\hat{C}^t(\omega)$  that is calculated based on equation (2.21) in a frame of reference that moves with the train. Figure 2.23 shows the real and imaginary part of the vertical track compliance  $\hat{C}^t(\omega)$  for a train speed of 0 km/h and 200 km/h. At a train speed of 0 km/h, the track compliance is identical to the track receptance in the case where a unit impact is applied at both rails and shows a peak that is due to the soil stratification and corresponds to the resonance of the top layer on the halfspace. Due to the increase of the train speed to 200 km/h, this peak shifts to a slightly lower frequency due to the Doppler effect.

The vehicle dynamics are described by means of the vehicle compliance matrix  $\hat{C}^v(\omega)$ . Figure 2.24 shows the real and imaginary part of the vertical vehicle compliance  $\hat{C}^v(\omega)$  for a single axle which is purely real. As the resonance of the unsprung mass ( $m_u = 2027 \text{ kg}$ ) on the Hertzian spring stiffness ( $k_H = 2.8 \times 10^9 \text{ N/m}$ ) occurs at a frequency far above the frequency range of interest, the influence of the Hertzian spring is negligible and the vehicle compliance is controlled by the unsprung mass. In the frequency range of interest, the real part of the vehicle compliance can therefore be approximated as:

$$\hat{C}^v(\omega) = -\frac{1}{m_u \omega^2} \quad (2.38)$$

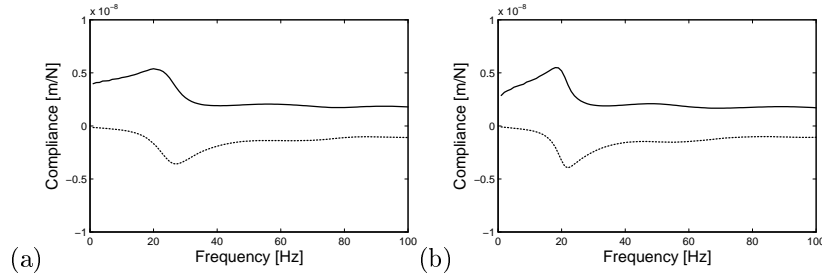


Figure 2.23: Real (solid line) and imaginary (dotted line) part of the vertical track compliance  $\hat{C}^t(\omega)$  for a train speed (a)  $v = 0$  km/h and (b)  $v = 200$  km/h.

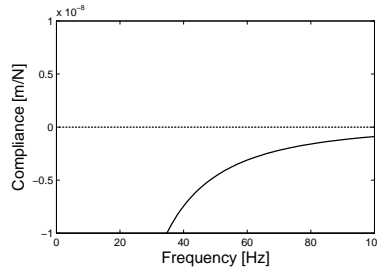


Figure 2.24: Real (solid line) and imaginary (dotted line) part of the vertical vehicle compliance  $\hat{C}^v(\omega)$  of a single axle.

The dynamic train–track interaction is determined by the combined compliance  $\hat{C}^t(\omega) + \hat{C}^v(\omega)$  of the track and the vehicle. Figure 2.25 shows the real and imaginary part of the combined compliance  $\hat{C}^t(\omega) + \hat{C}^v(\omega)$  for a single axle running at a speed of 200 km/h on the track. In the low frequency range, the vehicle compliance is much larger than the track compliance and the combined compliance tends to  $-\infty$ . In this frequency range, the vehicle–track interaction is dominated by the vehicle dynamics.

Around 80 Hz, the real part of the track compliance (figure 2.23b) and the vehicle compliance (figure 2.24) are equal but opposite in sign so that the real part of the combined compliance  $\hat{C}^t(\omega) + \hat{C}^v(\omega)$  equals zero (figure 2.25). Corresponding to equation (2.23), a peak will be observed in the axle load spectrum at this frequency, which is referred to as the resonance of the unsprung mass on the track stiffness [144] or P2 resonance [96]. Due to the non-zero imaginary part of the combined compliance at this frequency, this peak has a finite value.

As a summary, figure 2.26 shows the modulus of the track compliance  $\hat{C}^t(\omega)$ , the vehicle compliance  $\hat{C}^v(\omega)$ , and the combined compliance  $\hat{C}^t(\omega) + \hat{C}^v(\omega)$ . A

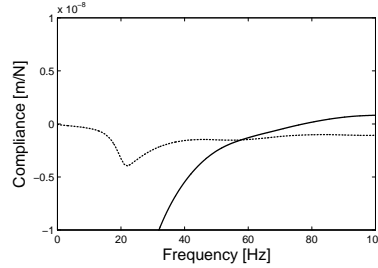


Figure 2.25: Real (solid line) and imaginary (dotted line) part of the vertical combined compliance  $\hat{C}^t(\omega) + \hat{C}^v(\omega)$  for a single axle (200 km/h) running on the track.

minimum is observed around 80 Hz in the modulus of the combined compliance that corresponds to the P2 resonance.

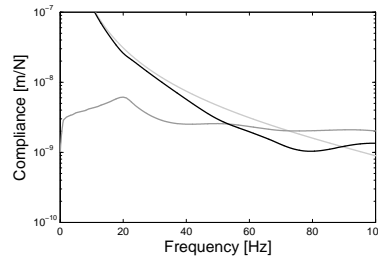


Figure 2.26: Modulus of the vertical track compliance  $\hat{C}^t(\omega)$  (dark grey line), vehicle compliance  $\hat{C}^v(\omega)$  (light grey line), and combined compliance  $\hat{C}^t(\omega) + \hat{C}^v(\omega)$  (black line) for a single axle (200 km/h) running on the track.

### Dynamic axle load

Figure 2.27a shows the PSD  $\hat{S}_{g_z}(\omega)$  of the vertical load of a single axle running at a speed of 200 km/h on the track, calculated according to equation (2.24) for a PSD of the unevenness according to FRA class 3. The PSD shows a clear peak around 80 Hz corresponding to the P2 resonance that occurs at the minimum of the modulus of the combined compliance  $\hat{C}^t(\omega) + \hat{C}^v(\omega)$  of the track and the vehicle (figure 2.26).

Figure 2.27b shows the spectrum  $\hat{g}_z(\omega)$  of the axle load obtained for a sample of the vertical unevenness generated according to equation (2.15) from the PSD of the unevenness according to FRA class 3. The profile is generated based on equation (2.14) with a dense wavenumber sampling  $k_{ym}$  with wavenumber

bin  $\Delta k_y = 0.005$  rad/m and subsequently resampled with a coarse wavenumber sampling  $k_{yn}$ . A fixed circular frequency sampling with a bin  $\Delta\omega_n = 2\pi$  rad/s is used to determine the wavenumber sampling  $k_{yn} = \omega_n/v$  for each train speed  $v$ . As the unevenness profile is complex, its modulus is affected by the interpolation of the densely sampled unevenness profile and peaks and troughs appear in the axle load spectrum. A similar behavior is observed as for the PSD (figure 2.27a) with a maximum value around 80 Hz.

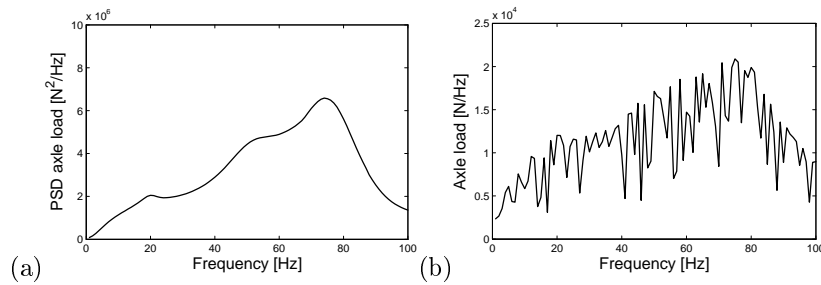


Figure 2.27: (a) PSD  $\hat{S}_{g_z}(\omega)$  and (b) narrow band spectrum  $\hat{g}_z(\omega)$  of the vertical dynamic load of a single axle (200 km/h) on the track on the layered halfspace.

### 2.5.4 Response due to a train passage

As discussed in section 2.2, the response to moving loads is computed based on the static and dynamic axle loads and the transfer function. The present subsection discusses the track and free field velocity due to the passage of a Thalys train running at a speed of 200 km/h on the ballasted track (table 2.3) on the layered halfspace (table 2.2). A detailed description of the characteristics of the Thalys train is given in subsection 3.6.1.

#### Quasi-static contribution

According to equation (2.11), the quasi-static contribution is the product of the response to a single axle and the signature of the train.

Figure 2.28 shows the time history and frequency content of the rail velocity due to a single axle that carries a total mass  $m_t = 17\,000$  kg. The spectrum is determined by the characteristics of the axle and the track.

Figure 2.29 shows the signature of the Thalys train with a speed of 200 km/h, showing a quasi-discrete spectrum that is determined by the train composition and the train speed.

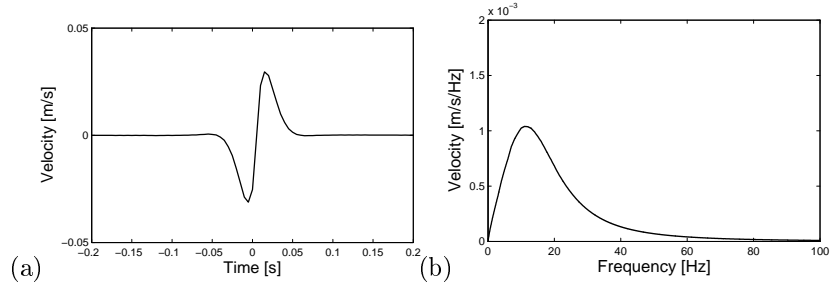


Figure 2.28: (a) Time history and (b) frequency content of the vertical quasi-static rail velocity during the passage of a single axle (200 km/h).

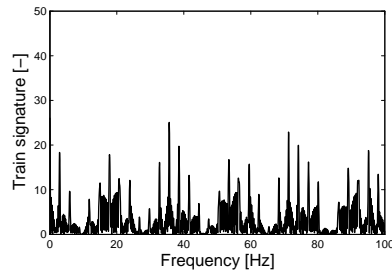


Figure 2.29: Signature of the Thalys train (200 km/h).

Figure 2.30 shows the quasi-static velocity of the rail during the passage of the Thalys train. The passage of single bogies and axles can clearly be distinguished in the time history of the rail velocity (figure 2.30a). The frequency spectrum (figure 2.30b) is obtained according to equation (2.11) as the product of the spectrum due to a single load (figure 2.28b) and the train signature (figure 2.29). This results in a spectrum that reaches a maximum value around 20 Hz and is furthermore characterized by the peaks and troughs observed in the train signature [7].

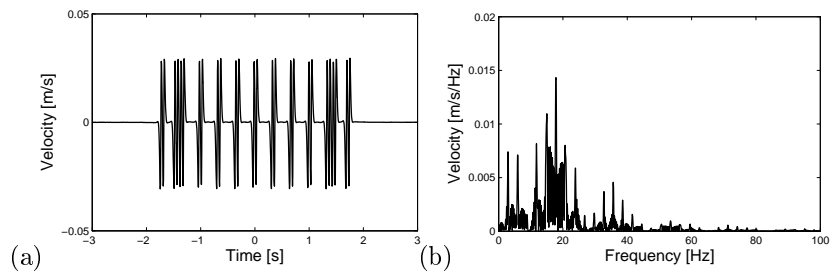


Figure 2.30: (a) Time history and (b) frequency content of the vertical quasi-static rail velocity during the passage of a Thalys train (200 km/h).

Figure 2.31 shows the quasi-static contribution to the free field response for the passage of the Thalys train. The response of the soil resembles a sequence of bowl shaped deflections traveling with each axle. The time variation of the response at a fixed point is therefore due to successive rising and falling of the response at the passage of each axle. At 6 m and 12 m, the response due to single bogies can still be distinguished in the time history of the velocity (figure 2.31a). At 24 m and 48 m, only the deflection due the multiple bogies or carriages is observed and the amplitude of the deflection has decreased. Due to this effect, the frequency content of the quasi-static contribution quickly shifts towards a lower frequency with increasing distance from the track. Only at very low frequencies a contribution is observed in the frequency spectrum, which is only shown up to 10 Hz in figure 2.31b.

### **Dynamic contribution**

Figure 2.32 shows the dynamic contribution to the rail velocity due to the passage of the Thalys train. The response due to different axles is observed less clearly than for the quasi-static contribution. The frequency spectrum shows a maximum around 80 Hz corresponding to the maximum in the axle load spectrum (figure 2.27) that is determined by the P2 resonance. Due to the interference of similar contributions of different axles, a quasi-discrete spectrum is obtained.

The dynamic contribution to the rail response (figure 2.32a) has a similar amplitude as the quasi-static contribution (figure 2.30a). The dynamic contribution has its maximum at a higher frequency of 80 Hz (figure 2.32b), however, while the quasi-static contribution is mainly concentrated in the low frequency range below 40 Hz (figure 2.30b).

Figure 2.33 shows the dynamic contribution to the free field velocity at 6 m, 12 m, 24 m, and 48 m from the track. The passage of individual axles is no longer observed due to overlap between the dynamic contributions of different axles. As the frequency spectrum of the response is attenuated with increasing distance and with increasing frequency, the peak of the spectrum moves to lower frequencies at larger distance from the track.

At 6 m from the track, the amplitude of the dynamic contribution (figure 2.33a) is about 100 times larger than the amplitude of the quasi-static contribution (figure 2.31a). While the dynamic axle loads contribute to the response in the entire frequency range of interest (figure 2.33b), the quasi-static contribution is much smaller and is concentrated at very low frequencies below 5 Hz (figure 2.31b). These results show that the response in the free field is dominated by

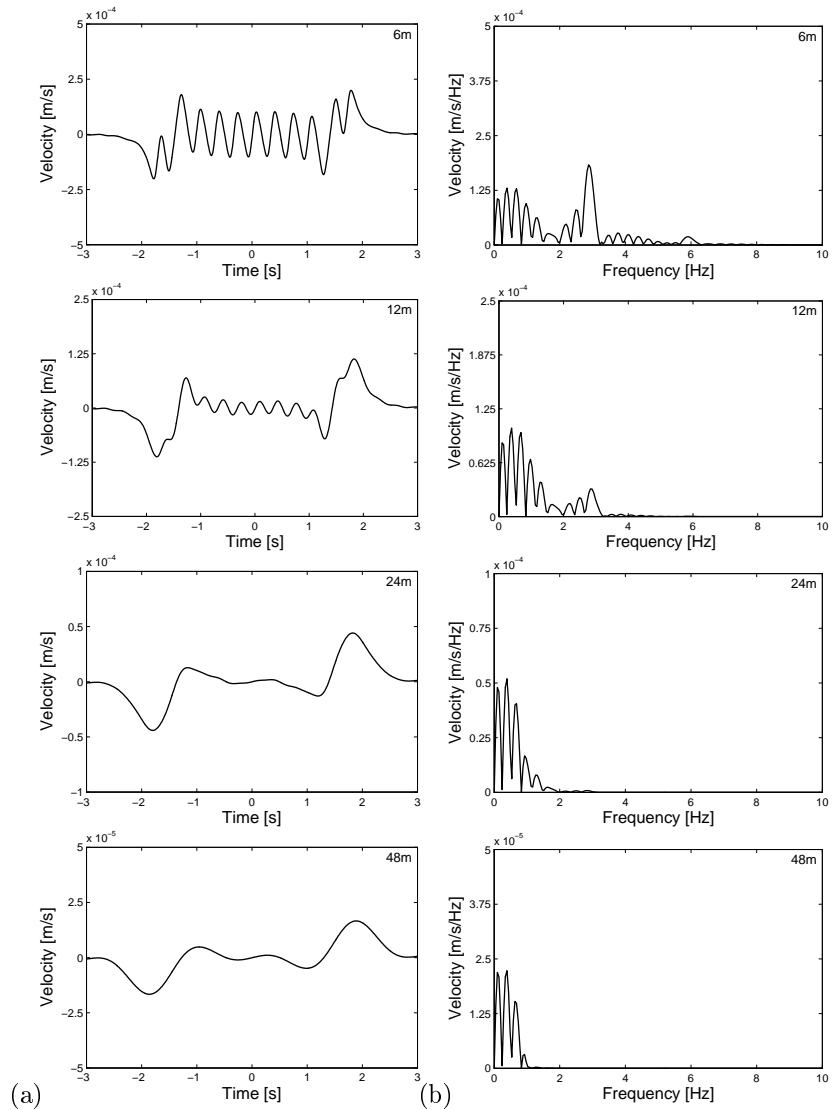


Figure 2.31: (a) Time history and (b) frequency content of the vertical quasi-static free field velocity at 6 m, 12 m, 24 m, and 48 m during the passage of a Thalys train (200 km/h).



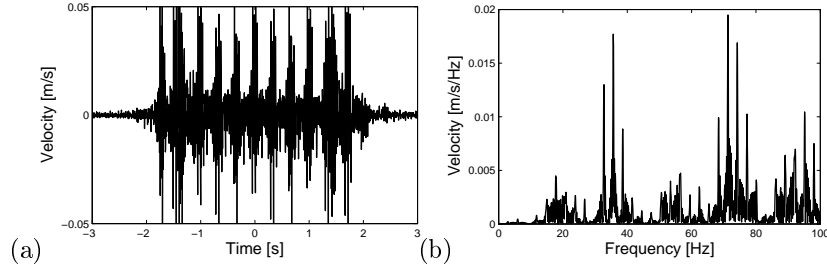


Figure 2.32: (a) Time history and (b) frequency content of the vertical dynamic rail velocity during the passage of a Thalys train (200 km/h).

the dynamic excitation above a frequency of 10 Hz and at more than a few meters from the track.

### Total response

The total track and soil displacement is obtained as the sum of the quasi-static and the dynamic contribution in equation (2.11) and equation (2.12), respectively. In the following, the focus is on the vertical ground velocity  $v_z(y, t)$ .

The running Root Mean Square (RMS) value  $v_{z\text{RMS}}(y, t)$  of the velocity is computed as:

$$v_{z\text{RMS}}(y, t) = \sqrt{\frac{1}{T_a} \int_{t-T_a/2}^{t+T_a/2} v_z^2(y, \tau) d\tau} \quad (2.39)$$

where  $T_a$  is the time window. In the present work, a time window  $T_a = 1$  s is applied as specified in the ISO standard 14873-1 [66].

As an illustration, figure 2.34 shows the time history  $v_z(y, t)$  and running RMS value  $v_{z\text{RMS}}(y, t)$  of the total free field velocity at 12 m from the track. The running RMS value  $v_{z\text{RMS}}(y, t)$  is characterized by an increasing amplitude when the train approaches, an approximately stationary amplitude during the pass-by, and a decreasing amplitude when the train moves away. The stationary part of the response during a train passage is selected using the German DIN standard [33] that distinguishes between three time intervals  $T_1$ ,  $T_2$ , and  $T_3$ . Time period  $T_1$  is the interval of 4 s around the maximum running RMS value  $v_{z\text{RMS}}(y, t)$  during the train passage. Within time period  $T_1$ , the maximum velocity  $v_{z\text{max}}(y) = \max[v_z(y, t)]$  is computed. Time period  $T_2$  is determined as the smallest extension of  $T_1$  such that the velocity  $v_z(y, t)$  does not exceed

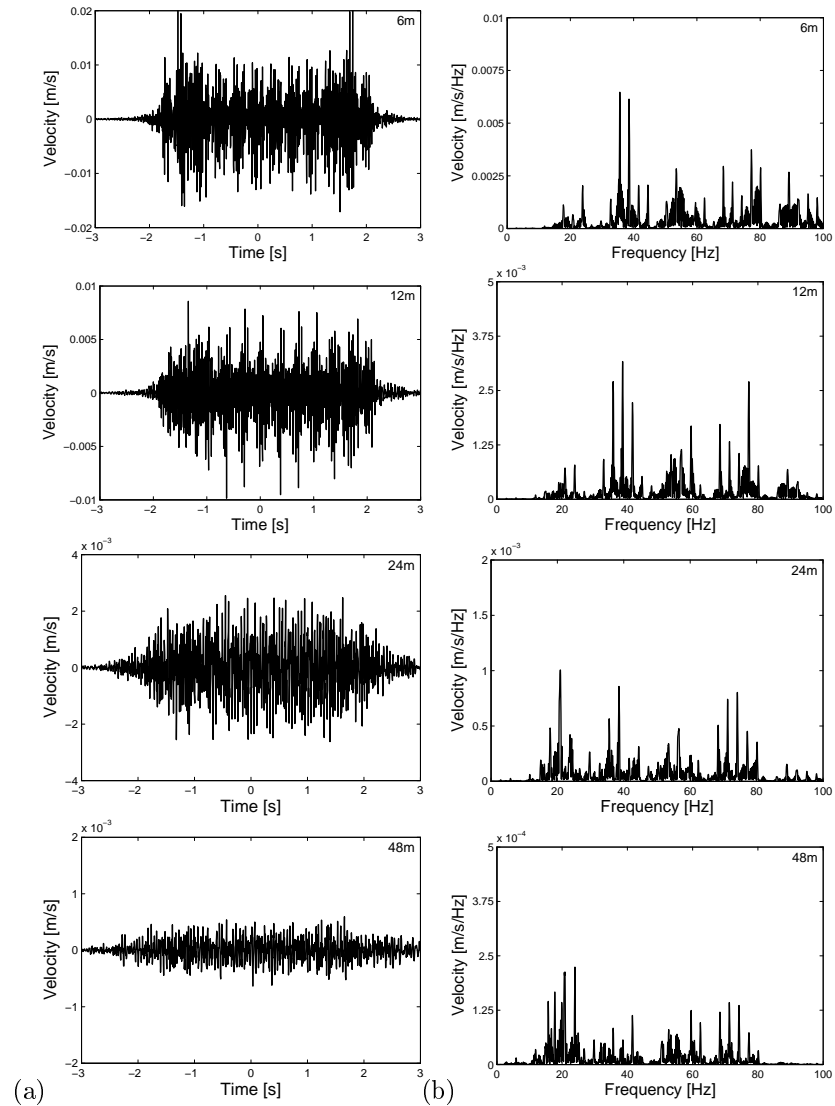


Figure 2.33: (a) Time history and (b) frequency content of the vertical dynamic free field velocity at 6 m, 12 m, 24 m, and 48 m during the passage of a Thalys train (200 km/h).

a value  $v_{z \max}(y)/4$  within 0.5 s just before and just after  $T_2$ . If necessary, the interval  $T_1$  is adjusted to make it a subset of  $T_2$ . Finally, the noise amplitude is defined as the mean value of  $v_{z \text{RMS}}(y, t)$  in the measured time interval outside the time period  $T_2$ . The time period  $T_3$  is determined as the largest extension of  $T_2$  in which  $v_{z \text{RMS}}(y, t)$  exceeds the noise amplitude. The obtained time periods  $T_1$ ,  $T_2$ , and  $T_3$  for the free field velocity at 12 m are indicated in figure 2.34.

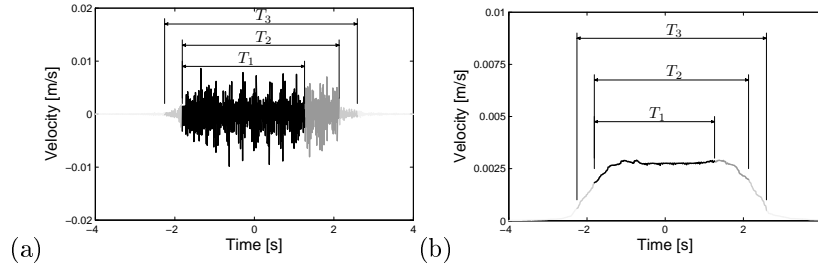


Figure 2.34: (a) Time history and (b) running RMS value of the vertical free field velocity at 12 m from the track during the passage of a Thalys train (200 km/h) indicating the time periods  $T_1$  (black line),  $T_2$  (dark grey line), and  $T_3$  (light grey line).

For a stationary signal, equation (2.39) can be applied with an infinitely long time window  $T_a$ . The result then no longer depends on the time  $t$  and is called the RMS value. According to Parseval's theorem, the RMS value  $x_{\text{RMS}m}$  of a stationary signal  $x(t)$  can also be computed in the  $m$ -th one-third octave band  $[\omega_{1m}, \omega_{2m}]$  based on the PSD  $\hat{S}_x(\omega)$ :

$$x_{\text{RMS}m} = \sqrt{\int_{\omega_{1m}}^{\omega_{2m}} \hat{S}_x(\omega) d\omega} \quad (2.40)$$

As the velocity  $v_z(y, t)$  due to a train passage is a transient signal, the PSD  $\hat{S}_{v_z}(y, \omega)$  of the stationary part of the velocity is approximated as [38]:

$$\hat{S}_{v_z}(y, \omega) = \mathbb{E}[|\hat{v}_{z \text{stat}}(y, \omega)|^2] \quad (2.41)$$

where  $\mathbb{E}[\ ]$  denotes the expected value operator and  $\hat{v}_{z \text{stat}}(y, \omega)$  is the truncated Fourier transform of the velocity  $v_z(y, t)$  in the stationary part  $[t_1, t_2]$  of the response:

$$\hat{v}_{z \text{stat}}(y, \omega) = \int_{t_1}^{t_2} v_z(y, t) \exp(-i\omega t) dt \quad (2.42)$$

In the following, the stationary part is selected based on the time period  $T_2$  [33]. The vibration velocity level  $L_v(y)$  is then defined as:

$$L_v(y) = 20 \log_{10}[v_{z\text{RMS}m}(y)] - L_{v0} \quad (2.43)$$

where  $L_{v0} = 20 \log_{10}[v_0]$  is a reference level. Reference velocities  $v_0 = 10^{-6}$  inch/s =  $2.54 \times 10^{-8}$  m/s,  $v_0 = 10^{-8}$  m/s, or  $v_0 = 5 \times 10^{-8}$  m/s are proposed in the literature [59]. In the present work, a reference velocity  $v_0 = 10^{-8}$  m/s is used.

Figure 2.35 shows the running RMS velocity and the vibration velocity level of the rail during the passage of the Thalys train at a speed of 200 km/h. The Thalys train has an articulated train composition and contains more axles at the front and the end than in the center of the train. This results in a higher amplitude of the running RMS value at the start and the end of the passage. In between, the stationary part of the response is clearly observed.

Figure 2.35b shows that both quasi-static and dynamic excitation significantly contribute to the rail velocity. The quasi-static excitation mainly contributes at lower frequencies, whereas the dynamic excitation mainly contributes at higher frequencies.

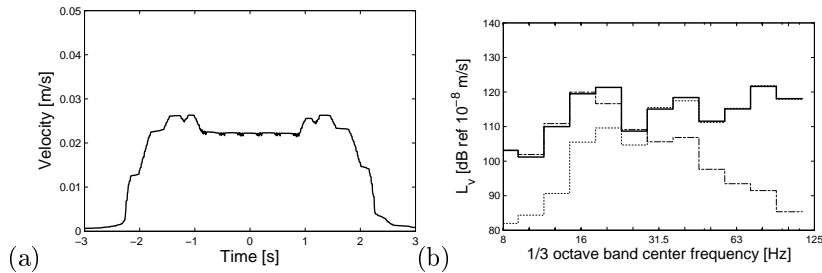


Figure 2.35: (a) Running RMS value and (b) one-third octave band RMS level of the vertical total rail velocity during the passage of a Thalys train (200 km/h). The quasi-static (dashdotted line) and dynamic (dotted line) one-third octave band RMS value are superimposed.

The dynamic contribution to the response is obtained based on a randomly generated unevenness sample according to equation (2.15). Figure 2.36 shows the running RMS velocity and the vibration velocity level in the free field for 10 samples of unevenness generated from the same PSD (FRA class 3). A considerable variation is observed with differences up to 10 dB in the entire frequency range. The running RMS value differs up to a factor of 2 (6 dB). This means that, even when the statistical properties of the unevenness are uniform along a track, substantial differences can be found in the free field

response due to a train passage at different sections of the same track-soil system.

The running RMS value shows a slightly higher amplitude at the start and the end of the passage due to the articulated train composition. The contributions from single axles have a longer duration and hence a larger overlap with increasing distance. At a larger distance, the peak at the start and the end of the passage is therefore less pronounced, resulting in a more constant value of the stationary part of the response.

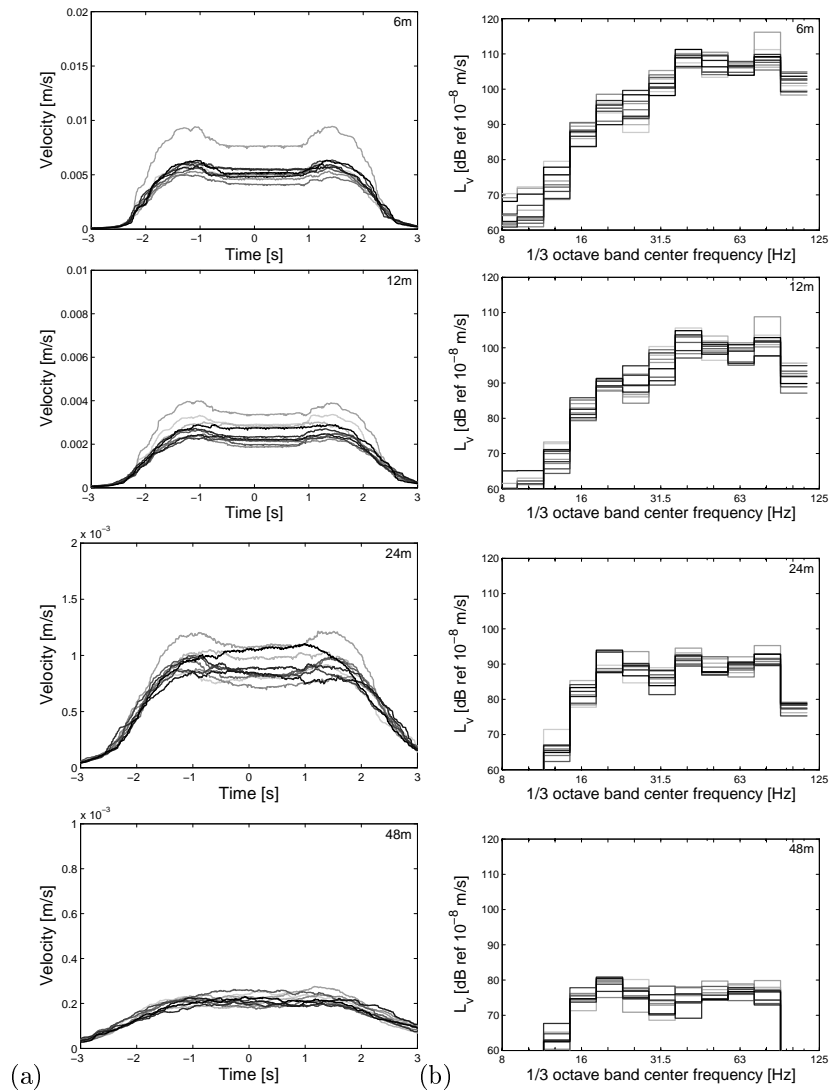


Figure 2.36: (a) Running RMS value and (b) one-third octave band RMS level of the vertical total free field velocity at 6 m, 12 m, 24 m, and 48 m during the passage of a Thalys train (200 km/h) for 10 unevenness samples based on FRA class 3 (black to grey lines).

## 2.6 Free field response for fixed and incoherent axle loads

The previous section shows that the free field response is dominated by the dynamic excitation at frequencies higher than 10 Hz and at more than a few meters from the track. Furthermore, it is shown that the free field response is characterized by an approximately stationary vibration amplitude during the passage of the train. In the present section, it is investigated if the quasi-stationary vibration amplitude can accurately be predicted based on the dynamic axle loads by introducing the assumptions of fixed and incoherent axle loads.

### 2.6.1 Assumption of fixed axle loads

In the following, the free field velocity  $\hat{\mathbf{v}}(y, \omega)$  due to a train passage is predicted based on equation (2.10):

$$\hat{\mathbf{v}}(y, \omega) = \sum_{k=1}^{n_a} \frac{1}{2\pi} \int_{-\infty}^{+\infty} \tilde{\mathbf{H}}_{\mathbf{v}}^{\text{T}}(k_y, \omega) \hat{\mathbf{g}}_{\text{dk}}(\omega - k_y v) \times \exp[-ik_y(y - y_{k0})] dk_y \quad (2.44)$$

where the  $3 \times 3$  transfer matrix  $\tilde{\mathbf{H}}_{\mathbf{v}}(k_y, \omega)$  collects the track – free field mobilities  $\tilde{h}_{vij}(k_y, \omega)$ .

The time history of the vibration velocity in a fixed point in the free field computed with equation (2.44) is a transient signal. The running RMS value (figure 2.36) shows that the response is characterized by a nearly stationary vibration amplitude during the train passage. An attempt is made to predict the amplitude of the stationary part of the response by assuming fixed axle loads [152]. This assumption is introduced in equation (2.44) by setting the train speed  $v$  equal to zero, which implies that the dynamic axle loads are assumed to be acting at fixed positions  $\mathbf{x}_k = \mathbf{x}_{k0}$ :

$$\hat{\mathbf{v}}(y, \omega) = \sum_{k=1}^{n_a} \frac{1}{2\pi} \int_{-\infty}^{+\infty} \tilde{\mathbf{H}}_{\mathbf{v}}^{\text{T}}(k_y, \omega) \hat{\mathbf{g}}_{\text{dk}}(\omega) \exp[-ik_y(y - y_{k0})] dk_y \quad (2.45)$$

As a result, the shift  $k_y v$  between the frequency content of the receiver and the frequency content of the source in equation (2.44) representing the Doppler effect is no longer present and the inverse wavenumber domain transformation in equation (2.45) can be elaborated as follows:

$$\hat{\mathbf{v}}(y, \omega) = \sum_{k=1}^{n_a} \hat{\mathbf{H}}_{\mathbf{v}}^T(y - y_{k0}, \omega) \hat{\mathbf{g}}_{dk}(\omega) \quad (2.46)$$

corresponding to the classical result for dynamic loads at a fixed position.

The assumption of fixed axle loads is illustrated in figure 2.37, showing the time history and the running RMS value of the free field velocity during the passage of a Thalys train at a speed of 200 km/h calculated with moving loads according to equation (2.44) and with fixed loads according to equation (2.46). Due to the fixed position of the axles, a stationary response is obtained in the second case. The response to the fixed axle loads agrees well with the response to the moving axle loads during the stationary part. In the following, the assumption of fixed axle loads is used to estimate the vibration amplitude during this stationary part.

As the dynamic axle loads are determined by random track unevenness, as discussed in subsection 2.3.1, they represent a random process. Corresponding to equation (2.46), the free field response  $\hat{\mathbf{v}}(y, \omega)$  due to random axle loads is a random process as well and can be characterized by the PSD  $\hat{\mathbf{S}}_{\mathbf{v}}(y, \omega)$  [38]:

$$\hat{\mathbf{S}}_{\mathbf{v}}(y, \omega) = \sum_{k=1}^{n_a} \sum_{l=1}^{n_a} \hat{\mathbf{H}}_{\mathbf{v}}^T(y - y_{k0}, \omega) \hat{\mathbf{S}}_{\mathbf{g}kl}(\omega) \hat{\mathbf{H}}_{\mathbf{v}}^*(y - y_{l0}, \omega) \quad (2.47)$$

where  $\hat{\mathbf{S}}_{\mathbf{g}kl}(\omega)$  is the  $3 \times 3$  cross-PSD matrix of the axle loads  $\hat{\mathbf{g}}_{dk}(\omega)$  and  $\hat{\mathbf{g}}_{dl}(\omega)$ . This matrix is a submatrix of the previously discussed cross-PSD matrix  $\hat{\mathbf{S}}_{\mathbf{g}}(\omega)$  in equation (2.24).

When only the vertical velocity due to vertical axle loads is considered, the cross-PSD matrix  $\hat{\mathbf{S}}_{\mathbf{g}kl}(\omega)$  reduces to a scalar-valued cross-PSD denoted as  $\hat{S}_{g_z kl}(\omega)$  and equation (2.47) can be simplified as follows for the computation of the PSD  $\hat{S}_{v_z}(y, \omega)$  of the vertical velocity:

$$\hat{S}_{v_z}(y, \omega) = \sum_{k=1}^{n_a} \sum_{l=1}^{n_a} \hat{h}_{v_z z}(y - y_{k0}, \omega) \hat{S}_{g_z kl}(\omega) \hat{h}_{v_z z}^*(y - y_{l0}, \omega) \quad (2.48)$$



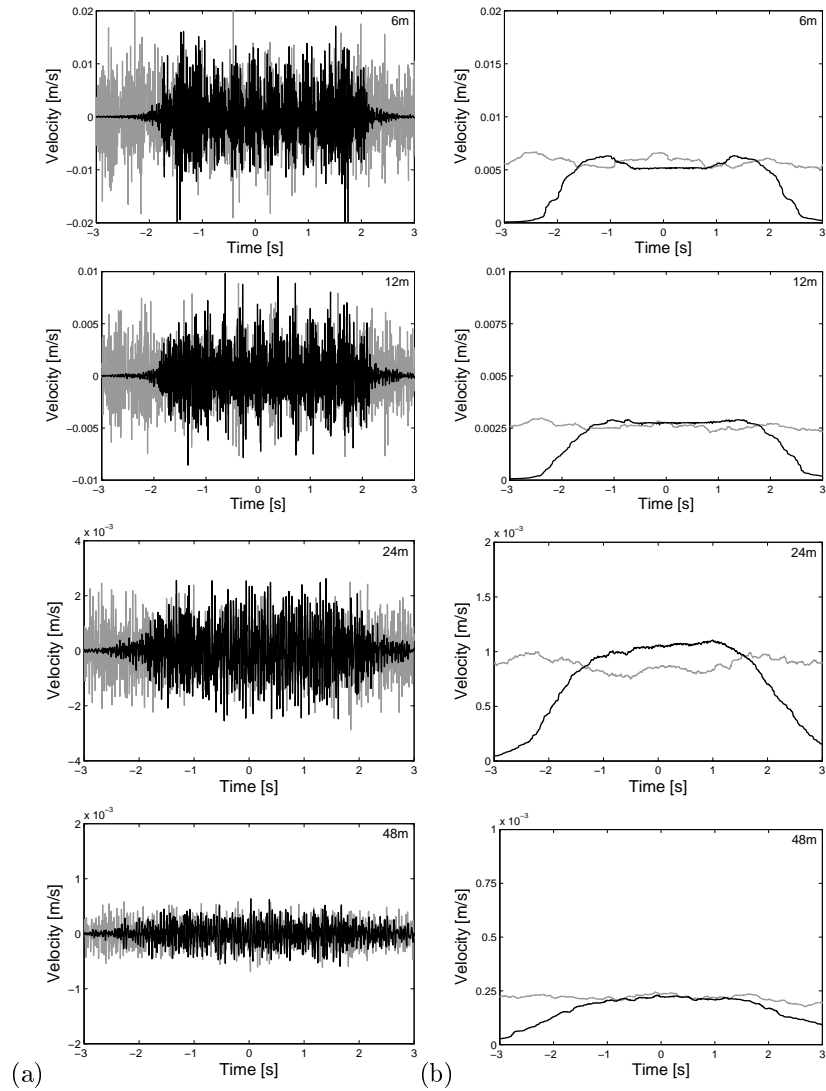


Figure 2.37: (a) Time history and (b) running RMS value of the vertical free field velocity at 6 m, 12 m, 24 m, and 48 m during the passage of a Thalys train (200 km/h) computed with moving (black line) and fixed (grey line) axle loads.

According to equation (2.40), the one-third octave band RMS value  $v_{z\text{RMS}m}(y)$  of the vertical velocity is computed in the frequency domain based on the PSD  $\hat{S}_{v_z}(y, \omega)$  of the vibration velocity given in equation (2.48):

$$v_{z\text{RMS}m}^2(y) = \int_{\omega_{1m}}^{\omega_{2m}} \sum_{k=1}^{n_a} \sum_{l=1}^{n_a} \hat{h}_{vzz}(y - y_{k0}, \omega) \hat{S}_{g_z kl}(\omega) \times \hat{h}_{vzz}^*(y - y_{l0}, \omega) d\omega \quad (2.49)$$

Figure 2.38 shows the one-third octave band free field vibration velocity level during the passage of the Thalys train, calculated for moving and fixed loads. The response due to moving loads is an average based on 10 unevenness samples. As the vibration velocity level is computed for the stationary part of the response, a relatively good agreement is found at all receivers. A difference up to 6 dB at most is found that is caused by disregarding the speed of the train. A similar conclusion is found for railway traffic in tunnels [152]. It can reasonably be expected that these assumptions hold for similar train passages where a long stationary part is observed in the response, e.g. for long trains composed of similar carriages or for low train speeds.

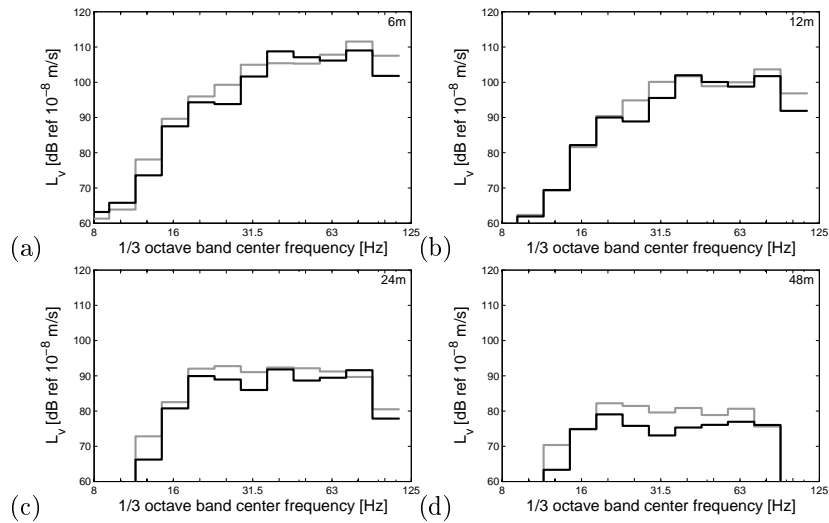


Figure 2.38: One-third octave band RMS level of the vertical free field velocity at (a) 6 m, (b) 12 m, (c) 24 m, and (d) 48 m during the passage of a Thalys train (200 km/h) computed with moving (black line) and fixed (grey line) axle loads.

### 2.6.2 Assumption of incoherent axle loads

In equation (2.49), the coherence between different axles  $k$  and  $l$  is taken into account by means of the cross-PSD  $\hat{S}_{g_z kl}(\omega)$ . The cross-PSD  $\hat{S}_{g_z kl}(\omega)$  for different axles  $k$  and  $l$  is an oscillating function in terms of  $\omega$  with a period determined by the time lag  $(y_{k0} - y_{l0})/v$ , resulting in an oscillating PSD  $\hat{S}_{v_z}(y, \omega)$  as well. When the vibration velocity level is calculated in sufficiently large frequency bands  $[\omega_{1m}, \omega_{2m}]$ , the oscillations observed in the PSD  $\hat{S}_{v_z}(y, \omega)$  are canceled by averaging within each frequency band [156] and the coherence between different axles  $k$  and  $l$  can be omitted by disregarding the contribution of the cross-PSDs  $\hat{S}_{g_z kl}(\omega)$  for  $k \neq l$  in equation (2.49):

$$v_{z\text{RMS}m}^2(y) = \int_{\omega_{1m}}^{\omega_{2m}} \hat{S}_{g_z kk}(\omega) \sum_{k=1}^{n_a} |\hat{h}_{v_z z}(y - y_{k0}, \omega)|^2 d\omega \quad (2.50)$$

Corresponding to equation (2.24), the (auto) PSDs  $\hat{S}_{g_z kk}(\omega)$  are determined by the combined vehicle and track compliance matrix. Due to differences in the unsprung mass of the axles and due to coupling of different axles through the track by means of the track compliance matrix, a different PSD is found for different axles  $k$ .

Figure 2.39 shows the PSD  $\hat{S}_{g_z kk}(\omega)$  of 26 axles of the Thalys train with equal unsprung mass. The PSD  $\hat{S}_{g_z}(\omega)$  for a single uncoupled axle is superimposed in the figure. At frequencies below 20 Hz, the train-track interaction is dominated by the vehicle dynamics and the PSDs  $\hat{S}_{g_z kk}(\omega)$  are identical. At higher frequencies, the track compliance affects the axle loads and results in slightly different PSDs  $\hat{S}_{g_z kk}(\omega)$  that oscillate around the PSD  $\hat{S}_{g_z}(\omega)$  of the single axle due to the effect of coupling through the track.

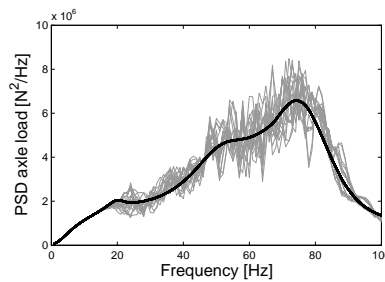


Figure 2.39: Modulus of the PSD of the vertical loads of a Thalys train for 26 coupled axles (grey lines) and a single uncoupled axle (black line).

As the vibration velocity level is calculated in sufficiently large frequency bands  $[\omega_{1m}, \omega_{2m}]$ , the oscillations of the PSDs  $\hat{S}_{g_z k k}(\omega)$  are averaged within each frequency band, and equation (2.50) can be further simplified by using the (average) PSD  $\hat{S}_{g_z}(\omega)$  of a single uncoupled axle:

$$v_{z\text{RMS}m}^2(y) = \int_{\omega_{1m}}^{\omega_{2m}} \hat{S}_{g_z}(\omega) \sum_{k=1}^{n_a} |\hat{h}_{vzz}(y - y_{k0}, \omega)|^2 d\omega \quad (2.51)$$

This simplification is only valid, however, when the unsprung mass of all axles of the train is equal (or similar).

The effect of the previous assumptions is illustrated in figure 2.40 where the PSD  $\hat{S}_{v_z}(y, \omega)$  is shown for the free field response due to the Thalys passage. Coherent axle loads are considered in the first case, while incoherent and uncoupled axle loads are considered in the second case. As expected, the result obtained with incoherent axle loads is much smoother than the result obtained with coherent axle loads.

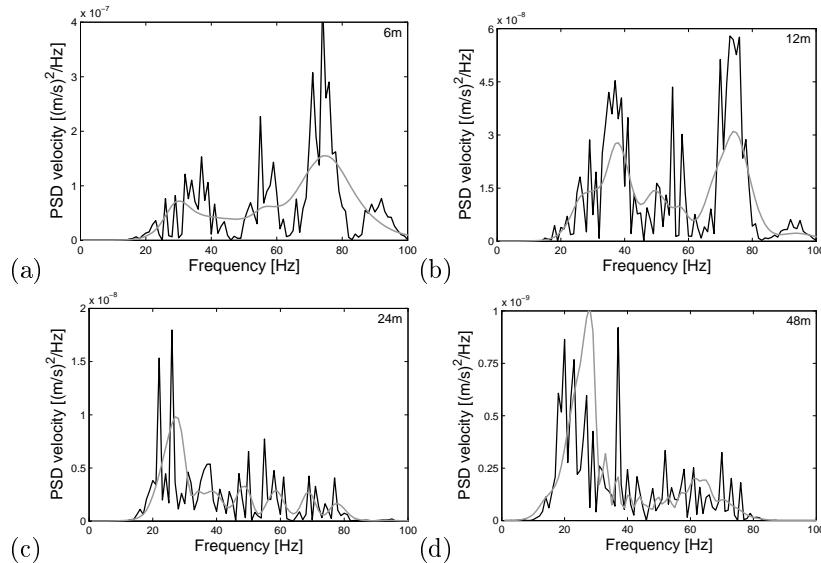


Figure 2.40: PSD of the vertical free field velocity at (a) 6 m, (b) 12 m, (c) 24 m, and (d) 48 m during the passage of a Thalys train (200 km/h) computed with coherent (black line) and incoherent (grey line) axle loads.

Figure 2.41 shows the vibration velocity level for the same passage, calculated with coherent axle loads according to equation (2.49) and with incoherent and

uncoupled axle loads according to equation (2.51). These results are the one-third octave band representation of the PSDs  $\hat{S}_{v_z}(y, \omega)$  shown in figure 2.40. The difference in figure 2.40 is averaged within each frequency band and a limited difference up to 4 dB is generally found between both results in one-third octave bands.

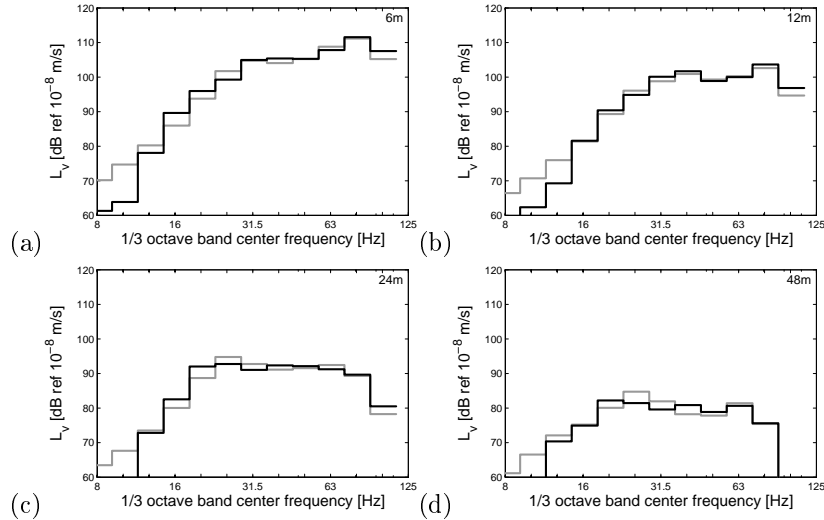


Figure 2.41: One-third octave band RMS level of the vertical free field velocity at (a) 6 m, (b) 12 m, (c) 24 m, and (d) 48 m during the passage of a Thalys train (200 km/h) computed with coherent (black line) and incoherent (grey line) axle loads.

Equation (2.51) offers an expression to calculate the vibration amplitude in the free field based directly on the statistical properties of the track unevenness, no longer requiring the generation of an unevenness sample. The assumptions of fixed and incoherent axle loads are shown to be valid in the considered example for the calculation of the vibration amplitude in one-third octave bands during the stationary part of the response.

## 2.7 Conclusion

This chapter presents the framework for the numerical prediction of railway induced vibration. The prediction of the response due to a train passage is based on the axle loads and the track – free field transfer function. A distinction is made between quasi-static and dynamic excitation.

The dynamic axle loads are calculated based on the dynamic train-track interaction by means of a compliance formulation. The dynamic track-soil interaction problem is solved to calculate the dynamic track stiffness and the track – free field transfer functions.

A numerical example shows the results for the case of a Thalys train running on a classical ballasted track and the effect of the soil properties on the transfer function and the track-soil interaction is illustrated by considering a homogeneous and a layered halfspace. Within the present work, the following two observations are particularly noteworthy.

First, the numerical example illustrates the effect of the dynamic track – soil interaction on the transfer function. The so-called track filtering effect results in a reduction of the transfer function in the higher frequency range and depends on the characteristics of the track and the soil.

Second, the vibration velocity in the free field due to a train passage is dominated by the dynamic contribution and is typically characterized by an approximately stationary part during the passage of the train. It is illustrated by means of an example that the stationary free field vibration amplitude can be predicted by introducing the simplifying assumptions of fixed and incoherent axle loads. The influence of these assumptions is limited to 6 dB (fixed axle loads) and 4 dB (incoherent axle loads) in the considered example when the vibration velocity level of the stationary part of the response is predicted in one-third octave bands. It can reasonably be expected that these assumptions hold when the response due to a train passage contains a long stationary part, e.g. for long trains or for low train speeds.

## Chapter 3

# Experimental validation

### 3.1 Introduction

In the present chapter, the accuracy of the numerical prediction model presented in chapter 2 is assessed by means of an experimental validation. For this purpose, an extensive measurement campaign has been carried out at a site in Lincet, Belgium. Compared to previous validation studies performed at the same site [94, 98, 99], a more detailed model is used that takes into account the excavation and the track subgrade at the site.

The site in Lincet is presented in section 3.2. Next, the numerical model is validated in different steps: the free field mobility in section 3.3, the track receptance in section 3.4, the track – free field mobility in section 3.5, and the response due to train passages in section 3.6. In each section, the identification of the relevant dynamic characteristics is discussed first and the influence of the excavation and the track subgrade is investigated next. Finally, the accuracy of each submodel is assessed by comparison to the measured results.

The conclusion is presented in section 3.7.

### 3.2 The site in Lincet

The high speed line L2 is the eastern part of the high speed railway network in Belgium connecting Brussels and Köln. The section between Brussels and

Liège has been constructed between 1998 and 2002 and mainly follows the E40 highway. The test site in Lincient is located next to the high speed line L2 at kilometer 61.450, near the access point in the Rue de la Bruyère. Figure 3.1 gives a plan of the measurement site.

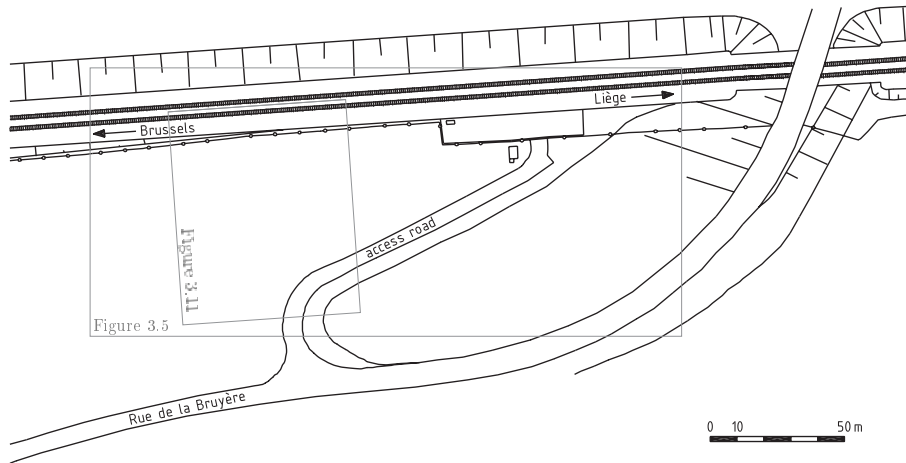


Figure 3.1: Plan of the site in Lincient [132].

The high speed railway line is constructed in an excavation and runs parallel to the E40 highway separated by an embankment. A cross section of the site is shown in figure 3.2. The access point in the Rue de la Bruyère is located at the opposite side of the embankment, where the free field has an approximately horizontal surface. The excavation, varying in depth along the railway line, is around 1.0 m deep near the access point. A view of the site is shown in figure 3.3a.

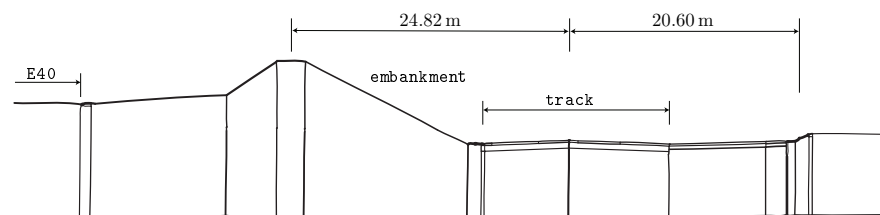


Figure 3.2: Cross section of the site in Lincient [132].

The high speed line L2 consists of two railway tracks, one track in the direction of Liège (track 1) and one track in the direction of Brussels (track 2). Both



tracks are a classical ballasted track (figure 2.4) with UIC 60 rails supported every 0.60 m by rubber pads on monoblock sleepers. The rails are continuously welded and are fixed with a Pandrol E2039 rail fastening system and supported by resilient studded rubber rail pads (type 5197) with a thickness of 11 mm. Each rail pad is preloaded with a clip toe load of about 20 kN per rail seat. The prestressed concrete monoblock sleepers have a length  $l_{sl} = 2.50$  m, a width  $w_{sl} = 0.235$  m, a height  $h_{sl} = 0.205$  m (under the rail), and a mass  $m_{sl} = 300$  kg. The track is supported by a porphyry ballast layer (caliber 25/50, thickness 0.35 m) and a limestone sub-ballast layer (thickness 0.60 m). The density of these ballast layers is  $1700 \text{ kg/m}^3$ . Below the ballast, the soil has been stabilized over a depth of 1.0 m by means of lime. A view of the track is shown in figure 3.3b.

Four different train types are operating on the line L2 in Lincant: the InterCity (IC) trains of type IC-A and IC-O and the Thalys and ICE HSTs. The characteristics of these trains are discussed in subsection 3.6.1.

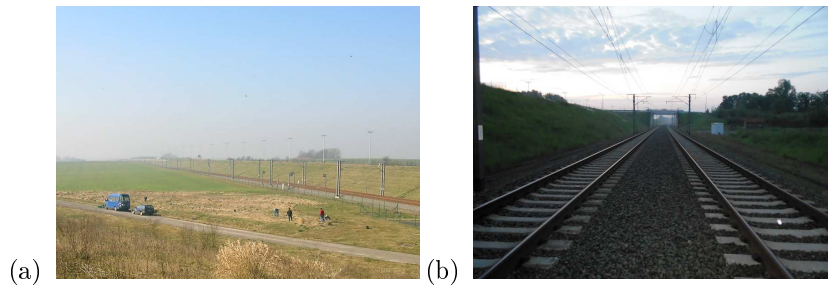


Figure 3.3: View of (a) the measurement site and (b) the track in Lincant.

A number of dynamic tests has previously been carried out at the site in Lincant. A first set of tests aimed at identifying the dynamic soil and track characteristics. The dynamic soil characteristics were determined by means of Seismic Cone Penetration Tests (SCPTs), Spectral Analysis of Surface Waves (SASW) tests, and Seismic Refraction (SR) tests and are discussed in subsection 3.3.1. The dynamic track characteristics were determined based on a track receptance test carried out in loaded and unloaded conditions and are discussed in subsection 3.4.1.

A second set of tests has been performed to validate the prediction of railway induced vibration. On the occasion of the homologation tests prior to the opening of the high speed line L2, the track and free field response were measured during 11 IC passages (155.9 – 225.3 km/h) and 12 Thalys passages (99.5 – 326.1 km/h) [77]. The track – free field mobility was measured by applying impacts at the right rail by means of a falling weight device [79].

Within the frame of the present work, additional measurement campaigns have been carried out in 2011 and 2012. An additional SASW test has been performed in 2011 to identify the dynamic soil characteristics close to the track [131]. The free field and track – free field mobilities have been determined by applying an excitation at the soil’s surface adjacent to the track or at the edge of the sleeper, respectively [150,151]. Furthermore, the response of the track and in the free field has been measured during 103 train passages [150].

The broad range of available data for the site in Lincent allows for a detailed analysis of dynamic track and soil characteristics and for a step-wise validation of different submodels for the numerical prediction of railway induced vibration, presented in the following sections.

### **3.3 The free field mobility**

In the present section, it is investigated to which extent the free field mobility can be predicted numerically based on input data of the soil provided by preliminary site investigation. First, the identification of the dynamic soil characteristics at the site in Lincent is discussed. Next, the influence of the excavation on the free field mobility is investigated by means of numerical simulations. Finally, the measured and predicted free field mobilities are compared.

#### **3.3.1 The identification of dynamic soil characteristics**

At the site in Lincent, several borings were carried out in preparation of the construction of the high speed railway track in order to identify the local geology. The result of the borings is summarized in figure 3.4 and is described as follows [94]. The borings reveal the presence of a shallow Quaternary top layer of silt with a thickness of 1.2 m, followed by a layer of fine sand up to a depth of 3.2 m. Between 3.2 and 7.5 m is a sequence of stiff layers of arenite (a sediment of a sandstone residue) embedded in clay. Below the arenite layers is a layer of clay (from 7.5 to 8.5 m depth), followed by fine sand (from 8.5 to 10 m), below which thin layers of fine sand and clay are found.

The depth of the ground water table was monitored from August 1993 to July 1997. It exhibited seasonal fluctuations between 6.0 m and 12.2 m, with an average value of 10.4 m [69].

A number of in situ tests is performed at the site in Lincent for the identification of the (small strain) dynamic soil characteristics. Figure 3.5 gives an overview

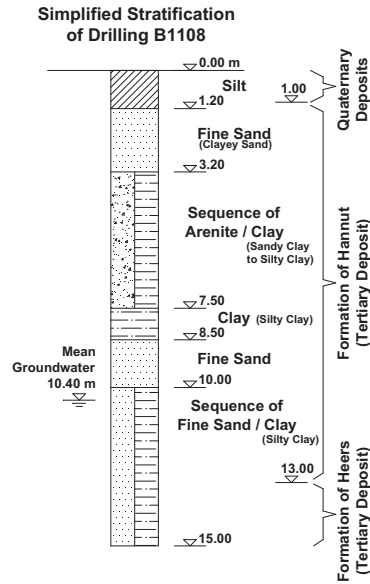


Figure 3.4: Local geology at the site in Lincent [69].

of the site with the location of two SCPTs and two SASW tests. The results from these tests are presented in the following.

In the SCPT technique, a seismic cone equipped with triaxial accelerometers or geophones is pushed into the soil and a lateral or vertical excitation is applied at the soil's surface [121]. Two SCPTs were carried out in 2003 with a dual accelerometer cone (SCPT1 and SCPT2) [70]. The location of the SCPTs is shown in figure 3.5.

The shear wave velocity of the soil is determined based on the cross correlation between the two simultaneously recorded signals in the dual accelerometer cone. In order to estimate the variation of the soil properties with depth, the experiment is repeated for different depths of the seismic cone.

Figure 3.6a shows the measured shear wave velocity for SCPT1 and SCPT2. The profiles show a nearly linear increase of the shear wave velocity from about 160 m/s at 1 m depth to about 310 m/s at 6.5 m depth.

The signals recorded in SCPT2 were obtained using two different excitation sources: a mechanical hammer (MH) and a sledgehammer (SH). These results were used to obtain an estimate of the material damping ratio using the Spectral Ratio Slope (SRS) method [18]. The results are shown in figure 3.6b and show

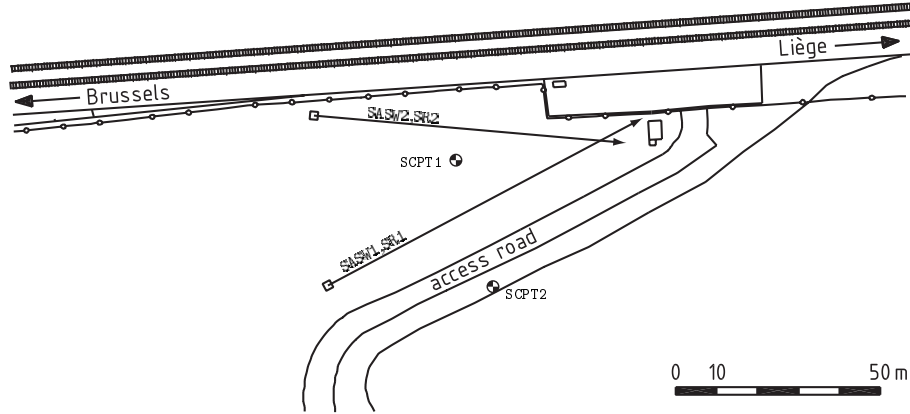


Figure 3.5: Location of the SCPT and SASW tests at the site in Lincent.

a large scatter with values between 0 and 0.06 at all depths [69].

In the SASW technique, surface waves are generated and the resulting response is recorded on a line of receivers at the soil's surface [108,159]. The orientation of the receiver line is indicated in figure 3.5 for two SASW tests carried out at the site in Lincent. In 2008, a SASW test was performed with a large number of measurement points in order to investigate the influence of the sensor placement (SASW1) [10]. In 2011, a new SASW test has been carried out within the framework of the present research to determine the soil characteristics close to the railway track (SASW2) [131].

The wave field measured along the line of receivers is used to determine the experimental dispersion curve of the surface waves. An inverse problem is solved to determine the shear wave velocity profile. Figure 3.6a shows the shear wave velocity obtained for SASW1 and SASW2. The results show a regular soil profile with a shear wave velocity increasing with depth and agree relatively well with the results of SCPT1 and SCPT2. At a depth between 3 and 4 m, the shear wave velocity increases from around 160 m/s up to around 310 m/s for both profiles, which can be related to the presence of the arenite layer found in the borings at a depth between 3.2 and 7.5 m (figure 3.4).

In SASW1 and SASW2, the material damping ratio has been estimated as well by simultaneously fitting the experimental dispersion curve and attenuation curve [90,120]. The attenuation curve is determined using the half-power bandwidth method [10]. The material damping ratio obtained from SASW1 and SASW2 is shown in figure 3.6b. SASW2 yields a relatively high material damping ratio of 0.09 at large depths. The damping ratio obtained with SASW1 does not exceed

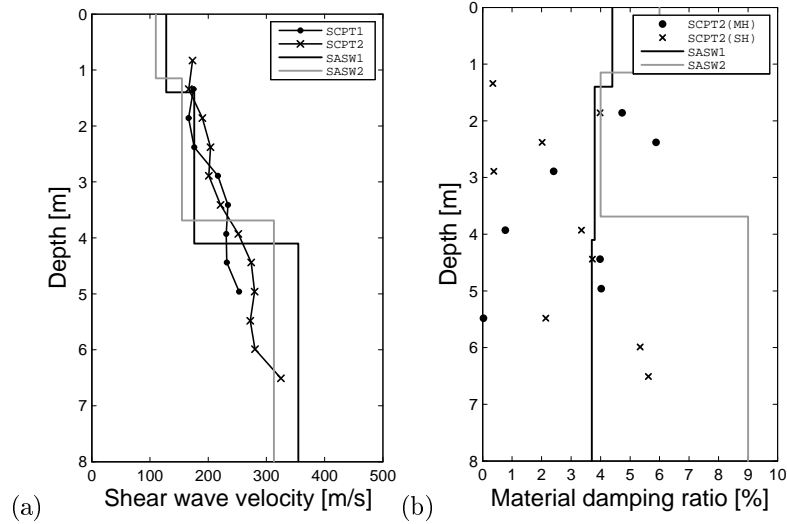


Figure 3.6: (a) Shear wave velocity and (b) material damping ratio obtained from SCPT1, SCPT2, SASW1, and SASW2 at the site in Lincent.

a value of 0.05 and decreases with depth, as would be expected. Due to the high scatter, the results obtained from the SCPTs (figure 3.6b) are difficult to compare with the results obtained from the SASW tests.

Simultaneously with the SASW tests, SR tests have been carried out in order to estimate the longitudinal wave velocity based on the arrival time of the first longitudinal wave. Two SR tests have been carried out at the site in Lincent (SR1 and SR2) corresponding to the previously described SASW tests as indicated in figure 3.5. Figure 3.7 shows the measured longitudinal wave velocity that exhibits a strong increase at a depth between 3 and 4 m related to the presence of the arenite layer.

Whereas the SASW method offers a valuable approach to identify dynamic soil characteristics, the technique also has its limitations. As the impact hammer used for the SASW tests at the site in Lincent generates waves up to a limited depth, the SASW method only results in a reliable identification at shallow depths. An attempt can be made to increase the maximum depth of the shear wave velocity estimation by applying a larger impact or by including results from passive vibration measurements [116]. Furthermore, the solution of the inverse problem obtained in the SASW technique is non-unique [122]. A probabilistic assessment of the SASW test at the site in Lincent shows that the uncertainty increases with increasing frequency and distance due to the increasing influence of small scale variations of the soil profile. Due to these

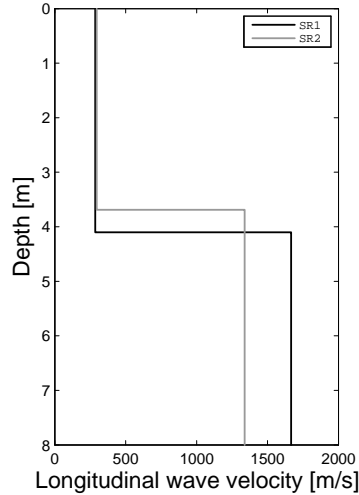


Figure 3.7: Longitudinal wave velocity obtained from SR1 and SR2 at the site in Lincent

limitations, the identification of the soil characteristics based on the SASW technique is expected to result in a more accurate prediction in an intermediate frequency interval between 20 and 50 Hz [133].

In the SASW technique, the assumption of a horizontally layered soil is used, introducing an additional uncertainty. Measurements at the site in Lincent show that results are influenced up to 6 dB by performing SASW tests with a different orientation [5].

The shear wave velocity profile determined with the SASW tests at the site in Lincent shows a good correspondence with the results from the SCPTs. A better accuracy of predicted results is found for SASW1 [10] than for SASW2 [131], however. The soil profile obtained in SASW1 is summarized in table 3.1 and is used in the following sections for the validation of the predicted free field mobility.

### 3.3.2 Influence of the excavation on the free field mobility

Before validation of the numerical prediction with the experimental results, the effect of the excavation on the free field mobility is studied by means of numerical simulation.

Layer	$h$ [m]	$C_s$ [m/s]	$C_p$ [m/s]	$\beta_s$ [-]	$\beta_p$ [-]	$\rho$ [kg/m <sup>3</sup> ]
1	1.4	128	286	0.044	0.044	1800
2	2.7	176	286	0.038	0.038	1800
3	$\infty$	355	1667	0.037	0.037	1800

Table 3.1: Dynamic soil characteristics at the site in Lincent obtained from SASW1 [10].

The dimensions of the excavation vary along the track. In the numerical model, however, the track–soil system and hence the geometry is assumed to be invariant in the direction  $\mathbf{e}_y$ . A geometry is therefore adopted that is representative for the excavation near the access point (figure 3.1). Figure 3.8 shows the assumed geometry of the excavation with upper width  $w_{eu} = 15$  m, lower width  $w_{el} = 14$  m, and depth  $h_e = 1$  m. The width of the excavation is chosen such that the distance between the center line of track 2 and the edge of the excavation is correct. Track 2 is assumed to be located in the center of the excavation. The embankment between the high speed line and the E40 highway is disregarded, as it is located at the opposite side of the access point (figure 3.2) and therefore has little influence on the free field mobility.

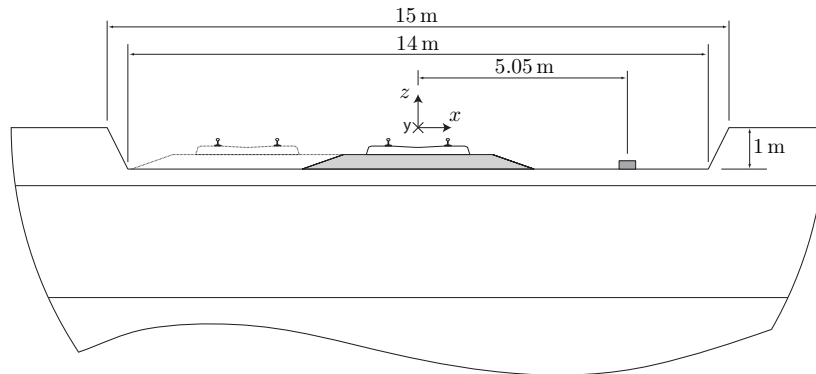


Figure 3.8: Assumed geometry of the excavation at the site in Lincent.

The free field mobility is determined by applying impacts to a foundation installed at the soil's surface adjacent to the track (figure 3.8). As this foundation is installed at 5.05 m from the track center line, it is located within the excavation at a depth of 1 m. The influence of the excavation on the free field mobility is investigated by using two different numerical models, shown in

figure 3.9. In each model, a rigid foundation is coupled to a BE model of the soil.

The first model (figure 3.9a) applies a simplified geometry, where the excavation is disregarded and the rigid foundation is located at the surface of the layered halfspace (excitation at the surface). The BE model of the soil only contains the contact area between the foundation and the soil where the displacement due to the applied hammer impact is imposed. In the second model (figure 3.9b), the excavation is taken into account and the foundation is located at a depth  $h_e = 1$  m (excitation in the excavation). The BE model of the soil additionally contains the free boundary of the excavation where traction free boundary conditions are imposed.

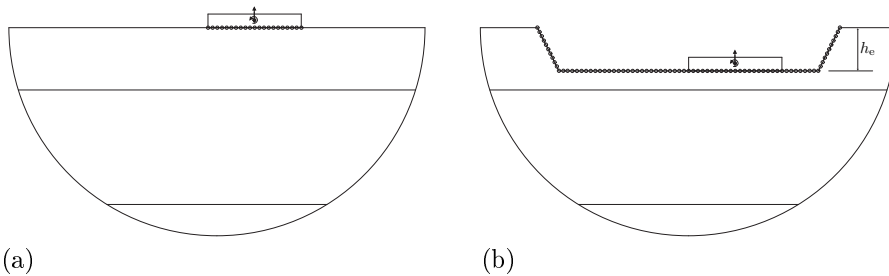


Figure 3.9: Cross section of the 2.5D soil model for excitation (a) at the surface and (b) in the excavation.

Figure 3.10 shows the mobilities computed with both models and shows a difference that increases up to 10 dB in the considered frequency range but generally relatively small.

At low frequencies, the wavelength in the soil is large compared to the excavation depth  $h_e$  and the mobility is not affected significantly. A very good agreement is therefore found up to around 20 Hz. Around 20 Hz, the wavelength in the top layer is of the same order of magnitude as the excavation depth  $h_e$  and starts to affect the mobility. At 6 m, the mobility is additionally affected by the reduced height of the top layer, as this receiver is located within the excavation, resulting in a poorer agreement below 20 Hz as well.

The excavation mainly affects the mobility close to the excitation point, where a difference around 6 dB is observed. For a larger source–receiver distance, the influence of the excavation diminishes, as the source–receiver distance is much higher than the dimensions of the excavation. In the following subsection, the prediction of the free field mobilities is validated for the case of excitation in the excavation (figure 3.9b).



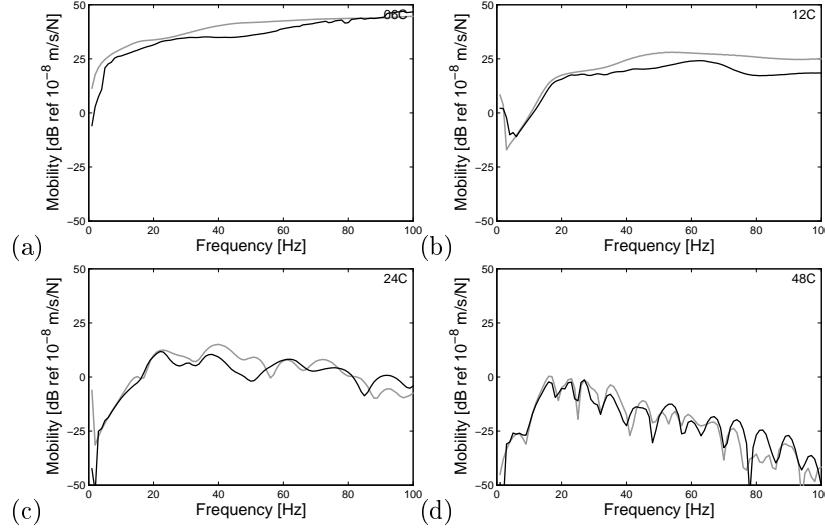


Figure 3.10: Predicted mobility level at line C ( $y = 0$  m) at (a) 6 m, (b) 12 m, (c) 24 m, and (d) 48 m from the track center line for a source point at the surface (grey line) and in the excavation (black line) at  $x = 5.05$  m and  $y = 0$  m.

### 3.3.3 Validation of the free field mobility

The free field mobility is determined at the site in Lincent by applying impacts at the soil's surface and measuring the corresponding response in the free field. The measurement setup is shown in figure 3.11 and is discussed in more detail in the following. A detailed description of the measurement setup is given in the measurement report [151].

The origin of the measurement setup is located at the center of track 2 in the direction of Brussels. The direction  $\mathbf{e}_y$  corresponds to the longitudinal direction of the track, while the direction  $\mathbf{e}_x$  is perpendicular to the track. The direction  $\mathbf{e}_z$  corresponds to the upward vertical direction (figure 3.11).

The acceleration in the free field is measured by means of high sensitivity seismic accelerometers (PCB 393 series). The horizontal response at the surface is of the same order of magnitude as the vertical response for railway traffic at grade. The choice has been made, however, to only measure the vertical response such that a larger number of receivers are included in the measurement setup. The vertical acceleration in the free field is measured in sixteen channels, located along five measurement lines perpendicular to the track (figure 3.11). The measurement lines A, B, C, D, and E are located at  $y = -19.8$  m,  $y = -10.2$  m,  $y = 0$  m,  $y = 10.2$  m, and  $y = 19.8$  m, respectively. Eight receiver points

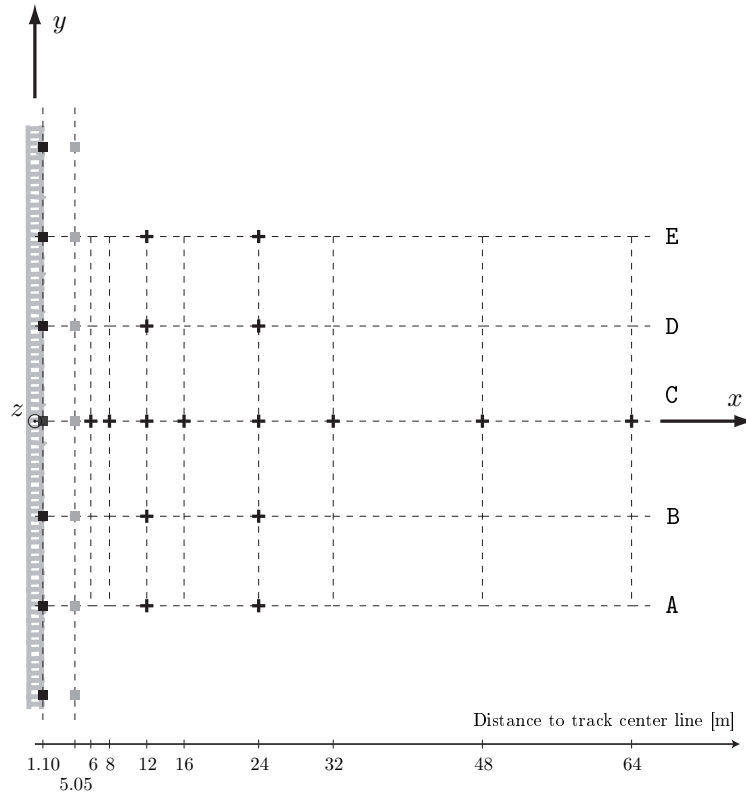


Figure 3.11: Measurement setup in the free field at the site in Lincet, indicating the receiver points ( $\oplus$ ) and the source points at the track ( $\blacksquare$ ) and at the soil's surface adjacent to the track ( $\blacksquare$ ).

are located on the reference measurement line C at  $y = 0$  m and two receiver points are located on each remaining measurement line. The receiver points are referred to as  $\mathbf{xxA}$ ,  $\mathbf{xxB}$ ,  $\mathbf{xxC}$ ,  $\mathbf{xxD}$ , and  $\mathbf{xxE}$ , referring to the respective measurement line, where the two-digit number  $\mathbf{xx}$  denotes the  $x$ -coordinate of the receiver point, e.g. 06C.

The mobility is determined by means of an impact hammer with a mass of 5.5 kg and a soft tip equipped with a force sensor (PCB 086D50) that measures the force exerted during the impact.

The data has been recorded by means of a National Instruments PXI-1050 chassis with four 4472B modules. The A/D conversion is performed by means of

the NI system within an amplitude range of  $\pm 10$  V and is based on oversampling. The conversion is performed at a frequency of 10 kHz. The digital signal is subsequently resampled at a sampling frequency  $f_s = 1000$  Hz, avoiding aliasing by means of a digital low-pass filter. The corresponding Nyquist frequency is  $f_{\text{Nyq}} = 500$  Hz.

For each hammer impact, 4096 data points are recorded, corresponding to a time period of 4.096 s. The measured force is used as a trigger with a trigger level of 2200 N where 1536 data points are stored before exceedance of the trigger level and 2560 data points are stored afterwards.

The free field mobility is determined by means of hammer impacts applied to an aluminum foundation installed at the soil's surface at a distance of 5.05 m from the center of the track. The foundation is located within the excavation 1 m below ground level. Impacts are applied at the foundation at 17 source points along the track from  $y = -80$  m to  $y = 80$  m with a spacing of 10 m, indicated by the grey squares in figure 3.11. The source points at the soil's surface are denoted as  $YyS$ , where the two-digit number  $yy$  denotes the  $y$ -coordinate of the source point, e.g. Y00S.

Figure 3.12 shows the measured force during the first impact at the soil's surface at  $y = 0$  m. The time history clearly shows a single impact of the hammer, while the frequency content shows that broad band excitation is applied covering the entire frequency range of interest.

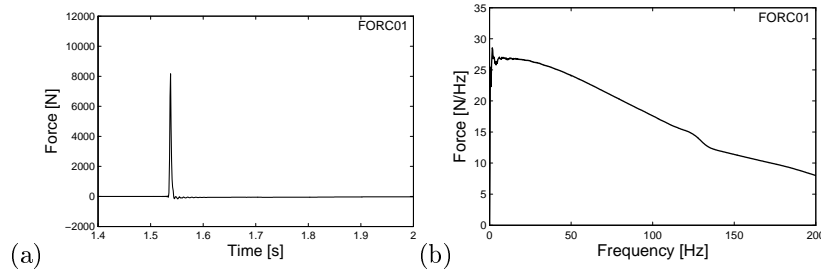


Figure 3.12: (a) Time history and (b) frequency content of the measured force during the first hammer impact at the soil's surface at  $x = 5.05$  m and  $y = 0$  m.

Figure 3.13 shows the acceleration at line C due to the first hammer impact at the soil's surface at  $y = 0$  m. While a clear response due to the hammer impact is observed at short distance, the response is strongly disturbed by background noise at a larger distance.

In order to increase the signal-to-noise ratio, stacking techniques are commonly used where a large number of events is recorded and the resulting time signals are added up [131]. Figure 3.14 shows the time history of the acceleration

stacked for 100 hammer impacts, showing a strong improvement of the signal-to-noise ratio compared to figure 3.13. The improvement is particularly clear at a larger distance where the stacked signal now clearly reveals the response due to the hammer impact.

The time history of the velocity  $v_i^k(t)$  in channel  $i$  for event  $k$  is obtained by integration of the measured acceleration  $a_i^k(t)$ . First, a Butterworth window is applied to smoothen the noise at the beginning and the end of the time window. A third order Chebyshev filter with high-pass frequency  $f_h = 4$  Hz, a low-pass filter  $f_l = 499$  Hz, and a ripple of 0.1 dB is applied to avoid drifting of the signal. The velocity is then computed by integration of the acceleration using a trapezium rule. The frequency content  $\hat{v}_i^k(\omega)$  is obtained by means of a forward Fourier transform from the time to the frequency domain.

The average mobility  $\hat{H}_{ij}(\omega)$  between two channels  $i$  and  $j$  is computed in the frequency domain by means of the  $H_1$  estimator [12, 42]:

$$\hat{H}_{ij}(\omega) = \frac{\hat{S}_{ij}(\omega)}{\hat{S}_{ii}(\omega)} \quad (3.1)$$

The average cross PSD  $\hat{S}_{ij}(\omega)$  between channels  $i$  and  $j$  is estimated as:

$$\hat{S}_{ij}(\omega) = \frac{1}{N} \sum_{k=1}^N \hat{x}_i^{k*}(\omega) \hat{x}_j^k(\omega) \quad (3.2)$$

where  $\hat{x}_i^k(\omega)$  is the Fourier transform of the signal measured in channel  $i$  for event  $k$ ,  $\hat{x}_i^{k*}(\omega)$  denotes the complex conjugate of  $\hat{x}_i^k(\omega)$ , and  $N$  refers to the number of recorded events. When  $i = j$ , this function is referred to as the auto PSD.

The transfer function  $\hat{H}_{ij}(\omega)$  obtained with the  $H_1$  estimator is a random variable, as each experiment gives rise to a different estimation. The estimated transfer function  $\hat{H}_{ij}(\omega)$  can therefore be characterized by a variance  $\hat{\sigma}_{\hat{H}_{ij}}^2(\omega)$ . Assuming that the noise fulfills the conditions stated by the central limit theorem [38], the variance  $\hat{\sigma}_{\hat{H}_{ij}}^2(\omega)$  is computed as [19]:

$$\hat{\sigma}_{\hat{H}_{ij}}^2(\omega) = \frac{1 - \hat{\gamma}_{ij}^2(\omega)}{N \hat{\gamma}_{ij}^2(\omega)} |\hat{H}_{ij}(\omega)|^2 \quad (3.3)$$

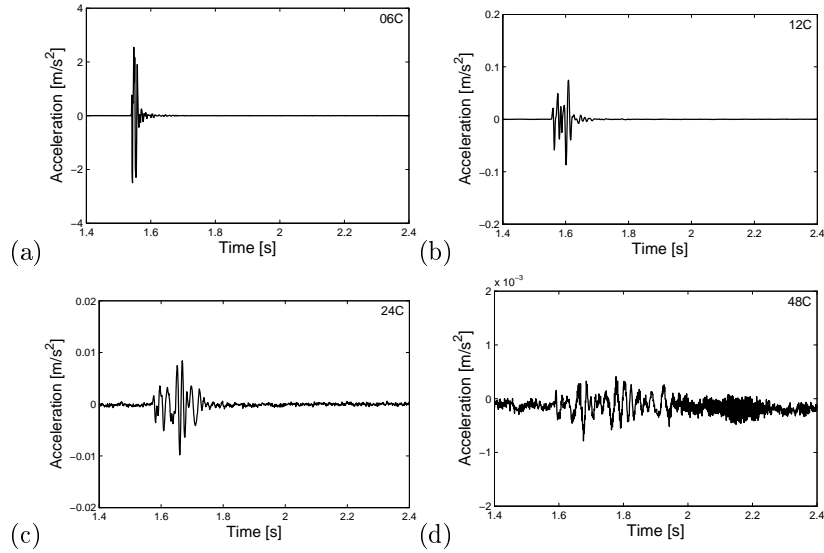


Figure 3.13: Measured vertical acceleration at line C ( $y = 0$  m) at (a) 6 m, (b) 12 m, (c) 24 m, and (d) 48 m from the track center line due to the first hammer impact at the soil's surface at  $x = 5.05$  m and  $y = 0$  m.

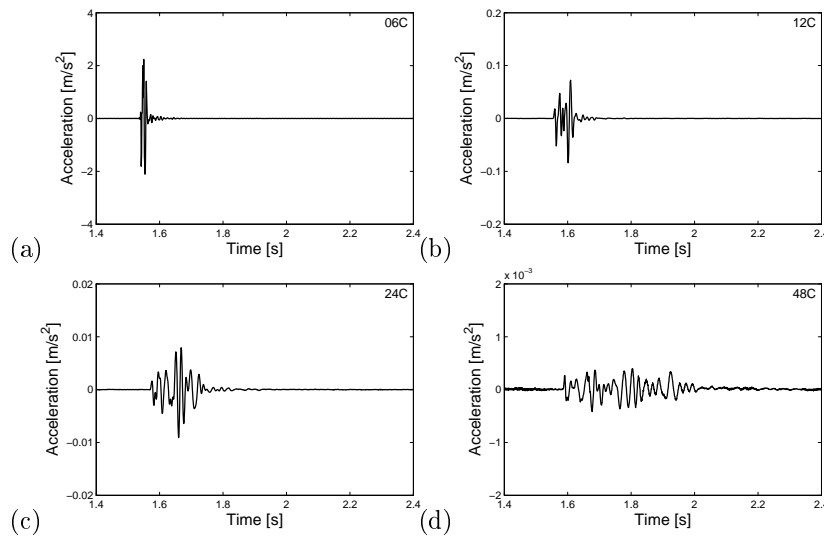


Figure 3.14: Measured vertical acceleration at line C ( $y = 0$  m) at (a) 6 m, (b) 12 m, (c) 24 m, and (d) 48 m from the track center line stacked for 100 hammer impacts at the soil's surface at  $x = 5.05$  m and  $y = 0$  m.

where  $\hat{\gamma}_{ij}(\omega)$  denotes the coherence between channels  $i$  and  $j$ :

$$\hat{\gamma}_{ij}^2(\omega) = \frac{\hat{S}_{ij}(\omega)\hat{S}_{ij}^*(\omega)}{\hat{S}_{jj}(\omega)\hat{S}_{ii}^*(\omega)} \quad (3.4)$$

The variance  $\hat{\sigma}_{H_{ij}}^2(\omega)$  is inversely proportional to  $N$ , so that the standard deviation  $\hat{\sigma}_{H_{ij}}(\omega)$  is inversely proportional to  $\sqrt{N}$ . In the present test, 100 hammer impacts have been recorded, which means that an improvement of the signal-to-noise ratio of the measured transfer function with a factor of 10 is expected as compared to the transfer function determined from a single event.

Assuming that the estimated transfer function  $\hat{H}_{ij}(\omega)$  follows a Gaussian probability distribution, its modulus follows a Rice distribution [119]. The bounds of the confidence interval of the modulus are estimated based on the inverse cumulative Rice distribution [131].

Figure 3.15 shows the mean value and the 95% confidence interval of the measured free field mobility at measurement line C for 100 hammer impacts at the soil's surface at  $y = 0$  m. For a small source–receiver distance, the confidence interval is very small and concentrated in a narrow region around the average value of the mobility. The response is attenuated with increasing distance from the track due to geometrical and material damping in the soil. As the attenuation due to material damping is stronger for higher frequencies, the mobility is attenuated especially at higher frequencies with increasing distance and the signal-to-noise ratio decreases accordingly. It is noted that the impact is applied at 5.05 m from the track such that the source–receiver distance is only 0.95 m for the receiver point at 6 m from the track.

The confidence interval also increases at frequencies below 20 Hz, in particular at larger distances from the source. The generation of surface waves at low frequencies requires the displacement of a large soil mass and therefore needs a high level of excitation. The energy introduced in the soil by the impact hammer is not sufficient to clearly measure the mobility. For receiver 48C, the mobility is only measured accurately in the intermediate frequency range between 20 and 75 Hz.

The uncertainty interval shown in figure 3.15 is estimated based on a noise model and characterizes the signal-to-noise ratio of the measured mobility. It can be used as a measure for the reproducibility of the measured mobility but does not account for other sources of uncertainty, e.g. introduced by measurement errors.

The predicted mobility is compared to the measured result in figure 3.15.

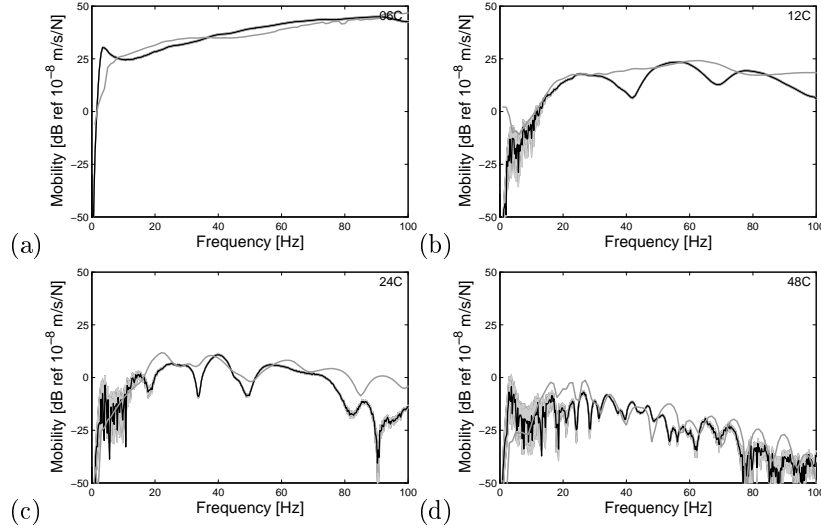


Figure 3.15: Predicted (grey line) and measured (black line) free field mobility level and confidence interval (grey region) at line C ( $y = 0$  m) at (a) 6 m, (b) 12 m, (c) 24 m, and (d) 48 m from the track center line for a source point at the soil's surface at  $x = 5.05$  m and  $y = 0$  m.

A good agreement is observed in the considered frequency range, indicating that both the prediction model and the identified soil parameters accurately represent the considered transfer of vibration.

The one-third octave band representation  $\langle H_{ij} \rangle_m$  of the transfer function  $\hat{H}_{ij}(\omega)$  is computed according to equation (2.36). As the modulus  $|\hat{H}_{ij}(\omega)|$  of the transfer function is a statistical variable, the one-third octave band transfer function  $\langle H_{ij} \rangle_m$  is a statistical variable as well. An estimation of the statistical properties of the estimated one-third octave band transfer function is made by assuming that the mobilities  $\hat{H}_{ij}(\omega)$  at different frequencies  $\omega$  are independent variables. The integral in equation (2.36) then represents a summation of a large number of independent variables within the frequency band  $[\omega_{1m}, \omega_{2m}]$  so that the one-third octave band mobility  $\langle H_{ij} \rangle_m$  can be considered to be a Gaussian variable according to the central limit theorem [38]. The bounds of the confidence interval of the modulus are estimated based on the inverse cumulative Gaussian distribution.

Figure 3.16 shows the mean value and the 95% confidence interval of the one-third octave band mobility at measurement line C for 100 hammer impacts at the soil's surface at  $y = 0$  m. As the one-third octave band mobility is an average value within each frequency band, the peaks and troughs in the

narrow band mobility (figure 3.15) are cancelled and the confidence interval in each frequency band is smaller. If the assumption holds that the mobilities at different frequencies are independent, the measured noise only has a small influence on the one-third octave band mobility in the considered frequency range. The uncertainty is slightly higher in the low frequency range, where the frequency bands are smaller and the averaging has a smaller effect.

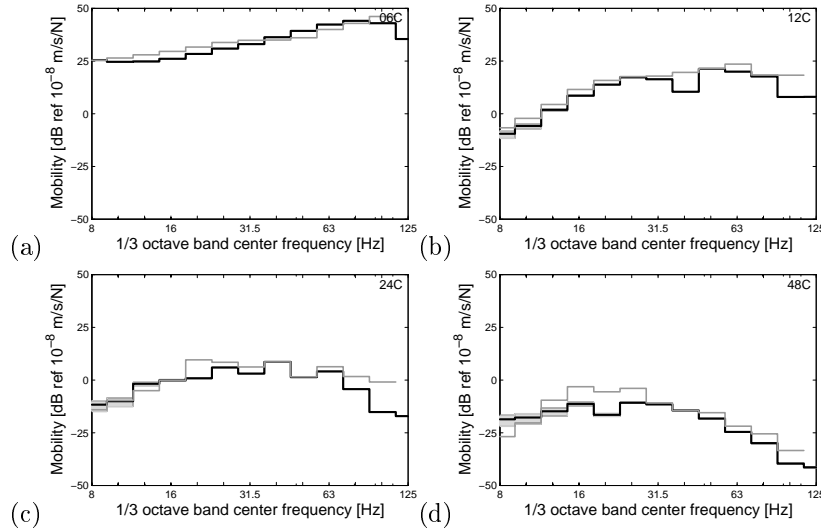


Figure 3.16: Predicted (grey line) and measured (black line) one-third octave band free field mobility level and confidence interval (grey region) at line C ( $y = 0$  m) at (a) 6 m, (b) 12 m, (c) 24 m, and (d) 48 m from the track center line for a source point at the soil's surface at  $x = 5.05$  m and  $y = 0$  m.

As the one-third octave band mobility represents an average value within each frequency band, it allows for a more clear comparison of the measured and predicted result. The validation in one-third octave bands confirms that a good agreement is found between the measured and predicted free field mobility.

Figure 3.17 shows the measured and predicted mobility at measurement line C for 100 hammer impacts at the soil's surface at  $y = 40$  m. Due to the larger source–receiver distance, the interval where an accurate measurement of the mobility is obtained has decreased. For receiver point 48C, the mobility is only measured accurately between 20 and 50 Hz.

The path between the source point at  $y = 40$  m and a receiver close to the track (e.g.  $x = 6$  m) at line C ( $y = 0$  m) almost runs parallel to the track (figure 3.11). The vibration transfer is mainly determined by the soil properties near the track. Due to the presence of a sub-ballast, soil improvement, and possible



compaction of the soil underneath the track, the soil properties near the track may be different from the soil properties identified in the free field. This results in a poorer agreement between the measured and predicted mobility for the receiver at  $x = 6$  m at line C.

The vibration transfer between the source point at the soil's surface at  $y = 40$  m and receivers at larger distance from the track (e.g.  $x = 24$  m or  $x = 48$  m), is again mainly determined by the free field soil properties and a better agreement is observed between the measured and predicted mobility.

Figure 3.18 shows the mean value and the 95% confidence interval of the one-third octave band mobility at measurement line C for 100 hammer impacts at the soil's surface at  $y = 40$  m. The confidence interval is slightly larger as compared to the result for a source point at  $y = 0$  m (figure 3.16) due to the increased source–receiver distance.

The comparison of the measured and predicted one-third octave band mobility confirms the observation made for the narrow band mobility. The vibration transfer in the free field is accurately predicted by the model and the identified soil properties, whereas the vibration transfer near the track is predicted less accurately. It can be concluded that the identified soil profile in the free field does not accurately represent the soil near the track.

The measurement of the free field mobility at different measurement lines allows to assess the variability of the measured mobility along the track. Figure 3.19 compares the one-third octave band mobility for the same source–receiver distance determined at different measurement lines A to E (figure 3.11), showing a difference up to 10 dB. This difference is due to the variation of the dynamic soil characteristics and geometry (excavation) along the track. This is a significant variation and has to be considered in the assessment of the prediction model and identified soil characteristics, since the accuracy of the prediction cannot be expected to be smaller than the scatter observed between measured results.

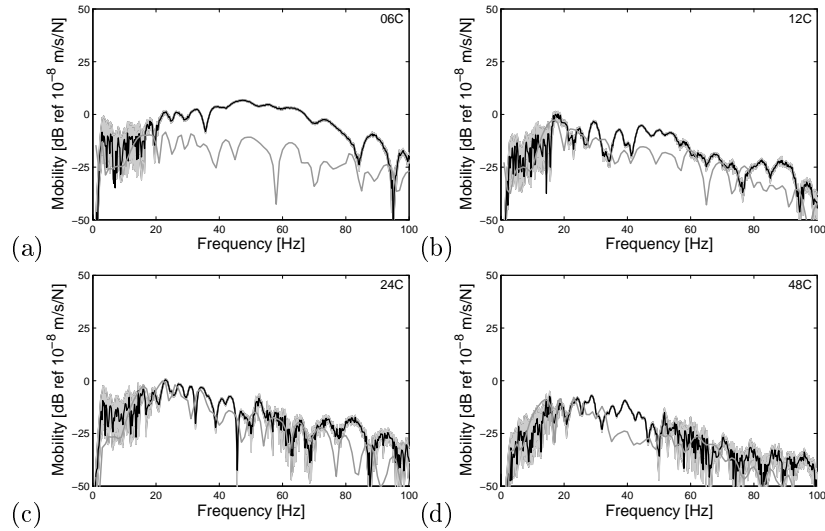


Figure 3.17: Predicted (grey line) and measured (black line) free field mobility level and confidence interval (grey region) at line C ( $y = 0$  m) at (a) 6 m, (b) 12 m, (c) 24 m, and (d) 48 m from the track center line for a source point at the soil's surface at  $x = 5.05$  m and  $y = 40$  m.

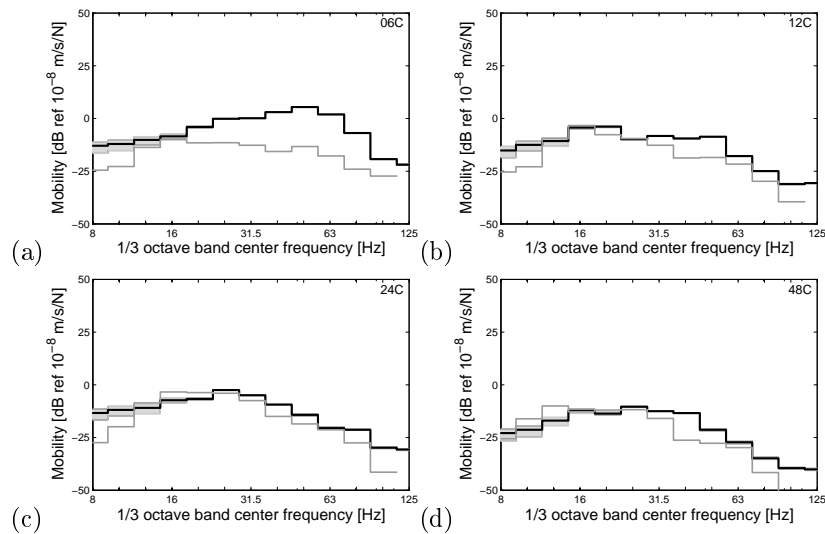


Figure 3.18: Predicted (grey line) and measured (black line) one-third octave band free field mobility level and confidence interval (grey region) at line C ( $y = 0$  m) at (a) 6 m, (b) 12 m, (c) 24 m, and (d) 48 m from the track center line for a source point at the soil's surface at  $x = 5.05$  m and  $y = 40$  m.

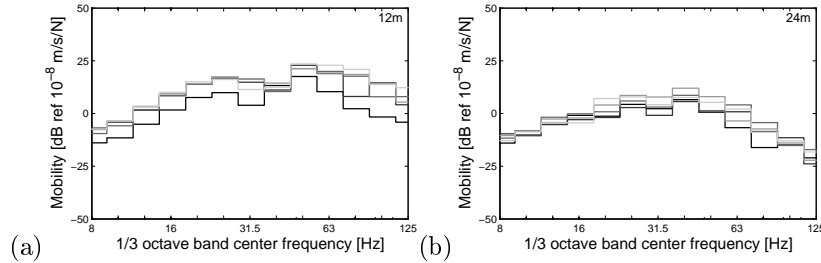


Figure 3.19: One-third octave band free field mobility level measured at five different measurement lines (grey to black lines) at (a) 12 m and (b) 24 m from the track center line for source points at the soil's surface at  $x = 5.05$  m and at the corresponding measurement line.

### 3.4 The track receptance

In the present section, the prediction of the track receptance based on design values and identified track parameters is investigated. First, the dynamic track characteristics at the site in Lincent are discussed. Next, the influence of the excavation and the track subgrade on the track receptance is investigated. Finally, the measured and predicted track receptances are compared. An updating of the track characteristics is carried out to obtain a better fit between the measured and predicted receptance.

#### 3.4.1 The dynamic track characteristics

The dynamic track characteristics are determined based on design values or identified based on the measured track response. It is important that the loading condition of the track is correctly taken into account as it influences the properties of track components that show a strong non-linear behavior such as the rail pad and the ballast. A distinction is generally made between loaded conditions, where a static load equivalent to a train is present on the track, and unloaded conditions. Obviously, a stiffer track behavior is expected in loaded conditions.

Previous work was carried out by Lombaert et al. [98] and Kogut and Degrande [78] to determine the track parameters at the site in Lincent based on the measured track receptance. In both approaches, the input parameters of the numerical model were determined indirectly by fitting the predicted track receptance to the measured result.

Lombaert et al. [98] predict the track receptance by means of a 2.5D coupled FE–BE model. Figure 3.20 shows the track model used by Lombaert et al. [98] that is similar to the track model presented in subsection 2.4.1 (figure 2.5). In the model of Lombaert et al. [98], however, the ballast is modeled as a layer of independent linear springs and dampers. Each sleeper is assumed to be only supported by that part of the ballast that is in contact with the sleeper. The ballast is therefore represented by a ballast stiffness  $k_b$  [N/m] and damping coefficient  $c_b$  [Ns/m] per sleeper. The equivalent continuous track model is obtained by using an equivalent stiffness  $\bar{k}_b = k_b/d_{sl}$  [N/m<sup>2</sup>] and damping coefficient  $\bar{c}_b = c_b/d_{sl}$  [Ns/m<sup>2</sup>], where  $d_{sl}$  is the sleeper distance.

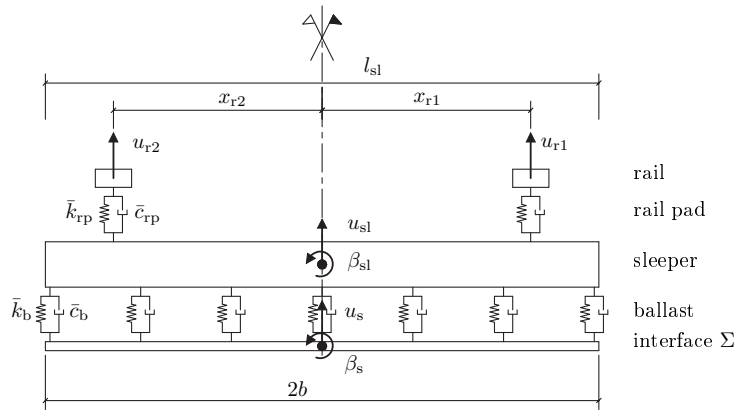


Figure 3.20: Cross section of the 2.5D track model used by Lombaert et al. [98].

The characteristics of the rails and the sleepers show a linear behavior and are determined based on design values. The UIC 60 rails are modeled with a bending stiffness  $E_r I_r = 6.45 \times 10^6 \text{ Nm}^2$  and mass per unit length  $\rho_r A_r = 60.3 \text{ kg/m}$  for each rail. The track gauge is 1.435 m. The sleepers have a distributed mass  $\bar{m}_{sl} = 500 \text{ kg/m}$  and a mass moment of inertia  $\rho_{sl} \bar{I}_{t\,sl} = 262.17 \text{ kgm}$  [98].

The characteristics of the rail pad and the ballast show a strong non-linear behavior. They have a large influence on the track stiffness, whereas the influence on the track – free field transfer functions remains limited [149]. The characteristics of the rail pad and the ballast are therefore determined by fitting the predicted track receptance to the track receptance measured in loaded conditions. The ballast mainly affects the track receptance at frequencies below 200 Hz. The rail pad affects the quasi-static track receptance at low frequencies but also determines the resonance of the rail on the rail pad that occurs at a frequency generally above 200 Hz. The updating of the ballast and rail pad properties is therefore performed by fitting the predicted track receptance in

a different frequency range. The results obtained by Lombaert et al. [98] are summarized in the following.

The rail pad properties are optimized in the frequency range 200 – 400 Hz resulting in a stiffness  $k_{\text{rp}} = 153.4 \times 10^6 \text{ N/m}$  and damping coefficient  $c_{\text{rp}} = 13.5 \times 10^3 \text{ Ns/m}$ . In the literature, the rail pad is often described in terms of the stiffness  $k_{\text{rp}}$  [54, 82, 144, 158]. Compared to reported values from  $60 \times 10^6 \text{ N/m}$  for soft rail pads to  $1300 \times 10^6 \text{ N/m}$  for very stiff rail pads, the stiffness obtained at the site in Lincent corresponds to a soft to medium rail pad.

The ballast properties are optimized in the frequency range 50–200 Hz resulting in a stiffness  $k_{\text{b}} = 920.7 \times 10^6 \text{ N/m}$  and damping coefficient  $c_{\text{b}} = 16.6 \times 10^3 \text{ Ns/m}$ . In the literature, the ballast is often described in terms of the stiffness  $k_{\text{b}}$  per sleeper [54, 82, 158, 160]. Compared to reported values of the ballast stiffness from  $12 \times 10^6 \text{ N/m}$  to  $190 \times 10^6 \text{ N/m}$ , the ballast stiffness obtained at the site in Lincent corresponds to a very stiff ballast layer. This is possibly due to compensation of an underestimation of the subgrade stiffness. Taking into account the support area  $A_{\text{sl}} = l_{\text{sl}} w_{\text{sl}}$  per sleeper allows to determine the ballast stiffness  $K_{\text{b}} = k_{\text{b}}/A_{\text{sl}} = 1567 \times 10^6 \text{ N/m}^3$ . The ballast Young's modulus is estimated by taking into account the height  $h_{\text{b}}$  of the ballast layer as  $E_{\text{b}} = K_{\text{b}} h_{\text{b}} = 548.5 \times 10^6 \text{ N/m}^2$  [98].

Kogut and Degrande [78] investigate the effect of the loading conditions on the identified track parameters with a similar approach. The model includes half of the track where a single rail pad is represented by a stiffness  $k_{\text{rp}}$  [N/m] and damping coefficient  $c_{\text{rp}}$  [Ns/m] and half of the ballast layer is represented by a stiffness  $k_{\text{b}}$  [N/m] and damping coefficient  $c_{\text{b}}$  [Ns/m]. The equivalent ballast stiffness  $K_{\text{b}}$  is obtained by taking into account half of the support area as  $K_{\text{b}} = 2k_{\text{b}}/A_{\text{sl}}$  and can therefore be compared to the ballast stiffness  $K_{\text{b}}$  obtained by Lombaert et al. [98].

The loading of the track leads to an increase of the dynamic rail pad stiffness from  $k_{\text{rp}} = 102 - 123 \times 10^6 \text{ N/m}$  to  $k_{\text{rp}} = 137 - 143 \times 10^6 \text{ N/m}$ . The ballast stiffness increases from  $K_{\text{b}} = 112 - 146 \times 10^6 \text{ N/m}^3$  to  $K_{\text{b}} = 225 - 340 \times 10^6 \text{ N/m}^3$ . While the values obtained for the rail pad are similar to the values obtained by Lombaert et al., the result for the ballast stiffness is much lower.

The previously presented results are obtained by fitting the predicted receptance to the measured result and are therefore valid for the considered model. In the present research, a different track model is used that has been presented in subsection 2.4.1 (figure 2.5). The input parameters for the present model are derived from the parameters obtained with the model of Lombaert et al. [98] (figure 3.20). As the rails, rail pads, and sleepers are modeled identically in both models, the previously identified characteristics are used in the present

model. The model for the ballast is different in both models, however. The ballast parameters for the present model are initially estimated in the following based on the parameters obtained with the model of Lombaert et al. [98] and will be updated in subsection 3.4.4.

Equivalent parameters are derived for the ballast with density  $\rho_b = 1700 \text{ kg/m}^3$  and Poisson's ratio  $\nu_b = 0.33$ . The estimated Young's modulus  $E_b = 548.5 \times 10^6 \text{ N/m}^2$  in loaded conditions corresponds to a shear wave velocity  $C_s = 347.9 \text{ m/s}$  and a longitudinal wave velocity  $C_p = 695.8 \text{ m/s}$ . The viscous damping  $c_b = 16.6 \times 10^3 \text{ Ns/m}$  corresponds to a loss factor  $\eta = 0.003$  at  $f = 50 \text{ Hz}$ .

In the following subsections, the dynamic track behavior of track 2 at the site in Lincent is predicted where the excavation and the track subgrade are also taken into account. The excavation is assumed to have upper width  $w_{eu} = 15 \text{ m}$ , lower width  $w_{el} = 14 \text{ m}$ , and height  $h_e = 1 \text{ m}$  (figure 3.8). It is assumed that the presence of track 1 does not affect the response of track 2 and in the free field. A single track model is therefore applied in the center of the excavation (figure 3.8).

The ballast layer is assumed to have a trapezoidal shape with upper width  $w_{bu} = 3.60 \text{ m}$ , lower width  $w_{bl} = 5.60 \text{ m}$ , and height  $h_b = 0.35 \text{ m}$  (figure 2.5).

The track subgrade is taken into account, as it affects the dynamic track behavior and the vibration transfer to the free field [3, 61]. It is not straightforward to determine the characteristics of the track subgrade, however. Non-intrusive methods include monitoring systems such as Ground Penetrating Radar (GPR) [41], High Speed Deflectograph (HSD) [41], continuous measurement of the dynamic track receptance [13], and SASW along a railway track [29]. Consoli et al. [26, 27] have performed laboratory tests to investigate the improvement of soil properties by mixing with cement [26] or lime [27]. The characteristics of the track subgrade are subject to large uncertainty, however, as they depend on the material of the sub-ballast, the applied technique of soil improvement, and the original soil properties.

At the site in Lincent, a sub-ballast layer has been installed with a depth of 0.60 m and the soil has been improved over a depth of 1 m by means of lime stabilization. No measurements have been carried out to determine the dynamic subgrade characteristics so that they need to be estimated.

A lime treatment leads to an increase of the shear wave velocity of the upper soil layer from 128 m/s (table 3.1) up to 200 – 400 m/s due to the combined effect of mixing with lime and soil compaction [27]. In the following, the effect of the track subgrade is investigated by including a layer underneath the track that has improved characteristics compared to the original soil. First,

a conservative value of  $C_s = 200$  m/s is assumed for the shear wave velocity. An increased density  $\rho_s = 1854$  kg/m<sup>3</sup> is assumed to account for soil compaction. These parameters are updated in subsection 3.4.4 in order to obtain a better fit between the measured and predicted track receptance. The track subgrade is assumed to have a width  $w_s = 5.60$  m, equal to the ballast width, and a depth  $h_s = 1$  m.

### 3.4.2 Influence of the excavation on the track receptance

The effect of the excavation on the track receptance is investigated by means of numerical simulations. Different geometries of the track and soil system are therefore used, presented in figure 3.21.

The influence of the excavation on the rail receptance is investigated by comparing model A (figure 3.21a) and model B (figure 3.21b).

Model A assumes a simplified geometry where the excavation is disregarded and the track is located at the surface of the layered halfspace. In model B, the excavation is taken into account and the track is located within the excavation.

Figure 3.22 compares the rail receptance computed with both models. The rail receptance exhibits a peak around 20 Hz which is due to soil stratification. This peak appears at a lower frequency when the excavation is disregarded and the thickness of the top layer is larger.

The rail receptance is affected by the presence of the excavation up to a frequency of 80 Hz. At higher frequencies, the wavelength decreases and the vibration of the track is concentrated in the upper track components. The track receptance is therefore no longer affected by the soil stratification or the excavation at higher frequencies.

As the rail receptance is mainly influenced by the soil layering directly underneath the track, a simplified model is presented by adapting the soil profile. In model C (figure 3.21c), the top layer of the soil has been reduced by the depth  $h_e$  of the excavation. This model accounts for the reduced thickness of the top layer under the track without explicitly modeling the excavation. The advantage of this model is that the BE mesh of the soil is much smaller and only contains nodes at the interface between the track and the soil, significantly reducing the computational cost.

Figure 3.23 compares the rail receptance computed with model B and model C. Both models yield exactly the same result. This indicates that the influence of the soil properties on the track receptance mainly relates to the soil

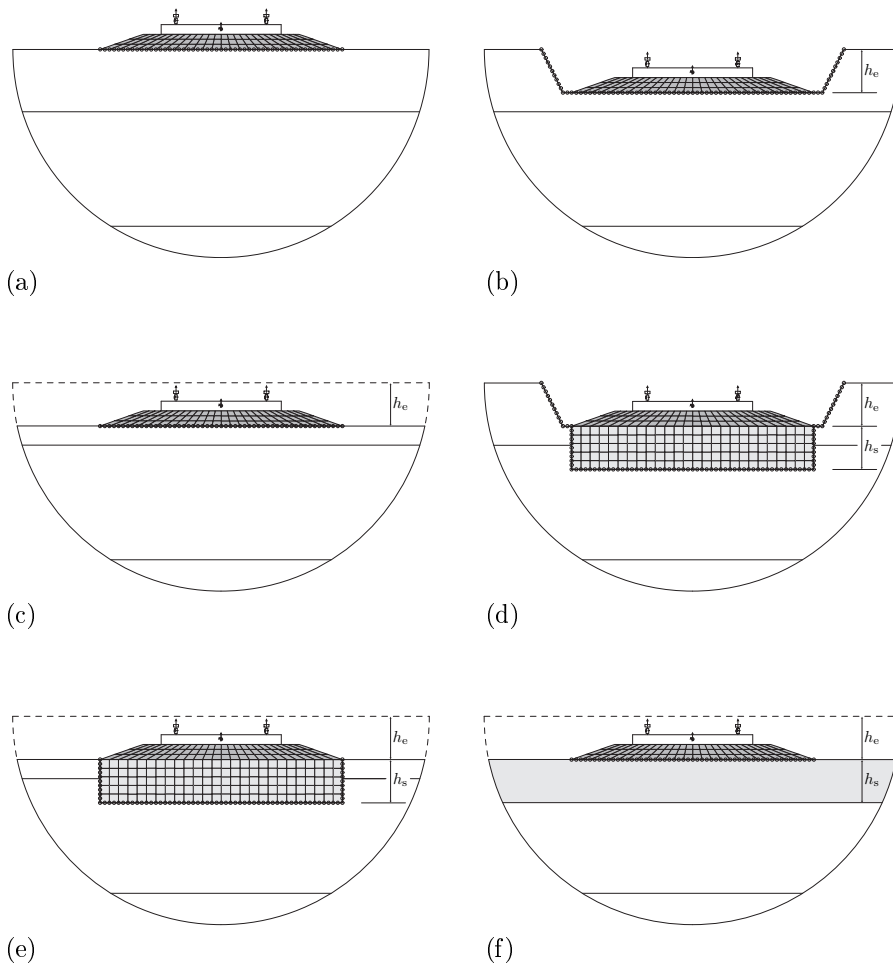


Figure 3.21: Cross section of the 2.5D track-soil model for (a) model A, (b) model B, (c) model C, (d) model D, (e) model E, and (f) model F, where  $h_e$  indicates the depth of the excavation and  $h_s$  indicates the depth of the track subgrade.



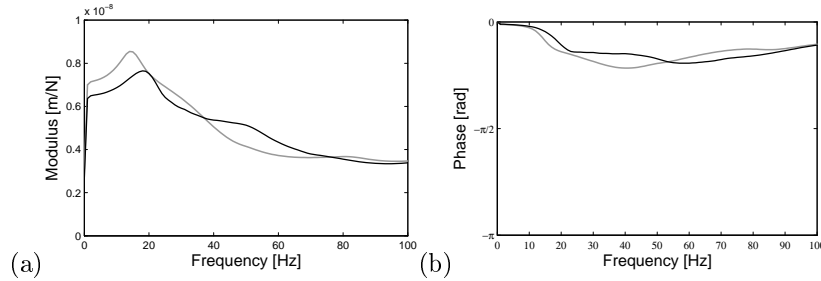


Figure 3.22: (a) Modulus and (b) phase of the vertical rail receptance predicted with model A (grey line) and model B (black line).

stratification directly underneath the track. Model C can therefore be used to predict the rail receptance more efficiently for tracks built in excavation.

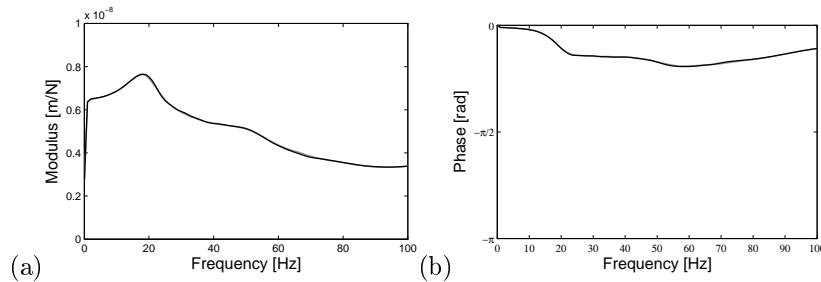


Figure 3.23: (a) Modulus and (b) phase of the vertical rail receptance predicted with model B (grey line) and model C (black line).

### 3.4.3 Influence of the track subgrade on the track receptance

The influence of the track subgrade on the rail receptance is investigated by comparing the results obtained with model B (figure 3.21b) and model D (figure 3.21d). In model B a track in excavation is considered and the track subgrade is disregarded, while in model D the track subgrade is taken into account.

Figure 3.24 shows the rail receptance computed with both models. The peak around 20 Hz related to the soil stratification is present in both models but decreases when the track subgrade is taken into account. Due to the track subgrade, a stiffer behavior is obtained at low frequencies.

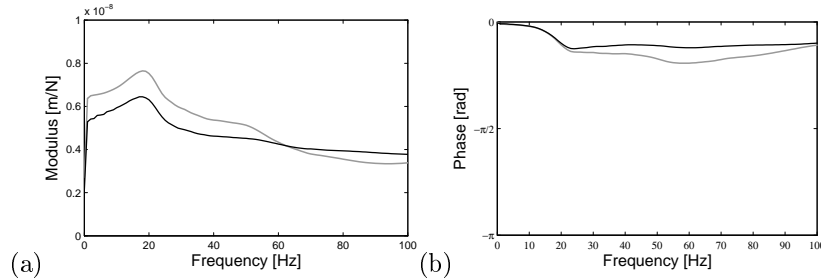


Figure 3.24: (a) Modulus and (b) phase of the vertical rail receptance predicted with model B (grey line) and model D (black line).

At frequencies above 60 Hz, a higher rail receptance is found when the track subgrade is taken into account. The resonance of the sleeper mass on the ballast stiffness generally occurs in this frequency range. This resonance is heavily damped by the soil and is not clearly observed in figure 3.24. Taking into account the track subgrade, however, leads to a smaller radiation of energy to the soil and increases the rail receptance.

The track subgrade is included in model D by means of 2.5D finite volume elements and coupled to the BE model of the soil. Including the track subgrade increases the size of the BE mesh and therefore significantly increases the computational cost. Two alternative models are therefore proposed by introducing the following modeling simplifications.

In model E (figure 3.21e), the excavation is modeled by reducing the top layer, while the track subgrade is modeled by means of 2.5D finite volume elements. As it is no longer needed to model the free boundary of the excavation, the BE mesh of the soil is reduced.

Model F (figure 3.21f) further simplifies the geometry of the problem, by applying the properties of the track subgrade to the entire soil domain. The BE mesh is now limited to the contact area between the ballast and the soil domain.

The track subgrade is taken into account in models D, E, and F, but a considerable simplification of the geometry is obtained in the latter model. Table 3.2 summarizes the required memory and computation time of each model at 100 Hz (carried out on a node with two quad-core Nehalem processors with clock speed 2.26 GHz) and shows that the simplifications in model E and F result in a significant reduction of the computational requirements.

Figure 3.25 compares the rail receptance predicted with model D (figure 3.21d), model E (figure 3.21e), and model F (figure 3.21f). All models yield a nearly

Model	Required memory [GBRAM]	Computation time [min]
D	45	1440
E	37	45
F	1	1

Table 3.2: Computational requirements for the track–soil models.

identical result. This confirms the observation of the previous subsection that the influence of the soil properties on the track receptance is mainly determined by the soil stratification directly underneath the track.

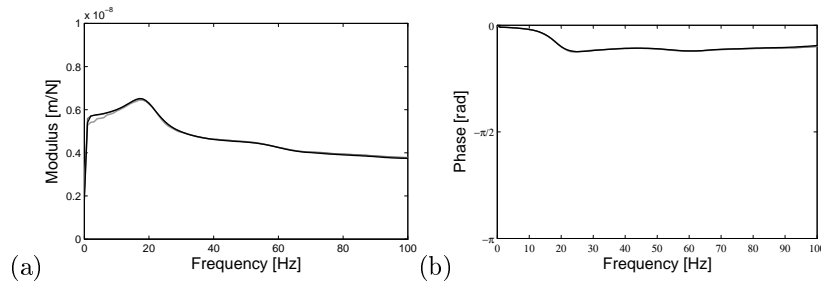


Figure 3.25: (a) Modulus and (b) phase of the vertical rail receptance predicted with model D (light grey line), model E (dark grey line), and model F (black line).

In the following, model F is used to predict the track receptance as it is more efficient and yields the same result.

### 3.4.4 Updating of the track parameters

The numerical prediction of the track receptance is validated based on the measured result at the site in Lincent.

The track receptance was measured in loaded and unloaded conditions prior to the opening of the high speed line L2 in 2002 [78] in order to determine the dynamic track characteristics in both conditions. A hammer impact was therefore applied at the rail head, while the corresponding response of the rail was measured. The experimental track receptance is obtained as the ratio of the measured displacement and the applied force.

The measurements were performed at three consecutive sleepers in unloaded conditions, while they were performed at one sleeper in loaded conditions. All measurements were carried out on track 2 in the direction of Brussels. The measurement setup is described by Kogut and Degrande [78] and is shown in figure 3.26.

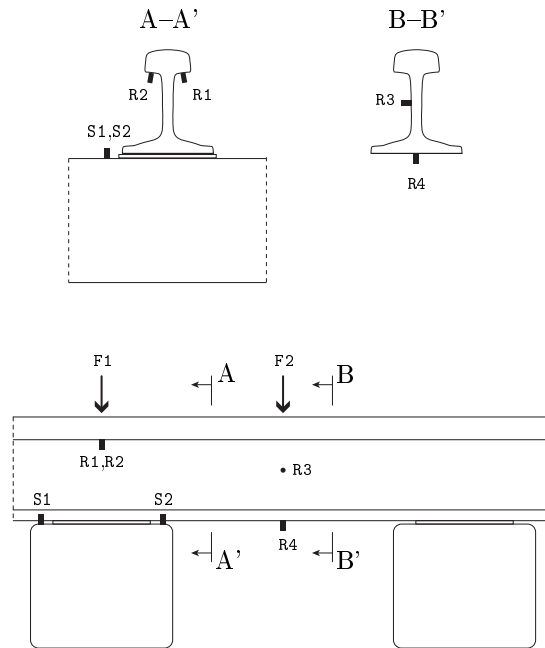


Figure 3.26: Position of the accelerometers and impact points used for the determination of the track receptance [78].

Four accelerometers were installed at the rail, two above a sleeper (R1 and R2) and two at mid span between two sleepers (R3 and R4), and two accelerometers were installed at the sleeper (S1 and S2) (figure 3.26). The excitation was applied by means of a small impact hammer with a mass of 0.2 kg and a large impact hammer with a mass of 5.5 kg. The excitation was applied above a sleeper (F1) as well as at mid span between two sleepers (F2), allowing for the determination of the direct and the cross receptance at both locations (figure 3.26).

The preload was applied by a locomotive on the track and the hammer impact was applied between two bogies at around 1.20 m from the first wheel of the second bogie. A view of the measurement setup in loaded conditions is shown in figure 3.27.



Figure 3.27: View of the measurement setup for the determination of the track receptance in loaded conditions. The impact location F1 is indicated by the red arrow.

The direct rail receptance is the ratio between the displacement and the applied force at the same location. Between 6 and 10 hammer impacts are applied to improve the signal-to-noise ratio and the average experimental rail receptance is determined by means of the  $H_1$  estimator, as explained in subsection 3.3.3. In the following, the direct rail receptance in loaded conditions is determined for excitation above a sleeper (F1), as indicated in figure 3.27, which only requires the measured force and response in channels R1 and R2.

Figure 3.28 shows the measured rail receptance in unloaded and loaded conditions in the frequency range up to 200 Hz. The rail receptance is strongly affected by the loading state of the track. As expected, the track behaves less stiff in unloaded condition than in loaded condition. A resonance of the sleeper on the relatively soft ballast layer is observed around 70 Hz. Due to the preloading of the track, the ballast behaves much stiffer and this resonance is not observed anymore for loaded conditions.

Figure 3.29 shows the rail receptance predicted with model F (figure 3.21f). A relatively large difference is observed with the measured rail receptance in loaded conditions. This is due to the fact that the track parameters have been identified with a different model for the ballast and without considering the track subgrade. The ballast parameters are therefore updated with the present track model (figure 2.5) by fitting the measured and predicted rail receptance.

The dynamic track characteristics strongly affect the rail receptance and, in turn, the rail receptance strongly affects the dynamic axle loads. The numerical

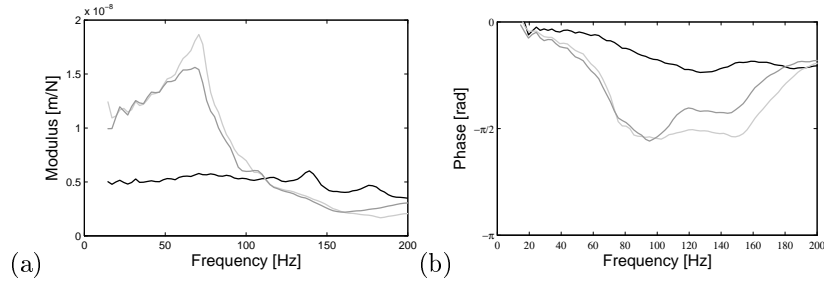


Figure 3.28: (a) Modulus and (b) phase of the measured vertical rail receptance in unloaded condition (grey lines) and loaded condition (black line).

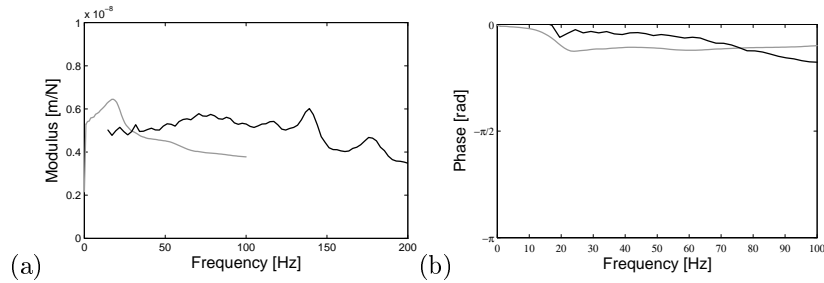


Figure 3.29: (a) Modulus and (b) phase of the predicted (grey line) and measured (black line) vertical rail receptance at the site in Lincent before updating of the track parameters.

receptance is therefore fitted to the measured receptance in loaded conditions, as this better corresponds to the situation during a train pass-by. The resulting track characteristics can also be used for the prediction of the track – free field mobility, as this is only slightly affected by variations in the track parameters [149, 153].

The updating of the track parameters is performed by solving a non-linear least squares problem by means of the MATLAB function `lsqnonlin`, where  $r(\mathbf{x})$  [ $10^{-8}$  m/N] is the residual sum of squares of the difference between the predicted rail receptance with parameter set  $\mathbf{x}$  and the measured rail receptance. An optimal fit is found for the parameter set  $\mathbf{x}$  that minimizes the residual  $r(\mathbf{x})$ . The parameter set  $\mathbf{x}$  includes the ballast shear wave velocity  $C_s$ , imposing a lower bound of 100 m/s and an upper bound of 500 m/s, and the ballast material damping ratio  $\beta_s$ , imposing a lower bound of 0.002 and an upper bound of 0.10. A fixed value is assumed for the density  $\rho_b = 1700$  kg/m<sup>3</sup> and Poisson's ratio  $\nu_b = 0.33$  of the ballast layer.

It has been shown in subsection 3.4.3 that the rail receptance is affected by the track subgrade. Disregarding the presence of the track subgrade will possibly lead to an overestimation of the ballast stiffness. The track subgrade is therefore taken into account in the optimization process by using model F (figure 3.21f). Updating the properties of the track subgrade, however, requires several computations of the soil stiffness, which is the most demanding computational part. This is avoided by performing a ‘grid search’, where the ballast properties are optimized for three different cases, adopting a value of  $C_s = 200$  m/s,  $C_s = 300$  m/s, and  $C_s = 400$  m/s for the shear wave velocity of the track subgrade, respectively. A fixed value is used for the density  $\rho_s = 1854$  kg/m<sup>3</sup> and Poisson’s ratio  $\nu_s = 0.33$  of the track subgrade.

The track subgrade and the ballast mainly affect the track receptance at frequencies below 200 Hz, while the experimental track receptance has only been measured accurately at frequencies above 30 Hz. The optimization is therefore carried out in the frequency range between 30 Hz and 200 Hz, taking into account the result at 69 frequencies with equal weights.

Figure 3.30 shows the rail receptance after updating the track parameters for case 2 where a shear wave velocity  $C_s = 300$  m/s has been used for the track subgrade. A good agreement is found for the receptance in the entire frequency range between 30 and 200 Hz. The updating process has been carried out for the modulus of the receptance, but a relatively good agreement is obtained for the phase of the receptance as well in the entire frequency range.

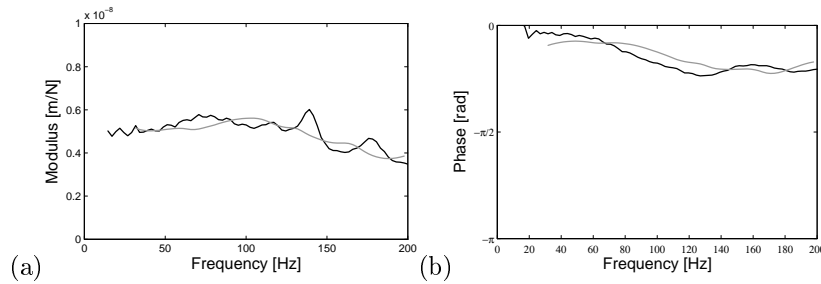


Figure 3.30: (a) Modulus and (b) phase of the predicted (grey line) and measured (black line) vertical rail receptance at the site in Lincent after updating the track parameters.

Table 3.3 shows the updated shear wave velocity  $C_s$  and material damping ratio  $\beta_s$  of the ballast layer and the corresponding minimum of the residual  $r(\mathbf{x})$  for each case. The lowest value of the residual is found for case 2, where a shear wave velocity  $C_s = 300$  m/s is used for the track subgrade. The corresponding shear wave velocity  $C_s = 153.7$  m/s and material damping ratio  $\beta_s = 0.03$  for

the ballast layer result in a good fit of the rail receptance (figure 3.30).

Case	Subgrade	Ballast		Residual
	$C_s$ [m/s]	$C_s$ [m/s]	$\beta_s$ [-]	$r(\mathbf{x})$ [ $10^{-8}$ m/N]
1	200	141.6	0.001	0.522
<b>2</b>	<b>300</b>	<b>153.7</b>	<b>0.032</b>	<b>0.324</b>
3	400	154.0	0.100	0.363

Table 3.3: Results of the optimization process of the dynamic track parameters.

The updating of the track parameters leads to a ballast shear wave velocity that is 2.25 times smaller than the initial estimate. The difference is due to the use of a different model, while the track subgrade is additionally taken into account. As discussed in subsection 3.4.1, the obtained result can be expressed as the ballast stiffness under a single sleeper, resulting in a value  $k_b = 180 \times 10^6$  N/m that better corresponds to reported ballast stiffness values from  $12 \times 10^6$  N/m to  $190 \times 10^6$  N/m [54, 82, 158, 160]. It is noted, however, that comparison with other models can only be used as an indication, since the model parameters depend on the assumptions that are made in each model.

Table 3.4 summarizes the identified dynamic track characteristics, indicating the equivalent parameters for the continuous model by a bar. In the following, these track parameters are used to predict the railway induced vibration.



Rail	Flexural stiffness (per rail)	$E_r I_r = 6.45 \times 10^6 \text{ Nm}^2$
	Mass per length (per rail)	$\rho_r A_r = 60.3 \text{ kg/m}$
	Position of left rail	$x_{r1} = -0.7175 \text{ m}$
	Position of right rail	$x_{r2} = +0.7175 \text{ m}$
Rail pad	Stiffness	$k_{rp} = 255.7 \times 10^6 \text{ N/m}^2$
	Viscous damping	$\bar{c}_{rp} = 22.5 \times 10^3 \text{ Ns/m}^2$
Sleeper	Mass per length	$\bar{m}_{sl} = 500 \text{ kg/m}$
	Mass moment of inertia	$\rho_{sl} \bar{I}_{t\,sl} = 262.17 \text{ kgm}$
	Length	$l_{sl} = 2.50 \text{ m}$
Ballast	Height	$h_b = 0.35 \text{ m}$
	Upper width	$w_{bu} = 3.60 \text{ m}$
	Lower width	$w_{bl} = 5.60 \text{ m}$
	Shear wave velocity	$C_s = 153.7 \text{ m/s}$
	Longitudinal wave velocity	$C_p = 307.4 \text{ m/s}$
	Shear damping ratio	$\beta_s = 0.03$
	Longitudinal damping ratio	$\beta_p = 0.03$
	Mass density	$\rho_b = 1700 \text{ kg/m}^3$
Track subgrade	Shear wave velocity	$C_s = 300 \text{ m/s}$
	Longitudinal wave velocity	$C_p = 600 \text{ m/s}$
	Shear damping ratio	$\beta_s = 0.044$
	Longitudinal damping ratio	$\beta_p = 0.044$
	Mass density	$\rho_s = 1854 \text{ kg/m}^3$
	Height	$h_s = 1 \text{ m}$

Table 3.4: Dynamic characteristics of the ballasted track at the site in Lincent after updating the track receptance.

### 3.5 The track – free field mobility

In the present section, it is investigated to which extent the track – free field mobility can be predicted numerically based on input data of the soil provided by preliminary site investigation and based on the identified track characteristics. First, the influence of the excavation and the track subgrade on the track – free field mobility is investigated by means of the models presented in figure 3.21. Next, the measured track – free field mobilities are used to assess the accuracy of the predicted results.

### 3.5.1 Influence of the excavation on the track – free field mobility

The influence of the excavation on the track – free field mobility is investigated by means of numerical simulation with the track models presented in figure 3.21. The influence of the excavation is investigated by comparing the results obtained with model A (figure 3.21a) for a track at surface and with model B (figure 3.21b) for a track in excavation. Model C (figure 3.21c) is not considered for the prediction of the mobility, as it does not correctly represent the wave propagation in the free field due to the reduced height of the top layer. The influence of the excavation is investigated without taking into account the track subgrade, which is treated in the following subsection.

Figure 3.31 compares the mobilities predicted with both models and shows a difference due to the excavation that increases up to around 6 dB but is generally relatively small.

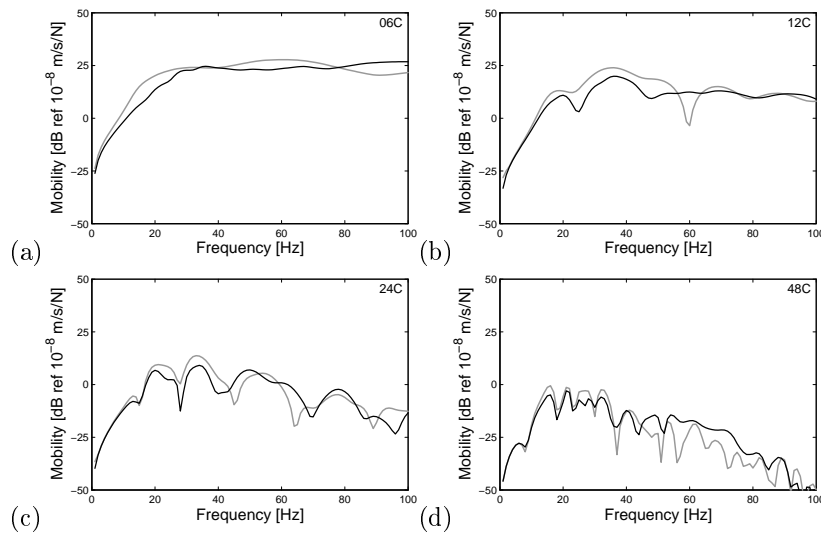


Figure 3.31: Predicted track – free field mobility level at line C ( $y = 0$  m) at (a) 6 m, (b) 12 m, (c) 24 m, and (d) 48 m from the track center line for a source point at the edge of the sleeper at  $x = 1.10$  m and  $y = 0$  m for model A (grey line) and model B (black line).

The influence of the excavation is of the same order of magnitude for the free field mobility (figure 3.10) as for the track – free field mobility (figure 3.31). The excavation starts to affect the mobilities around 20 Hz, where the wavelength in the top layer is of the same order of magnitude as the dimensions of the

excavation. At 6 m, the mobility is additionally affected by the reduced height of the top layer, as this receiver point is located within the excavation.

Figure 3.31 demonstrates that the excavation has a small but non-negligible influence on the track – free field mobility. In the following, the excavation is therefore taken into account in the predictions.

### 3.5.2 Influence of the track subgrade on the track – free field mobility

The influence of the track subgrade on the mobilities is investigated by comparing the results obtained with model B (figure 3.21b), disregarding the track subgrade, and with model D (figure 3.21d), taking into account the track subgrade. Models E (figure 3.21e) and F (figure 3.21f) are not considered for the prediction of the mobility, as they do not correctly represent the wave propagation in the free field due to the reduced height of the top layer.

Figure 3.32 compares the mobilities predicted with both models. Below 20 Hz, the governing wavelength in the soil is large compared to the depth of the subgrade and the vibration transfer is hardly affected by its presence.

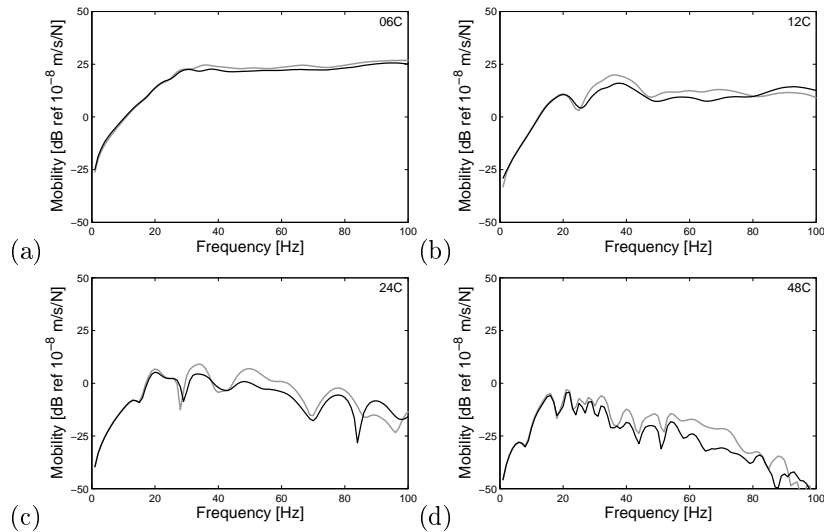


Figure 3.32: Predicted track – free field mobility level at line C ( $y = 0$  m) at (a) 6 m, (b) 12 m, (c) 24 m, and (d) 48 m from the track center line for a source point at the edge of the sleeper at  $x = 1.10$  m and  $y = 0$  m with model B (grey line) and model D (black line).

Around 20 Hz, the wavelength in the soil is of the same order of magnitude as the dimensions of the subgrade and a difference up to 10 dB is observed between the mobilities obtained with both models. A higher influence of the track subgrade on the mobility up to 20 dB is reported in cases where much stiffer materials such as soil–cement mixtures or concrete are used in the track subgrade [3, 61].

In the following, the excavation and the track subgrade are taken into account and model D (figure 3.21d) is applied to predict the track – free field mobility.

### 3.5.3 Validation of the track – free field mobility

The track – free field mobility is measured at the site in Lincent by applying a hammer impact at the track and measuring the response by means of accelerometers installed in the free field. The setup in the free field is identical to the setup used for the measurement of the free field transfer functions (figure 3.11) The data acquisition and signal processing are also performed analogously. A detailed description of the setup and the data acquisition is given in the measurement report [150].

The hammer impacts are applied to the edge of the sleeper at a distance of 1.10 m from the center of the track. Impacts are applied at 21 source points along the track from  $y = -100$  m to  $y = 100$  m with a spacing of 10 m, indicated by the black squares in figure 3.11. The source points at the track are denoted as  $YyyT$ , where the two-digit number  $yy$  denotes the  $y$ -coordinate of the source point, e.g. Y00T.

Based on the measured force and free field response, the average experimental mobility is determined by means of the  $H_1$  estimator, as discussed in subsection 3.3.3. Figure 3.33 shows the mean value and the 95% confidence interval of the track – free field mobility measured at line C for 100 hammer impacts at the edge of the sleeper at  $y = 0$  m. As for the free field mobility, the track – free field mobility is measured accurately in an intermediate frequency range. At 48 m from the track, the mobility is measured accurately between 20 and 100 Hz.

The predicted mobility is compared to the measured result in figure 3.33. and generally shows a good agreement. Close to the track, an underestimation is observed around 50 Hz, which is no longer observed at higher distances.

Figure 3.34 shows the mean value and the 95% confidence interval of the one-third octave band mobility at measurement line C for 100 hammer impacts at the edge of the sleeper at  $y = 0$  m. Due to averaging within each frequency

band, a smaller confidence interval is obtained indicating a small influence of the noise on the measured mobility.

As the peaks and troughs observed in the narrow band spectrum are averaged within each frequency band, the one-third octave band spectrum allows for a more clear comparison of the measured and predicted mobility. It confirms that a good agreement is found, particularly at a larger distance from the track where the difference is generally limited to 6 dB.

Figure 3.35 shows the measured and predicted mobility at measurement line C for 100 hammer impacts at the edge of the sleeper at  $y = 40$  m. The propagation path between the source point at  $y = 40$  m and a receiver at line C ( $y = 0$  m) close to the track (e.g.  $x = 6$  m) almost runs parallel to the track (figure 3.11) and is mainly determined by the properties of the track and the track subgrade. A significantly better agreement is found for the track – free field mobility (figure 3.35a) as compared to the free field mobility for the corresponding source and receiver point (figure 3.17a). This suggests that the vibration transfer along the track is modeled more accurately when the track (and the track subgrade) is taken into account.

Figure 3.36 shows the mean value and the 95% confidence interval of the one-third octave band mobility at measurement line C for 100 hammer impacts at the edge of the sleeper at  $y = 40$  m. A better agreement is found than for the one-third octave band free field mobility (figure 3.18). A relatively large difference up to 15 dB at most is still observed, however.

Figure 3.37 compares the one-third octave band mobilities determined at different measurement lines A to E (figure 3.11). Changing the measurement position along the track results in a difference up to 15 dB in the measured mobilities, which is due to variation of the dynamic soil characteristics and geometry (excavation) along the track. A similar scatter is observed as for the free field mobilities (figure 3.19).

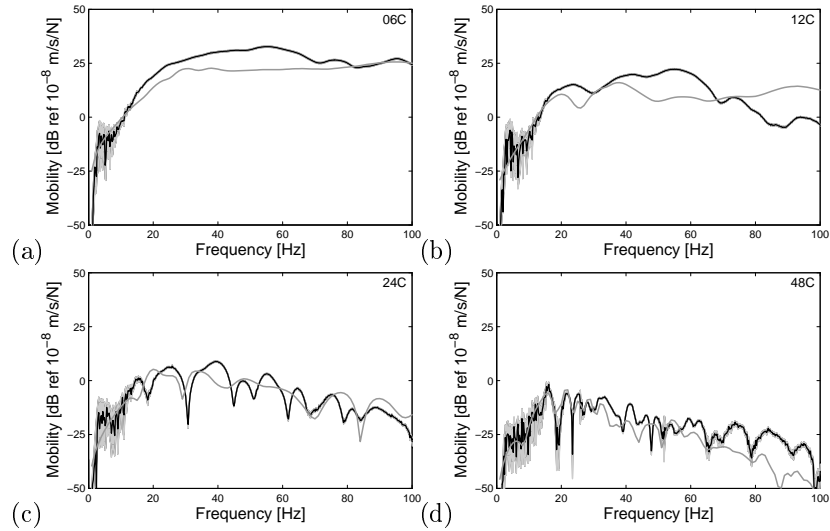


Figure 3.33: Predicted (grey line) and measured (black line) track – free field mobility level and confidence interval (grey region) at line C ( $y = 0$  m) at (a) 6 m, (b) 12 m, (c) 24 m, and (d) 48 m from the track center line for a source point at the edge of the sleeper at  $x = 1.10$  m and  $y = 0$  m.

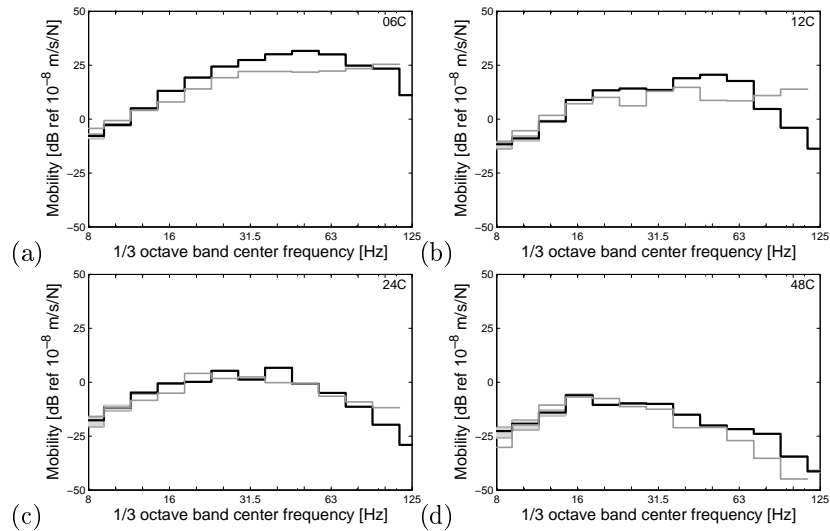


Figure 3.34: Predicted (grey line) and measured (black line) one-third octave band track – free field mobility level and confidence interval (grey region) at line C ( $y = 0$  m) at (a) 6 m, (b) 12 m, (c) 24 m, and (d) 48 m from the track center line for a source point at the edge of the sleeper at  $x = 1.10$  m and  $y = 0$  m.

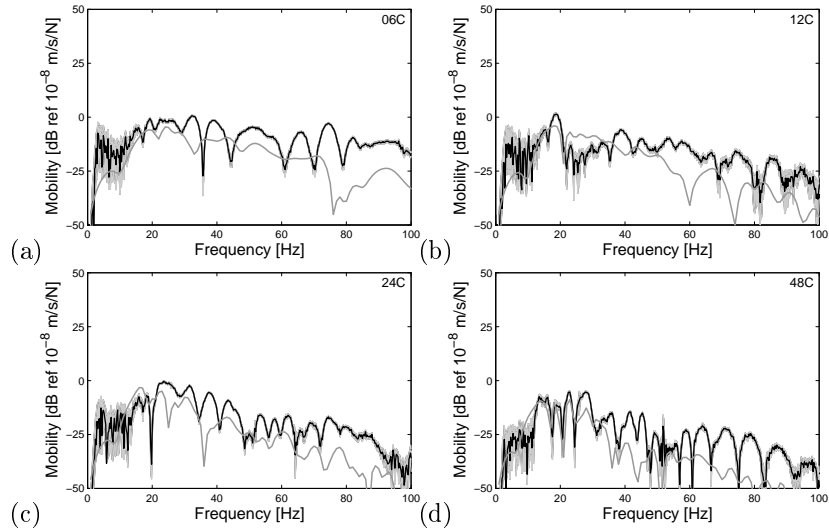


Figure 3.35: Predicted (grey line) and measured (black line) track – free field mobility level and confidence interval (grey region) at line C ( $y = 0$  m) at (a) 6 m, (b) 12 m, (c) 24 m, and (d) 48 m from the track center line for a source point at the edge of the sleeper at  $x = 1.10$  m and  $y = 40$  m.

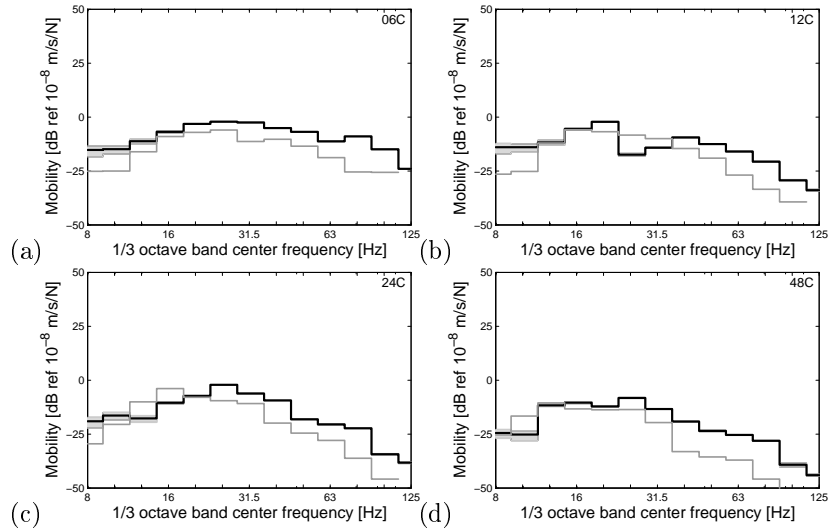


Figure 3.36: Predicted (grey line) and measured (black line) one-third octave band track – free field mobility level and confidence interval (grey region) at line C ( $y = 0$  m) at (a) 6 m, (b) 12 m, (c) 24 m, and (d) 48 m from the track center line for a source point at the edge of the sleeper at  $x = 1.10$  m and  $y = 40$  m.

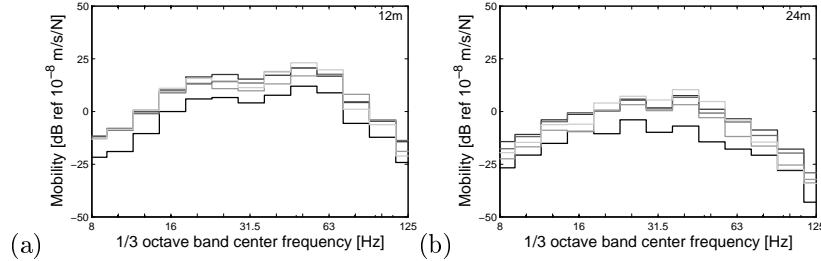


Figure 3.37: One-third octave band track – free field mobility level measured at five different measurement lines (grey to black lines) at (a) 12 m and (b) 24 m from the track center line for source points at the edge of the sleeper at  $x = 1.10$  m and at the corresponding measurement line.

### 3.6 Train passages

After the validation of the different submodels, the present section addresses the validation of the prediction of train induced vibration. The response has been measured at the site in Lincent for different train types. A prediction is made based on the identified train, track, and soil characteristics and the measured unevenness profile. The accuracy of the prediction is assessed for the passage of an IC train (198 km/h) and a Thalys train (300 km/h) by comparison with the measured results.

#### 3.6.1 The dynamic train characteristics

Figure 3.38 shows an IC train and a Thalys train passing at the site in Lincent.

Both the quasi-static and dynamic contribution are taken into account in the prediction. The quasi-static excitation is determined by the total axle load, while the dynamic excitation is determined by the dynamic behavior of the vehicle. The latter is computed by means of a simplified vehicle model (figure 2.3) that only accounts for the unsprung axle mass. As the modes of the carriage and the bogies only affect the vehicle response at very low frequencies, this model is accurate in the frequency range of interest [144]. A Hertzian spring stiffness  $k_H = 2.8 \times 10^9$  N/m is used to model the contact between the wheel set and the rails [67,144]. The characteristics of both trains are described in the following.



### IC train

Two IC train types (IC-A and IC-O types) are operating on the line L2. The considered IC passage corresponds to the IC-A type. The IC-A train consists of 1 locomotive HLE 13, 11 standard carriages I11, and 1 side carriage I11 BDx and has a total length  $L_t = 335.91$  m (from first to last axle). The IC-A train is in push mode in the direction of Liège and in pull mode in the direction of Brussels.

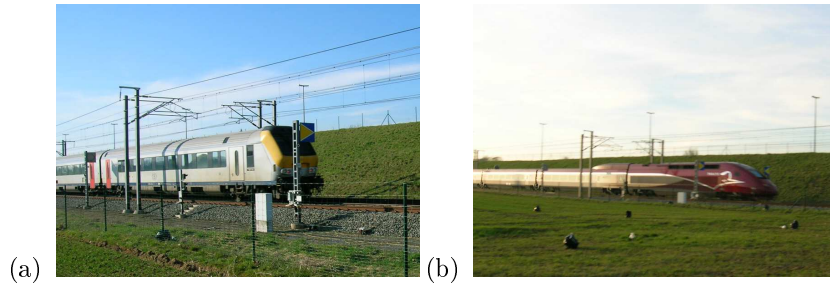


Figure 3.38: View of (a) an IC train and (b) a Thalys HST passing at the site in Lincent.

Every locomotive and carriage has two independent bogies and four axles. The car length  $L_c$ , the bogie distance  $L_b$ , the axle distance  $L_a$ , the total axle mass  $M_t$ , the sprung axle mass  $M_s$ , and the unsprung axle mass  $M_u$  of all cars are summarized in table 3.5.

	Number of axles	$L_c$ [m]	$L_b$ [m]	$L_a$ [m]	$M_t$ [kg]	$M_s$ [kg]	$M_u$ [kg]
Locomotive	4	19.11	10.40	3.00	22500	19677	2823
Central carriage	4	26.40	18.40	2.56	11610	10100	1500
Side carriage	4	26.40	18.40	2.56	11830	10286	1544

Table 3.5: Geometrical and mass characteristics of the IC train.

### Thalys HST

The Thalys HST (figure 3.38b) operating on the line L2 is of the type PBKA. It consists of 2 locomotives, one at each side of the train, and 8 carriages in between and has a total length  $L_t = 200.19$  m (from first to last axle). Each locomotive is supported by two bogies and has four axles. The side carriages, next to the locomotive, have one independent bogie and share the

second bogie with the neighboring carriage. The six remaining central carriages share both bogies with their neighboring carriages, resulting in an articulated train composition, shown in figure 3.39. The total number of bogies equals 13 and, consequently, the total number of axles is 26.

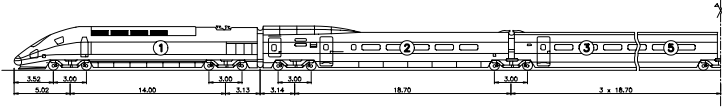


Figure 3.39: Configuration of the Thalys HST.

The car length  $L_c$ , the bogie distance  $L_b$ , the axle distance  $L_a$ , the total axle mass  $M_t$ , the sprung axle mass  $M_s$ , and the unsprung axle mass  $M_u$  of all cars are summarized in table 3.6.

	Number of axles	$L_c$ [m]	$L_b$ [m]	$L_a$ [m]	$M_t$ [kg]	$M_s$ [kg]	$M_u$ [kg]
Locomotive	4	22.15	14.00	3.00	17000	14973	2027
Side carriage	3	21.84	18.70	3.00	17000	14973	2027
Central carriage	2	18.70	18.70	3.00	17000	14973	2027

Table 3.6: Geometrical and mass characteristics of the Thalys HST.

### 3.6.2 The track unevenness

The Belgian Railway Company NMBS uses the EM130 measurement vehicle equipped with an Applanix POS/TG system [114,162] to record the irregularity and alignment of both rails and the curvature, superelevation, and grade of the track. The irregularity of the rail is measured indirectly based on the axle displacements and therefore contains a contribution from both parametric and unevenness excitation, as discussed in subsection 2.3.1. The track unevenness at the site in Lincent has been measured during a passage on track 1 in the direction of Liège in April 2011, one month after the measurement of the train passages.

Figure 3.40 shows the vertical unevenness  $u_{w/rz}(y)$  and the horizontal unevenness  $u_{w/rx}(y)$  of both rails of track 1 from km 52.4 to km 53.1 on the high speed line L2. As both tracks on line L2 have been built at the same time and are subject to the same traffic volume, the profile is considered to be representative for both tracks at the site in Lincent.

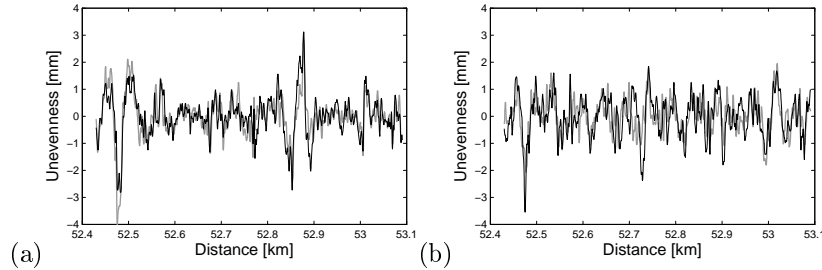


Figure 3.40: Measured (a) vertical and (b) horizontal unevenness of the right rail (grey line) and the left rail (black line) of track 1 at the site in Lincent.

Figure 3.41 shows the PSD  $\tilde{S}_{u_w/rz}(k_y)$  of the average vertical unevenness of both rails. The measuring bandwidth of the track recording cars is generally restricted to wavelengths ranging from a few meters to 20 or 30 m [41]. The measured PSD is only shown in the wavenumber range from 0.1 to 2 rad/m, corresponding to a wavelength range from 3 to 63 m, where a reliable measurement of the unevenness has been obtained. This corresponds to an excitation in the frequency range from 0.9 to 17 Hz at a train speed of 198 km/h and in the frequency range from 1.3 to 27 Hz at a train speed of 300 km/h. The unevenness corresponding to higher wavenumbers is obtained by fitting the measured data in the reliable wavenumber range to the PSD in equation (2.37) proposed by the FRA [56]. The fitted PSD is obtained by minimizing the difference with the measured PSD using equidistantly sampled wavenumbers on a linear scale between 0.1 and 2 rad/m. The fit is shown in figure 3.41 and is better in the lower wavenumber range where the PSD of the measured unevenness is higher, resulting in a value  $A = 4.75 \times 10^{-9}$  m. At wavenumbers between 0.6 and 2 rad/m, the measured unevenness is slightly underestimated by the fitted PSD.

The FRA defines six classes of unevenness (table 2.4), of which the limiting class 1 and class 6 are shown in figure 3.41. The value of the fitted PSD is much lower, indicating a low roughness and a very good track quality at the site in Lincent compared to the tracks in the FRA database.

As a comparison, the fitted PSD based on measurements at the same site in 2002 [98] is shown in figure 3.41. A similar result is found at high wavenumbers, whereas a higher value is found at low wavenumbers.

The fitted PSD is used to generate samples of the vertical rail unevenness, accounting for the entire frequency range of interest. The generation of unevenness samples  $\hat{u}_{w/rz}(\omega)$  is based on equation (2.15).

Figure 3.42 shows the modulus of an artificial vertical unevenness profile in

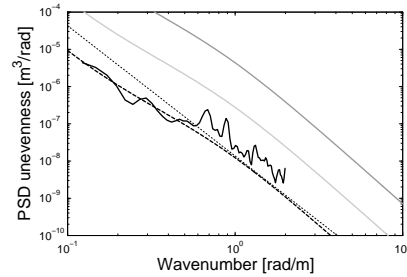


Figure 3.41: Measured (solid black line) and fitted (dashed black line) PSD of the vertical rail unevenness at the site in Lincent and according to FRA class 1 (dark grey line) and class 6 (light grey line). The fitted PSD based on measurements in 2002 (dotted black line) is added as a reference [98].

the frequency domain, evaluated for a train speed of 198 km/h and 300 km/h. An increase of the train speed results in a higher level of excitation as it shifts the frequency content of the unevenness to higher frequencies. In the following subsection, artificial vertical unevenness profiles are used to predict the response of the rail and in the free field. The horizontal unevenness is not taken into account.

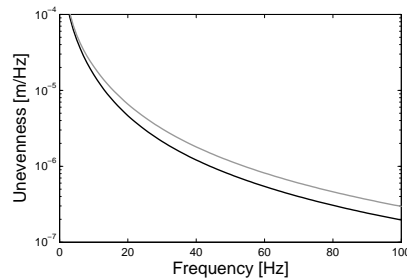


Figure 3.42: Modulus of a sample of vertical track unevenness generated for a train speed of 198 km/h (black line) and 300 km/h (grey line).

### 3.6.3 Validation of the response due to train passages

The response during the train passages has been measured on the track and in the free field. The reference coordinate system and the setup in the free field are identical to those used for the measurement of the free field transfer functions

(figure 3.11). A detailed description of the setup is given in the measurement report [150].

The track has additionally been instrumented with five accelerometers at the edge of the sleeper ( $x = +1\text{ m}$ ) and five accelerometers at the right rail ( $x = +0.7175\text{ m}$ ), both measuring the vertical acceleration. The position of the accelerometers on the sleeper and the rail is indicated in figure 3.43. These accelerometers are installed at five locations corresponding to the measurement lines used in the free field setup (figure 3.11). The measurement points are referred to as *TSL* and *TRL* to indicate the receiver points on the sleeper and the rail, respectively, where the character *L* indicates at which measurement line the point is located.

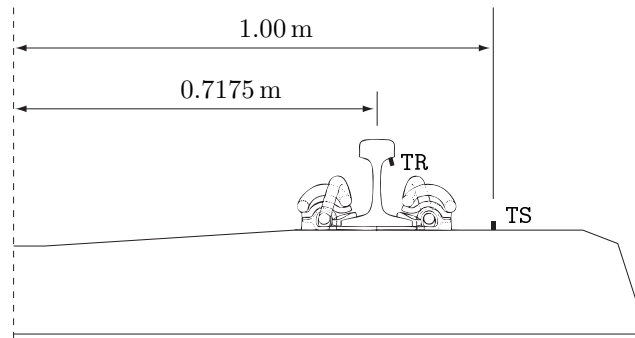


Figure 3.43: Measurement setup on the track indicating the position of the accelerometers at the rail (TR) and at the edge of the sleeper (TS).

The data acquisition system is identical as for the measurement of the free field transfer functions and a sampling frequency  $f_s = 1000\text{ Hz}$  is used. For each train passage, 32 768 data points are recorded, corresponding to a time period of 32.768 s. The acceleration in the first measurement point in the free field (06C) is used as a trigger with a trigger level of  $\pm 0.5\text{ m/s}^2$  where 8192 data points are stored before exceedance of the trigger level and 24 576 data points are stored afterwards.

The time history of the velocity  $v_i^k(t)$  in channel  $i$  for train passage  $k$  is obtained by integration of the measured acceleration  $a_i^k(t)$ . The integration and filtering of the signal are identical as described in subsection 3.3.3. The frequency content  $\hat{v}_i^k(\omega)$  is obtained by means of a forward Fourier transform from the time to the frequency domain.

The train speed is estimated based on the measured rail response, which is similar at two measurement points on the rail except for a time delay

determined by the speed of the train and the distance between both points. As the distance between both measurement points is known, the estimation of the time delay allows for an estimation of the train speed.

A common method to determine the time delay between the measured acceleration in channels  $i$  and  $j$  is based on the estimation of the cross correlation  $R_{ij}(\tau)$  between both signals [74]:

$$R_{ij}(\tau) = \frac{1}{T - \tau} \int_{\tau}^T a_i(t - \tau) a_j(t) dt \quad (3.5)$$

where  $a_i(t)$  and  $a_j(t)$  are the measured accelerations in channels  $i$  and  $j$ , respectively, and  $T$  is the time period of the measured signal. The value of  $\tau$  that maximizes the cross correlation  $R_{ij}(\tau)$  indicates the time shift for which the highest resemblance of both measured signals is obtained and provides an estimate of the time delay.

The cross correlation is computed as the inverse Fourier transform of the cross PSD  $\hat{S}_{ij}(\omega)$ , according to the Wiener–Kintsjin theorem [38]:

$$R_{ij}(\tau) = \frac{1}{2\pi} \int_{-\infty}^{+\infty} \hat{S}_{ij}(\omega) \exp(+i\omega\tau) d\omega \quad (3.6)$$

The cross PSD  $\hat{S}_{ij}(\omega)$  between channels  $i$  and  $j$  is estimated based on equation (3.2) for a single event ( $N = 1$ ).

During the measurements on 21-22 March 2011, a total of 103 train passages has been recorded during operation of the line L2. The recorded events contain 51 passages on track 1 in the direction of Liège, of which 33 IC-A passages (148 – 209 km/h), 6 IC-O passages (169 – 186 km/h), 8 Thalys passages (205 – 285 km/h), and 4 ICE passages (228 – 238 km/h) and 52 passages on track 2 in the direction of Brussels, of which 30 IC-A passages (160 – 214 km/h), 10 IC-O passages (192 – 201 km/h), 7 Thalys passages (160 – 300 km/h), and 5 ICE passages (214 – 245 km/h).

In the following, the measured and predicted results are presented for the passages of IC trains (IC-A type) and Thalys trains on track 2 in the direction of Brussels. For the numerical prediction based on equation (2.10), the track receptance is computed in a moving frame of reference with track–soil model F (figure 3.21f) and the track – free field mobility is computed with track–soil model D (figure 3.21d).

**IC train**

First, the passage of an IC train running at a speed of 198 km/h on track 2 is considered.

The axle loads are calculated based on the compliance formulation in equation (2.23). Figure 3.44 shows the modulus of the first and fifth diagonal element of the track compliance  $\hat{\mathbf{C}}^t(\omega)$ , vehicle compliance  $\hat{\mathbf{C}}^v(\omega)$ , and combined compliance  $\hat{\mathbf{C}}^t(\omega) + \hat{\mathbf{C}}^v(\omega)$ , corresponding to the first axle of the locomotive and the first carriage, for the IC train.

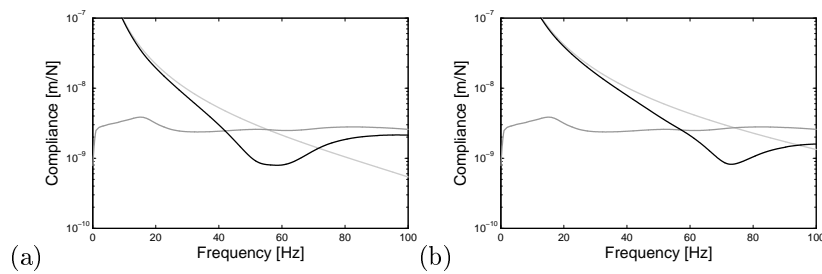


Figure 3.44: Modulus of the (a) first and (b) fifth diagonal element of the vertical track compliance (dark grey line), vehicle compliance (light grey line), and combined compliance (black line) for an IC train (198 km/h).

As discussed in subsection 2.5.3, the combined compliance reaches a minimum when the track and vehicle compliance are equal but opposite in sign. This minimum is reached around 75 Hz for the carriage axle (figure 3.44b). As the modulus of the vehicle compliance is inversely proportional to the unsprung mass of the axle, the higher unsprung mass of the locomotive yields a lower vehicle compliance and the minimum of the combined compliance is reached at a lower frequency around 55 Hz (figure 3.44a).

Figure 3.45 shows the predicted load of the first axle of the locomotive and the first carriage of an IC train running at a speed of 198 km/h. The peak in the axle load spectrum corresponds to the minimum of the combined compliance and is found at a lower frequency for the locomotive. Furthermore, as the unevenness excitation is higher in the lower frequency range (figure 3.42), the peak of the axle load spectrum is higher for the locomotive, as can be observed in figure 3.45.

Figure 3.46 shows the measured and predicted time history and narrow band spectrum of the rail velocity for a single unevenness sample and figure 3.47 shows the measured and predicted running RMS value and one-third octave

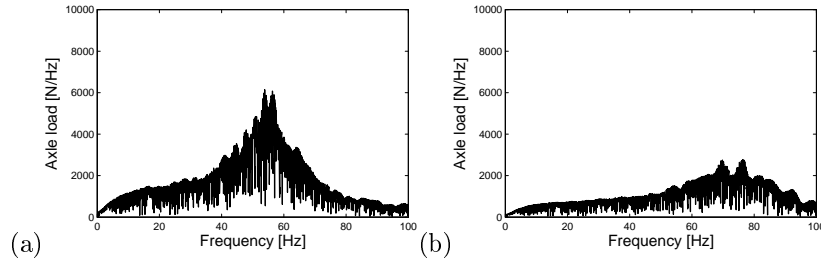


Figure 3.45: Vertical dynamic load at the first axle of (a) the locomotive and (b) the first carriage of an IC train (198 km/h).

band RMS value of the rail velocity for 10 unevenness samples during the passage of the IC train.

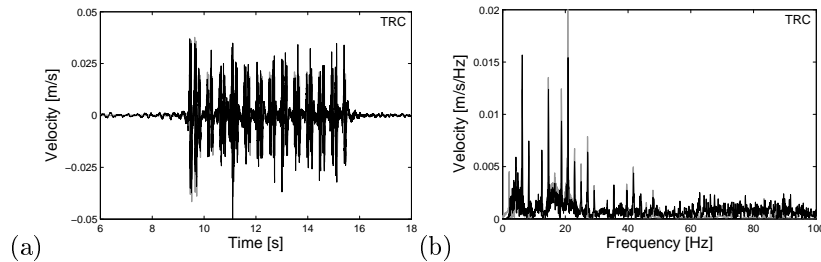


Figure 3.46: (a) Time history and (b) frequency content of the measured (black line) and predicted (1 unevenness sample, grey line) vertical rail velocity at line C during the passage of an IC train (198 km/h).

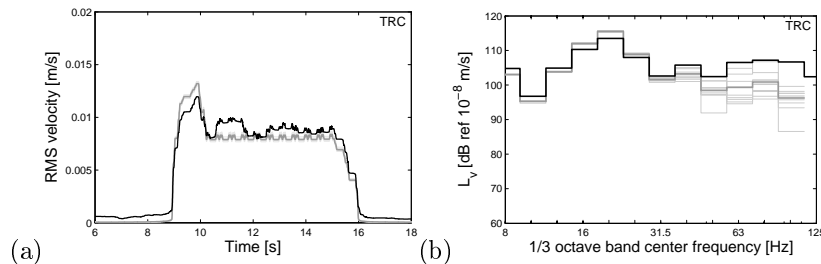


Figure 3.47: (a) Running RMS value and (b) one-third octave band RMS level of the measured (black line) and predicted (10 unevenness samples, grey lines) vertical rail velocity at line C during the passage of an IC train (198 km/h).

The passage of single bogies and axles can clearly be distinguished in the time history of the rail response (figure 3.46a). The first four axles of the train result in a slightly higher response, as they belong to the locomotive with a higher



total axle load (the IC trains on track 2 are in pull mode). A higher value is also observed in the running RMS value (figure 3.47a) during the passage of the locomotive, while a more or less constant value is obtained during the passage of the other carriages.

A quasi-discrete narrow band spectrum is observed, determined by the composition of the train (figure 3.46b). These peaks are averaged in the one-third octave band RMS spectrum (figure 3.47b), showing a relatively flat vibration level up to 125 Hz, with a small peak around 20 Hz.

The prediction shows a good agreement with the measured result in the time as well as the frequency domain. The response due to the first four axles, belonging to the locomotive is slightly overestimated, whereas the response to the axles of the carriages is predicted very accurately. The spectrum shows a good agreement in the low frequency range, where the quasi-static excitation dominates. At frequencies above 60 Hz, the response is slightly underestimated. In this frequency range, the rail response is mainly determined by the dynamic axle loads and a larger variation due to the different unevenness samples is observed.

Figure 3.48 shows the measured and predicted time history and narrow band spectrum of the free field velocity for a single unevenness sample and figure 3.49 shows the measured and predicted running RMS value and one-third octave band RMS spectrum of the free field velocity for 10 unevenness samples during the passage of the IC train.

In the time history of the response in the free field (figure 3.48a), the passage of single axles or bogies can no longer be distinguished. The dynamic response to a single axle has a longer duration, so that contributions from different axles overlap. Even the passage of the locomotive with a higher unsprung mass is not clearly visible in the response.

A quasi-discrete narrow band spectrum is observed (figure 3.48b), due to the fact that the response is composed of similar contributions from different axles with a certain time delay. The frequency spectrum due to the IC train passage is characterized by two peaks: a first peak around 20 Hz and a second broad band peak between 50 Hz and 63 Hz. Close to the track, the response is dominated by the peak between 50 and 63 Hz. As the effect of material damping with increasing distance is stronger for higher frequencies, this peak is attenuated more strongly and the peak around 20 Hz becomes dominant at larger distances. A small additional peak is observed in the narrow band spectrum around 90 Hz, corresponding to the sleeper passage frequency  $f_{sl} = v/d_{sl} = 91.7$  Hz observed for a train speed  $v = 198$  km/h and a sleeper spacing  $d_{sl} = 0.60$  m.

Due to the overlap of the contributions from different axles, an approximately

stationary part is observed in the running RMS value during the passage of the train (figure 3.49a). Furthermore, the peaks observed in the narrow band spectrum are observed in the RMS spectrum as well (figure 3.49b) and characterize the passage of the IC train.

The comparison of the measured and predicted free field velocity shows that the measured response is generally underestimated. At a distance of 6 m, the running RMS value (figure 3.49a) is underestimated for all unevenness samples up to a factor of 2 (6 dB). This underestimation is slightly smaller at other distances. A relatively good quantitative and qualitative agreement is observed in the RMS spectrum (figure 3.49b), where the difference between the average prediction and the measured result is generally below 6 dB. The difference arising in the predicted response due to different unevenness samples also increases up to 6 dB in the entire frequency range.

The prediction of the free field response is determined by the dynamic axle loads that are based on the fitted unevenness spectrum. At a train speed of 198 km/h, however, only the measured results in the frequency range from 0.9 to 17 Hz are reliable. Furthermore, the fitted PSD slightly overestimates the measured results in the frequency range from 5 to 17 Hz.

Figure 3.50 shows the RMS spectrum at different distances from the track for 17 IC passages in the speed range  $v = 193 - 203$  km/h. The train speed is indicated by the greyscale, where a darker shade indicates a higher speed. A considerable variation is observed in the frequency spectrum due to different train passages, even in the relatively small speed range considered. A difference up to about 6 dB is observed at frequencies below 31.5 Hz, while a variation up to 14 dB is observed at higher frequencies. The latter is mainly due to variation in the characteristics of the trains such as the wheel unevenness. No clear trend is observed in the vibration velocity level for different train speeds, as a change in the speed might influence the level of the vibration but might also lead to a shift of the peaks.

Figure 3.51 shows the RMS spectrum for a single IC train passage at a speed of 198 km/h recorded at different measurement lines. It has been demonstrated in sections 3.3.3 and 3.5.3 that a considerable difference is observed along the track for the free field mobility (figure 3.19) and the track – free field mobility (figure 3.37) due to spatial variation of the soil and track characteristics. The variation of the vibration level due to train passages along the track is additionally determined by the spatial variation of the track unevenness along the track but remains limited to 6 dB.

Figures 3.50 and 3.51 show that considerable differences are observed in the measured vibration level depending on the passage and the measurement

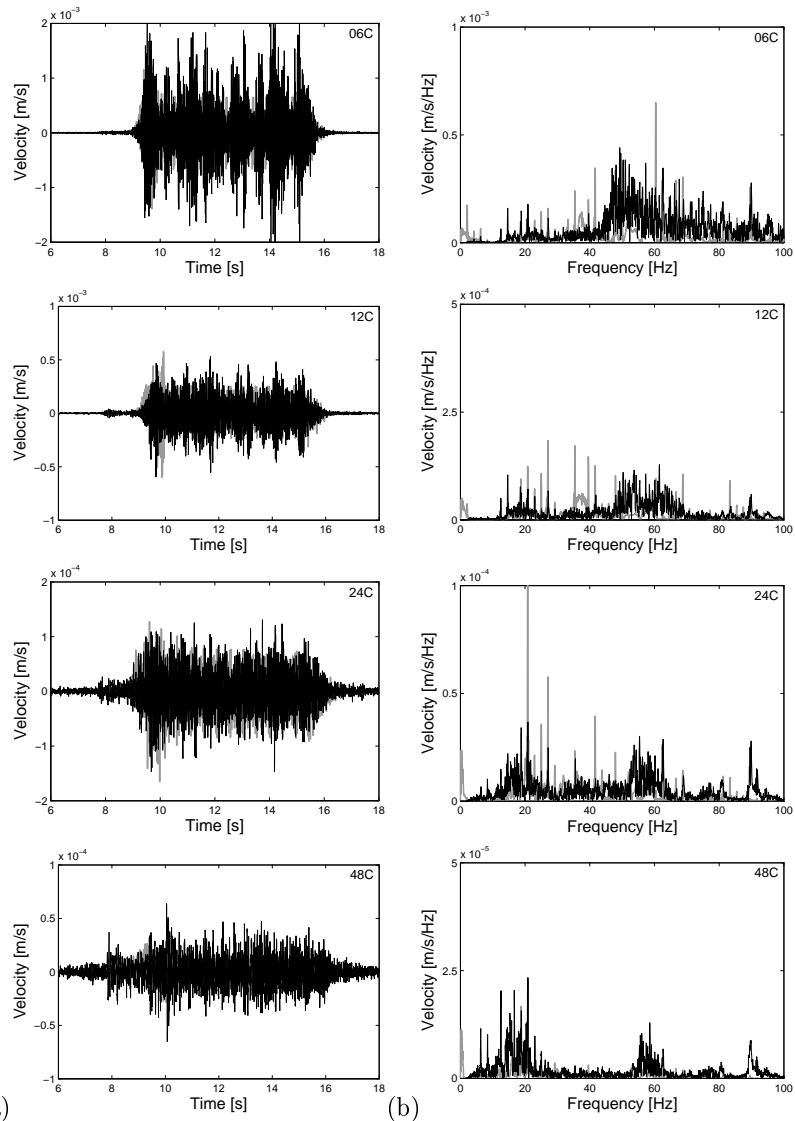


Figure 3.48: (a) Time history and (b) frequency content of the measured (black line) and predicted (1 unevenness sample, grey line) vertical free field velocity at line C ( $y = 0$  m) at (a) 6 m, (b) 12 m, (c) 24 m, and (d) 48 m from the track center line during the passage of an IC train (198 km/h).

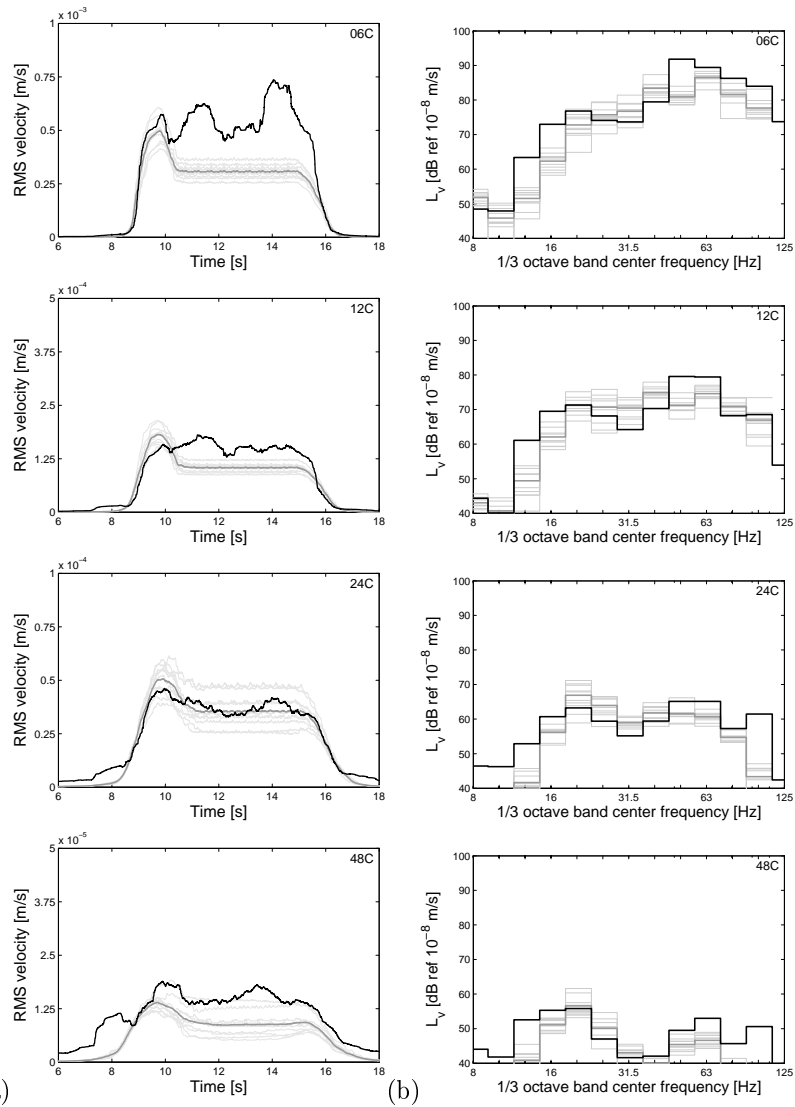


Figure 3.49: (a) Running RMS value and (b) one-third octave band RMS level of the measured (black line) and predicted (10 unevenness samples, grey lines) vertical free field velocity at line C ( $y = 0$  m) at (a) 6 m, (b) 12 m, (c) 24 m, and (d) 48 m from the track center line during the passage of an IC train (198 km/h).

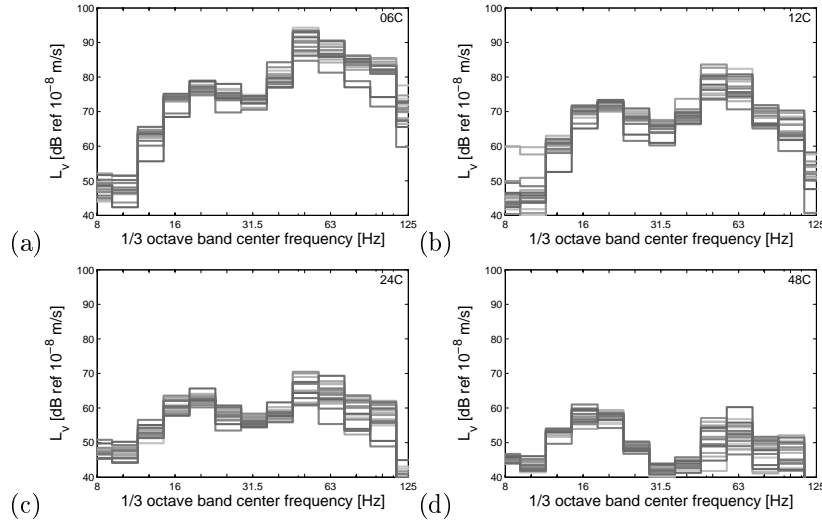


Figure 3.50: One-third octave band RMS level of the measured vertical free field velocity at line C ( $y = 0$  m) at (a) 6 m, (b) 12 m, (c) 24 m, and (d) 48 m from the track center line during the passage of 17 IC trains (193 – 203 km/h).

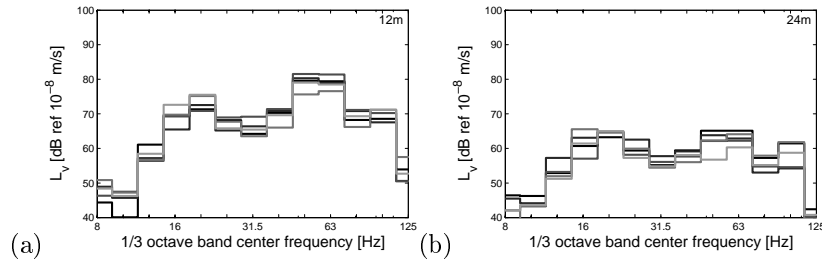


Figure 3.51: One-third octave band RMS level of the measured vertical free field velocity at five different measurement lines (grey to black lines) at (a) 12 m and (b) 24 m from the track center line during the passage of an IC train (198 km/h).

location, even for similar trains and at the same site.

### Thalys train

Next, the passage of a Thalys train running at a speed of 300 km/h on track 2 is considered.

Figure 3.52 shows the modulus of the first diagonal element of the track compliance  $\hat{C}^t(\omega)$ , vehicle compliance  $\hat{C}^v(\omega)$ , and combined compliance  $\hat{C}^t(\omega) + \hat{C}^v(\omega)$  for the Thalys train. The first diagonal element corresponds to the first axle and is representative for all axles of the Thalys train as they have the same unsprung mass. Due to the increased train speed, the resonance peak in the track compliance has shifted to a slightly lower frequency compared to the track compliance obtained for the IC passage (figure 3.44). The minimum of the combined compliance is found around 65 Hz, which is a lower frequency than for the carriage of the IC train (figure 3.44b) due to the higher unsprung mass.

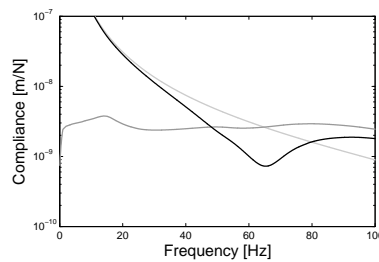


Figure 3.52: Modulus of the first diagonal element of the vertical track compliance (dark grey line), vehicle compliance (light grey line), and combined compliance (black line) for a Thalys train (300 km/h).

Figure 3.53 shows the resulting load at the first axle that shows a peak around 65 Hz corresponding to the minimum of the combined compliance (figure 3.52).

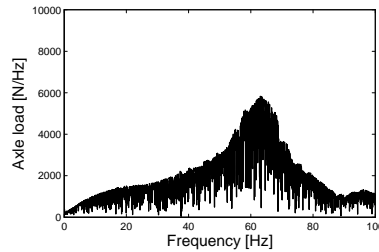


Figure 3.53: Vertical dynamic load at the first axle of the Thalys train (300 km/h).

Figure 3.54 shows the measured and predicted time history and narrow band spectrum of the rail velocity for a single unevenness sample and figure 3.55 shows the measured and predicted running RMS value and one-third octave band RMS spectrum of the rail velocity for 10 unevenness samples during the passage of the Thalys train.

The passage of single bogies and axles can clearly be distinguished in the time history of the rail response (figure 3.54a). As all axles of the Thalys train have approximately the same axle weight, the response to each axle is similar, resulting in a relatively constant running RMS value (figure 3.55a) during the passage of the entire train.

A quasi-discrete narrow band spectrum is observed, determined by the composition of the train (figure 3.54b). Due to averaging, a relatively flat one-third octave band RMS spectrum is obtained (figure 3.55b). A small peak is observed, which has shifted to 30 Hz compared to 20 Hz for the IC train due to the increase of the train speed from 198 to 300 km/h.

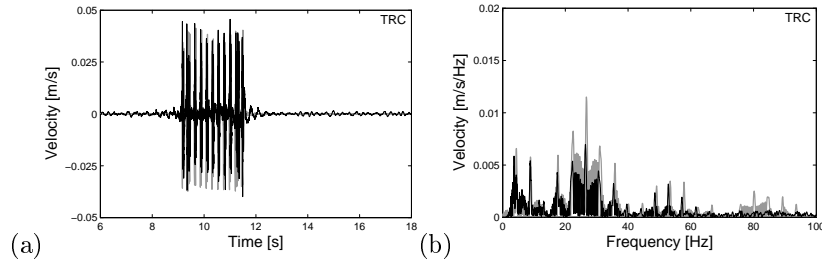


Figure 3.54: (a) Time history and (b) frequency content of the measured (black line) and predicted (1 unevenness sample, grey line) vertical rail velocity at line C during the passage of a Thalys train (300 km/h).

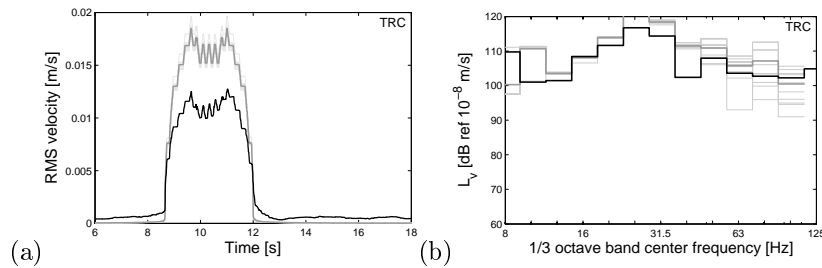


Figure 3.55: (a) Running RMS value and (b) one-third octave band RMS level of the measured (black line) and predicted (10 unevenness samples, grey lines) vertical rail velocity at line C during the passage of a Thalys train (300 km/h).

A reasonably good agreement is observed between the measured and predicted rail velocity in figures 3.54 and 3.55. The running RMS value (figure 3.55a) is overestimated by a factor of 1.5 during the entire passage. A relatively good quantitative and qualitative agreement is observed in the one-third octave band RMS spectrum (figure 3.55b), where a higher variation due to different

unevenness samples is observed at higher frequencies where the dynamic contribution is higher.

Figure 3.56 shows the measured and predicted time history and narrow band spectrum of the free field velocity for a single unevenness sample and figure 3.57 shows the measured and predicted running RMS value and one-third octave band RMS spectrum of the free field velocity for 10 unevenness samples during the passage of the Thalys train.

In the time history of the measured velocity (figure 3.56a), the passage of single axles or bogies can no longer be distinguished. A quasi-discrete narrow band spectrum is observed (figure 3.56b), which is characterized by a peak around 25 Hz. The train speed  $v = 300$  km/h leads to a sleeper passage frequency  $f_{sl} = 138.9$  Hz outside the range of the figure.

The one-third octave band spectra (figure 3.57b) also reveal the peak around 25 Hz that is observed in the narrow band spectra (figure 3.56b).

The predicted velocity overestimates the measured result, in particular around 50 Hz. The response is attenuated more strongly for higher frequencies with increasing distance so that a better agreement is observed at a larger distance from the track. The predicted running RMS value (figure 3.57a) also overestimates the measured result up to 8 dB close to the track, while a better agreement is again obtained at a larger distance due to attenuation of the response.

The prediction of the free field response is strongly influenced by the dynamic axle loads that are based on the fitted unevenness spectrum. At a train speed of 300 km/h, however, only the measured results in the frequency range from 1.3 to 27 Hz are reliable. Furthermore, the fitted PSD slightly overestimates the measured results in the frequency range from 7 to 27 Hz.

Figure 3.58 shows the one-third octave band spectrum at different distances from the track for 5 Thalys passages in the speed range  $v = 290 - 300$  km/h. A difference up to about 6 dB is observed in the entire frequency range, which is smaller than for the IC train passages and indicates a smaller variation in the properties of different Thalys trains.

Figure 3.59 shows the RMS spectrum for a single Thalys train passage at a speed of 300 km/h recorded at different measurement lines. Changing the measurement position along the track, results in a difference up to 8 dB.

Notwithstanding the variation between different trains of the same type, the response during passages of IC and Thalys trains clearly show characteristic spectra. Figure 3.60 shows the average measured one-third octave band spectrum for the IC train and the Thalys train. The spectrum of the IC train is



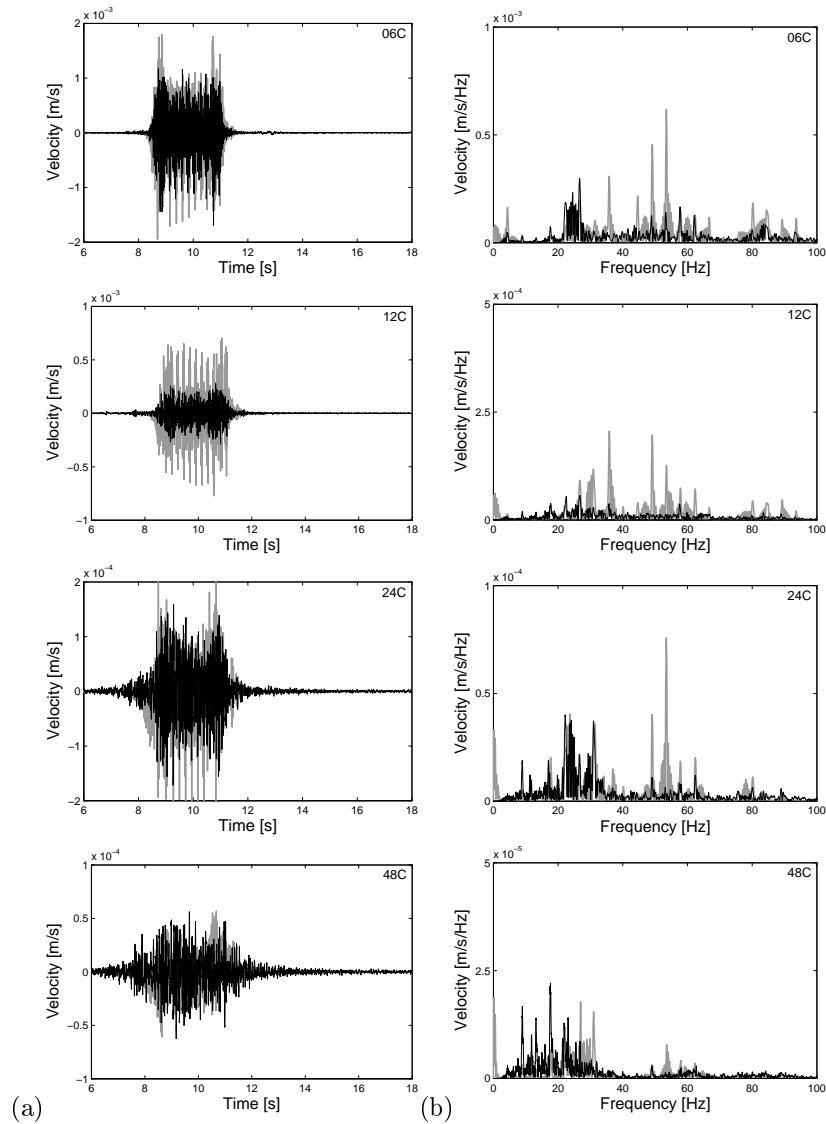


Figure 3.56: (a) Time history and (b) frequency content of the measured (black line) and predicted (1 unevenness sample, grey line) vertical free field velocity at line C ( $y = 0$  m) at (a) 6 m, (b) 12 m, (c) 24 m, and (d) 48 m from the track center line during the passage of a Thalys train (300 km/h).

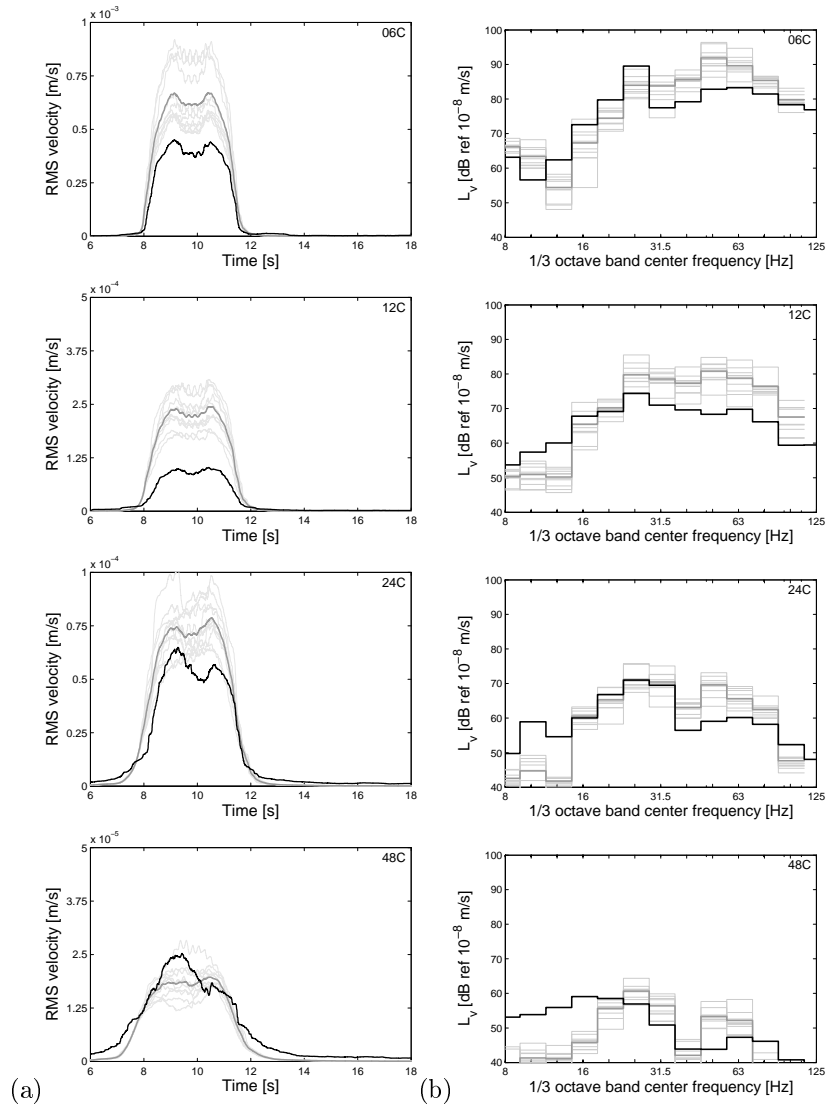


Figure 3.57: (a) Running RMS value and (b) one-third octave band RMS level of the measured (black line) and predicted (10 unevenness samples, grey lines) vertical free field velocity at line C ( $y = 0$  m) at (a) 6 m, (b) 12 m, (c) 24 m, and (d) 48 m from the track center line during the passage of a Thalys train (300 km/h).

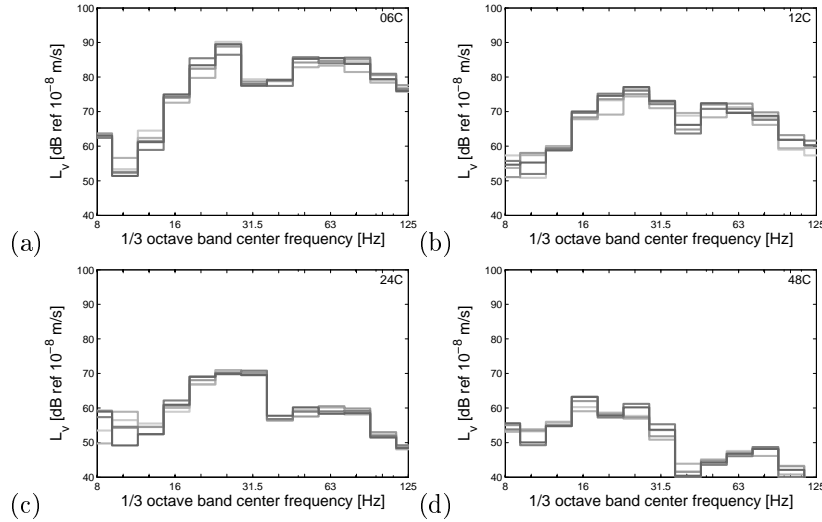


Figure 3.58: One-third octave band RMS level of the measured vertical free field velocity at line C ( $y = 0$  m) at (a) 6 m, (b) 12 m, (c) 24 m, and (d) 48 m from the track center line during the passage of 5 Thalys trains (290 – 300 km/h).

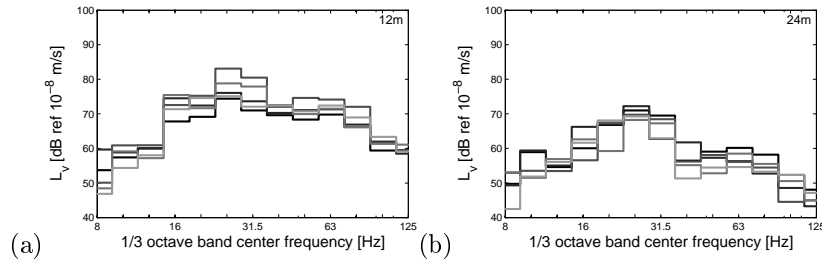


Figure 3.59: One-third octave band RMS level of the measured vertical free field velocity at five different measurement lines (grey to black lines) at (a) 12 m and (b) 24 m from the track center line during the passage of a Thalys train (300 km/h).

dominated by a broad peak around 60 Hz that is increasingly attenuated with increasing distance, whereas the spectrum of the Thalys train is dominated by the peak around 25 Hz.

The results presented in the present subsection show a reasonable agreement both for the IC train and the Thalys train. A similar accuracy has been obtained for the free field response as with the models by Lombaert and Degrande [94], where larger deviations are observed in the higher

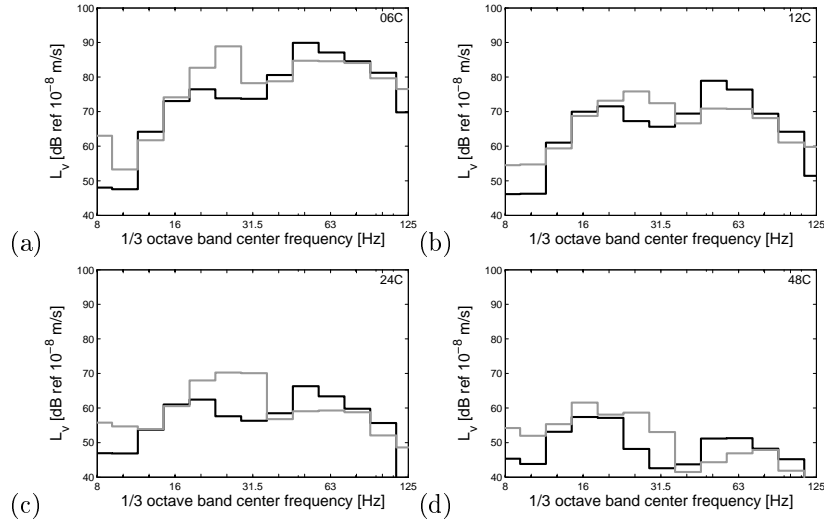


Figure 3.60: Average one-third octave band RMS level of the measured vertical free field velocity at line C ( $y = 0$  m) at (a) 6 m, (b) 12 m, (c) 24 m, and (d) 48 m from the track center line during the passage of an IC train (198 km/h, black line) and a Thalys train (300 km/h, grey line).

frequency range around 100 Hz, and by Kouroussis et al. [81], where a good correspondence between measured and predicted results is obtained up to 50 Hz. A better agreement is generally found for the rail response which is dominated by the quasi-static contribution than for the free field response which is dominated by the dynamic contribution. This is due to the fact that the dynamic axle loads are determined by the dynamic train and track characteristics and by the track unevenness, and are therefore subject to a larger uncertainty than the static axle loads. As the free field response is dominated by the dynamic contribution, an accurate identification of the unevenness and the dynamic track behavior is crucial for its accurate prediction.

The experimental results obtained at the site in Lincent clearly show a considerable variation of the response during train passages along the track, caused by variation of the track and soil characteristics and the excitation. A variation is observed as well due to different passages caused by differences in the speed, train characteristics, and wheel unevenness. Compared to this difference, a reasonable accuracy is obtained with the numerical model. A more elaborate numerical prediction should take into account the variation of these input parameters in a probabilistic approach, however, in order to compare the prediction uncertainty with the experimental results.

### 3.7 Conclusion

Within the present work, an elaborate measurement campaign has been carried out at a site in Lincent (Belgium) allowing for a step-wise validation of the different submodels of the numerical model presented in chapter 2. The validation is consecutively performed for the free field mobility, the track receptance, the track – free field mobility, and the response during railway traffic.

First, the dynamic parameters are identified for each submodel. The soil characteristics are determined by preliminary soil tests. The track characteristics are obtained from design values and are updated based on the measured track receptance. The train characteristics are based on design values as well.

Next, the numerical model is applied at the site in Lincent. First, the influence of the excavation and the track subgrade is assessed. It is shown that they have a considerable influence on the track receptance, that is mainly determined by the soil layering underneath the track. This observation allows for a simplification of the problem geometry in a prediction model that correctly accounts for the soil profile underneath the track, but avoids the need to explicitly model the excavation and track subgrade.

The (track –) free field mobility is not influenced at low frequencies where the wavelength in the soil is large compared to the dimensions of the track. At higher frequencies, the influence locally increases, which is partly due to the shift of peaks in the mobility, but generally remains limited.

Finally, the numerical model is validated based on the experimental results obtained at the site in Lincent, including the (track –) free field mobility and the response due to train passages. A considerable difference is observed at the site in Lincent between different sections along the track for the measured (track –) free field mobility (up to 10 dB) and for the measured response due to a single train passage (up to 6 dB). Furthermore, a considerable difference is observed in the free field response between different passages of the IC train (up to 14 dB) and the Thalys train (up to 6 dB) at similar speeds.

The validation of the numerical model generally shows a reasonably good agreement between the predicted and the measured results, illustrating the accuracy of both the model and the identified dynamic characteristics of the train, track, and soil.

The validation of the free field mobility shows that a better agreement is found for the vibration transfer in a direction perpendicular to the track than for

the vibration transfer in a parallel direction close to the track. This shows that the identified soil profile in the free field is not representative for the soil parameters near the track which are affected by the track subgrade. A better agreement is found in the latter case for the track – free field mobility, showing that the vibration transfer in a parallel direction close to the track is modeled more accurately when the track and the track subgrade are taken into account.

The validation of the response during train passages shows that the accuracy is slightly better for the rail response, dominated by the quasi-static excitation, than for the free field response, dominated by the dynamic excitation. This is due to the fact that the dynamic axle loads are determined by the dynamic train and track characteristics and by the track unevenness, and are therefore subject to a larger uncertainty than the static axle loads. Furthermore, the considered excitation only includes vertical rail unevenness and relies on a unevenness spectrum that is only measured reliably in a limited wavenumber range.

## Chapter 4

# Empirical methods

### 4.1 Introduction

This chapter discusses the empirical prediction of railway induced vibration. The focus is on detailed models that predict the vibration amplitude  $A(f)$  as a function of the frequency as given in equation (1.1). The prediction of the free field velocity is considered by disregarding the receiver term  $R(f)$  in equation (1.1).

In empirical models, both the source term  $S(f)$  and the propagation term or vibration transfer  $P(f)$  are determined experimentally. A distinction can be made between different empirical models based on the determination of the source term  $S(f)$ . The following two approaches are distinguished.

In the Detailed Vibration Assessment of the U.S. DOT [58, 59], hereafter referred to as the FRA procedure, equation (1.1) is applied to predict the free field vibration amplitude at a distance  $r$ , omitting the receiver term  $R(f)$ :

$$A(r, f) = S(r_0, f)P(r, f) \quad (4.1)$$

The term  $P(r, f)$  characterizing the vibration transfer between the track and a receiver at a distance  $r$  is determined from field measurements by adding contributions from different incoherent point sources on the track, leading to the so-called line source transfer mobility. The source strength  $S(r_0, f)$  or force density is determined indirectly based on equation (4.1) by dividing the ground vibration amplitude  $A(r_0, f)$  measured during a train passage at a

reference distance  $r_0$  by the propagation path term  $P(r_0, f)$  measured at the same reference distance. The force density therefore represents a normalized source strength that also depends on the reference distance  $r_0$  at which it has been determined. Extrapolation of the source strength allows for a prediction of the ground vibration amplitude at sites where the line source transfer mobility has been determined. A correction is proposed for the train speed.

In the methods by SBB [86,161] and Madshus et al. [102], the source strength  $S(f)$  in equation (4.1) is eliminated by measuring the ground vibration at a reference distance  $r_0$ . The vibration amplitude  $A(r, f)$  at a distance  $r$  is obtained as:

$$A(r, f) = A(r_0, f) \frac{P(r, f)}{P(r_0, f)} \quad (4.2)$$

where the fraction on the right hand side is the transfer ratio between the receiver point and the reference point and represents the attenuation between both points in the free field. It is determined experimentally by measuring the response at both distances during a train passage or analytically based on an attenuation law of the form  $r^{-n}$  that accounts for geometrical and material damping. In the latter case, a semi-empirical method is obtained. Different values of the exponent  $n$  are proposed based on the soil properties [86, 102]. Corrections are proposed for the train speed [102] and for the track quality [86, 102]. Again, extrapolation of the reference vibration amplitude  $A(r_0, f)$  allows for a prediction of the ground vibration amplitude at sites where the transfer ratio is known.

Both approaches are similar and characterize the source experimentally by measuring the response at a reference distance from the track. In the models by Madshus et al. and SBB, the vibration amplitude at the reference distance is directly used, whereas it is used to determine an equivalent source term in the FRA procedure. Reference distances of 3 m [86], 8 m [161], and 15 m [102] are proposed. No indication of the reference distance is provided in the FRA procedure.

In the present chapter, the application and limitations of empirical methods are investigated, focusing on the FRA procedure that is presented in more detail in section 4.2.

In equation (4.1) and equation (4.2), the free field vibration at a certain frequency  $f$  is predicted based on the product of a source term and a propagation term at the same frequency. This is strictly speaking not valid for moving sources due to the Doppler effect illustrated in equation (2.13). In



section 4.3, analytical expressions are derived for the FRA procedure based on the assumption of fixed and incoherent axle loads introduced in section 2.6.

As empirical methods fully rely on experimental data, an accurate determination of the source strength and the vibration transfer is crucial for their prediction quality. For instance, the determination of the source strength depends on the reference distance  $r_0$ . The determination of the source strength and the vibration transfer is critically assessed in sections 4.4 and 4.5, respectively.

In most empirical models, a prediction of the ground vibration is made by extrapolation of a measured source strength. The error introduced by the extrapolation is investigated in section 4.6.

The conclusion of the chapter is presented in section 4.7.

## 4.2 The FRA procedure

The FRA procedure, described in the guidance manuals of the FRA [58] and the FTA [59] is based on the empirical prediction procedure proposed by Bovey [15] and elaborated by Nelson and Saurenman [110]. Up to date, the FRA procedure is widely used in its original form [124] and is applied for the assessment of noise and vibration induced by railway traffic [146, 148, 154] and by construction activities [30, 62].

The FRA procedure predicts the one-third octave band RMS level of the ground vibration which, expressed on a dB scale, is called the vibration velocity level according to equation (2.43).

In the FRA procedure, the vibration velocity level  $L_v(\mathbf{x}')$  at a receiver point  $\mathbf{x}'$  is predicted as the sum of a force density level  $L_F(\mathbf{X}, \mathbf{x}')$  and a line source transfer mobility level  $TM_L(\mathbf{X}, \mathbf{x}')$  [58, 59]:

$$L_v(\mathbf{x}') = L_F(\mathbf{X}, \mathbf{x}') + TM_L(\mathbf{X}, \mathbf{x}') \quad (4.3)$$

where  $\mathbf{X}$  is the matrix that collects all source points used for the experimental determination. Equation (4.3) corresponds to equation (4.1) expressed on a dB scale. It is understood that the terms in equation (4.3) are one-third octave band values where the subscript  $m$  indicating the frequency band is omitted to improve readability.

The source is characterized by the force density level  $L_F(\mathbf{X}, \mathbf{x}')$  [dB ref  $1 \text{ N}/\sqrt{\text{m}}$ ] that is a measure for the force per unit length applied by the train. The

vibration transfer is characterized by the line source transfer mobility level  $\text{TM}_L(\mathbf{X}, \mathbf{x}')$  [dB ref  $10^{-8} \text{ (m/s)}/(N/\sqrt{m})$ ] that is a measure for the vibration transfer due to a line source such as a train. Both levels are determined experimentally.

The line source transfer mobility level  $\text{TM}_L(\mathbf{X}, \mathbf{x}')$  is determined based on wave propagation tests consisting of a line of source points parallel to the track, where impacts are applied and a line of receiver points perpendicular to the track, where the corresponding response is measured. Examples of the measurement setup are shown in figures 4.1 and 4.2. The one-third octave band mobility  $\langle h_{vzz}(\mathbf{x}_k, \mathbf{x}') \rangle_m$  between source point  $\mathbf{x}_k$  and receiver point  $\mathbf{x}'$  is, expressed on a dB scale, called the point source transfer mobility level  $\text{TM}_P(\mathbf{x}_k, \mathbf{x}')$  [dB ref  $10^{-8} \text{ (m/s)}/N$ ]:

$$\begin{aligned} \text{TM}_P(\mathbf{x}_k, \mathbf{x}') &= 10 \log_{10} \langle h_{vzz}(\mathbf{x}_k, \mathbf{x}') \rangle_m^2 \\ &= 10 \log_{10} \left[ \frac{1}{\omega_{2m} - \omega_{1m}} \int_{\omega_{1m}}^{\omega_{2m}} |\hat{h}_{vzz}(\mathbf{x}_k, \mathbf{x}', \omega)|^2 d\omega \right] \end{aligned} \quad (4.4)$$

where the subscript  $m$  indicating the frequency band is omitted on the left hand side to improve readability.

The line source transfer mobility level  $\text{TM}_L(\mathbf{X}, \mathbf{x}')$  is obtained by the superposition of the point source transfer mobility levels for  $n$  equidistant source points along the track with spacing  $h$ :

$$\text{TM}_L(\mathbf{X}, \mathbf{x}') = 10 \log_{10} \left[ h \sum_{k=1}^n 10^{\frac{\text{TM}_P(\mathbf{x}_k, \mathbf{x}')}{10}} \right] \quad (4.5)$$

The point source transfer mobility level  $\text{TM}_P(\mathbf{x}_k, \mathbf{x}')$  depends on the position of the source  $\mathbf{x}_k$  and receiver  $\mathbf{x}'$ . The source positions  $\mathbf{x}_k = \{x, y_k, z\}^T$  used to determine  $n$  point source transfer mobility levels are collected in the source coordinate matrix  $\mathbf{X}$ :

$$\mathbf{X} = [\mathbf{x}_1, \mathbf{x}_2, \dots, \mathbf{x}_n] \quad (4.6)$$

The number  $n$  and the spacing  $h$  of the source points  $\mathbf{x}_k$  is discussed in more detail in section 4.3. The same receiver coordinate  $\mathbf{x}' = \{x', y', z'\}^T$  is used for all point source transfer mobility levels.

The force density level  $L_F(\mathbf{X}, \mathbf{x}')$  is obtained indirectly from equation (4.3) by subtracting the line source transfer mobility level  $\text{TM}_L(\mathbf{X}, \mathbf{x}')$  from the

vibration velocity level  $L_v(\mathbf{x}')$  measured during a train passage:

$$L_F(\mathbf{X}, \mathbf{x}') = L_v(\mathbf{x}') - TM_L(\mathbf{X}, \mathbf{x}') \quad (4.7)$$

resulting in a normalized force density level that characterizes the source strength of the train passage. Due to the indirect determination, the force density level  $L_F(\mathbf{X}, \mathbf{x}')$  depends on the position  $\mathbf{x}'$  where the response is measured and the position  $\mathbf{X}$  where the impacts are applied for the determination of the line source transfer mobility level. The dependency of the force density level  $L_F(\mathbf{X}, \mathbf{x}')$  on the source and receiver position is discussed in more detail in section 4.5.

In order to normalize the force density level to a reference train speed, a correction is proposed by assuming that the force density level is proportional to  $20 \log_{10}(v)$ . This relation is based on empirical data for trains in the speed range from 80 to 240 km/h [58]. The dependency on the train speed  $v$  is caused by the influence it has on the unevenness spectrum, as illustrated in equation (2.15), and therefore also depends on the level of unevenness excitation in the corresponding wavenumber range. It does not account for the effect of parametric excitation, however. The theoretical dependency is found to be  $25 \log_{10}(v)$  based on the PSD of Braun and Hellenbroich [16] or  $30 \log_{10}(v)$  based on the PSD of Hamid and Yang [56]. Measurements show that the dependency on the train speed is generally lower [94]. A speed dependency of  $18 \log_{10}(v)$  to  $22 \log_{10}(v)$  is proposed by Madshus et al. [102], while a dependency of  $10 \log_{10}(v)$  to  $15 \log_{10}(v)$  has recently been measured for HSTs [117]. The speed dependency strongly depends on the characteristics of the track [117] and the soil [102]. Wrongly estimating the speed dependency may provoke errors up to 4 dB when it is used to correct of a large difference in train speeds [117].

As in most empirical models, a prediction with the FRA procedure is based on the extrapolation of a measured force density level between two sites. A distinction is made between the assessment site (site 1), where a prediction of the vibration velocity level is required, and the measurement site (site 2), where the force density level is measured. A prediction of the vibration velocity level  $L_v^1(\mathbf{x}'_1)$  at the assessment site is obtained by introducing equation (4.7), applied on the measurement site, in equation (4.3), applied on the assessment site:

$$L_v^1(\mathbf{x}'_1) = L_v^2(\mathbf{x}'_2) - TM_L^2(\mathbf{X}_2, \mathbf{x}'_2) + TM_L^1(\mathbf{X}_1, \mathbf{x}'_1) \quad (4.8)$$

where the superscripts 1 and 2 indicate the site where the measurement has been carried out,  $\mathbf{X}_1$  and  $\mathbf{x}'_1$  are the source and receiver points used at site 1,

and  $\mathbf{X}_2$  and  $\mathbf{x}'_2$  are the source and receiver points used at site 2. The location of the source points  $\mathbf{X}_1$  and  $\mathbf{X}_2$  at both sites should be identical but depends on the specific situation at both sites. In the following, two cases are elaborated.

First, consider the case in figure 4.1 where a track is present at site 1 but new rolling stock will be used. The vibration velocity level  $L_v^1(\mathbf{x}'_1)$  due to the new rolling stock can therefore not be measured directly at site 1. As a track is present at site 1, however, the line source transfer mobility level  $TM_L^1(\mathbf{X}_1, \mathbf{x}'_1)$  can be determined at this site with source points  $\mathbf{X}_1$  at the track (figure 4.1a). A prediction of the vibration velocity level  $L_v^1(\mathbf{x}'_1)$  with equation (4.8) is based on the extrapolation of a force density level measured at site 2. Therefore, the vibration velocity level  $L_v^2(\mathbf{x}'_2)$  due to a similar train passage is measured at site 2 and the line source transfer mobility level  $TM_L^2(\mathbf{X}_2, \mathbf{x}'_2)$  is determined with source points  $\mathbf{X}_2$  at the track as well (figure 4.1b).

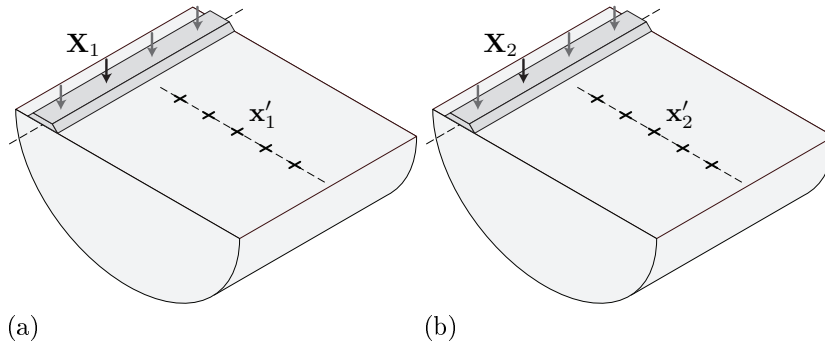


Figure 4.1: Position of the source and receiver points at (a) the assessment site and (b) the measurement site for the case where a track is present at the assessment site.

Second, consider the case in figure 4.2 where a new track will be built at site 1. As no track is present, the line source transfer mobility level  $TM_L^1(\mathbf{X}_1, \mathbf{x}'_1)$  at site 1 is determined with source points  $\mathbf{X}_1$  at the soil's surface (figure 4.2a). A prediction of the vibration velocity level  $L_v^1(\mathbf{x}'_1)$  with equation (4.8) is again based on the extrapolation of a force density level measured at site 2. Therefore, the vibration velocity level  $L_v^2(\mathbf{x}'_2)$  due to a similar train passage is measured at site 2. The line source transfer mobility level  $TM_L^2(\mathbf{X}_2, \mathbf{x}'_2)$  should be determined with source points  $\mathbf{X}_2$  at the soil's surface adjacent to the track (figure 4.2b), corresponding to the source points  $\mathbf{X}_1$  at site 1 (figure 4.2a). In this case, an equivalent force density level is obtained at site 2, that represents the equivalent line source that has to be applied at the corresponding source points to result in the same vibration velocity level as for the train passage.

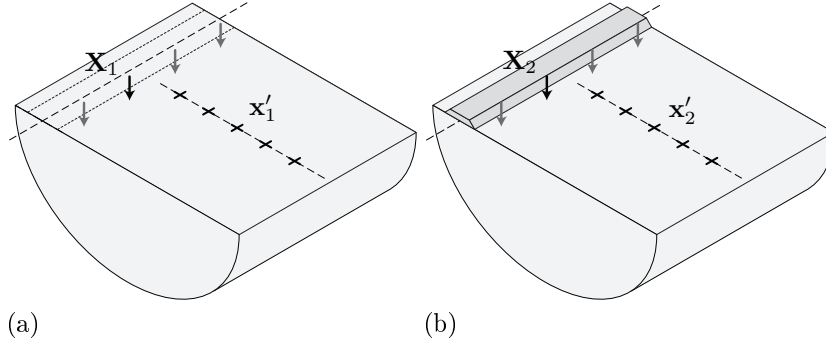


Figure 4.2: Position of the source and receiver points at (a) the assessment site and (b) the measurement site for the case where no track is present at the assessment site.

A more detailed description of the source points at the track or at the soil's surface is given in section 4.4.

### 4.3 Analytical expressions for the empirical model

As in most empirical models, the free field vibration amplitude at a frequency  $f$  is predicted in the FRA procedure as the product of a source term and a vibration transfer at the same frequency  $f$ , as illustrated in equation (4.1). It has been shown in equation (2.13) that this is not valid for moving sources due to the frequency shift between source and receiver caused by the Doppler effect. In section 2.6, however, it is shown that a reasonable estimate of the one-third octave band velocity level is obtained when fixed and incoherent axle loads are assumed. This observation allows to derive analytical expressions for the force density level and the line source transfer mobility level.

Based on equation (2.51), the RMS velocity  $v_{z\text{RMS}m}(\mathbf{x}')$  during a train passage can be computed based on the PSD  $\hat{S}_{g_z}(\omega)$  of the axle loads and the transfer functions  $\hat{h}_{vzz}(\mathbf{x}_k, \mathbf{x}', \omega)$  between source points  $\mathbf{x}_k$  and receiver points  $\mathbf{x}'$ :

If the transfer function  $\hat{h}_{vzz}(y - y_{k0}, \omega)$  between the  $k$ -th axle load at position  $\mathbf{x}_k$  and the receiver point  $\mathbf{x}'$  is indicated as  $\hat{h}_{vzz}(\mathbf{x}_k, \mathbf{x}', \omega)$ , equation (2.51) is

rewritten as:

$$v_{z\text{RMS}m}^2(\mathbf{x}') = \int_{\omega_{1m}}^{\omega_{2m}} \hat{S}_{g_z}(\omega) \sum_{k=1}^{n_a} |\hat{h}_{vzz}(\mathbf{x}_k, \mathbf{x}', \omega)|^2 d\omega \quad (4.9)$$

In equation (4.9), the term  $\hat{S}_{g_z}(\omega)$  corresponds to the PSD of the load of a single uncoupled axle and represents the average PSD of all axles of the train.

The terms characterizing the source and the propagation path in equation (4.9) are separated by replacing the square of the transfer function  $|\hat{h}_{vzz}(\mathbf{x}_k, \mathbf{x}', \omega)|^2$  by its average value within each frequency band  $[\omega_{1m}, \omega_{2m}]$ :

$$v_{z\text{RMS}m}^2(\mathbf{x}') = \int_{\omega_{1m}}^{\omega_{2m}} \hat{S}_{g_z}(\omega) d\omega \times \sum_{k=1}^{n_a} \frac{1}{\omega_{2m} - \omega_{1m}} \int_{\omega_{1m}}^{\omega_{2m}} |\hat{h}_{vzz}(\mathbf{x}_k, \mathbf{x}', \omega)|^2 d\omega \quad (4.10)$$

The first integral on the right hand side of equation (4.10) represents the square of the RMS value  $g_{z\text{RMS}m}$  of the axle loads and the term behind the summation on the right hand side of equation (4.10) represents the square of the one-third octave band mobility as determined in equation (2.36).

$$v_{z\text{RMS}m}^2(\mathbf{x}') = g_{z\text{RMS}m}^2 \sum_{k=1}^{n_a} \langle h_{vzz}(\mathbf{x}_k, \mathbf{x}') \rangle_m^2 \quad (4.11)$$

When expressed on a dB scale, equation (4.11) has a similar form as equation (4.3) of the FRA procedure. In the FRA procedure, however, the force density level represents a source strength per unit length and the line source transfer mobility level represents the vibration transfer due to a line source. This is obtained by introducing the train length  $L_t$  and the number of axles  $n_a$  in equation (4.11):

$$L_v(\mathbf{x}') = 10 \log_{10} \left[ \frac{n_a}{L_t} g_{z\text{RMS}m}^2 \right] + 10 \log_{10} \left[ \frac{L_t}{n_a} \sum_{k=1}^{n_a} \langle h_{vzz}(\mathbf{x}_k, \mathbf{x}') \rangle_m^2 \right] \quad (4.12)$$

The first term on the right hand side of equation (4.12) represents the total energy  $n_a g_{z\text{RMS}m}^2$  of all axles distributed over the train length  $L_t$  and

corresponds to the force density level:

$$L_F = 10 \log_{10} \left[ \frac{n_a}{L_t} g_{zRMSm}^2 \right] \quad (4.13)$$

The force density level in equation (4.13) represents the force per unit length that is applied by the axles at the wheel/rail contact point at a fixed position. In contrast with the force density level that is determined indirectly based on measurements, it does not depend on the source and receiver distance.

The second term on the right hand side of equation (4.12) corresponds to the line source transfer mobility level:

$$TM_L(\mathbf{X}, \mathbf{x}') = 10 \log_{10} \left[ \frac{L_t}{n_a} \sum_{k=1}^{n_a} 10^{\frac{TM_P(\mathbf{x}_k, \mathbf{x}')}{10}} \right] \quad (4.14)$$

where  $TM_P(\mathbf{x}_k, \mathbf{x}')$  represents the point source transfer mobility level as defined in equation (4.4).

The ratio between the sum and the number of axles  $n_a$  on the right hand side of equation (4.14) is the average value of the transferred vibration energy for all axles, each represented by an impact at position  $\mathbf{x}_k$ . The vibration transfer due to a line source is obtained by multiplying this average vibration transfer with the train length  $L_t$ .

The line source transfer mobility level can be determined using different source locations  $\mathbf{x}_k$  along the track. This is illustrated in figure 4.3 where a stretch of the track with length  $L_t$  is considered for a train with eight axles, corresponding to two carriages. In figure 4.3a,  $n_a$  sources are considered at the axle locations, corresponding to equation (4.14). Alternatively,  $n_b = n_a/2$  sources are located at the center of each bogie as shown in figure 4.3b. The vibration transfer for a single source point is affected by its exact position. It can be expected, however, that the average transfer for a long train is relatively insensitive to the exact positions of the axles, so that it can also be represented by  $n_a$  equidistant source points, as shown in figure 4.3c.

Furthermore, as the ratio of the sum and the number of axles  $n_a$  on the right hand side of equation (4.14) is the average value of the vibration transfer, it is not strongly affected by a change of the number  $n_a$  of considered source points. An arbitrarily chosen number of  $n$  source locations with spacing  $h$  can be used to represent the line source with length  $L_t$  as shown in figure 4.3d, provided that the sampling of the line source is sufficiently dense. When the spacing  $h = L_t/n$  is introduced in equation (4.14), expression (4.5) is obtained.

An alternative approach is proposed in the FRA procedure [58], where two edge points are considered as shown in figure 4.3e and a different spacing  $h' = n/(n-1)h$  is used. The contribution of the edge points is only accounted for half according to the trapezoidal rule:

$$\begin{aligned} \text{TM}_L(\mathbf{X}, \mathbf{x}') = 10 \log_{10} & \left[ h' \left( \frac{1}{2} 10^{\frac{\text{TMP}(\mathbf{x}_1, \mathbf{x}')}{10}} + 10^{\frac{\text{TMP}(\mathbf{x}_2, \mathbf{x}')}{10}} + \dots \right. \right. \\ & \left. \left. + 10^{\frac{\text{TMP}(\mathbf{x}_{n-1}, \mathbf{x}')}{10}} + \frac{1}{2} 10^{\frac{\text{TMP}(\mathbf{x}_n, \mathbf{x}')}{10}} \right) \right] \end{aligned} \quad (4.15)$$

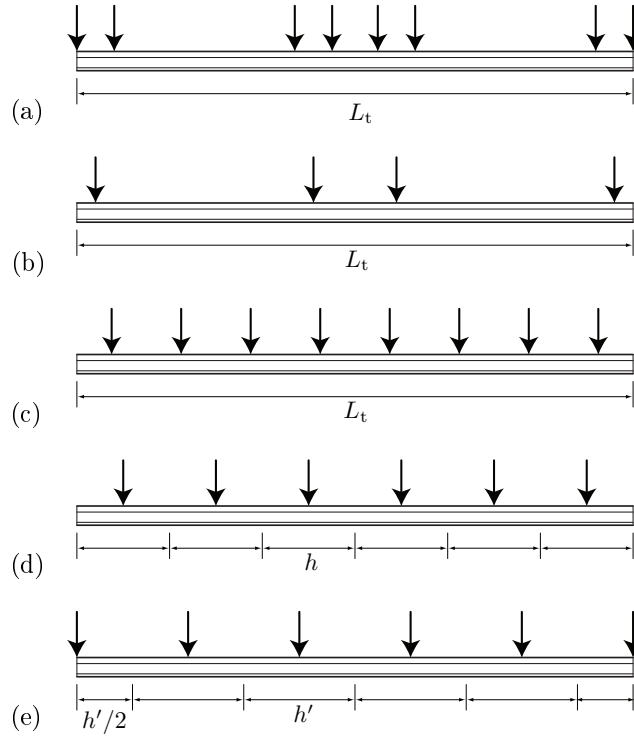


Figure 4.3: Location of the source points for the determination of the line source transfer mobility level with (a)  $n_a$  source points corresponding to the axle locations, (b)  $n_b$  source points corresponding to the bogie locations, (c)  $n_a$  equidistant source points, (d)  $n$  equidistant source points with spacing  $h$ , and (e)  $n$  equidistant source points with spacing  $h'$  including two edge points.



Equation (4.13) and equation (4.14) offer analytical expressions for the force density level and the line source transfer mobility level, respectively. In equation (4.13), the force density level is related directly to the axle loads that are applied to the track at the wheel/rail contact point. This force density level can be used in combination with a line source transfer mobility level  $TM_L(\mathbf{X}, \mathbf{x}')$  that is determined with source points at the head of both rails. For other locations of the source points, a different line source transfer mobility level is obtained that can no longer be used in combination with the force density level in equation (4.13). The position of the source points is investigated in more detail in section 4.4.

The derivation of the analytical expressions reveals another important aspect of the empirical FRA procedure. As shown in the previous derivation, analytical expressions can be derived for the FRA procedure based on the assumption of fixed and incoherent axle loads. This means that when the force density level is determined indirectly according to equation (4.7) by subtracting the line source transfer mobility level from the measured vibration level due to a moving train, in fact an equivalent fixed line source is determined that results in the same vibration level as the moving train. As the assumption of fixed and incoherent axle loads only holds approximately, the determination of the equivalent fixed line source depends on the receiver point as well.

In the following sections, the experimental determination of the line source transfer mobility level and the force density level is discussed in more detail and the effect of the position of the source and receiver is investigated.

#### 4.4 Determination of the line source transfer mobility level

As empirical prediction methods fully rely on measured data, a correct determination of the terms describing the source and the propagation path is of the greatest importance. In the present section the experimental determination of the line source transfer mobility level is discussed for the particular case of the site in Lincent, presented in chapter 3. The determination of the force density level is discussed in the next section.

First, the determination of the line source transfer mobility level is investigated by means of a numerical simulation based on model D (figure 3.21d), taking into account the excavation and the track subgrade. The dynamic train, track, and soil characteristics have been presented in chapter 3. Second, the experimental

results obtained at the site in Lincent are used to assess the determination of the line source transfer mobility level experimentally.

As discussed in section 4.2, the determination of the line source transfer mobility level  $TM_L(\mathbf{X}, \mathbf{x}')$  is based on wave propagation tests and requires a number of source points  $\mathbf{x}_k$  and a receiver point  $\mathbf{x}'$ . Whereas the choice of the receiver point  $\mathbf{x}'$  is mainly governed by the purpose of the measurement, e.g. the determination of a force density level at a reference distance or the prediction of a vibration velocity level at a certain distance in the free field, the source points  $\mathbf{x}_k$  should be chosen such that the line source transfer mobility level accurately represents the transfer from a line load on the track to the free field. The influence of the position of the source points on the line source transfer mobility level is addressed in the present section.

#### 4.4.1 Numerical assessment

##### Equidistant source points

As discussed in section 4.3, the line source transfer mobility level can be determined by means of source points at the axle locations (figure 4.3a) corresponding to expression (4.14) or by means of equidistant source points (figure 4.3d) corresponding to expression (4.5).

Figure 4.4 compares the line source transfer mobility level determined with source locations corresponding to the axles of a Thalys train with the line source transfer mobility level determined with the same number of equidistant source points covering the same length as the Thalys train. Relocating the source positions mainly affects the line source transfer mobility level close to the track. This is due to the fact that the line source transfer mobility level is mainly determined here by the source points close to the receiver line where the influence of the exact source location on the source–receiver distance is larger, particularly at higher frequencies. At a larger distance from the track, the influence is very small. At all distances, the influence is limited to 6 dB at most. It is concluded that for the considered train type, equidistant source points accurately represent the line source.

##### Sampling of the line source

The accurate determination of the line source transfer mobility level requires the measurement of the transfer function for a sufficiently large number of source points along the track. The determination of the transfer function at

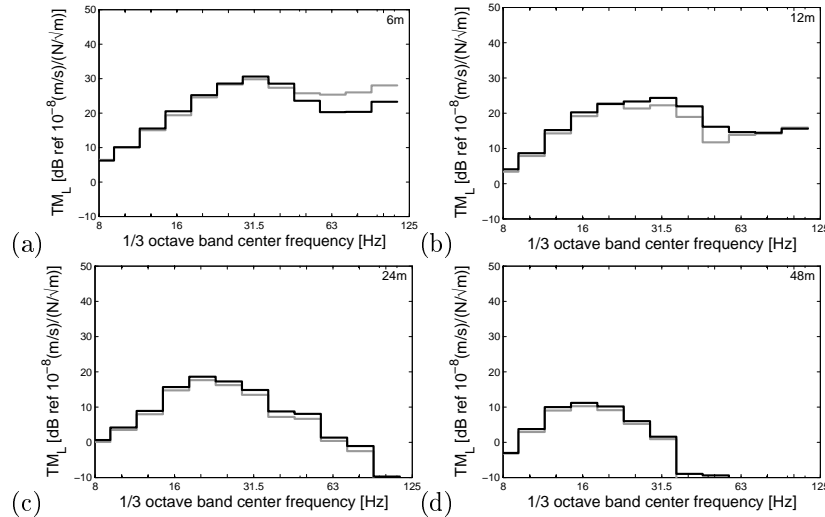


Figure 4.4: Predicted line source transfer mobility level at (a) 6 m, (b) 12 m, (c) 24 m, and (d) 48 m determined with source points corresponding to the axle locations of a Thalys train (grey line) and with equidistant points with a source length of 202 m and a source point spacing of 7.76 m (black line).

each source point is time consuming, however. An accurate measurement of each transfer function requires a large number of impacts  $N$  or a high level of excitation  $\hat{S}_{ii}(\omega)$ , as shown in equation (3.3) and equation (3.4). Whereas impact devices such as falling weights provide a high impact load, they generally require a large installation effort and are not very well suited to apply impacts at a large number of source points. Impact devices such as hammers are better suited to apply impacts at a large number of source points, but they generally provide a smaller impact load and require a large number of impacts to obtain an accurate measurement. In both cases, it is advantageous to reduce the number of source points.

As discussed in section 4.3, an arbitrary number  $n$  of equidistant source points can be used to determine the line source transfer mobility level (figure 4.3d). It is investigated which number of source points is required for an accurate characterization of the line source.

The FRA manual [58] suggests to use an impact point spacing from 3 m to 6 m, requiring 33 to 67 source points to represent a line source with a length of 200 m corresponding to the Thalys train. Figure 4.5 compares the predicted line source transfer mobility level for a line source with a length of 200 m determined with a source point spacing of 3 m, 6 m, 10 m, 20 m, and 40 m. The spacing of

the source points mainly affects the line source transfer mobility level close to the track, where a spacing of 40 m no longer results in a good agreement. This is due to the larger influence of the exact location of the source point on the source–receiver distance for receivers close to the track. For all other values considered in the simulation, however, the effect is relatively small and a good agreement is found at all distances.

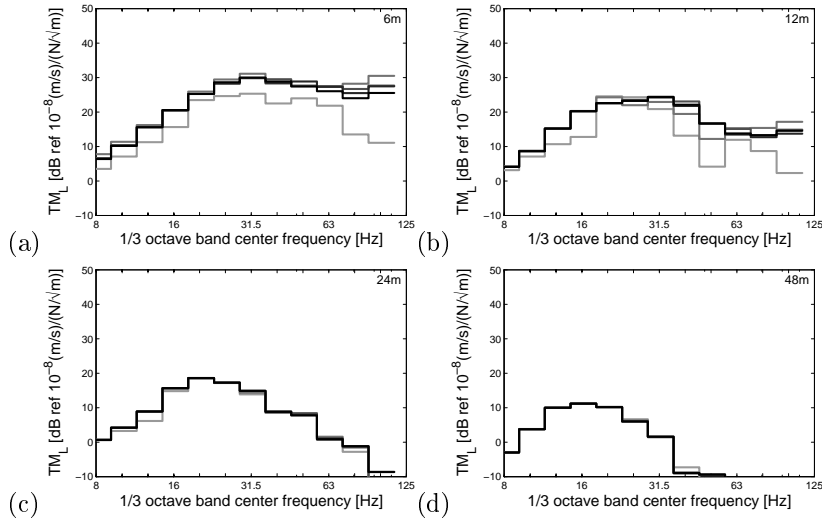


Figure 4.5: Predicted line source transfer mobility level at (a) 6 m, (b) 12 m, (c) 24 m, and (d) 48 m for a source length of 200 m and a source point spacing of 40 m, 20 m, 10 m, 6 m, and 3 m (grey to black lines).

As shown in equation (4.14), the line source transfer mobility level contains the information on the source length and is determined by source points that cover the entire length  $L_t$ . It is expected that the source points at a larger distance from the receiver line contribute less to the line source transfer mobility level and can therefore be omitted without strongly affecting the result. A smaller source length is hence obtained which reduces the required number of source points.

Figure 4.6 compares the predicted line source transfer mobility level for a source length of 200 m, 180 m, 160 m, 140 m, 120 m, and 100 m determined with a source point spacing of 10 m. Close to the track, the length of the source is large compared to the distance from the track and the result is dominated by the contribution of sources close the receiver line. The effect of the source length is therefore negligible. At a larger distance from the track, the contribution of source points at a larger distance from the receiver line becomes slightly more important, in particular at low frequencies where the effect of attenuation

with distance is smaller. The effect is limited to 4 dB at very low frequencies, however. The line source of 200 m is accurately represented by the line source of 100 m, allowing for a substantial reduction of the required number of source points.

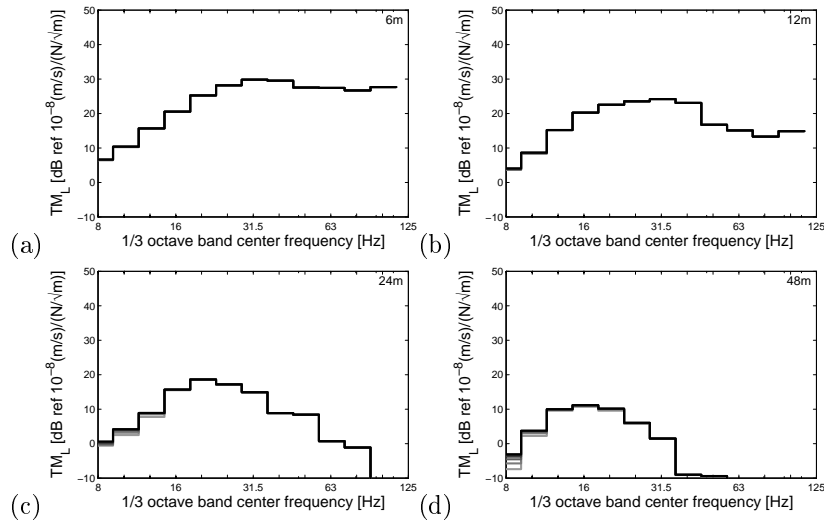


Figure 4.6: Predicted line source transfer mobility level at (a) 6 m, (b) 12 m, (c) 24 m, and (d) 48 m for a source length of 100 m, 120 m, 140 m, 160 m, 180 m, and 200 m (grey to black lines) and a source point spacing of 10 m.

### Position of the source point

The line source transfer mobility level is determined by means of impacts at the track or at the soil's surface, depending on the specific cases discussed in section 4.2. The influence of the exact position of the source point on the line source transfer mobility level is discussed in the following. Figure 4.7 shows a number of source positions at the track.

As the axle loads are applied at the wheel/rail contact point, i.e. the head of both rails, the prediction of the free field response requires the transfer functions determined with source points at both rails (RB). In an experimental setup, this could be obtained by applying a simultaneous impact at both rails, e.g. by mounting a falling weight on a stiff beam exciting both rails. An impact force equally distributed over both rails applies a symmetric excitation to the track. Alternatively, the transfer function with source point at both rails is obtained as the superposition of half of the transfer functions with source points at the

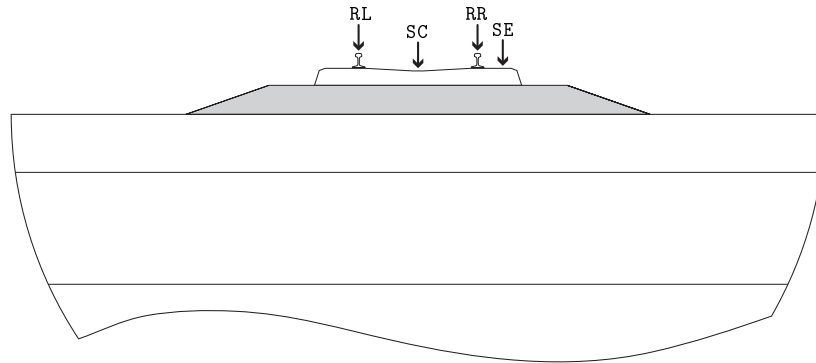


Figure 4.7: Position of the source point at the head of the right rail (RR) and the left rail (RL), at the edge of the sleeper (SE), and at the center of the sleeper (SC).

left rail (RL) and the right rail (RR), hence requiring the determination of two transfer functions.

Alternatively, a symmetric excitation of the track is obtained by applying an impact at the center of the sleeper (SC), whereas the track is excited asymmetrically by applying an impact at the edge of the sleeper (SE). The difference between source points at the rail and at the sleeper is that the influence of the rail and rail pad is disregarded in the latter.

It has been shown in subsection 3.4.4 that the dynamic track behavior is strongly influenced by the loading conditions (figure 3.28), as they substantially affect the dynamic properties of the rail pad and the ballast. The track – free field mobility is relatively insensitive to the dynamic track characteristics in the frequency range of interest [149], however, such that the effect of the preload on the track – free field mobility is relatively small. The determination of the line source transfer mobility level can therefore generally be carried out without preloading the track.

All previous source positions require access to the track which is not always possible, e.g. before the construction of a new track or during operation of an existing track. If necessary, the line source transfer mobility level is determined with source points at the soil's surface, as discussed in section 4.2. This is generally carried out by applying impacts to a foundation which is installed at the soil's surface. Figure 4.8 shows a number of source points at the soil's surface.

Prior to the construction of a new track, the foundation can be installed at

the soil's surface at the track center line (FC). When a track is present, the foundation has to be installed adjacent to the track at a distance  $d$  from the track center line (FA).

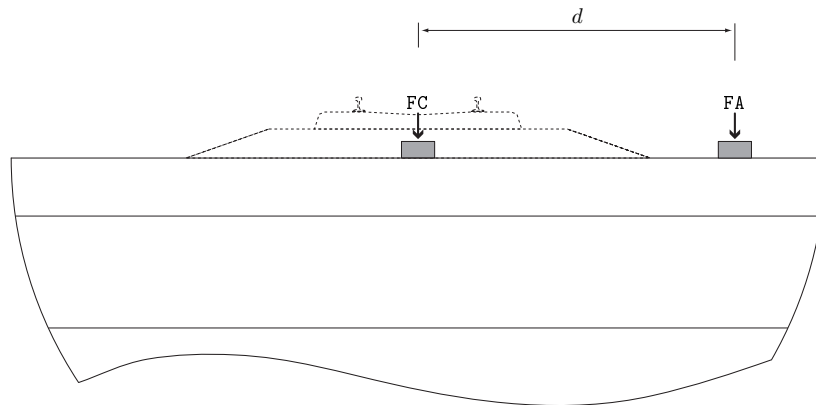


Figure 4.8: Position of the source point at a foundation installed at the soil's surface at the center line of the future track (FC) or adjacent to the track (FA).

At the site in Lincent, the impacts at the track are applied at the edge of the sleeper (SE) and the impacts at the soil's surface are applied adjacent to the track (FA) at a distance  $d = 5.05$  m from the track center line (figure 3.11). The same receiver points are used in both cases (figure 3.11), resulting in a smaller source–receiver distance in the case of source points at the soil's surface.

In the following, the influence of the exact position of the source point on the line source transfer mobility level is investigated in different steps by comparing the predicted line source transfer mobility levels determined with different source points. The line source transfer mobility level is determined with a source length of 200 m and a source point spacing of 10 m.

Figure 4.9 compares the line source transfer mobility level determined with source points at the right rail (RR) and at both rails (RB). The first case corresponds to an asymmetric load distribution and results in a translation and rotation of the sleeper, whereas the second case corresponds to a symmetric load distribution and only results in a translation of the sleeper (figure 2.5). At low frequencies, the wavelength in the soil is large compared to the sleeper length and the difference between both cases is small. At a frequency of 25 Hz, the sleeper length is approximately equal to half the wavelength in the top layer of the soil. Above this frequency, the rotation of the sleeper affects the line source transfer mobility level and results in a difference up to 6 dB.

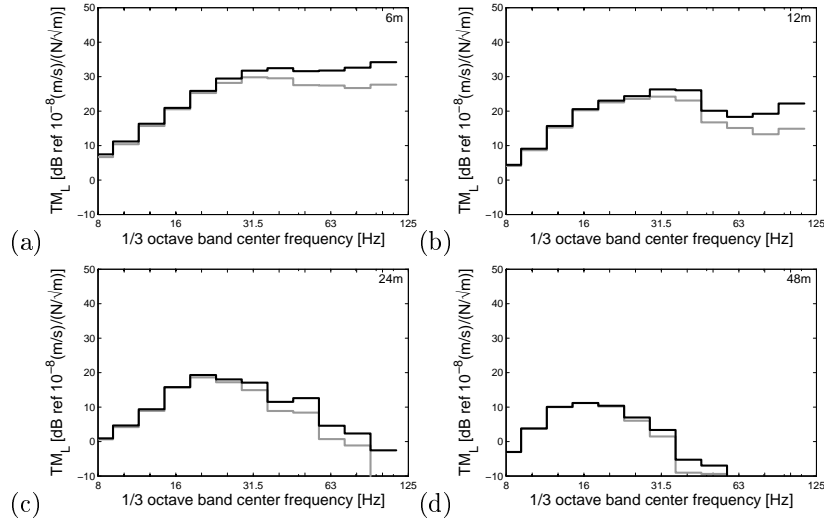


Figure 4.9: Predicted line source transfer mobility level at (a) 6 m, (b) 12 m, (c) 24 m, and (d) 48 m determined with source points  $X_{RR}$  at the right rail (black line) and  $X_{RB}$  at both rails (grey line).

Figure 4.10 compares the line source transfer mobility level determined with source points at both rails (RB) and at the center of the sleeper (SC). As both source positions result in a symmetric loading of the track, the only difference between both source points is the effect of taking into account the rail and rail pad in the first case.

The rail pad allows for the distribution of the load from the rail to the sleeper and isolates the rail from the track structure at frequencies above the resonance of the rail on the rail pad. As this resonance occurs at a frequency far above the frequency range of interest, the force applied at the rail is transmitted quasi-statically to the sleeper. The difference between both source positions is therefore negligible in the considered frequency range, as shown in figure 4.10.

The influence of the source point on the line source transfer mobility level is investigated experimentally in subsection 4.4.2. As the transfer functions have been measured by means of source points at the edge of the sleeper, the difference between source points at both rails (RB) and at the edge of the sleeper (SE) is first assessed numerically in figure 4.11. Both source points are different due to the symmetric (RB) and asymmetric (SE) excitation. Furthermore, the rail and rail pad are taken into account in the first case (RB), whereas they are disregarded in the second case (SE). As discussed in the previous, a much larger influence is due to the difference between a symmetric and asymmetric



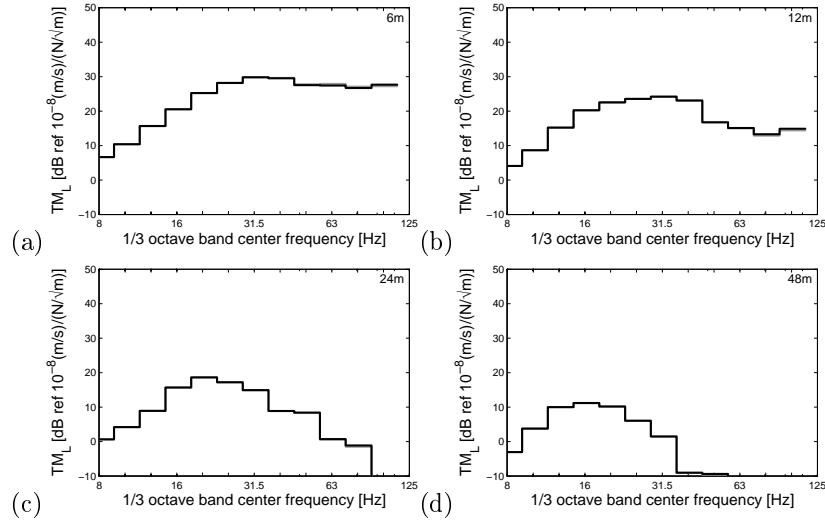


Figure 4.10: Predicted line source transfer mobility level at (a) 6 m, (b) 12 m, (c) 24 m, and (d) 48 m determined with source points  $\mathbf{X}_{RB}$  at both rails (black line) and  $\mathbf{X}_{SC}$  at the center of the sleeper (grey line).

load application and the difference in figure 4.11 is mainly determined by this effect.

Figure 4.12 compares the line source transfer mobility level determined with source points at both rails (RB) and at the soil's surface at the track center line (FC). While the dynamic track–soil interaction is taken into account in the first case, it is disregarded in the second case. The effect of the track–soil interaction on the transfer function is described as the track filtering effect and has been illustrated in section 2.5.2. Below 20 Hz, the effect of track–soil interaction is negligible. Above 20 Hz, the track filtering effect reduces the line source transfer mobility level leading to a difference up to 10 dB. The track filtering effect is observed at all distances from the track and slightly decreases with increasing distance. This is due to the shift of characteristic peaks and troughs averaged within each frequency band as explained in section 2.5.2.

As it is not possible to apply an excitation at the soil's surface at the track center line when a track is present, an impact can be applied at the soil's surface at a distance  $d$  from the track center line (FA). When the receiver is shifted over the same distance, the source–receiver distance remains unaffected and this case corresponds to the case of source points at the soil's surface at the track center line (FC), provided that the site has a horizontal soil stratification.

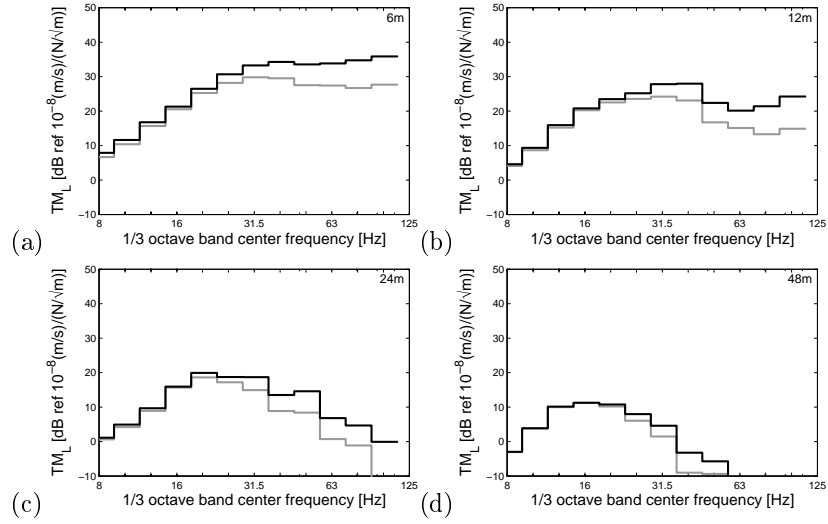


Figure 4.11: Predicted line source transfer mobility level at (a) 6 m, (b) 12 m, (c) 24 m, and (d) 48 m determined with source points  $\mathbf{X}_{RB}$  at both rails (grey line) and  $\mathbf{X}_{SE}$  at the edge of the sleeper (black line).

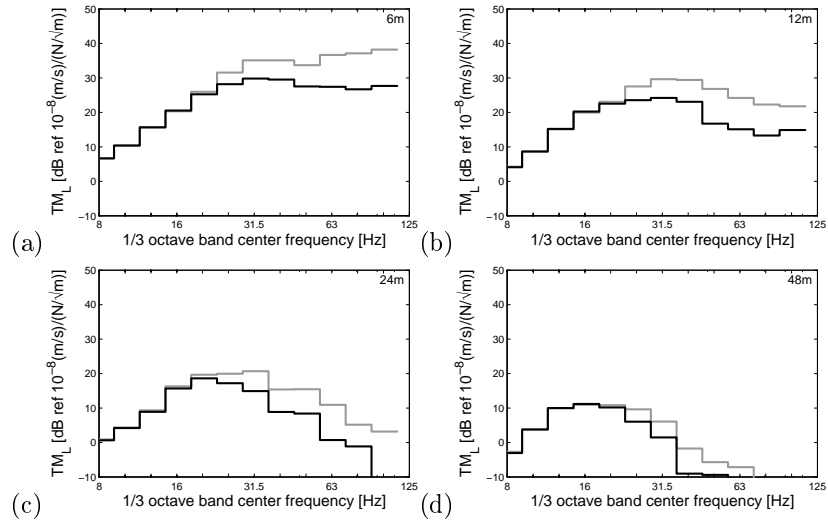


Figure 4.12: Predicted line source transfer mobility level at (a) 6 m, (b) 12 m, (c) 24 m, and (d) 48 m determined with source points  $\mathbf{X}_{RB}$  at both rails (black line) and  $\mathbf{X}_{FC}$  at the soil's surface at the track center line (grey line).

At the site in Lincent, the line source transfer mobility level has been determined with source points at the soil's surface at a distance  $d = 5.05$  m from the track center line while the same receiver points are used as for source points at the edge of the sleeper (figure 3.11). This results in a different source–receiver distance that additionally affects the line source transfer mobility level. The effect of a modified source–receiver distance is shown in figure 4.13 by comparing the predicted line source transfer mobility levels determined with source points  $\mathbf{X}_{FC}$  at the soil's surface at the track center line and  $\mathbf{X}_{FA}$  at the soil's surface adjacent to the track. The difference is larger for receivers close to the track, as the shift of the source point has a larger effect on the source–receiver distance for these receivers.

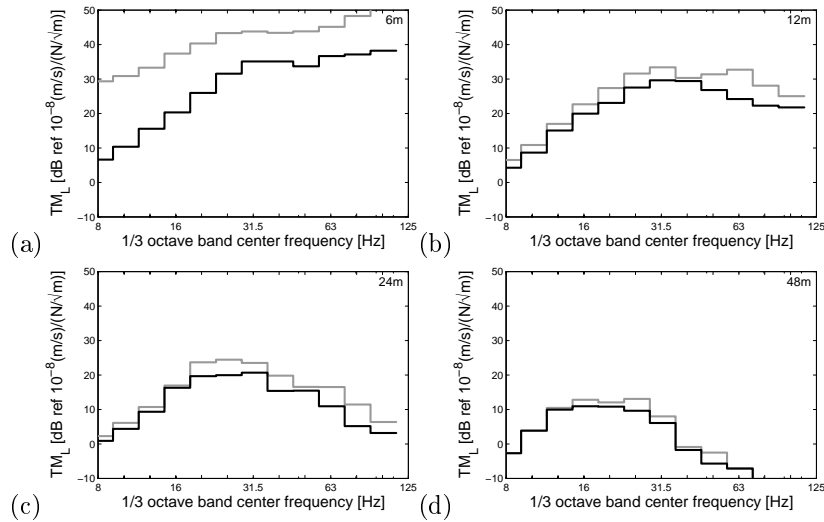


Figure 4.13: Predicted line source transfer mobility level at (a) 6 m, (b) 12 m, (c) 24 m, and (d) 48 m determined with source points  $\mathbf{X}_{FC}$  at the soil's surface at the track center line (black line) and  $\mathbf{X}_{FA}$  at the soil's surface adjacent to the track (grey line).

It is noted that the large difference for the receiver at 6 m is mainly due to the source point at  $y = 0$  m, for which the source–receiver distance is less than 1 m. As can be expected, the effect on the line source transfer mobility level decreases with increasing distance from the track. At 48 m, only a difference up to 3 dB is observed.

## 4.4.2 Experimental assessment

During the measurement campaign in Lincent, the transfer functions have been measured for source points at the edge of the sleeper (SE) from  $y = -100$  m to  $y = 100$  m with a spacing of 10 m (21 source locations) and at the soil's surface adjacent to the track (FA) from  $y = -80$  m to  $y = 80$  m with a spacing of 10 m (17 source locations) allowing to assess the influence of the sampling of the line source and the position of the source point experimentally.

### Sampling of the line source

Figure 4.14 compares the measured line source transfer mobility level for a line source with a length of 200 m determined with a source point spacing of 10 m, 20 m, and 40 m. The experimental assessment confirms that the spacing of the source points mainly affects the line source transfer mobility level close to the track where a spacing of 40 m no longer results in a good agreement, as observed in the numerical assessment as well. The results obtained with a spacing of 20 m and 10 m show a good agreement at all distances.

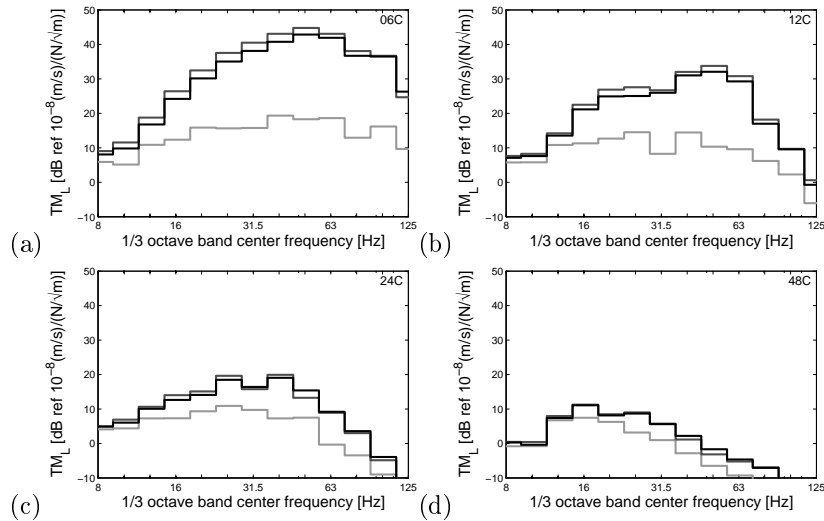


Figure 4.14: Measured line source transfer mobility level at (a) 6 m, (b) 12 m, (c) 24 m, and (d) 48 m determined with source points  $\mathbf{X}_{SE}$  at the edge of the sleeper for a source length of 200 m and a source point spacing of 40 m, 20 m, and 10 m (grey to black lines).

Figure 4.15 compares the measured line source transfer mobility level for a source length of 200 m, 180 m, 160 m, 140 m, 120 m, and 100 m determined with a source point spacing of 10 m. The results again confirm the observation made in the numerical assessment. Close to the track, the influence is negligible, while a limited influence is observed at a large distance.

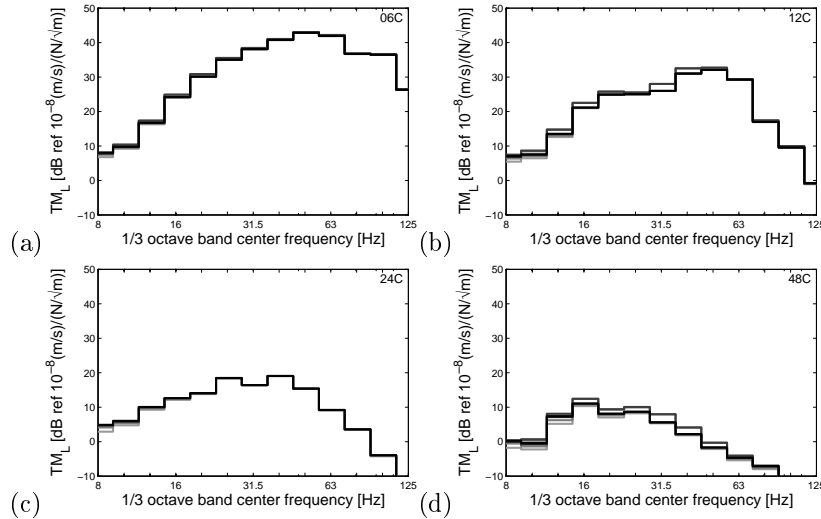


Figure 4.15: Measured line source transfer mobility level at (a) 6 m, (b) 12 m, (c) 24 m, and (d) 48 m determined with source points  $\mathbf{X}_{SE}$  at the edge of the sleeper for a source length of 100 m, 120 m, 140 m, 160 m, 180 m, and 200 m (grey to black lines) and a source point spacing of 10 m.

The numerical and experimental assessment show that a line source of 200 m is still accurately represented by a line source of length 100 m, while a source point spacing of 20 m is sufficiently dense. It can be concluded that an accurate representation of a line source is already obtained at the site in Lincent with 6 source points between  $y = -50$  m and  $y = 50$  m with a spacing of 20 m.

### Position of the source point

The line source transfer mobility level has been determined at the site in Lincent for source points at the edge of the sleeper and at the soil's surface adjacent to the track. Figure 4.16 shows both line source transfer mobility levels determined with a source length of 160 m and a source point spacing of 10 m. The difference between both line source transfer mobility levels is determined by the combined effect of the asymmetric loading of the track, the track filtering,

and the modified source–receiver distance, as previously discussed. As observed in the numerical simulation, the modified source–receiver distance has the strongest influence on the line source transfer mobility level, particularly at a small distance from the track.

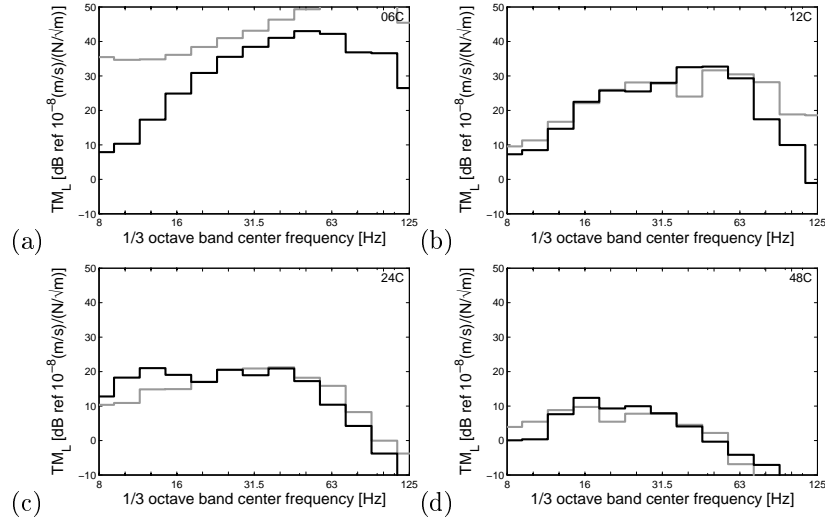


Figure 4.16: Measured line source transfer mobility level at (a) 6 m, (b) 12 m, (c) 24 m, and (d) 48 m determined with source points  $\mathbf{X}_{SE}$  at the edge of the sleeper (black line) and  $\mathbf{X}_{FA}$  at the soil's surface adjacent to the track (grey line).

It is observed in figure 4.16 that the difference between both line source transfer mobility levels decreases with increasing distance from the track. At a distance larger than 24 m, the difference is limited to 6 dB at most. This means that the line source transfer mobility level determined with source points at the edge of the sleeper can be approximated at larger distances by using source points at the soil's surface adjacent to the track, without the need for access to the track. It is noted that the difference in figure 4.16c below 20 Hz is mainly due to the smaller accuracy of the measured transfer functions at low frequencies as discussed in subsection 3.3.3. Furthermore, a smaller difference is expected when the effect of the modified source–receiver distance is eliminated by moving the receiver points over the same distance as the source points. This requires a horizontally invariant problem domain, however.

## 4.5 Determination of the force density level

The present section focuses on the determination of the force density level. This is discussed for the particular case of the site in Lincent based on numerical simulations and experimental results.

According to equation (4.7), the force density level is determined indirectly based on the free field vibration velocity level measured during a train passage and the line source transfer mobility level determined at the same site. The force density level  $L_F(\mathbf{X}, \mathbf{x}')$  is influenced by the position of the source points  $\mathbf{X}$  used for the determination of the line source transfer mobility level as well as by the position of the receiver point  $\mathbf{x}'$ . The influence of the position of the source and receiver on the force density level is assessed numerically and experimentally. The line source transfer mobility level is determined with a source length of 200 m and a source point spacing of 10 m in the numerical assessment and with a source length of 160 m and a source point spacing of 10 m in the experimental assessment.

### 4.5.1 Numerical assessment

#### Reference distance

Due to the different nature of dynamic and quasi-static excitation, as given in equation (2.12) and equation (2.11), the quasi-static contribution in the free field due to a fixed source cannot be cast into the form of equation (2.46). In contrast to the dynamic response, the quasi-static response measured at a small distance from the track can therefore not be extrapolated to other distances based on the transfer function.

It is investigated for which receiver distance  $\mathbf{x}'$  the quasi-static excitation contributes to the free field response. Figure 4.17 shows the predicted force density level for an IC train at a speed of 198 km/h based on the response at different distances from the track. The force density level based on the dynamic contribution only is indicated as well to illustrate the influence of the quasi-static excitation.

At 6 m from the track, the quasi-static excitation influences the force density level only at frequencies below 10 Hz. At larger distances, the force density level coincides with the force density level based on the dynamic contribution and the effect of quasi-static excitation is negligible in the frequency range of interest. When the force density level determined based on the response at 6 m is used to predict the response at a larger distance, it will result in an overestimation

of the response below 10 Hz. At higher distances and higher frequencies, the quasi-static contribution is negligible, allowing for a valid extrapolation of the force density level to other receiver distances.

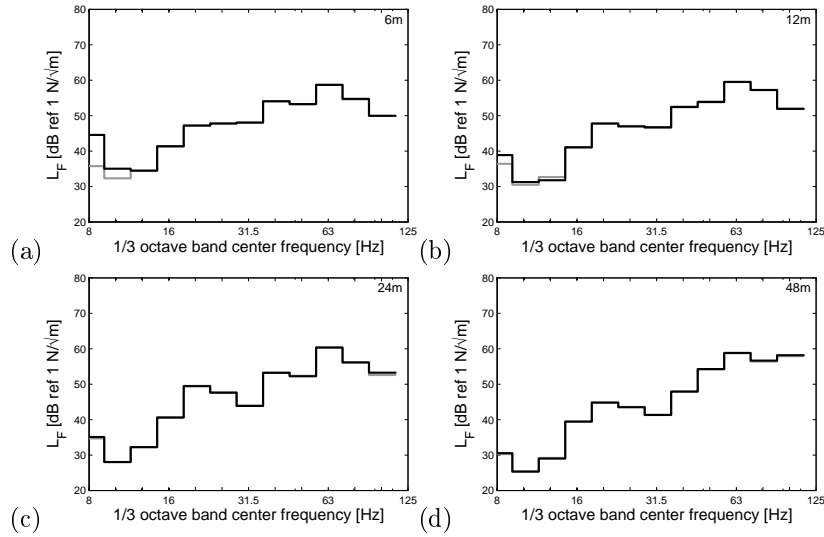


Figure 4.17: Predicted force density level based on the total response (black line) and the dynamic contribution (grey line) at (a) 6 m, (b) 12 m, (c) 24 m, and (d) 48 m for an IC train (198 km/h).

### Position of the source point

It has been shown in section 4.4 that the line source transfer mobility level  $TM_L(\mathbf{X}, \mathbf{x}')$  is affected by the position  $\mathbf{X}$  of the source points. Due to the indirect determination of the force density level according to equation (4.7), the effect of the source position on the force density level  $L_F(\mathbf{X}, \mathbf{x}')$  is exactly the same. This means that a different force density level is obtained when different source positions are used. This is illustrated in figure 4.18 that compares the force density level determined with source points at both rails (RB) and at the soil's surface at the track center line (FC) and adjacent to the track (FA).

The difference between source points at both rails and at the soil's surface at the track center line is caused by the track–soil interaction. As source points at both rails result in a lower value of the line source transfer mobility level (figure 4.12), they result in a higher value of the force density level at frequencies above 20 Hz.



In case of source points adjacent to the track, an additional difference is introduced due to the modified source–receiver distance that decreases with increasing distance. As source points adjacent to the track result in a higher value of the line source transfer mobility level (figure 4.13), they result in a lower value of the force density level.

These results clearly show that a different force density level is obtained for different source positions. It is very important that each force density level is combined with a line source transfer mobility level determined with the same source points in order to correctly predict the free field vibration level.

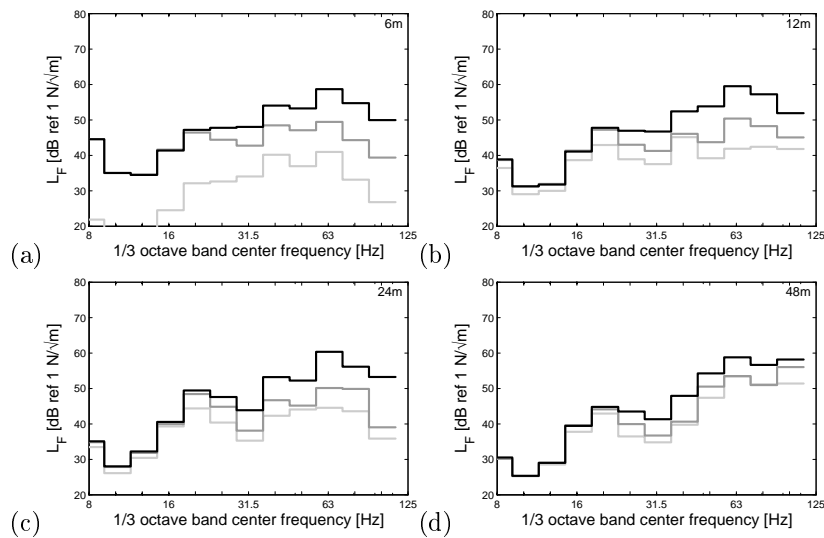


Figure 4.18: Predicted force density level based on the response at (a) 6 m, (b) 12 m, (c) 24 m, and (d) 48 m for an IC train (198 km/h) determined with source points  $\mathbf{X}_{RB}$  at both rails (black line),  $\mathbf{X}_{FC}$  at the soil's surface at the track center line (dark grey line) and  $\mathbf{X}_{FA}$  at the soil's surface adjacent to the track (light grey line).

### Location of the receiver point

As discussed in section 4.3, the force density level  $L_F(\mathbf{X}, \mathbf{x}')$  represents an equivalent fixed line source that results in the same free field vibration velocity level as the train passage. The assumption of fixed axle loads only holds approximately, however, due to the Doppler effect that results in a shift of the frequency between the source and the receiver, as explained in equation (2.13). Furthermore, the force density level is affected by the exact position of

the point loads used to determine the line source transfer mobility level that are assumed to be at a fixed instead of a moving position. The equivalent fixed line source is therefore affected by the receiver distance  $\mathbf{x}'$  at which it is determined.

The influence of the receiver distance is investigated in figures 4.19 and 4.20. In the case of source points  $\mathbf{X}_{\text{RB}}$  at both rails (figure 4.19a), the difference between the force density levels determined at several distances from the track is caused by the Doppler effect, resulting in a shift of the frequency between the source and the receiver. The shifted peaks and troughs in the narrow band spectrum are averaged within each frequency band and no clear trend in function of the receiver distance is observed in the one-third octave band spectrum in figure 4.19a. The results shows that a mismatch up to 10 dB is expected when a force density level  $L_{\text{F}}(\mathbf{X}_{\text{RB}}, \mathbf{x}'_1)$  determined at a receiver  $\mathbf{x}'_1$  is used to predict the vibration velocity level  $L_{\text{v}}(\mathbf{x}'_2)$  at a different receiver  $\mathbf{x}'_2$ .

Based on equation (4.7), a force density level  $L_{\text{F}}(\mathbf{X}_1, \mathbf{x}')$  determined with source points  $\mathbf{X}_1$  can be related to the force density level  $L_{\text{F}}(\mathbf{X}_{\text{RB}}, \mathbf{x}')$  determined with source points  $\mathbf{X}_{\text{RB}}$  at both rails as follows:

$$L_{\text{F}}(\mathbf{X}_1, \mathbf{x}') = L_{\text{F}}(\mathbf{X}_{\text{RB}}, \mathbf{x}') + \text{TM}_{\text{L}}(\mathbf{X}_{\text{RB}}, \mathbf{x}') - \text{TM}_{\text{L}}(\mathbf{X}_1, \mathbf{x}') \quad (4.16)$$

As the source point  $\mathbf{X}_{\text{RB}}$  at both rails corresponds to the wheel/rail contact point, the force density level  $L_{\text{F}}(\mathbf{X}_{\text{RB}}, \mathbf{x}')$  only depends on the receiver distance due to the Doppler effect, as previously described. For other source points  $\mathbf{X}_1$ , the force density level  $L_{\text{F}}(\mathbf{X}_1, \mathbf{x}')$  is additionally affected by difference  $\text{TM}_{\text{L}}(\mathbf{X}_{\text{RB}}, \mathbf{x}') - \text{TM}_{\text{L}}(\mathbf{X}_1, \mathbf{x}')$ .

Figure 4.19b shows the influence of the receiver distance on the force density level determined with source points  $\mathbf{X}_{\text{RR}}$  at the right rail. In this case, an asymmetric load is applied to the track and the difference  $\text{TM}_{\text{L}}(\mathbf{X}_{\text{RB}}, \mathbf{x}') - \text{TM}_{\text{L}}(\mathbf{X}_{\text{RR}}, \mathbf{x}')$  corresponds to the difference due to symmetric and asymmetric loading of the track observed in figure 4.9. As this difference only slightly changes in function of the distance from the track, the influence of the receiver on the force density level only slightly increases and is similar as for the force density level determined with source points at both rails (figure 4.19a).

Figure 4.20a shows the influence of the receiver on the force density level determined with source points  $\mathbf{X}_{\text{FC}}$  at the soil's surface at the track center line. The difference  $\text{TM}_{\text{L}}(\mathbf{X}_{\text{RB}}, \mathbf{x}') - \text{TM}_{\text{L}}(\mathbf{X}_{\text{FC}}, \mathbf{x}')$  is now additionally affected by the track filtering effect observed in figure 4.12. The track filtering effect slightly decreases with increasing distance from the track so that a small trend in function of the receiver distance is observed in figure 4.20a in the higher

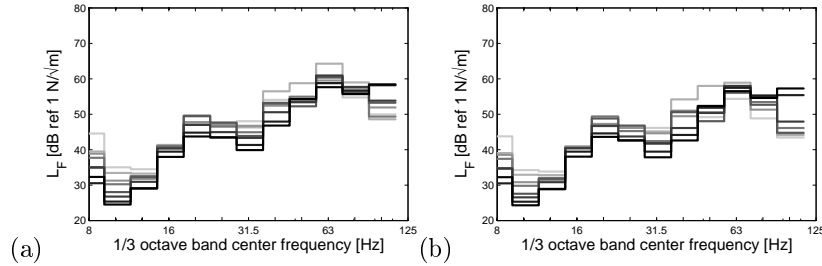


Figure 4.19: Predicted force density level based on the response at 6 m to 64 m (grey to black lines) for an IC train (198 km/h) determined with source points (a)  $\mathbf{X}_{RB}$  at both rails and (b)  $\mathbf{X}_{RB}$  at the right rail.

frequency range. The influence of the receiver on the force density level is slightly higher compared to source points at both rails (figure 4.19a).

Finally, figure 4.20b shows the influence of the receiver on the force density level determined with source points  $\mathbf{X}_{FA}$  at the soil’s surface adjacent to the track. Compared to the previous case, the difference  $TM_L(\mathbf{X}_{RB}, \mathbf{x}') - TM_L(\mathbf{X}_{FA}, \mathbf{x}')$  is additionally affected by the modified source–receiver distance that has a strong effect on the line source transfer mobility level, as observed in figure 4.13, and hence on the force density level as well. As this effect is strongly influenced by the distance from the track, a clear trend in function of the receiver is now observed in the force density level in figure 4.20b, particularly in the higher frequency range. The difference between the force density levels increases up to 20 dB for different receiver positions.

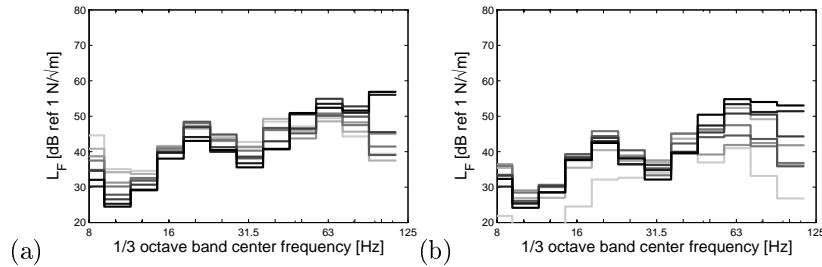


Figure 4.20: Predicted force density level based on the response at 6 m to 64 m (grey to black lines) for an IC train (198 km/h) determined with source points (a)  $\mathbf{X}_{FC}$  at the soil’s surface at the track center line and (b)  $\mathbf{X}_{FA}$  at the soil’s surface adjacent to the track.

The previous results show that the force density level is affected by the position of the receiver point at which it is determined. A prediction of the vibration

velocity level  $L_v(\mathbf{x}')$  at a receiver point  $\mathbf{x}'$  should therefore be made based on a force density level  $L_F(\mathbf{X}, \mathbf{x}')$  determined at the same receiver point  $\mathbf{x}'$ . This is particularly true in the case of source points  $\mathbf{X}_{FC}$  and  $\mathbf{X}_{FA}$  at the soil's surface at the track center line and adjacent to the track, respectively, as the influence of the receiver on the force density level is stronger and shows a more clear trend in these cases. In the case of source points at the track, particularly for source points  $\mathbf{X}_{RB}$  at both rails, a less clear trend and a smaller influence are observed. Source points at both rails should therefore be used in order to limit the effect of the receiver on the force density level.

### 4.5.2 Experimental assessment

The determination of the force density level is now assessed based on the data measured at the site in Lincent. First, it is investigated which difference arises when the force density level is measured at a different line along the track or for a different train passage. Next, the influence of the source and receiver point is assessed experimentally.

#### Position of the measurement line

Figure 4.21 compares the measured force density level at different lines based on the response at 12 m and 24 m from the track. The location of the source points is adapted for each line source transfer mobility level so that the line source is centered around the corresponding measurement line. At 12 m, a difference up to 12 dB is observed for different measurement lines, while at 24 m the difference is generally smaller. Even within a relatively small track section at the same site, a relatively large difference is observed in the experimental force density level.

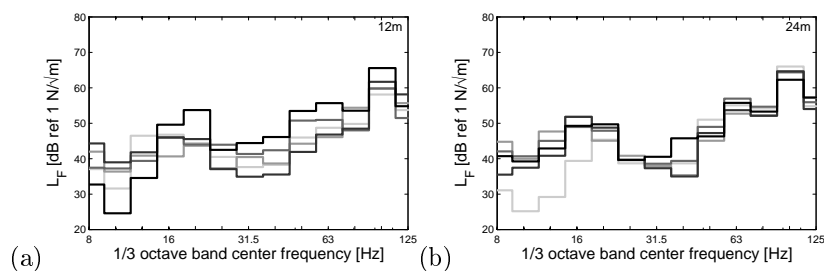


Figure 4.21: Measured force density level based on the response at five different measurement lines (grey to black lines) at (a) 12 m and (b) 24 m from the track for an IC train (198 km/h).

### Different passages of the same train type

Since a large number of train passages has been recorded, the variation of the force density level between different passages can be assessed. Figure 4.22 shows the force density level determined for 12 passages of IC trains within a limited speed range between 192 and 200 km/h. At low frequencies the variation between different train passages is limited to around 4 dB, while at higher frequencies the variation increases up to 12 dB, especially at larger distances from the track. The variation between the passages is due to differences in speed, train characteristics, and excitation due to wheel unevenness.

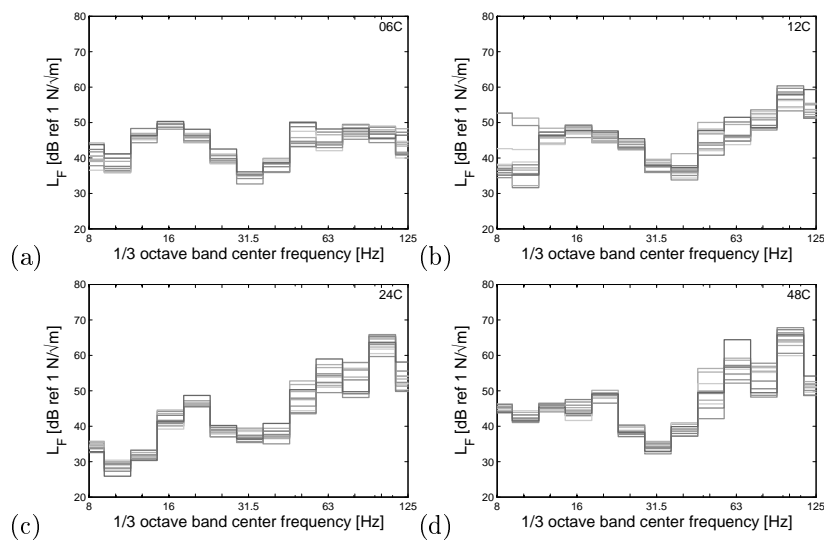


Figure 4.22: Measured force density level based on the response at (a) 6 m, (b) 12 m, (c) 24 m, and (d) 48 m for 12 IC trains (192 – 200 km/h) (grey to black lines).

The relatively large difference that is obtained for different train passages (figure 4.22) and at different measurement lines (figure 4.21) illustrates the uncertainty that can be expected in the experimental determination of the force density level. The observed difference up to 12 dB shows that an often desired prediction accuracy of 6 dB is unlikely to be obtained in empirical prediction models.

### Position of the source point

The line source transfer mobility level has been determined at the site in Lincent by means of impacts at the edge of the sleeper as well as at the soil's surface adjacent to the track, allowing to determine the force density level due to a train passage for both cases.

Figure 4.23 shows the difference between the measured force density levels determined with source points at the edge of the sleeper (SE) and at the soil's surface adjacent to the track (FA). As neither of these source points corresponds to the wheel/rail contact point, these force density levels represent the equivalent line load at the corresponding source point that results in the same vibration velocity level as the train passage. The difference between both force density levels is due to the combined effect of the asymmetric loading of the track, the track filtering, and the modified source–receiver distance, as discussed in subsection 4.4.1, and is particularly high close to the track. This means that the position of the source should be taken into account in a prediction with the FRA procedure by combining a force density level  $L_F(\mathbf{X}, \mathbf{x}')$  with a line source transfer mobility level  $TM_L(\mathbf{X}, \mathbf{x}')$  determined with the same source points  $\mathbf{X}$ .

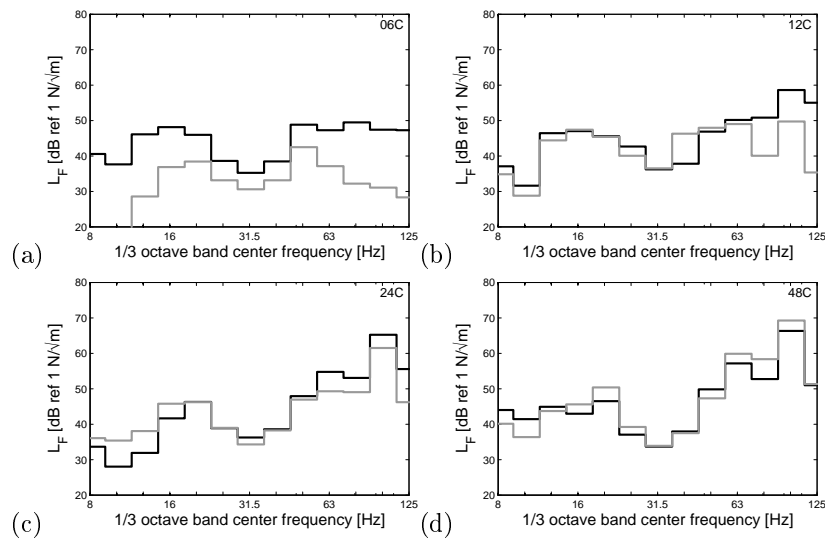


Figure 4.23: Measured force density level based on the response at (a) 6 m, (b) 12 m, (c) 24 m, and (d) 48 m for an IC train (198 km/h) determined with source points  $\mathbf{X}_{SE}$  at the edge of the sleeper (black line) and  $\mathbf{X}_{FA}$  at the soil's surface adjacent to the track (grey line).

At distances larger than 24 m from the track, the difference between both force density levels is relatively small, in particular when it is compared to the difference that is observed between the experimental force density levels (figures 4.21 and 4.22). Although these force density levels represent the equivalent fixed line load at a different source position, this observation allows to use the force density level determined with source points at the soil's surface adjacent to the track as an approximation for the force density level determined with source points at the edge of the sleeper. This is very useful, since in the first case no access to the track is required. If possible, however, the same source points for the force density level and line source transfer mobility level should be used so that this difference is eliminated.

### **Location of the receiver point**

The influence of the receiver point on the force density level is investigated experimentally in figure 4.24 that compares the measured force density level based on the response at different distances from the track. Two cases are considered. In the first case, the force density level is determined with source points  $\mathbf{X}_{SE}$  at the edge of the sleeper (figure 4.24a) and a difference is observed up to 10 dB. In the higher frequency range, the force density level decreases with increasing distance which is partly due to the asymmetric loading of the track as observed in the predicted results (figure 4.19b).

In the second case, the force density level is determined with source points  $\mathbf{X}_{FA}$  at the soil's surface adjacent to the track (figure 4.24b) and a much larger difference is observed, mainly caused by the modified source–receiver distance as illustrated by the numerical simulations in subsection 4.5.2. A clear trend is now observed that shows an increase of the force density level measured at an increasing distance from the track, similar as for the predicted results (figure 4.20b). The comparison of the predicted (figure 4.20b) and measured force density levels (figure 4.24b) shows a difference in absolute levels but a similar dependency on the distance.

Although a difference is observed in the case for source points at the edge of the sleeper, it is generally of the same order of magnitude as the difference that is observed between the experimental force density levels (figures 4.21 and 4.22) and no clear trend in function of the distance is observed. As previously stated, the force density level should be determined with source points at the track (preferably at both rails) in order to limit the influence of the receiver point.

In the case of source points at the soil's surface adjacent to the track, a clear trend in function of the distance and much larger differences are observed. It

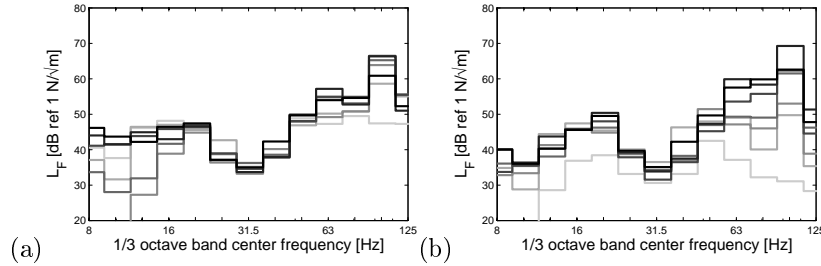


Figure 4.24: Measured force density level based on the response at 6 m to 64 m (grey to black lines) for an IC train (198 km/h) determined with source points (a)  $\mathbf{X}_{SE}$  at the edge of the sleeper and (b)  $\mathbf{X}_{FA}$  at the soil's surface adjacent to the track.

is therefore not valid to use the force density level  $L_F(\mathbf{X}_{FA}, \mathbf{x}'_1)$  determined at a receiver point  $\mathbf{x}'_1$  to predict the vibration velocity level  $L_v(\mathbf{x}'_2)$  at a different receiver point  $\mathbf{x}'_2$ . This means that the force density level should be determined at each receiver distance where a prediction is required.

## 4.6 Influence of the track and soil characteristics on the force density level

As discussed in section 4.2, the vibration velocity level is predicted in the FRA procedure based on the extrapolation of a force density level from a measurement site to an assessment site. The present section investigates the influence of the soil and track characteristics on the extrapolated force density level.

The force density level is influenced by the train characteristics such as the unsprung mass, the suspension, and the wheel unevenness. The uncertainty that can be expected in the measured force density level for different passages of the same train type has been demonstrated in figure 4.22.

Furthermore, the force density level is influenced by the track and the soil conditions. The measured result is affected by the track type (e.g. ballasted tracks or slab tracks), the presence of vibration mitigation measures, (e.g. soft rail pads, under sleeper pads, or ballast mats), the rail unevenness, the track subgrade (e.g. sub-ballast, soil improvement), and the soil conditions.

As this force density level is influenced by the train, track, and soil characteristics, it is crucial for an accurate prediction that the force density level



is determined at a measurement site with similar conditions as the assessment site. This is an important limitation of empirical methods, as a representative measurement site is not always available. In the following, the force density level is predicted numerically for different track and soil characteristics to illustrate how a mismatch between the conditions at the measurement and assessment site will affect the prediction accuracy.

#### 4.6.1 Influence of the soil characteristics

The vibration velocity level is predicted for to the passage of an IC train (table 3.5) running at a speed of 200 km/h on a classical ballasted track (table 2.3) by means of the numerical model presented in chapter 2.

The track is supported by a halfspace, considering three different soil types representing a soft, medium, and stiff soil in order to assess the influence of the soil. The soil properties are summarized in table 4.1.

Soil type	$C_s$ [m/s]	$C_p$ [m/s]	$\beta_s$ [-]	$\beta_p$ [-]	$\rho$ [kg/m <sup>3</sup> ]
Soft	100	200	0.025	0.025	1800
Medium	200	400	0.025	0.025	1800
Stiff	400	800	0.025	0.025	1800

Table 4.1: Dynamic characteristics of the three soil types.

The considered excitation mechanisms are quasi-static and dynamic excitation. An unevenness sample is generated from the PSD according to FRA class 3 [56].

Figure 4.25 shows the predicted vibration velocity level due to the IC train passage for three different soil types. The response is influenced by the soil stiffness through the dynamic axle loads and through the track – free field transfer function.

The dynamic axle loads are partly determined by the track compliance and hence by the soil stiffness, as explained in subsection 2.5.3. This results in a shift of the frequency at which the resonance of the unsprung mass on the track occurs and, given the excitation amplitude in the corresponding frequency range, may result in a higher or lower axle load.

The track – free field transfer function is affected by the soil properties by means of two mechanisms. First, the track filtering effect, described in section 2.5.2, reduces the transfer function. As this reduction depends on the ratio of the

width of the track and the wavelength in the soil, it is more important at higher frequencies and for soft soils. Second, the track – free field transfer function also decreases with increasing distance from the track due to the attenuation in the soil determined by geometrical and material damping. The attenuation due to material damping depends on the ratio of the distance and the wavelength in the soil, so that it is more important at higher frequencies and for soft soils.

The attenuation with distance is observed in the response in figure 4.25, where the highest response is found for the soft soil close to the track and for the stiff soil at a larger distance from the track.

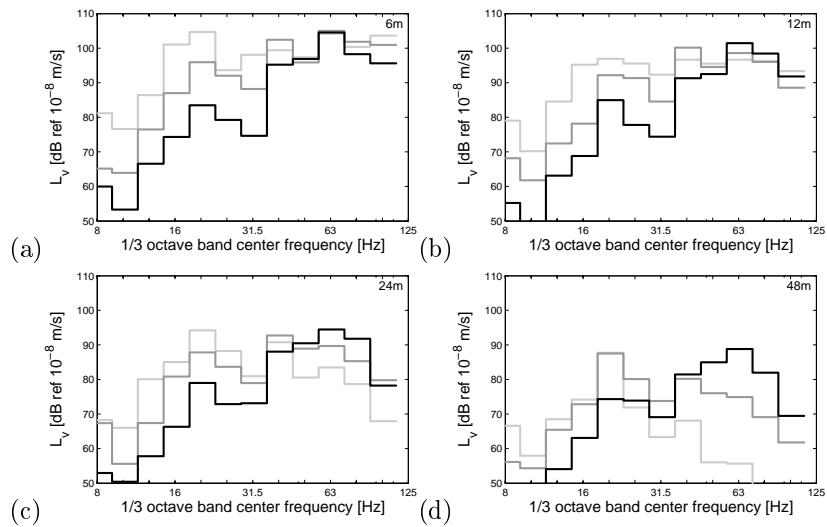


Figure 4.25: Predicted vibration velocity level at (a) 6 m, (b) 12 m, (c) 24 m, and (d) 48 m for an IC train (200 km/h) at a site with soft, medium, and stiff soil (grey to black lines).

In the next step, the line source transfer mobility level is computed for each soil type both for source points  $\mathbf{X}_{RB}$  at both rails and for source points  $\mathbf{X}_{FC}$  at the soil's surface at the track center line. By comparing these source points, the effects of asymmetrical loading of the track (figure 4.9) and a modified source–receiver distance (figure 4.13) are eliminated. The only difference between both source positions is determined by the track filtering effect which is discussed in the following. The line source transfer mobility levels are determined with a source length of 200 m and a source point spacing of 10 m.

Figure 4.26 compares the predicted line source transfer mobility level determined with source points at both rails which is, as expected, strongly influenced by the soil stiffness. At low frequencies and close to the track, the highest

response is obtained for the soft soil. As previously described, the vibration is attenuated more strongly with increasing distance at higher frequencies and for soft soils.

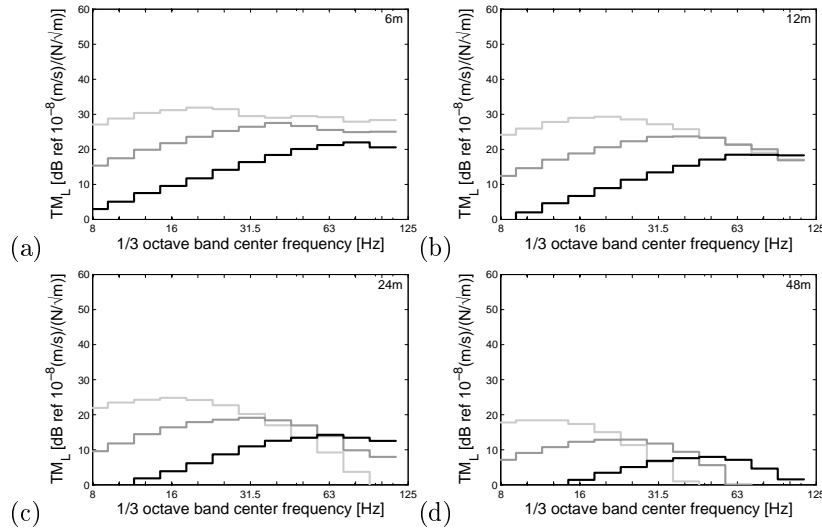


Figure 4.26: Predicted line source transfer mobility level at (a) 6 m, (b) 12 m, (c) 24 m, and (d) 48 m at a site with soft, medium, and stiff soil (grey to black lines) determined with source points  $\mathbf{X}_{RB}$  at both rails.

Figure 4.27 compares the predicted line source transfer mobility level determined with impacts at the soil’s surface. As the track filtering effect is not accounted for, the decrease at higher frequencies is smaller compared to the case of source points at both rails. The difference between the line source transfer mobility levels determined with source points at both rails (figure 4.26) and at the soil’s surface (figure 4.27) is exactly determined by the track filtering effect. By comparing both results, it is observed that the track filtering is indeed stronger for soft soils.

The force density level is computed based on equation (4.7) as the difference of the previously shown vibration velocity level and line source transfer mobility level. Both cases of source points at both rails and at the soil’s surface are considered.

Figure 4.28 compares the predicted force density levels determined with source points at both rails. As previously discussed, the free field vibration velocity level is affected by the soil properties in two ways. First, the soil properties affect the track stiffness and hence the dynamic axle loads. Second, the soil properties affect the track – free field transfer function due to the track filtering

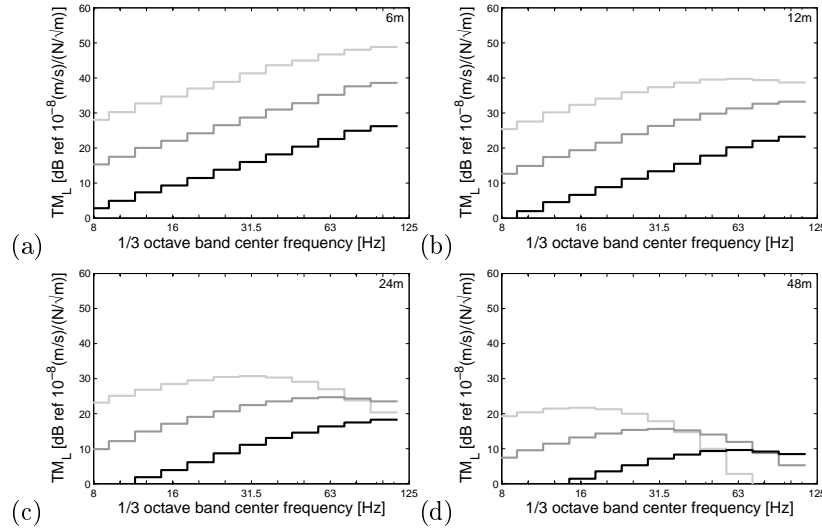


Figure 4.27: Predicted line source transfer mobility level at (a) 6 m, (b) 12 m, (c) 24 m, and (d) 48 m at a site with soft, medium, and stiff soil (grey to black lines) determined with source points  $\mathbf{X}_{FC}$  at the soil's surface at the track center line.

effect and due to the attenuation in the soil. In the case of source points at both rails, the effect of the soil on the track filtering and attenuation are accounted for in the line source transfer mobility level as well and are therefore eliminated in the force density level computed with equation (4.7). The difference between the force density levels for the three soil types is therefore predominantly determined by the effect of the soil stiffness on the axle loads such that a different force density level is obtained at each soil type. Figure 4.28 shows that this difference increases up to around 6 dB, particularly in the higher frequency range where the P2 resonance occurs and the effect of the soil stiffness on the axle loads is larger.

Figure 4.29 compares the predicted force density levels determined with source points at the soil's surface. In this case, the effect of the soil on the track filtering is taken into account in the vibration velocity level, but is not accounted for in the line source transfer mobility level. Compared to the case of source points at both rails, the force density level is therefore additionally affected by the influence of the soil stiffness on the track filtering effect. The difference between the force density levels has increased up to 25 dB, especially in the higher frequency range where the track filtering effect is stronger.

The previous figures show that the force density level is influenced by the soil

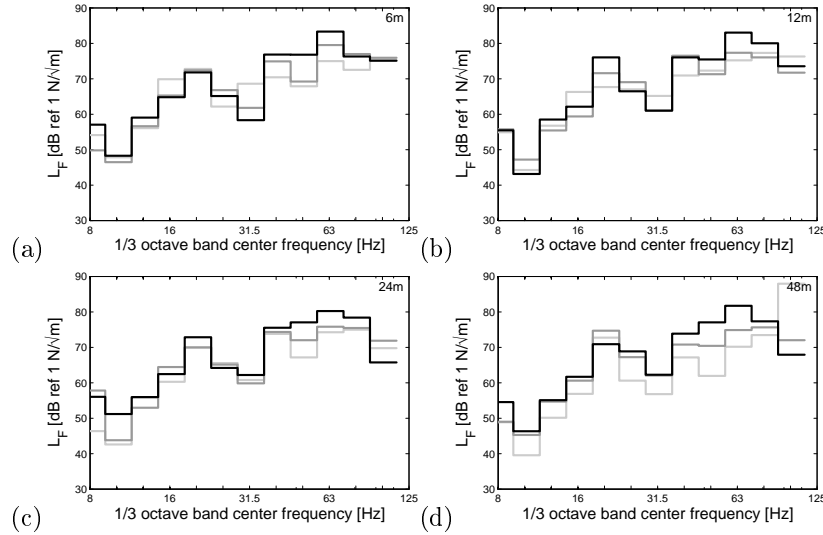


Figure 4.28: Predicted force density level based on the response at (a) 6 m, (b) 12 m, (c) 24 m, and (d) 48 m for an IC train (200 km/h) at a site with soft, medium, and stiff soil (grey to black lines) determined with source points  $\mathbf{X}_{RB}$  at both rails.

properties. This means that when the force density level  $L_F^2(\mathbf{X}, \mathbf{x}')$  determined at a measurement site is extrapolated to an assessment site where the vibration velocity level  $L_V^1(\mathbf{x}')$  is predicted according to equation (4.8), a mismatch in the soil properties between both sites will result in a wrong prediction. In the case of source points at both rails, this error would be limited to 6 dB for the considered soil types. As this is relatively small compared to the differences observed between measured force density levels (figures 4.21 and 4.22), a relatively good accuracy would still be obtained. In the case of source points at the soil's surface, the difference increases and the extrapolation of a force density level to other sites will lead to a prohibitively large error.

For the case of source points at both rails, the force density level is mainly affected by the soil conditions through the dynamic axle loads of the moving train. In practice, however, the effect of a mismatch in soil conditions is expected to be smaller, as the track stiffness usually increases due to the presence of a track subgrade, particularly at sites with soft soil. The simulation is therefore repeated and the force density level is determined again for a track with subgrade at a site with soft, medium, and stiff soil. The characteristics of the track subgrade are listed in table 4.2.

Figure 4.30 compares the force density levels determined with impacts at both

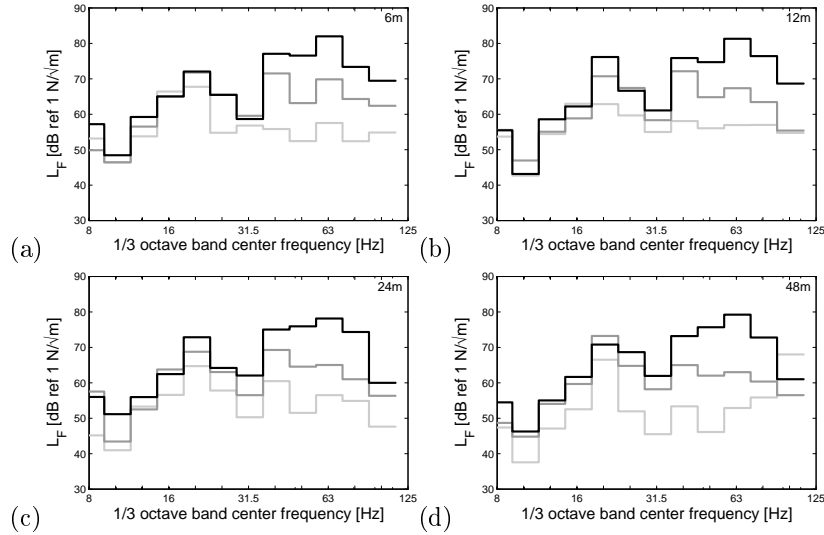


Figure 4.29: Predicted force density level based on the response at (a) 6 m, (b) 12 m, (c) 24 m, and (d) 48 m for an IC train (200 km/h) at a site with soft, medium, and stiff soil (grey to black lines) determined with source points  $\mathbf{X}_{FC}$  at the soil's surface at the track center line.

$C_s$	$C_p$	$\beta_s$	$\beta_p$	$\rho$
[m/s]	[m/s]	[-]	[-]	[kg/m <sup>3</sup> ]
300	600	0.025	0.025	1854

Table 4.2: Dynamic characteristics of the track subgrade.

rails for a track at a site with soft, medium, and stiff soil where the track subgrade is taken into account.

For the sites with soft and medium soil, the track subgrade leads to an increased track stiffness, resulting in a smaller difference between the track stiffness at the three sites and hence also between the dynamic axle loads. The difference between the force density levels therefore slightly reduces, particularly at a larger distance from the track. The result is still affected by the soil type, however, with a difference increasing up to around 6 dB for the considered properties of the track subgrade.

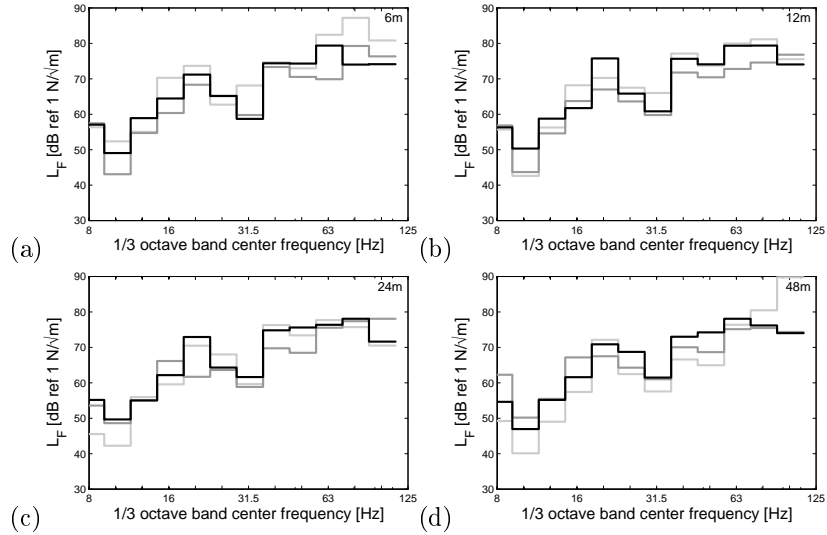


Figure 4.30: Predicted force density level based on the response at (a) 6 m, (b) 12 m, (c) 24 m, and (d) 48 m for an IC train (200 km/h) at a site with soft, medium, and stiff soil (grey to black lines) determined with source points  $\mathbf{X}_{RB}$  at both rails for a track with subgrade.

### 4.6.2 Influence of the track characteristics

The force density level and the resulting prediction of the vibration velocity level are also affected by a mismatch in the track characteristics between the measurement and the assessment site. In order to illustrate the effect of the track characteristics on the force density level, it is predicted for three tracks with different rail pad characteristics.

The passage of an IC train with a speed of 200 km/h on a classical ballasted track (table 2.3) is considered at a site with medium soil (table 4.1). The excitation considered is an unevenness sample according to FRA class 3 [56].

Three different values are assumed for the rail pad stiffness, representing a soft, medium, and stiff rail pad, in order to assess the influence of the track conditions on the determined force density level. The rail pad properties are summarized in table 4.3.

Figure 4.31 shows the predicted vibration velocity level for the IC train passage for the three rail pad types. The peak value around 60 Hz is due to the resonance of the wheels on the track. The rail pad stiffness influences the track stiffness and the axle loads, and hence the free field response as well. A

Rail pad type	$k_{rp}$ [ $10^6$ N/m]
Soft	75
Medium	150
Stiff	300

Table 4.3: Dynamic characteristics of the three rail pads.

difference around 4 dB is generally observed for the considered rail pad types. The attenuation of the vibration velocity with increasing distance from the track is of course insensitive to the rail pad stiffness.

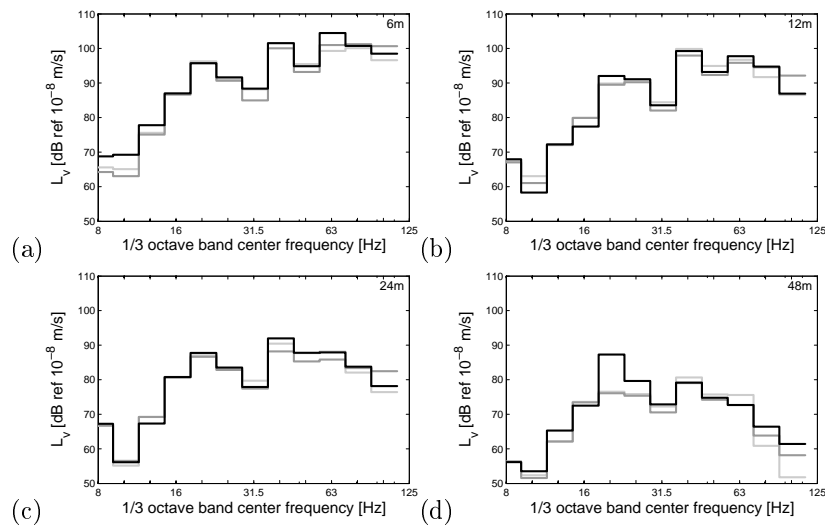


Figure 4.31: Predicted vibration velocity level at (a) 6 m, (b) 12 m, (c) 24 m, and (d) 48 m for an IC train (200 km/h) at a track with soft, medium, and stiff rail pad (grey to black lines).

Figure 4.32 compares the predicted line source transfer mobility level determined with a force applied to both rails and determined with a source length of 200 m and a source point spacing of 10 m. As the frequency range of interest is far below the resonance of the rail on the rail pad, the force on the rail is transmitted quasi-statically to the sleeper. The rail pad stiffness further affects the distribution of the load from the rail to the sleeper. A difference smaller than 2 dB is observed for the considered values of the rail pad stiffness.

Figure 4.33 compares the predicted force density levels determined with source



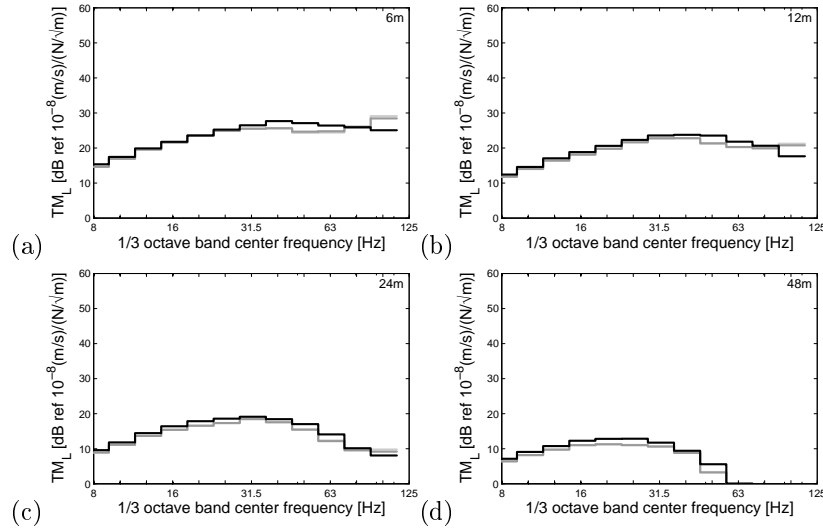


Figure 4.32: Predicted line source transfer mobility level at (a) 6 m, (b) 12 m, (c) 24 m, and (d) 48 m for a track with soft, medium, and stiff rail pad (grey to black lines) determined with source points  $\mathbf{X}_{RB}$  at both rails.

points at both rails. As the rail pad affects the track stiffness and hence the dynamic axle loads, the vibration velocity level is modified by the rail pad stiffness (figure 4.31). The effect of the rail pad stiffness on the line source transfer mobility level is smaller, however (figure 4.32). This leads to a difference between the predicted force density levels determined at tracks with a different rail pad stiffness. For the considered values of the rail pad stiffness the difference is generally limited to 4 dB, however.

The previous results show the effect of the rail pad stiffness on the force density level and illustrate the error that is expected in the predicted vibration velocity level when the force density level is extrapolated from a measurement site with a track with different rail pad characteristics. For the considered values of the rail pad stiffness, the influence remains limited to 4 dB. A similar influence is expected for ballasted tracks from other resilient track components, such as the ballast, while a smaller influence is expected from other track components such as sleepers or rails.

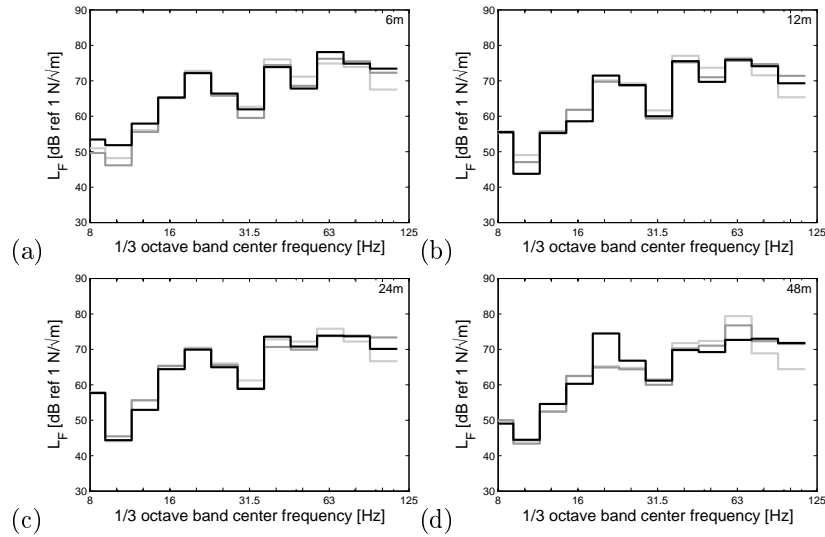


Figure 4.33: Predicted force density level based on the response at (a) 6 m, (b) 12 m, (c) 24 m, and (d) 48 m for an IC train (200 km/h) at a track with soft, medium, and stiff rail pad (grey to black lines) determined with source points  $\mathbf{X}_{RB}$  at both rails.

## 4.7 Conclusion

The present chapter investigates the empirical FRA procedure, where the vibration velocity level due to a train passage is predicted as the sum of a force density level and a line source transfer mobility level. It is shown that the force density level represents an equivalent fixed line source that results in the same vibration velocity level as the train passage. Analytical expressions have been derived for the force density level and the line source transfer mobility level based on the assumption of fixed and incoherent axle loads.

When the force density level is determined based on source points at both rails, it corresponds to the dynamic axle loads applied at a fixed position. Using a different position of the source point affects the force density level which then represents an equivalent line source that has to be applied at the corresponding source point to result in the same vibration velocity level as the train passage. For source points at a single rail, a different force density level is obtained due to the asymmetric excitation of the track. For source points at the soil's surface, the force density level is affected by the track–soil interaction.

Furthermore, as the approximation of fixed and incoherent axle loads only holds

approximately, the force density level depends on the position of the receiver point. In case of source points at both rails, this dependency is only determined by the Doppler effect that results in a shift of the frequency content between the moving source and the receiver. No clear trend is observed in function of the distance and the difference is in the same order of magnitude as the experimental difference observed due to spatial variation or between different train passages. For different source points, an additional dependency on the receiver points is introduced that corresponds to the difference in the vibration transfer. This is most pronounced for source points at the soil's surface adjacent to the track, where a clear trend in function of the distance is observed.

In a prediction with the FRA procedure, the position of the source and receiver should be taken into account. In order to obtain an accurate prediction, a force density level should be combined with a line source transfer mobility level that has been determined with identical source and receiver points. It is shown, however, that the influence of the receiver point is smaller in the case of source points at both rails. The force density level determined at a reference distance can be used to approximate the vibration velocity level at other distances. In the case of source points at the soil's surface adjacent to the track, the force density level strongly depends on the receiver distance. A prediction of the vibration velocity level should be made with a force density level determined at the same distance. On the other hand, it is shown that the influence of the source point on the force density level is smaller in case of a receiver point at a larger distance from the track. In this case, a force density level determined with source points at both rails can be approximated by a force density level determined with source points at the soil's surface adjacent to the track.

In a prediction with the FRA procedure, a force density level is extrapolated from a measurement site to an assessment site where a prediction of the vibration velocity level is desired. It is stated that the train, track, and soil conditions at both sites should be similar to obtain an accurate prediction. The influence of a mismatch between both sites has been investigated for different soil and track characteristics. In the case of source points on the track, a limited influence of the soil conditions on the force density level is observed. In the case of source points at the soil's surface, the influence of the soil conditions strongly increases. In this case, the extrapolation of the force density level to sites with different soil conditions is no longer valid. The effect of the track characteristics is illustrated for different values of the rail pad stiffness and is shown to be limited.



# Chapter 5

## Hybrid methods

### 5.1 Introduction

Hybrid or semi-empirical methods are defined as a combination of parametric models and empirical models [66]. In a hybrid model, one or a number of components is provided by measurements while the other components are predicted numerically.

The empirical methods of SBB [86, 161] and Madshus et al. [102] discussed in chapter 4 are to some extent hybrid approaches, as a measured source characterization is combined with an analytical attenuation law for the characterization of the propagation path. The present state of the art in the numerical prediction of railway induced vibration allows for more elaborate hybrid models, however.

In the present chapter, a hybrid model is presented that is based on the framework of the empirical FRA procedure. In this empirical method, the vibration velocity level  $L_v^1(\mathbf{x}'_1)$  at an assessment site (site 1) is obtained by combining a force density level  $L_F^2(\mathbf{X}_2, \mathbf{x}'_2)$  determined at a measurement site (site 2) with a line source transfer mobility level  $TM_L^1(\mathbf{X}_1, \mathbf{x}'_1)$  measured at the assessment site:

$$L_v^1(\mathbf{x}'_1) = L_F^2(\mathbf{X}_2, \mathbf{x}'_2) + TM_L^1(\mathbf{X}_1, \mathbf{x}'_1) \quad (5.1)$$

The empirical prediction with equation (5.1) has a number of limitations, however, as discussed in chapter 4. These limitations are partly eliminated by

combining the empirical FRA procedure with numerical predictions, resulting in a hybrid model. Different hybrid approaches are obtained by replacing different components in equation (5.1) by numerical predictions. In the present chapter, these hybrid approaches are assessed at the site in Lincent, presented in chapter 3.

In case of a hybrid approach, measurements are only carried out at an assessment site while the other data are provided numerically. The superscripts 1 and 2 are therefore replaced by the superscripts EXP, NUM, and HYB, indicating a measured, predicted, and hybrid result, respectively.

In section 5.2, a first hybrid approach is discussed where the force density level  $L_F^2(\mathbf{X}_2, \mathbf{x}'_2)$  in equation (5.1) is predicted numerically. A second hybrid approach is discussed in section 5.3 where the line source transfer mobility level  $TM_L^1(\mathbf{X}_1, \mathbf{x}'_1)$  in equation (5.1) is predicted numerically. In section 5.4, a third hybrid approach is obtained by introducing a numerical correction for the source point positions  $\mathbf{X}_1$  and  $\mathbf{X}_2$  in equation (5.1). The conclusion is presented in section 5.5.

## 5.2 Numerical prediction of the force density level

A first hybrid prediction of the vibration velocity level is obtained by introducing a numerical prediction of the force density level in equation (5.1) and combining it with an experimental line source transfer mobility level.

This hybrid approach is inspired on the following considerations. First, in numerical predictions, the dynamic soil characteristics are often identified based on preliminary measurements and the vibration transfer is predicted by introducing simplifying assumptions such as the horizontal layering of soils. In the hybrid approach, the parameter identification and the introduction of simplifying assumptions is avoided and the local transfer of vibration is adequately accounted for by means of the measured line source transfer mobility level.

Second, it has been shown in chapter 4 that the extrapolation of a measured force density level is limited to sites where similar conditions for the train, track, and soil are present. Such experimental data may not always be available, limiting the practical use of the empirical method. The numerical prediction of the force density level offers the flexibility to assess a wide range of parameters and can therefore be used to assess the vibration level for new tracks, new rolling stock, or modifications to existing tracks.

This hybrid approach is particularly appealing at sites where a complex soil stratification prevents an accurate prediction of the vibration transfer and where no appropriate force density level is available, i.e. when no measurement site is found with similar characteristics for the train, track, and soil.

A distinction is made between two cases of the hybrid prediction. In the first case, the force density level is predicted directly based on the analytical expression that has been derived in section 4.3. In the second case, the force density level is predicted numerically by simulation of the empirical FRA procedure.

### 5.2.1 Direct prediction of the force density level

#### Force density level

A direct prediction of the force density level based on the average spectrum  $g_{\text{RMS}}$  of the axle loads of the train is obtained based on equation (4.13):

$$L_{\text{F}}^{\text{NUM}} = 10 \log_{10} \left[ \frac{n_{\text{a}}}{L_{\text{t}}} g_{\text{RMS}}^2 \right] \quad (5.2)$$

The prediction of the force density level  $L_{\text{F}}^{\text{NUM}}$  only requires the modeling of the track–soil interaction for the computation of the track compliance and does not rely on predicted transfer functions. This allows to use computationally efficient models to take into account additional track layers, embankments, or excavations, as discussed in section 3.4.

Figure 5.1 shows the predicted force density level  $L_{\text{F}}^{\text{NUM}}$  for the passage of the IC train (198 km/h) and the Thalys train (300 km/h). As discussed in section 4.3, the force density level in equation (5.2) corresponds to a fixed line source and therefore disregards the movement of the train. It does not depend on a receiver point such that a single value is obtained in each frequency band.

#### Line source transfer mobility level

At the site in Lincent, the line source transfer mobility level has been determined for two cases. Figure 5.2 shows the measured line source transfer mobility level  $\text{TM}_{\text{L}}^{\text{EXP}}(\mathbf{X}, \mathbf{x}')$ , determined with source points at the edge of the sleeper ( $\mathbf{X} = \mathbf{X}_{\text{SE}}$ ) and at the soil's surface adjacent to the track ( $\mathbf{X} = \mathbf{X}_{\text{FA}}$ ) with a source length of 160 m and a source point spacing of 10 m. It is noted that in

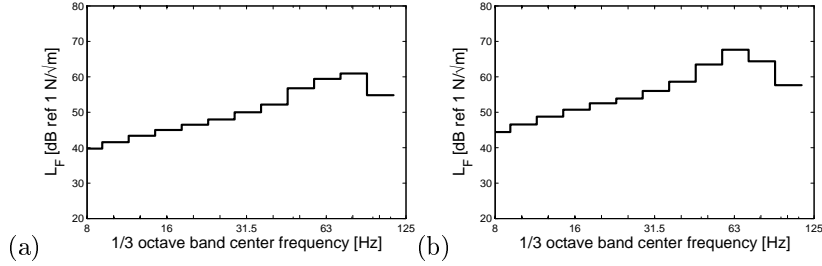


Figure 5.1: Directly predicted force density level for (a) an IC train (198 km/h) and (b) a Thalys train (300 km/h).

the latter case the receivers have not been moved correspondingly, resulting in a smaller source–receiver distance. This results in a high value of the line source transfer mobility level at 6 m for source points at the soil’s surface (figure 5.2b). An increasing attenuation is observed with increasing distance and frequency.

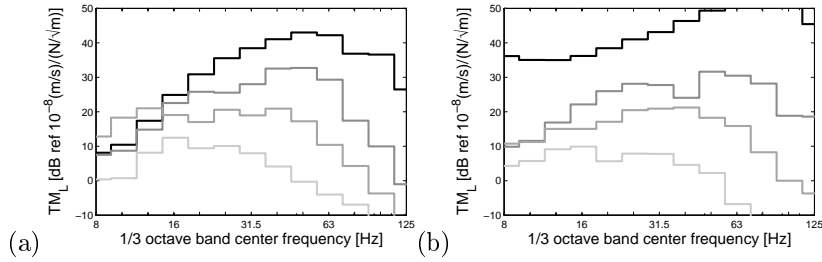


Figure 5.2: Measured line source transfer mobility level at 6 m, 12 m, 24 m, and 48 m (black to grey lines) for source points (a)  $\mathbf{X}_{SE}$  at the edge of the sleeper and (b)  $\mathbf{X}_{FA}$  at the soil’s surface adjacent to the track.

### Vibration velocity level

As the force density level  $L_F^{NUM}$  in equation (5.2) is computed based on the axle loads that are applied at the wheel/rail contact point at both rails, it should be combined with a line source transfer mobility level  $TM_L^{EXP}(\mathbf{X}_{RB}, \mathbf{x}'_1)$  that is determined with source points  $\mathbf{X}_{RB}$  at both rails, leading to a hybrid prediction of the vibration velocity level  $L_v^{HYB}(\mathbf{x}')$ :

$$L_v^{HYB}(\mathbf{x}') = L_F^{NUM} + TM_L^{EXP}(\mathbf{X}_{RB}, \mathbf{x}') \quad (5.3)$$



The application of equation (5.3) is limited to cases where the line source transfer mobility level can be determined with source points at both rails. At the site in Lincent, such a line source transfer mobility level has not been determined. Equation (5.3) is therefore first applied with the line source transfer mobility level  $TM_L^{EXP}(\mathbf{X}_{SE}, \mathbf{x}')$  determined with source points at the edge of the sleeper (figure 5.2a).

Figure 5.3 shows the hybrid prediction of the vibration velocity level for the IC train, compared with the numerical prediction and the measured result. The difference between the hybrid prediction and the measured result increases up to around 15 dB, particularly in the frequency range between 31.5 Hz and 63 Hz. This difference is partly determined by the prediction of the force density level  $L_F^{NUM}$  where the movement of the source is disregarded in equation (5.2). As previously explained, however, this difference is also due to the mismatch in the source positions, as the line source transfer mobility level is determined with impacts at the edge of the sleeper instead of both rails.

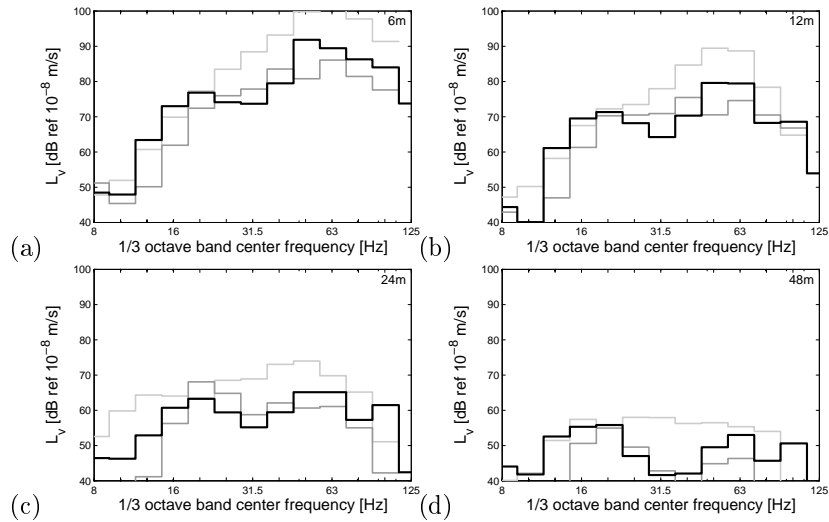


Figure 5.3: Hybrid prediction based on a directly predicted force density level (light grey line), numerical prediction (dark grey line), and measured result (black line) of the vibration velocity level at (a) 6 m, (b) 12 m, (c) 24 m, and (d) 48 m for an IC train (198 km/h).

Figure 5.4 shows the hybrid prediction of the vibration velocity level for the Thalys train, allowing to draw similar conclusions. In the high frequency range, the difference is even higher compared with the IC train (figure 5.3).

The effect of a mismatch in the position of the source points can be eliminated

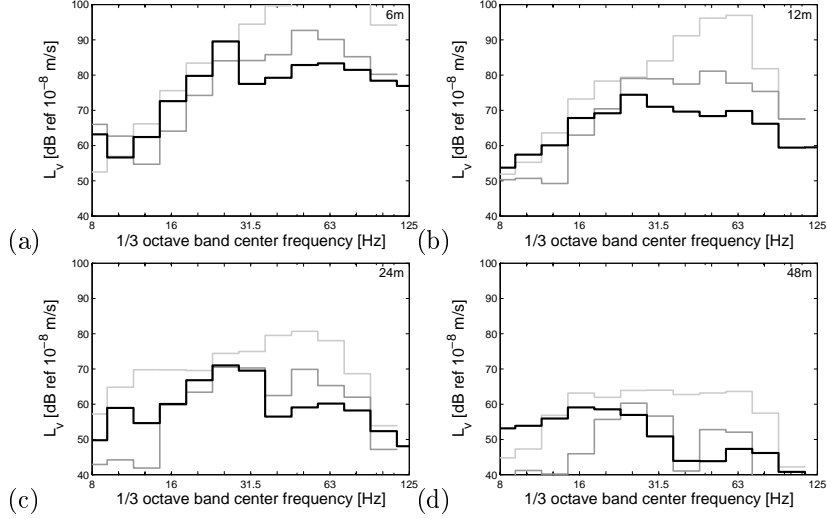


Figure 5.4: Hybrid prediction based on a directly predicted force density level (light grey line), numerical prediction (dark grey line), and measured result (black line) of the vibration velocity level at (a) 6 m, (b) 12 m, (c) 24 m, and (d) 48 m for a Thalys train (300 km/h).

numerically by introducing a correction  $\Delta TM_L^{NUM}(\mathbf{X}_1, \mathbf{X}_{RB}, \mathbf{x}')$  in equation (5.3) that accounts for the difference between the line source transfer mobility levels determined with different source points  $\mathbf{X}_{RB}$  and  $\mathbf{X}_1$ :

$$L_V^{HYB}(\mathbf{x}') = L_F^{NUM} + \underbrace{TM_L^{NUM}(\mathbf{X}_{RB}, \mathbf{x}') - TM_L^{NUM}(\mathbf{X}_1, \mathbf{x}')}_{\Delta TM_L^{NUM}(\mathbf{X}_1, \mathbf{X}_{RB}, \mathbf{x}')} + TM_L^{EXP}(\mathbf{X}_1, \mathbf{x}') \quad (5.4)$$

where the line source transfer mobility levels  $TM_L^{NUM}(\mathbf{X}_{RB}, \mathbf{x}')$  and  $TM_L^{NUM}(\mathbf{X}_1, \mathbf{x}')$  are determined with source points  $\mathbf{X}_{RB}$  at both rails and with source points  $\mathbf{X}_1$  corresponding to the source points used for the determination of the line source transfer mobility level  $TM_L^{EXP}(\mathbf{X}_1, \mathbf{x}')$ , respectively. In the following, a correction  $\Delta TM_L^{NUM}(\mathbf{X}_{SE}, \mathbf{X}_{RB}, \mathbf{x}')$  is applied so that the force density level can be combined with an experimental line source transfer mobility level  $TM_L^{EXP}(\mathbf{X}_{SE}, \mathbf{x}')$  determined with source points  $\mathbf{X}_{SE}$  at the edge of the sleeper.

Figure 5.5 shows the hybrid prediction for the IC train where the correction  $\Delta TM_L^{NUM}(\mathbf{X}_{SE}, \mathbf{X}_{RB}, \mathbf{x}')$  is taken into account to eliminate the effect of a mismatch of the source points numerically. A much better agreement with both

the numerical and the experimental result is now observed, with a difference generally below 10 dB.

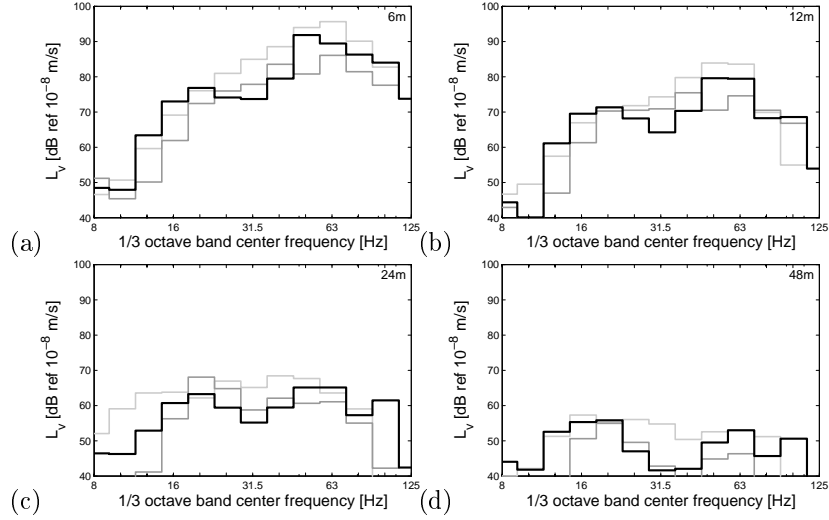


Figure 5.5: Hybrid prediction based on a directly predicted force density level with correction for the source position (light grey line), numerical prediction (dark grey line), and measured result (black line) of the vibration velocity level at (a) 6 m, (b) 12 m, (c) 24 m, and (d) 48 m for an IC train (198 km/h).

Figure 5.6 shows the hybrid prediction for the Thalys train where the correction  $\Delta TM_L^{NUM}(\mathbf{X}_{SE}, \mathbf{X}_{RB}, \mathbf{x}')$  is taken into account. A much better agreement is observed as well, but a difference up to 20 dB is still observed in the frequency range around 63 Hz particularly close to the track. It decreases to 15 dB at a larger distance due to the stronger attenuation at higher frequencies.

## 5.2.2 Indirect prediction of the force density level

### Force density level

An indirect prediction of the force density level  $L_F^{NUM}(\mathbf{X}, \mathbf{x}')$  is obtained by means of numerical simulation of the empirical FRA procedure as the difference between the predicted vibration velocity level  $L_v^{NUM}(\mathbf{x}')$  and line source transfer mobility level  $TM_L^{NUM}(\mathbf{X}, \mathbf{x}')$ :

$$L_F^{NUM}(\mathbf{X}, \mathbf{x}') = L_v^{NUM}(\mathbf{x}') - TM_L^{NUM}(\mathbf{X}, \mathbf{x}') \quad (5.5)$$

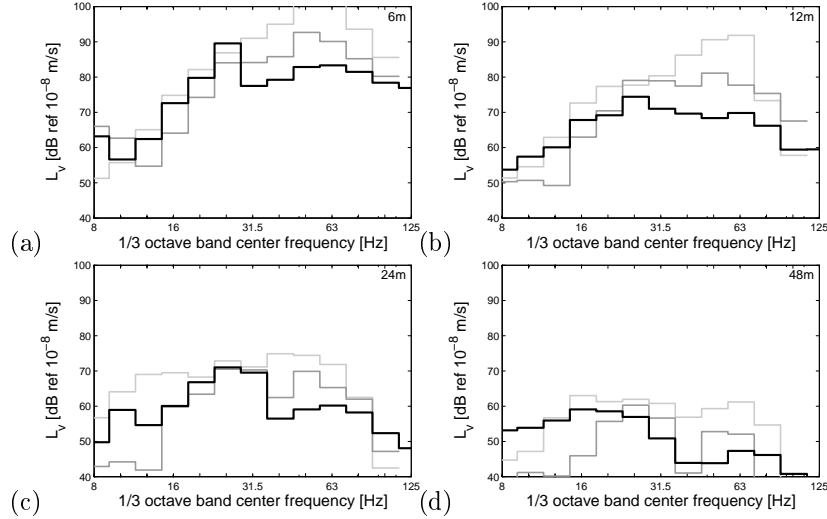


Figure 5.6: Hybrid prediction based on a directly predicted force density level with correction for the source position (light grey line), numerical prediction (dark grey line), and measured result (black line) of the vibration velocity level at (a) 6 m, (b) 12 m, (c) 24 m, and (d) 48 m for a Thalys train (300 km/h).

Compared to the direct prediction given in equation (5.2), the indirect prediction of the force density level is based on the vibration velocity level due to a train passage and takes into account the movement of the train. The force density level in equation (5.5) represents the equivalent fixed line source that results in the same vibration velocity level as the train passage and depends on the position of the receiver point. The position of the source  $\mathbf{X}$  and receiver  $\mathbf{x}'$  is inherently taken into account in the predicted force density level  $L_F^{\text{NUM}}(\mathbf{X}, \mathbf{x}')$ .

Figure 5.7 shows the predicted force density level based on the response at 6 m, 12 m, 24 m, and 48 m for the passage of the IC train and the Thalys train and determined with source points  $\mathbf{X}_{\text{SE}}$  at the edge of the sleeper. A different result is found for each receiver point.

Figure 5.8 shows the predicted force density level for the passage of the IC train and the Thalys train determined with source points  $\mathbf{X}_{\text{FA}}$  at the soil's surface. As expected, a larger difference in function of the receiver point is observed compared to the case of source points at the edge of the sleeper (figure 5.7).

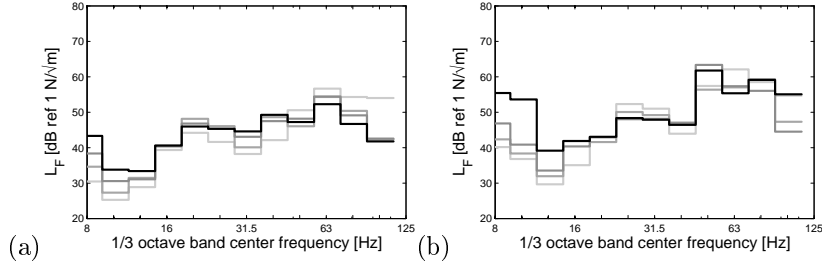


Figure 5.7: Indirectly predicted force density level based on the response at 6 m, 12 m, 24 m, and 48 m (black to grey lines) for (a) an IC train (198 km/h) and (b) a Thalys train (300 km/h) determined with source points  $\mathbf{X}_{SE}$  at the edge of the sleeper.

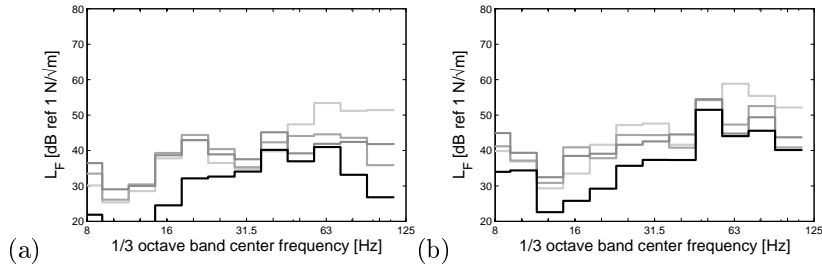


Figure 5.8: Indirectly predicted force density level based on the response at 6 m, 12 m, 24 m, and 48 m (black to grey lines) for (a) an IC train (198 km/h) and (b) a Thalys train (300 km/h) determined with source points  $\mathbf{X}_{FA}$  at the soil's surface adjacent to the track.

### Vibration velocity level

The combination of the indirect prediction of the force density level  $L_F^{NUM}(\mathbf{X}, \mathbf{x}')$  in equation (5.5) and the experimental line source transfer mobility level  $TM_L^{EXP}(\mathbf{X}, \mathbf{x}')$  leads to the hybrid prediction of the vibration velocity level  $L_V^{HYB}(\mathbf{x}')$ :

$$L_V^{HYB}(\mathbf{x}') = L_V^{NUM}(\mathbf{x}') - TM_L^{NUM}(\mathbf{X}, \mathbf{x}') + TM_L^{EXP}(\mathbf{X}, \mathbf{x}') \quad (5.6)$$

The experimental line source transfer mobility level  $TM_L^{EXP}(\mathbf{X}, \mathbf{x}')$  has been shown in subsection 5.2.1 and is not repeated here.

Equation (5.6) shows that the hybrid prediction corresponds to a predictor-corrector approach. First, a prediction  $L_V^{NUM}(\mathbf{x}')$  is made by means of a

numerical model. Second, the prediction is refined by applying a correction  $\text{TM}_L^{\text{EXP}}(\mathbf{X}, \mathbf{x}') - \text{TM}_L^{\text{NUM}}(\mathbf{X}, \mathbf{x}')$  for the vibration transfer. This hybrid approach is therefore particularly appealing when a large difference is found between the measured and predicted line source transfer mobility level. This is, for instance, the case when a complex soil stratification prevents an accurate prediction of the vibration transfer.

First, the line source transfer mobility level  $\text{TM}_L^{\text{EXP}}(\mathbf{X}_{\text{SE}}, \mathbf{x}')$  determined with source points  $\mathbf{X}_{\text{SE}}$  at the edge of the sleeper (figure 5.2a) is combined with the force density level  $L_F^{\text{NUM}}(\mathbf{X}_{\text{SE}}, \mathbf{x}')$  determined with source points  $\mathbf{X}_{\text{SE}}$  at the same location (figure 5.7).

Figure 5.9 shows the hybrid prediction of the vibration velocity level for the IC train, compared with the numerical prediction and the measured result. A relatively good agreement is found, showing a difference generally around 6 dB and up to 10 dB at most. Compared with the result obtained with the direct prediction of the force density level (figure 5.5), the movement of the train is now taken into account, leading to a slightly better agreement.

Figure 5.10 shows the hybrid prediction of the vibration velocity level for the Thalys train. Similar as for the IC train, the indirect prediction of the force density level leads to a slightly better agreement compared to the direct prediction (figure 5.6). A difference around 15 dB is still observed in the higher frequency range, however, corresponding to the peak in the axle load spectrum that has been predicted less accurately for the Thalys train than for the IC train.

Next, the line source transfer mobility level  $\text{TM}_L^{\text{EXP}}(\mathbf{X}_{\text{FA}}, \mathbf{x}')$  determined with source points  $\mathbf{X}_{\text{FA}}$  at the soil's surface (figure 5.2b) is combined with the force density level  $L_F^{\text{NUM}}(\mathbf{X}_{\text{FA}}, \mathbf{x}')$  determined with source points  $\mathbf{X}_{\text{FA}}$  at the same location (figure 5.8).

Figure 5.11 compares the hybrid prediction for the IC train with the numerical prediction and measured result. A relatively good agreement is again observed. The result closely resembles the case with source points at the edge of the sleeper (figure 5.9). Given the impact of the considered source points on the line source transfer mobility level, as observed in figure 5.2, this illustrates that the position of the source point is adequately accounted for in the predicted force density level.

Figure 5.12 shows the hybrid prediction of the vibration velocity for the Thalys train. A relatively high difference is again found around 50 Hz due to the prediction of the axle loads. The comparison with source points at the edge of the sleeper allows to draw similar conclusions as for the IC train.

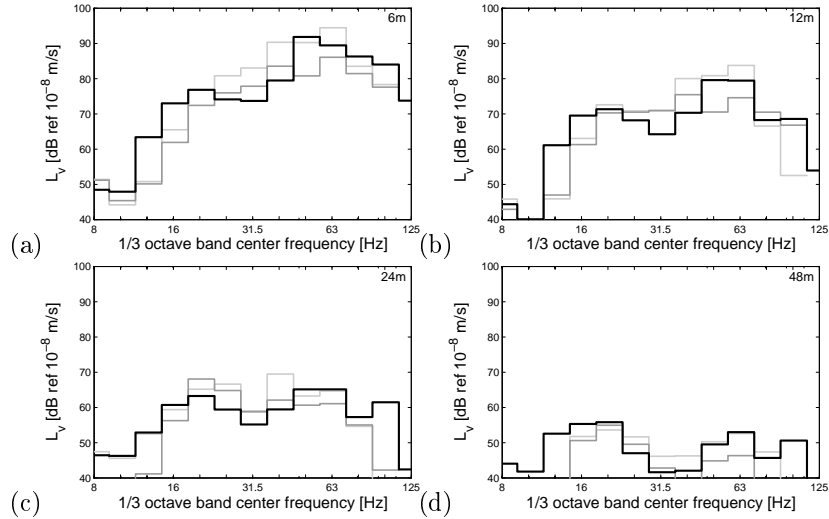


Figure 5.9: Hybrid prediction based on an indirectly predicted force density level determined with source points  $\mathbf{X}_{SE}$  at the edge of the sleeper (light grey line), numerical prediction (dark grey line), and measured result (black line) of the vibration velocity level at (a) 6 m, (b) 12 m, (c) 24 m, and (d) 48 m for an IC train (198 km/h).

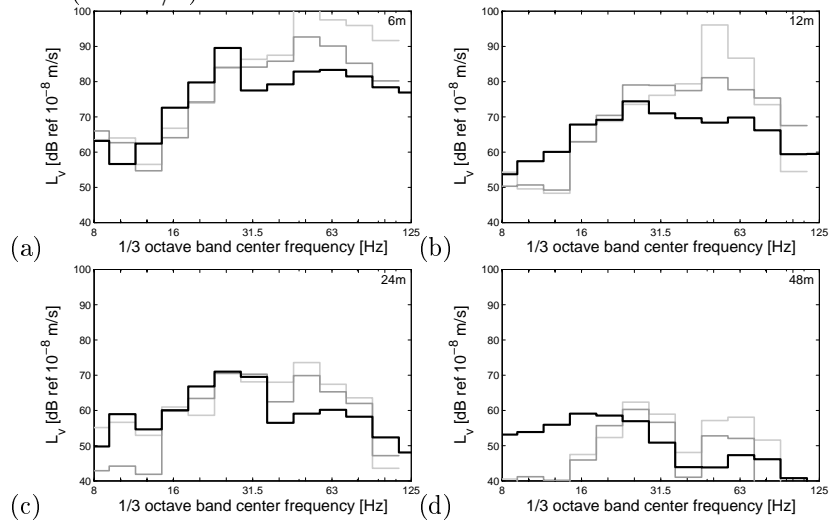


Figure 5.10: Hybrid prediction based on an indirectly predicted force density level determined with source points  $\mathbf{X}_{SE}$  at the edge of the sleeper (light grey line), numerical prediction (dark grey line), and measured result (black line) of the vibration velocity level at (a) 6 m, (b) 12 m, (c) 24 m, and (d) 48 m for a Thalys train (300 km/h).

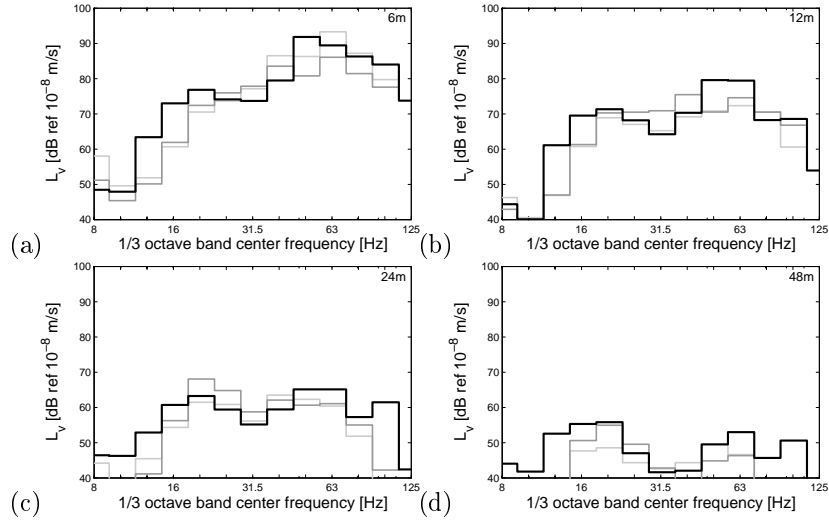


Figure 5.11: Hybrid prediction based on an indirectly predicted force density level determined with source points  $\mathbf{X}_{FA}$  at the soil's surface adjacent to the track (light grey line), numerical prediction (dark grey line), and measured result (black line) of the vibration velocity level at (a) 6 m, (b) 12 m, (c) 24 m, and (d) 48 m for an IC train (198 km/h).

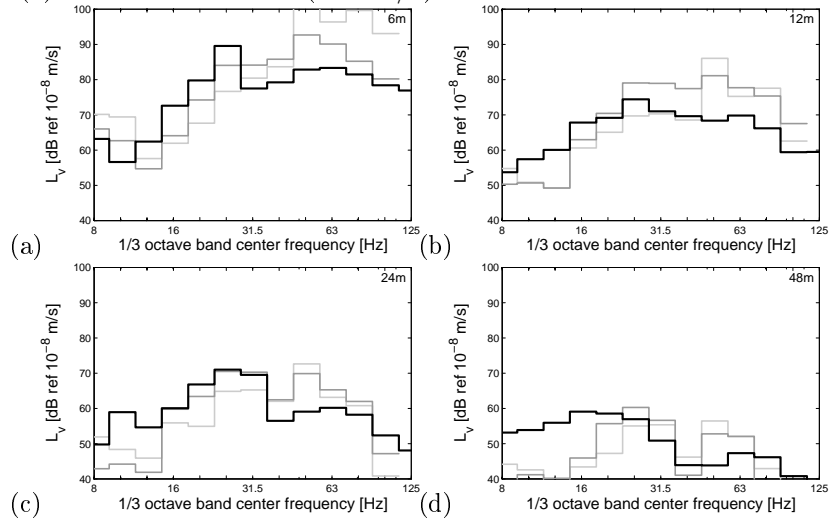


Figure 5.12: Hybrid prediction based on an indirectly predicted force density level determined with source points  $\mathbf{X}_{FA}$  at the soil's surface adjacent to the track (light grey line), numerical prediction (dark grey line), and measured result (black line) of the vibration velocity level at (a) 6 m, (b) 12 m, (c) 24 m, and (d) 48 m for a Thalys train (300 km/h).



The results in this section show that a reasonably good accuracy is obtained at the site in Lincent when a numerical force density level is combined with an experimental line source transfer mobility level. The best accuracy is obtained for the IC train with the indirect prediction of the force density level (figures 5.9 and 5.11), where the difference between the hybrid prediction and the measured result is generally below 6 dB. Only a slight increase of the difference is found for the direct prediction of the force density level (figure 5.5), which is due to the assumption of a fixed line source. This confirms that a reasonable approximation is obtained when fixed axle loads are assumed and allows for a direct prediction of the force density level based on equation (5.2).

A less good agreement between the hybrid prediction and the measured result is obtained in case of a mismatch in the source positions used for the determination of the force density level and the line source transfer mobility level. For the IC train, the difference increases up to 15 dB (figure 5.3). When the same source point position is used for the force density level and the line source transfer mobility level, a much better agreement is found. This confirms that it is important that a force density level is adequately combined with the corresponding line source transfer mobility level, i.e. both are determined with the same source points.

A less good agreement is generally obtained for the Thalys train which is mainly due to the prediction of the dynamic axle loads, illustrating the complexity of accurately modeling the dynamic train–track–soil interaction. The hybrid approach in the present section is particularly useful in the case where the axle loads are accurately predicted, requiring a correct identification of the dynamic characteristics of the train, the track, and the soil underneath the track. It offers the advantage compared to the numerical model that it does not require the identification of the free field soil characteristics or the introduction of simplifying assumptions, e.g. regarding the soil stratification.

In the case where the line source transfer mobility level  $\text{TM}_L^{\text{EXP}}(\mathbf{X}, \mathbf{x}')$  is determined with source points  $\mathbf{X}_{\text{FA}}$  at the soil's surface adjacent to the track, a similar agreement is found as for the case with source points  $\mathbf{X}_{\text{SE}}$  at the edge of the sleeper. Hence, the vibration transfer can be determined experimentally in absence of the track, so that the hybrid approach can also be applied for the prediction at sites where a track is planned prior to construction or where access to the track is not possible.

### 5.3 Numerical prediction of the line source transfer mobility level

A second hybrid prediction of the vibration velocity level is obtained by replacing the experimental line source transfer mobility level in equation (5.1) by a numerical prediction. This approach is motivated as follows. The prediction of the dynamic axle loads requires an accurate modeling of the train–track–soil interaction. The force density level is determined by the track stiffness, that is sensitive to the properties of the ballast and the track subgrade as discussed in section 3.4, and by several excitation mechanisms, such as wheel and track unevenness and parametric excitation. When an experimental force density level is used, the (difficult) characterization of these properties is avoided.

The use of a predicted line source transfer mobility level offers an advantage in a number of applications. First, it can be used to take into account a modification in the vibration transfer, e.g. due to the installation of vibration mitigation measures in the propagation path. Second, it allows to predict the vibration velocity level at a receiver where no experimental result is available. Consider, for instance, the case where a new building will be constructed close to a railway track and a prediction of the vibration is required at the foundation of the building. Whereas a direct measurement of the vibration during a train passage is not possible at depth, the numerical prediction of the line source transfer mobility level allows for a prediction at these receivers. Furthermore, it allows to predict the response at additional receivers. In the case where the response at a large number of receivers is required, e.g. to predict the incident wave field at the foundation of a building, the numerical prediction of the line source transfer mobility level allows to increase the number of receivers, avoiding the experimental measurement of the response at each receiver.

#### Force density level

As explained in section 4.2, the experimental force density level  $L_F^{\text{EXP}}(\mathbf{X}, \mathbf{x}'_1)$  is characterized based on a measured vibration velocity level  $L_v^{\text{EXP}}(\mathbf{x}'_1)$  and line source transfer mobility level  $\text{TM}_L^{\text{EXP}}(\mathbf{X}, \mathbf{x}'_1)$  as:

$$L_F^{\text{EXP}}(\mathbf{X}, \mathbf{x}'_1) = L_v^{\text{EXP}}(\mathbf{x}'_1) - \text{TM}_L^{\text{EXP}}(\mathbf{X}, \mathbf{x}'_1) \quad (5.7)$$

As shown in figures 3.50 and 3.58, the measured vibration velocity level  $L_v^{\text{EXP}}(\mathbf{x}'_1)$  in equation (5.7) is different for different train passages of the same

type. The experimental force density level is therefore determined based on the average measured vibration velocity level due to different passages of the same train type in a limited speed range.

The indirect measurement of the force density level based on equation (5.7) involves the determination of a line source transfer mobility level  $\text{TM}_L^{\text{EXP}}(\mathbf{X}, \mathbf{x}'_1)$ . The force density level  $L_F^{\text{EXP}}(\mathbf{X}, \mathbf{x}'_1)$  is affected by the position of the source  $\mathbf{X}$  and receiver  $\mathbf{x}'_1$  used for the determination of  $\text{TM}_L^{\text{EXP}}(\mathbf{X}, \mathbf{x}'_1)$ . In the following, different source positions are used to determine the experimental force density level. A line source transfer mobility level  $\text{TM}_L^{\text{EXP}}(\mathbf{X}, \mathbf{x}'_1)$  determined with a source length of 160 m and a source point spacing of 10 m is used.

Figure 5.13 shows the force density level  $L_F^{\text{EXP}}(\mathbf{X}_{\text{SE}}, \mathbf{x}'_1)$  for the IC and Thalys trains determined with source points  $\mathbf{X}_{\text{SE}}$  at the edge of the sleeper and shows a moderate influence of the receiver point.

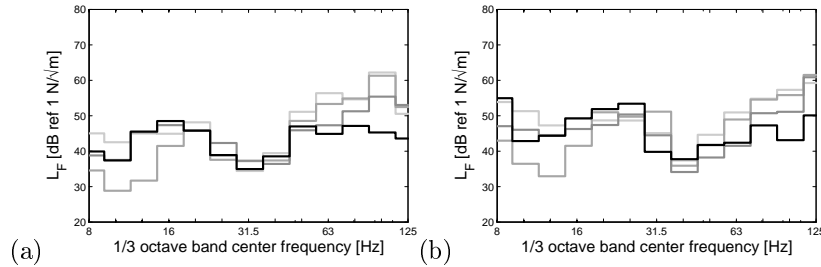


Figure 5.13: Average measured force density level determined with source points  $\mathbf{X}_{\text{SE}}$  at the edge of the sleeper for (a) IC trains (193 – 202 km/h) and (b) Thalys trains (291 – 300 km/h) based on the response at 6 m, 12 m, 24 m, and 48 m (black to grey lines).

Figure 5.14 shows the force density level  $L_F^{\text{EXP}}(\mathbf{X}_{\text{FA}}, \mathbf{x}'_1)$  for the IC and Thalys trains determined with source points  $\mathbf{X}_{\text{FA}}$  at the soil's surface adjacent to the track and shows a larger influence of the receiver point than for source points  $\mathbf{X}_{\text{SE}}$  at the edge of the sleeper.

The force density level  $L_F^{\text{EXP}}(\mathbf{X}, \mathbf{x}'_1)$  is determined experimentally and inherently takes into account the movement of the train and all relevant parameters of the coupled train–track–soil system. The influence of the source point  $\mathbf{X}$  is observed by comparing figures 5.13 and 5.14.

### Line source transfer mobility level

The line source transfer mobility level  $\text{TM}_L^{\text{NUM}}(\mathbf{X}, \mathbf{x}'_2)$  is predicted numerically based on equation (4.5) with a source length of 160 m and a source point spacing

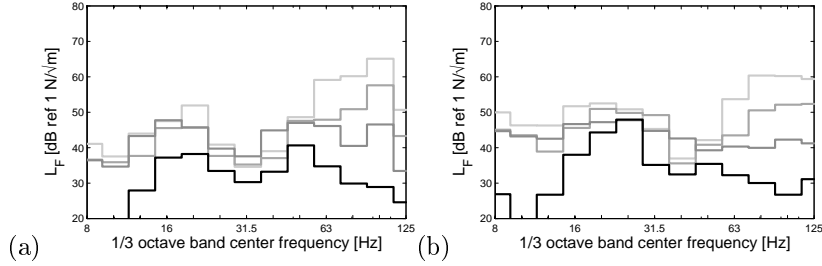


Figure 5.14: Average measured force density level determined with source points  $\mathbf{X}_{\text{FA}}$  at the soil's surface adjacent to the track for (a) IC trains (193 – 202 km/h) and (b) Thalys trains (291 – 300 km/h) based on the response at 6 m, 12 m, 24 m, and 48 m (black to grey lines).

of 10 m. For source points  $\mathbf{X}_{\text{SE}}$  at the edge of the sleeper, the dynamic track–soil interaction is taken into account in the model, whereas for source points  $\mathbf{X}_{\text{FA}}$  at the soil's surface, the prediction of the line source transfer mobility level only requires the modeling of the soil domain.

Figure 5.15 shows the line source transfer mobility levels determined with source points at the edge of the sleeper and at the soil's surface.

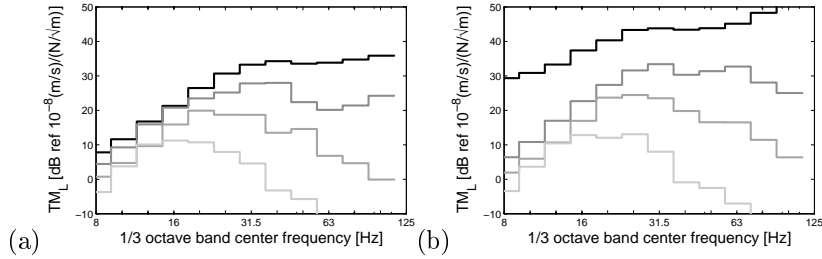


Figure 5.15: Predicted line source transfer mobility level determined with source points (a)  $\mathbf{X}_{\text{SE}}$  at the edge of the sleeper and (b)  $\mathbf{X}_{\text{FA}}$  at the soil's surface adjacent to the track at 6 m, 12 m, 24 m, and 48 m (black to grey lines).

### Vibration velocity level

The combination of the experimental force density level  $L_{\text{F}}^{\text{EXP}}(\mathbf{X}, \mathbf{x}'_1)$  in equation (5.7) and the numerical line source transfer mobility level  $\text{TM}_{\text{L}}^{\text{NUM}}(\mathbf{X}, \mathbf{x}'_2)$  leads to the hybrid prediction of the vibration velocity level  $L_{\text{V}}^{\text{HYB}}(\mathbf{x}'_2)$ :

$$L_{\text{V}}^{\text{HYB}}(\mathbf{x}'_2) = L_{\text{F}}^{\text{EXP}}(\mathbf{x}'_1) - \text{TM}_{\text{L}}^{\text{EXP}}(\mathbf{X}, \mathbf{x}'_1) + \text{TM}_{\text{L}}^{\text{NUM}}(\mathbf{X}, \mathbf{x}'_2) \quad (5.8)$$

Equation (5.8) illustrates that the hybrid prediction  $L_v^{\text{HYB}}(\mathbf{x}'_2)$  in fact corresponds to a correction of the measured vibration velocity level  $L_v^{\text{EXP}}(\mathbf{x}'_1)$ . This approach is therefore only useful when a difference  $\text{TM}_L^{\text{NUM}}(\mathbf{X}, \mathbf{x}'_2) - \text{TM}_L^{\text{EXP}}(\mathbf{X}, \mathbf{x}'_1)$  is found between the predicted and measured line source transfer mobility level. This is the case in the following applications.

First, the hybrid prediction in equation (5.8) allows for an assessment of the vibration velocity level after the installation of a mitigation measure at the propagation path. Therefore, the force density level is measured on site before the installation of the measure, while the numerical line source transfer mobility level allows to take into account the mitigation measure.

Second, equation (5.8) allows to predict the vibration velocity level at a receiver  $\mathbf{x}'_2$  that is different from receiver  $\mathbf{x}'_1$  where the response has been measured. This is particularly useful when a measurement at receiver  $\mathbf{x}'_2$  is not (yet) possible, as previously discussed. Due to the dependency on the receiver discussed in section 4.5, however, the difference between the receivers  $\mathbf{x}'_1$  and  $\mathbf{x}'_2$  should be limited, particularly in the case of source points at the soil's surface.

In the following, the hybrid prediction is assessed at the site in Lincent. The hybrid prediction is based on the average measured force density level (figures 5.13 and 5.14). It is noted that the difference between the hybrid prediction with equation (5.8) and the measured result is mainly due to the difference  $\text{TM}_L^{\text{NUM}}(\mathbf{X}, \mathbf{x}'_2) - \text{TM}_L^{\text{EXP}}(\mathbf{X}, \mathbf{x}'_1)$  between the predicted and measured line source transfer mobility level. The assessment of the hybrid approach in the present section therefore mainly relies on the accuracy of the prediction of the line source transfer mobility level.

First, the force density level  $L_F^{\text{EXP}}(\mathbf{X}_{\text{SE}}, \mathbf{x}'_1)$  determined with source points  $\mathbf{X}_{\text{SE}}$  at the edge of the sleeper (figure 5.13) is combined with the line source transfer mobility level  $\text{TM}_L^{\text{NUM}}(\mathbf{X}_{\text{SE}}, \mathbf{x}'_1)$  determined with source points  $\mathbf{X}_{\text{SE}}$  at the same location (figure 5.15a).

Figure 5.16 shows the hybrid prediction of the vibration velocity level for the IC train, compared with the numerical prediction and the measured result. A relatively good agreement is found, showing a difference around 6 dB.

Figure 5.17 shows the vibration velocity level for the Thalys train. Compared to case of the IC train, a slightly higher difference is found up to 10 dB.

Next, the force density level  $L_F^{\text{EXP}}(\mathbf{X}_{\text{FA}}, \mathbf{x}'_1)$  determined with source points  $\mathbf{X}_{\text{FA}}$  at the soil's surface (figure 5.14) is combined with the line source transfer mobility level  $\text{TM}_L^{\text{NUM}}(\mathbf{X}_{\text{FA}}, \mathbf{x}'_1)$  determined with source points  $\mathbf{X}_{\text{FA}}$  at the same location (figure 5.15b).

Figure 5.18 shows the hybrid prediction of the vibration velocity level for the

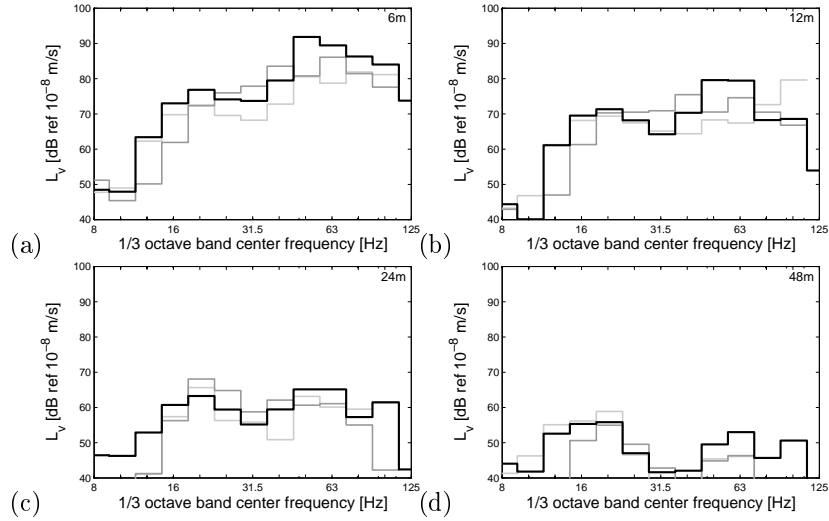


Figure 5.16: Hybrid prediction based on a predicted line source transfer mobility level determined with source points  $\mathbf{X}_{SE}$  at the edge of the sleeper (light grey line), numerical prediction (dark grey line), and measured result (black line) of the vibration velocity level at (a) 6 m, (b) 12 m, (c) 24 m, and (d) 48 m for an IC train (198 km/h).

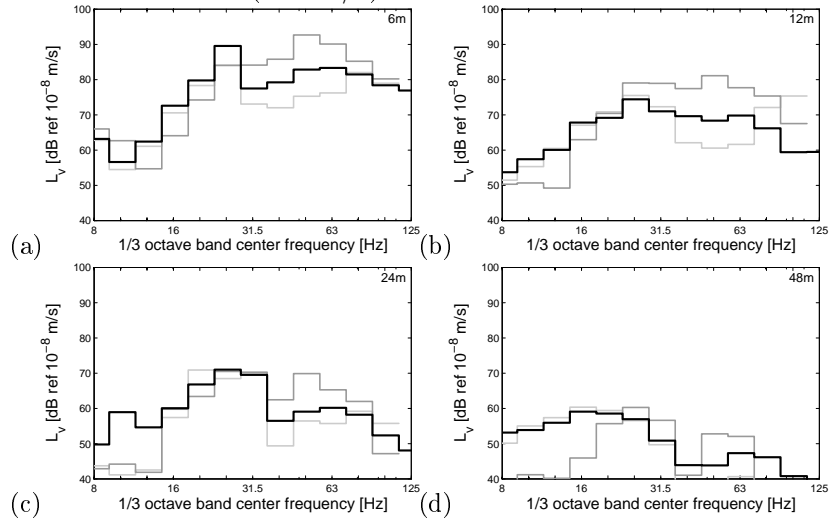


Figure 5.17: Hybrid prediction based on a predicted line source transfer mobility level determined with source points  $\mathbf{X}_{SE}$  at the edge of the sleeper (light grey line), numerical prediction (dark grey line), and measured result (black line) of the vibration velocity level at (a) 6 m, (b) 12 m, (c) 24 m, and (d) 48 m for a Thalys train (300 km/h).

IC train, compared with the numerical prediction and the measured result. A relatively good agreement is found again.

Figure 5.19 shows the hybrid prediction of the vibration velocity level for the Thalys train. Compared to the case with source points at the edge of the sleeper, the difference between the hybrid prediction and the measured result has further decreased and is generally below 6 dB. This is due to the fact that the dynamic track–soil interaction is now only accounted for in the force density level  $L_F^{\text{EXP}}(\mathbf{X}_{\text{FA}}, \mathbf{x}'_1)$  and does not need to be modeled in the numerical prediction of the line source transfer mobility level  $\text{TM}_L^{\text{NUM}}(\mathbf{X}_{\text{FA}}, \mathbf{x}'_1)$ . The hybrid prediction therefore shows a better accuracy than the numerical prediction.

The previous results show a relatively good agreement between the hybrid prediction and the measured result for source points at the edge of the sleeper as well as at the soil's surface. This confirms that the vibration transfer is accurately predicted at the site in Lincet, as previously verified in chapter 3. The case of source points at the soil's surface is particularly appealing, since the computation of the line source transfer mobility level does not involve the modeling of the track–soil interaction.

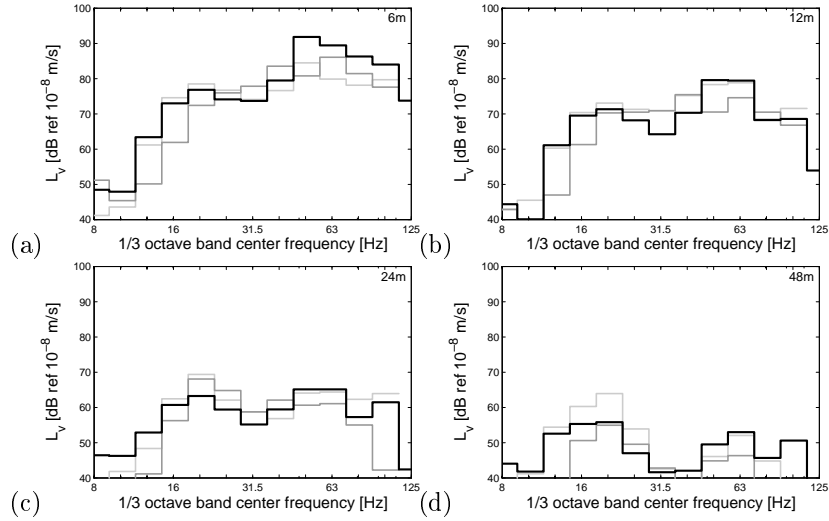


Figure 5.18: Hybrid prediction based on a predicted line source transfer mobility level determined with source points  $\mathbf{X}_{FA}$  at the soil's surface adjacent to the track (light grey line), numerical prediction (dark grey line), and measured result (black line) of the vibration velocity level at (a) 6 m, (b) 12 m, (c) 24 m, and (d) 48 m for an IC train (198 km/h).

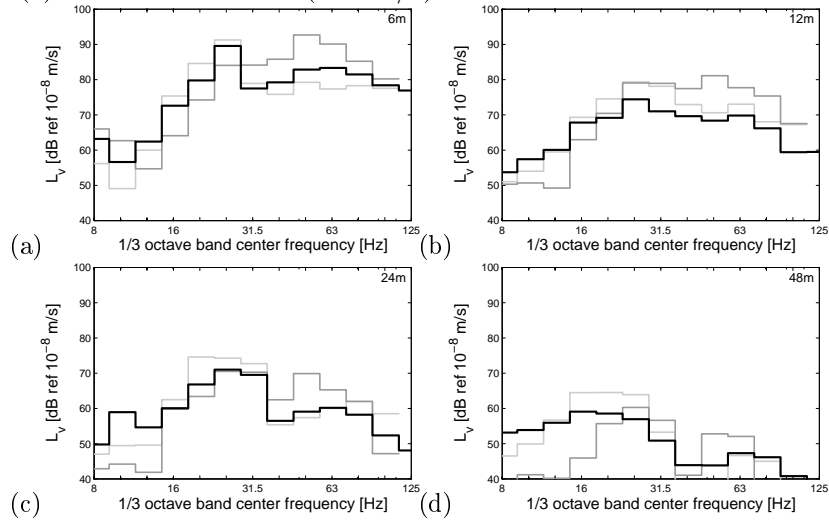


Figure 5.19: Hybrid prediction based on a predicted line source transfer mobility level determined with source points  $\mathbf{X}_{FA}$  at the soil's surface adjacent to the track (light grey line), numerical prediction (dark grey line), and measured result (black line) of the vibration velocity level at (a) 6 m, (b) 12 m, (c) 24 m, and (d) 48 m for a Thalys train (300 km/h).



## 5.4 Numerical correction for the position of the source point

A third hybrid prediction of the vibration velocity level is obtained by introducing a numerical correction  $\Delta\text{TM}_L^{\text{NUM}}(\mathbf{X}_1, \mathbf{X}_2, \mathbf{x}')$  in equation (5.1) that accounts for a mismatch between the source point  $\mathbf{X}_2$  used for the experimental determination of the force density level  $L_F^{\text{EXP}}(\mathbf{X}_2, \mathbf{x}')$  and the source point  $\mathbf{X}_1$  used for the experimental determination of the line source transfer mobility level  $\text{TM}_L^{\text{EXP}}(\mathbf{X}_1, \mathbf{x}')$ :

$$L_v^{\text{HYB}}(\mathbf{x}') = L_F^{\text{EXP}}(\mathbf{X}_2, \mathbf{x}') + \underbrace{\text{TM}_L^{\text{NUM}}(\mathbf{X}_2, \mathbf{x}') - \text{TM}_L^{\text{NUM}}(\mathbf{X}_1, \mathbf{x}')}_{\Delta\text{TM}_L^{\text{NUM}}(\mathbf{X}_1, \mathbf{X}_2, \mathbf{x}')} + \text{TM}_L^{\text{EXP}}(\mathbf{X}_1, \mathbf{x}') \quad (5.9)$$

This approach is particularly useful when an experimental force density level  $L_F^{\text{EXP}}(\mathbf{X}_2, \mathbf{x}')$  and line source transfer mobility level  $\text{TM}_L^{\text{EXP}}(\mathbf{X}_1, \mathbf{x}')$  are available that are determined with different source points  $\mathbf{X}_1$  and  $\mathbf{X}_2$ . Consider the case where a new track will be built at the assessment site and an appropriate force density level determined with source points  $\mathbf{X}_2$  at the track is available (e.g. in a database). The line source transfer mobility level can only be determined at the assessment site with source points  $\mathbf{X}_1$  at the soil's surface as no track is present yet, resulting in a mismatch in the position of the source points. This mismatch is eliminated by introducing the numerical correction  $\Delta\text{TM}_L^{\text{NUM}}(\mathbf{X}_1, \mathbf{X}_2, \mathbf{x}')$ .

This approach offers the advantage of empirical models that the train-track-soil interaction is inherently taken into account in the experimental force density level and the local vibration transfer is adequately characterized by the experimental line source transfer mobility level. The accuracy of the empirical model is improved by eliminating the mismatch in the source position.

In the following, a hybrid prediction is made at the site in Lincent by combining the experimental force density level  $L_F^{\text{EXP}}(\mathbf{X}_{\text{SE}}, \mathbf{x}')$  determined with source points  $\mathbf{X}_{\text{SE}}$  at the edge of the sleeper with the experimental line source transfer mobility level  $\text{TM}_L^{\text{EXP}}(\mathbf{X}_{\text{FA}}, \mathbf{x}')$  determined with source points  $\mathbf{X}_{\text{FA}}$  at the soil's surface adjacent to the track. The mismatch in the position of the source points is accounted for by means of the numerical correction  $\Delta\text{TM}_L^{\text{NUM}}(\mathbf{X}_{\text{FA}}, \mathbf{X}_{\text{SE}}, \mathbf{x}')$ . All line source transfer mobility levels are determined with a source length of 160 m and a source point spacing of 10 m.

Figure 5.20 shows the hybrid prediction of the vibration velocity level for the IC train, compared with the numerical prediction and the measured result. A

good agreement is observed between the hybrid prediction and the measured result, with a difference generally below 6 dB.

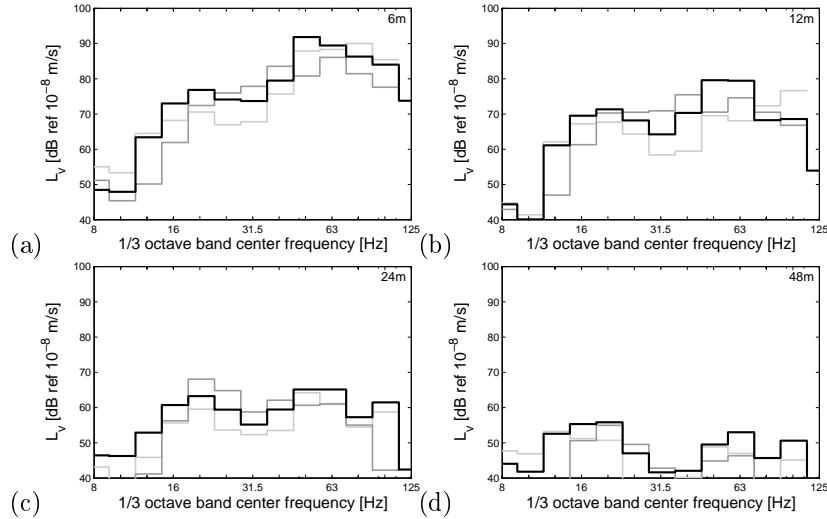


Figure 5.20: Hybrid prediction with a numerical correction for the position of the source point (light grey line), numerical prediction (dark grey line), and measured result (black line) of the vibration velocity level at (a) 6 m, (b) 12 m, (c) 24 m, and (d) 48 m for an IC train (198 km/h).

Figure 5.21 shows the hybrid prediction of the vibration velocity level for the Thalys train. A good agreement between the hybrid prediction and the measured result is found as well. The agreement is generally better than for the numerical prediction. The difference between the hybrid prediction and the numerical prediction is larger than for the IC train, which is due to the fact that the prediction of the axle loads is less good for the Thalys train. The advantage of the hybrid prediction is therefore larger for the Thalys train in the present example.

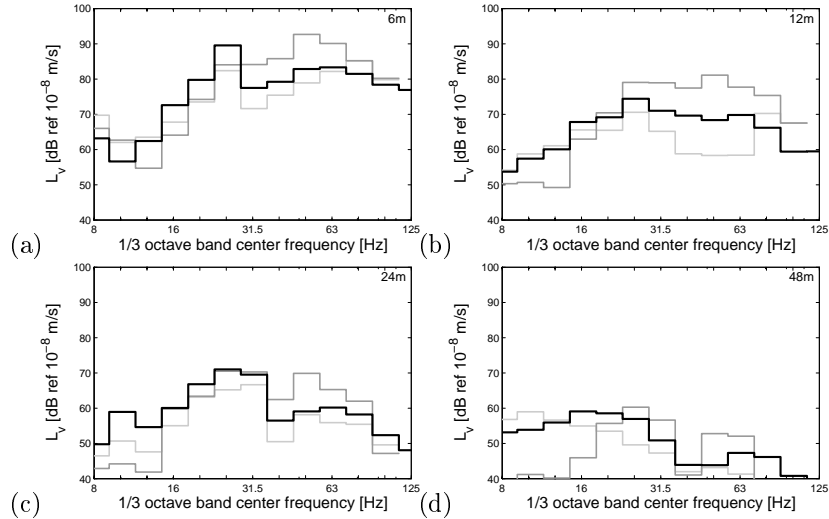


Figure 5.21: Hybrid prediction with a numerical correction for the position of the source point (light grey line), numerical prediction (dark grey line), and measured result (black line) of the vibration velocity level at (a) 6 m, (b) 12 m, (c) 24 m, and (d) 48 m for a Thalys train (300 km/h).

## 5.5 Conclusion

In the present chapter, a hybrid model is presented based on the framework of the empirical FRA procedure. Different hybrid approaches are presented based on different combinations of experimental and numerical data. As each approach has specific advantages and limitations compared to numerical and empirical models, they are useful in particular applications.

In the first approach, a numerical force density level is combined with an experimental line source transfer mobility level. A distinction is made between a direct prediction of the force density level based on the dynamic axle loads and an indirect prediction of the force density level by simulating the experimental determination. This hybrid approach offers the advantage that the local vibration transfer is adequately characterized by the measured line source transfer mobility level. At the same time, it offers the flexibility of numerical models to assess a wide range of parameters and can therefore be used to assess the vibration level for new tracks, new rolling stock, or modifications to existing tracks. This approach is particularly appealing to provide a prediction at a site where a complex soil stratification prevents an accurate prediction of the vibration transfer and where no appropriate force density level is available,

i.e. when no measurement site is found with similar characteristics for the train, track, and soil.

In the second approach, an experimental force density level is combined with a numerical line source transfer mobility level. This hybrid approach offers the advantage that the complex train–track–soil interaction is inherently taken into account in the experimental force density level and the identification of the train, track, and subgrade properties is avoided. The identification of the free field soil properties is required to predict the vibration transfer, however. As this hybrid approach in fact corresponds to a correction of the vibration transfer, it is only useful in the case where a difference is present between the measured and predicted line source transfer mobility level. A first application is the prediction of the expected vibration velocity level after the installation of a mitigation measure at the propagation path. A second application is the prediction of the vibration velocity level at receivers where no experimental results are available.

A third hybrid approach is obtained by introducing a numerical correction for the position of the source point in the empirical prediction. In this case the experimental characterization of the source and the propagation path ensures that the all relevant dynamic parameters are inherently accounted for. A possible mismatch between the source points used for the determination of the force density level and the line source transfer mobility level is eliminated by means of a numerical correction. This numerical correction in fact improves the accuracy of the empirical FRA procedure and can be used in the case where accurate experimental data are available but a mismatch in the source points is present, i.e. the force density level and line source transfer mobility level have been determined with different source points.

The hybrid prediction has been assessed at the site in Lincent, where experimental as well as numerical data are available. A reasonable accuracy is found for all approaches, provided that the force density level and line source transfer mobility level are adequately combined, i.e. they are determined with the same source points. An increasing accuracy is obtained with the hybrid model when more experimental data is included in the prediction, as the validation is carried out at a single site. It is shown, however, that all approaches offer a reasonable accuracy and provide an alternative prediction model. The hybrid models are particularly interesting compared to numerical and empirical models in the previously described applications.

## Chapter 6

# Conclusions and recommendations for further research

### 6.1 Conclusions

This work investigates the prediction of railway induced vibration by means of numerical, empirical, and hybrid methods. For the validation of these methods, a measurement campaign has been carried out at a site in Lincet, Belgium, measuring transfer functions and the response during train passages.

A considerable uncertainty is observed in the measured results at the site in Lincet, that should be taken into account in the assessment of the prediction models. The difference between the measured transfer functions increases up to 10 dB due to spatial variation of the track and soil characteristics, while the difference in the measured response due to train passages increases up to 6 dB due to spatial variation of the train, track, and soil characteristics and up to 14 dB due to variation between different trains. These values are only mentioned as an indication of the variation as they have been measured at a single site.

In the following, the main conclusions for each prediction method are summarized.

### Numerical methods

A numerical model is used that allows for a detailed modeling of different track components. The dynamic train, track, and soil characteristics for the site in Lincent are obtained from preliminary tests. The soil characteristics are identified from geophysical tests, including SCPT and SASW tests. The track characteristics are based on design values and are updated based on a measured track receptance. The train characteristics are based on design values.

The numerical model is applied to assess commonly made simplifying assumptions with respect to the track geometry. At the site in Lincent, the track is constructed in an excavation. The influence of the excavation and the track subgrade on the track receptance and the (track –) free field transfer functions is investigated in particular.

It is shown that the track receptance is significantly influenced by the presence of the excavation and the track subgrade and is mainly determined by the soil layering underneath the track. This observation allows to use a simplified model that correctly represents the soil underneath the track but disregards the the geometry of the excavation and track subgrade.

At low frequencies where the wavelength in the soil is large compared to the dimensions of the excavation and track subgrade, the (track –) free field mobilities are insensitive to their presence. At higher frequencies, a limited influence is observed.

The numerical model and the identified characteristics are validated based on the experimental results obtained at the site in Lincent. The discrepancy between the measured and predicted results is of the same order of magnitude as the differences observed between the experimental results so that it is concluded that a reasonable accuracy is obtained with the numerical model. Two particular observations are highlighted below.

First, the validation shows a better accuracy for the vibration transfer in the free field than for the vibration transfer close to the track. The identified soil profile adequately represents the free field vibration transfer. The soil properties close to the track are affected e.g. by the track subgrade, soil improvement, or soil compaction due to train passages, however, and are different from the free field soil properties. As the track stiffness is substantially influenced by (the modification of) the soil properties underneath the track, considerable attention should be paid to the identification of these properties.

Second, the validation of the response during train passages shows a better agreement for the rail response, dominated by the quasi-static excitation, than for the free field response, dominated by the dynamic excitation. This is due to

the uncertainty related to the prediction of the dynamic axle loads and the track – free field transfer function. Particularly the dynamic axle loads are sensitive to a large number of parameters regarding the unevenness excitation and train–track–soil interaction and an accurate prediction is not straightforward.

The main advantage of numerical models is that they offer the flexibility to take into account a wide range of model parameters, making them particularly suited for the prediction of relative vibration amplitudes, e.g. due to the installation of mitigation measures. They crucially depend on accurate parameter identification for the prediction of absolute vibration amplitudes, however. It is shown at the site in Lincent that the absolute vibration amplitudes are predicted with reasonable accuracy for train, track, and soil characteristics that have been identified based on preliminary tests.

### **Empirical methods**

The empirical prediction of railway induced vibration is studied based on the FRA procedure that predicts the vibration velocity level due to a train passage as the sum of a force density and a line source transfer mobility. This method is critically assessed and a number of limitations are identified.

First, it is shown that the force density represents an equivalent fixed line source that results in the same vibration velocity level as for the actual moving axle loads. The force density is determined indirectly based on a measured response and vibration transfer and therefore depends on the position of the source used during the measurement of the vibration transfer, where a distinction is made between source points at the track and at the soil's surface. Furthermore, the force density depends on the actual distance from the track at which it is determined. Hence, it is important in a prediction with the FRA procedure that the force density is combined with a line source transfer mobility that is determined with the same source and receiver points. It is recommended that the force density is determined with source points at the track, preferably at both rails or at the center of the sleeper, in order to reduce its dependency on the distance from the track.

Second, it is shown that the force density depends on the track and soil conditions at the measurement site. The extrapolation of the force density to an assessment site is therefore only valid when similar train, track, and soil conditions are present at both sites. This is particularly the case when the force density is determined with source points at the soil's surface.

The main advantage of empirical models is that they are based on measured data allowing for an accurate characterization of the source and the vibration

transfer and avoiding the introduction of simplifying assumptions and the identification of model parameters. Their application is limited by the appropriateness of the available measurement data, however, as previously pointed out.

### **Hybrid methods**

A hybrid model is formulated according to the FRA procedure. Three different hybrid approaches are presented based on different combinations of experimental and numerical data.

First, a numerical force density is combined with an experimental line source transfer mobility. This approach is particularly appealing at a site where the accurate prediction of the vibration transfer is not possible, e.g. due to a complex soil stratification or geometry, and where no appropriate force density is available, i.e. when no measurement site is found with similar characteristics for the train, track, and soil. It offers the advantage that the local vibration transfer is adequately characterized. At the same time, the numerical prediction of the force density allows assessing a wide range of parameters and can therefore be used to assess the vibration amplitude for new tracks, new rolling stock, or modifications to existing tracks.

Second, an experimental force density is combined with a numerical line source transfer mobility. This hybrid approach corresponds to a correction of the measured vibration transfer and is therefore useful in the case where a difference is present between the measured and predicted vibration transfer. It can be used, for instance, for the prediction of the free field response after the installation of a mitigation measure at the propagation path or for the prediction of the response at receivers where an experimental measurement is not possible. This approach offers the advantage that the complex train-track-soil interaction is inherently taken into account avoiding the identification of the train, track, and subgrade properties. The identification of the free field soil properties is required for the prediction of the vibration transfer.

Third, a variant of the empirical model is obtained when an experimental force density and line source transfer mobility are used and a numerical correction for the position of the source point is introduced. This approach allows to improve the accuracy of the empirical model in the case of a mismatch between the source points used for the determination of the force density and the line source transfer mobility.

The hybrid prediction models are assessed at the site in Lincent, where experimental as well as numerical data are available. A reasonable accuracy is



observed for all approaches when the position of the source point is adequately taken into account, i.e. the force density is combined with a line source transfer mobility determined with the same source points.

It is shown in the present work that a reasonably good prediction of railway induced vibration at the site in Lincent is obtained by means of the numerical and the hybrid model. The empirical model has been critically assessed but cannot be validated at a single site. The question whether a numerical, empirical, or hybrid approach is most suited depends on the availability of appropriate information (model parameters or measurement data) and the complexity of the problem.

## 6.2 Recommendations for further research

Based on the main conclusions of this work, a number of recommendations for future research can be made, summarized in the following.

At the site in Lincent, a considerable difference is observed between the measured transfer functions, caused by spatial variation of the soil and track characteristics. A considerable difference is observed as well between the measured velocities during a single train passage, caused by spatial variation of the characteristics of the soil and track, and during different train passages, caused by differences in the speed, train characteristics, and wheel unevenness. A more elaborate numerical model should account for uncertainty in the prediction of railway induced vibration. The effect of variations of model parameters on the response can be investigated by means of a parametric probabilistic approach [52].

The prediction of the free field response is mainly determined by dynamic excitation. The considered excitation mechanism only includes vertical rail unevenness and relies on measurements in a limited wavenumber range up to 2 rad/m by means of a track recording car. In order to obtain a more reliable prediction of the dynamic axle loads, the identification of the rail unevenness in the relevant wavenumber range above 2 rad/m should be included, e.g. by means of measurement devices such as trolleys. Other sources of unevenness excitation such as wheel unevenness (wheel flats and out-of-roundness) and horizontal rail unevenness should also be investigated. Furthermore, the measurements show a large contribution of the free field response at the sleeper passage frequency. Excitation by periodic support structures such as the sleepers can be included in 2.5D models by means of an equivalent unevenness and needs further attention.

The ground vibration predicted by numerical models crucially depends on the accurate identification of parameters. The response is significantly affected by the dynamic track characteristics and is only predicted accurately after updating of these characteristics based on the measured track receptance. The model updating process consists in solving an inverse problem that is ill-posed and does not guarantee the uniqueness of the solution. For instance, the identified ballast stiffness depends on the assumptions made regarding the track subgrade. Physically meaningful parameters can only be obtained if the track subgrade properties are known or can be jointly identified from measured data. Methods that are already applied for the inspection of the track subgrade are Ground Penetrating Radar and High Speed Deflectograph measurements [41]. Other methods include the continuous measurement of the dynamic track receptance [13] and the performance of an SASW test along a railway track [29]. The latter methods will be influenced by the loading conditions of the track. The identification of the track subgrade characteristics in the frequency range of interest needs considerable attention.

In new-build situations, the ballast parameters cannot be updated based on measured data and should be obtained from design values or laboratory tests. It is difficult, however, to relate the equivalent parameters of the longitudinally invariant model to physical properties of the ballast. Periodic or 3D models can be used to investigate how model parameters are affected by the assumptions made in 2.5D models, such as the continuous support of sleepers by the ballast.

The empirical FRA procedure has been comprehensively analyzed by means of numerical simulations and experimental data at the site in Lincent. The validation of the empirical prediction cannot be carried out at a single site, however, but should take into account at least two sites. The force density determined at a measurement site should therefore be extrapolated to an assessment site where it is used to predict the vibration velocity level. The accuracy of the empirical prediction should be assessed at the assessment site by comparison with the measured vibration velocity level.

The hybrid model presented in the present work is only assessed experimentally at a single site. A more elaborate assessment of the hybrid model is required. In the first approach, the vibration transfer is directly measured and the force density is predicted numerically based on the available information of the soil conditions underneath the track. This hybrid approach is useful at sites where an accurate prediction of the vibration transfer is difficult and where no appropriate force density is available. It has been assessed at the site in Lincent, but a more elaborate assessment can be carried out for other train, track, and soil conditions at sites where a track is present. In the second approach, an experimental force density is combined with a numerical line source transfer mobility. This hybrid approach can be used e.g. to predict the

vibration amplitude after the planned installation of a mitigation measure at the propagation path. It can be assessed at a site where a vibration mitigation measure will be installed. The force density is measured prior to the installation and combined with a predicted line source transfer mobility that takes into account the mitigation measure. The predicted vibration amplitude should be validated by means of measurements after installation.

Finally, the vibration inside a building can be included in the prediction. Whereas in a numerical model this would require a complex soil–structure interaction model and the identification of the dynamic characteristics of the structure, it can be performed in the empirical and hybrid models by measuring the response inside an existing building close to a (planned) railway track. In this case, the line source transfer mobility can be measured between (the future location of) the track and the building. The combination with an experimental or numerical force density respectively leads to the empirical or hybrid prediction of the response inside the building.



# Bibliography

- [1] ACHENBACH, J. *Wave propagation in elastic solids*, vol. 16 of *North-Holland Series in Applied Mathematics and Mechanics*. North-Holland, Amsterdam, The Netherlands, 1973.
- [2] ADOLFSSON, K., ANDRÉASSON, B., BENGTSON, P.-E., BODARE, A., MADSHUS, C., MASSARCH, R., WALLMARK, G., AND ZACKRISSON, P. High speed lines on soft ground. Evaluation and analyses of measurements from the West Coast Line. Tech. rep., Banverket, Sweden, 1999.
- [3] ANDERSEN, L., AND NIELSEN, S. Reduction of ground vibration by means of barriers or soil improvement along a railway track. *Soil Dynamics and Earthquake Engineering* 25 (2005), 701–716.
- [4] APSEL, R., AND LUCO, J. On the Green’s functions for a layered half-space. Part II. *Bulletin of the Seismological Society of America* 73, 4 (1983), 931–951.
- [5] ARNST, M., TA, Q., TAHERZADEH, R., COTTEREAU, R., SCHEVENELS, M., LOMBAERT, G., CLOUTEAU, D., BONNET, M., AND DEGRANDE, G. Measurements at a site in Lincent: transfer functions, dispersion curves and seismograms. Tech. rep., Laboratoire de Mécanique des Sols, Structures et Matériaux, Ecole Centrale de Paris, 2006.
- [6] AUBRY, D., CLOUTEAU, D., AND BONNET, G. Modelling of wave propagation due to fixed or mobile dynamic sources. In *Workshop Wave ’94, Wave propagation and Reduction of Vibrations* (Ruhr Universität Bochum, Germany, December 1994), N. Chouw and G. Schmid, Eds., pp. 109–121.
- [7] AUERSCH, L. The excitation of ground vibration by rail traffic: theory of vehicle-track-soil interaction and measurements on high-speed lines. *Journal of Sound and Vibration* 284, 1-2 (2005), 103–132.

- [8] AUERSCH, L. Ground vibration due to railway traffic – The calculation of the effects of moving static loads and their experimental verification. *Journal of Sound and Vibration* 293 (2006), 599–610.
- [9] AUERSCH, L. Dynamic interaction of various beams with the underlying soil – finite and infinite, half-space and winkler models. *European Journal of Mechanics, A/Solids* 27 (2008), 933–958.
- [10] BADSAR, S., SCHEVENELS, M., HAEGEMAN, W., AND DEGRANDE, G. Determination of the damping ratio in the soil from SASW tests using the half-power bandwidth method. *Geophysical Journal International* 182, 3 (2010), 1493–1508.
- [11] BAHREKAZEMI, M. *Train-induced ground vibration and its prediction*. PhD thesis, Royal Institute of Technology, 2004.
- [12] BENDAT, J., AND PIERSOL, A. *Random data: analysis and measurement procedures*. John Wiley & Sons, New York, 1971.
- [13] BERGGREN, E., KAYNIA, A., AND DEHLBOM, B. Identification of substructure properties of railway tracks by dynamic stiffness measurements and simulations. *Journal of Sound and Vibration* 329, 19 (2010), 3999–4016.
- [14] BERGGREN, E., VIALLETTEL, H., RODRIGUEZ, M., CUELLAR, V., AND SAUSSINE, G. Methods of track stiffness measurements. Deliverable d2.1.11, INNOTRACK, Project No. TIP5-CT-2006-031415, June 2009.
- [15] BOVEY, E. Development of an impact method to determine the vibration transfer characteristics of railway installations. *Journal of Sound and Vibration* 87, 2 (1983), 357–370.
- [16] BRAUN, H., AND HELLENBROICH, T. Messergebnisse von Strassenunebenheiten. *VDI Berichte* 877 (1991), 47–80.
- [17] BRITISH STANDARDS INSTITUTION. *BS 6472:1992: Evaluation of human exposure to vibration in buildings (1 Hz to 80 Hz)*, 1992.
- [18] CAMPANELLA, R., AND STEWART, W. Seismic cone analysis using digital signal-processing for dynamic site characterization. *Canadian Geotechnical Journal* 29, 3 (1992), 477–486.
- [19] CAUBERGHE, B. *Applied frequency-domain system identification in the field of experimental and operational modal analysis*. PhD thesis, Vrije Universiteit Brussel, 2004.

- [20] CLOUTEAU, D. *MISS Revision 2.1, Manuel Utilisateur*. Laboratoire de Mécanique des Sols, Structures et Matériaux, Ecole Centrale de Paris, 1993.
- [21] CLOUTEAU, D., ARNST, M., AL-HUSSAINI, T., AND DEGRANDE, G. Freefield vibrations due to dynamic loading on a tunnel embedded in a stratified medium. *Journal of Sound and Vibration* 283, 1–2 (2005), 173–199.
- [22] CLOUTEAU, D., AUBRY, D., ELHABRE, M., AND SAVIN, E. Periodic and stochastic BEM for large structures embedded in an elastic half-space. In *Mathematical Aspects of Boundary Element Methods*. CRC Press, London, 1999, pp. 91–102.
- [23] CLOUTEAU, D., DEGRANDE, G., AND LOMBAERT, G. Numerical modelling of traffic induced vibrations. *Meccanica* 36, 4 (2001), 401–420.
- [24] CLOUTEAU, D., ELHABRE, M., AND AUBRY, D. Periodic BEM and FEM-BEM coupling: application to seismic behaviour of very long structures. *Computational Mechanics* 25 (2000), 567–577.
- [25] CONNOLLY, D., GIANNOPOULOS, A., AND FORDE, M. Numerical modelling of ground borne vibrations from high speed rail lines on embankments. *Soil Dynamics and Earthquake Engineering* 46, 0 (2013), 13 – 19.
- [26] CONSOLI, N., DA FONSECA, A., SILVA, S., CRUZ, R., AND FONINI, A. Parameters controlling stiffness and strength of artificially cemented soils. *Géotechnique* 62, 2 (2012), 177–183.
- [27] CONSOLI, N., LOPES JR., L., PRIETTO, P., FESTUGATO, L., AND CRUZ, R. Variables controlling stiffness and strength of lime-stabilized soils. *Journal of Geotechnical and Geoenvironmental Engineering, Proceedings of the ASCE* 137, 6 (2011), 628 – 632.
- [28] COULIER, P., FRANÇOIS, S., DEGRANDE, G., AND LOMBAERT, G. Subgrade stiffening next to the track as a wave impeding barrier for railway induced vibrations. *Soil Dynamics and Earthquake Engineering* 48 (2013), 119–131.
- [29] CUELLAR, V., AND VALERIO, J. Use of the SASW method to evaluate soil improvement techniques. In *Proceedings of the 14th international conference soil mechanics and foundation engineering* (Hamburg, 1997), pp. 461–464.

- [30] DAVIS, D. A review of prediction methods for ground-borne noise due to construction activities. In *Proceedings of the 20th International Congress on Acoustics, ICA2010* (Sydney, Australia, August 2010).
- [31] DEGRANDE, G., CLOUTEAU, D., OTHMAN, R., ARNST, M., CHEBLI, H., KLEIN, R., CHATTERJEE, P., AND JANSSENS, B. A numerical model for ground-borne vibrations from underground railway traffic based on a periodic finite element - boundary element formulation. *Journal of Sound and Vibration* 293, 3-5 (2006), 645–666.
- [32] DEGRANDE, G., AND LOMBAERT, G. An efficient formulation of Krylov’s prediction model for train induced vibrations based on the dynamic reciprocity theorem. *Journal of the Acoustical Society of America* 110, 3 (2001), 1379–1390.
- [33] DEUTSCHES INSTITUT FÜR NORMUNG. *DIN 45672 Teil 2: Schwingungsmessungen in der Umgebung von Schienenverkehrswegen: Auswerteverfahren*, 1995.
- [34] DEUTSCHES INSTITUT FÜR NORMUNG. *DIN 4150 Teil 2: Erschütterungen im Bauwesen, Einwirkungen auf Menschen in Gebäuden*, 1999.
- [35] DEUTSCHES INSTITUT FÜR NORMUNG. *DIN 4150 Teil 3: Erschütterungen im Bauwesen, Einwirkungen auf bauliche Anlagen*, 1999.
- [36] DIETERMAN, H., AND METRIKINE, A. The equivalent stiffness of a halfspace interacting with a beam. Critical velocities of a moving load along the beam. *European Journal of Mechanics, A/Solids* 15, 1 (1996), 67–90.
- [37] DIETERMAN, H., AND METRIKINE, A. Steady-state displacements of a beam on an elastic half-space due to a uniformly moving constant load. *European Journal of Mechanics, A/Solids* 16, 2 (1997), 295–306.
- [38] DOUGHERTY, E. *Random processes for image and signal processing*. SPIE Press, Bellingham, WA, 1999.
- [39] EKEVID, T., LANE, H., AND WIBERG, N.-E. Adaptive solid wave propagation – influences of boundary conditions in high-speed train applications. *Computer Methods in Applied Mechanics and Engineering* 195 (2006), 236–250.
- [40] EKEVID, T., AND WIBERG, N.-E. Wave propagation related to high-speed train. A scaled boundary FE-approach for unbounded domains. *Computer Methods in Applied Mechanics and Engineering* 191 (2002), 3947–3964.



- [41] ESVELD, C. *Modern railway track. Second Edition*. MRT-Productions, Zaltbommel, 2001.
- [42] EWINS, D. *Modal testing: theory and practice*. Research Studies Press Ltd., Letchworth, UK, 1984.
- [43] FENTON, G. Random field modeling of CPT data. *Journal of Geotechnical and Geoenvironmental Engineering, Proceedings of the ASCE 125*, 6 (1999), 486–535.
- [44] FRANÇOIS, S. *Nonlinear modelling of the response of structures due to ground vibrations*. PhD thesis, Department of Civil Engineering, KU Leuven, 2008.
- [45] FRANÇOIS, S., SCHEVENELS, M., AND DEGRANDE, G. BEMFUN: MATLAB toolbox for boundary elements in elastodynamics. Version 2.1 Build 16. User's guide BWM-2009-26, Department of Civil Engineering, KU Leuven, December 2009.
- [46] FRANÇOIS, S., SCHEVENELS, M., LOMBAERT, G., GALVÍN, P., AND DEGRANDE, G. A 2.5D coupled FE-BE methodology for the dynamic interaction between longitudinally invariant structures and a layered halfspace. *Computer Methods in Applied Mechanics and Engineering 199*, 23-24 (2010), 1536–1548.
- [47] FRYBA, L. *Vibration of Solids and Structures under Moving Loads*. Noordhoff International Publishing, Groningen, Netherlands, 1972.
- [48] GALVÍN, P., AND DOMÍNGUEZ, J. High-speed train-induced ground motion and interaction with structures. *Journal of Sound and Vibration 307* (2007), 755–777.
- [49] GALVÍN, P., FRANÇOIS, S., SCHEVENELS, M., BONGINI, E., DEGRANDE, G., AND LOMBAERT, G. A 2.5D coupled FE-BE model for the prediction of railway induced vibrations. *Soil Dynamics and Earthquake Engineering 30*, 12 (2010), 1500–1512.
- [50] GALVÍN, P., ROMERO, A., AND DOMÍNGUEZ, J. Fully three-dimensional analysis of high-speed train-track-soil-structure dynamic interaction. *Journal of Sound and Vibration 329* (2010), 5147–5163.
- [51] GARG, V., AND DUKKIPATI, R. *Dynamics of railway vehicle systems*. Academic Press, Canada, 1984.
- [52] GHANEM, R., AND SPANOS, P. *Stochastic finite elements: a spectral approach*, 2nd ed. Dover Publications, New York, 2003.

- [53] GORDON, C., AND UNGAR, E. Vibration as a parameter in the design of microelectronic facilities. In *Proceedings of Internoise 83* (Edinburgh, UK, July 1983), pp. 483–490.
- [54] GRASSIE, S., GREGORY, R., HARRISON, D., AND JOHNSON, K. The dynamic response of railway track to high frequency vertical excitation. *Journal of Mechanical Engineering Science* 24, 2 (1982), 77–90.
- [55] GRUNDMANN, H., LIEB, M., AND TROMMER, E. The response of a layered half-space to traffic loads moving along its surface. *Archive of Applied Mechanics* 69 (1999), 55–67.
- [56] HAMID, A., AND YANG, T. Analytical description of track-geometry vibrations. *Transportation Research Record* 838 (1981), 19–26.
- [57] HANSON, C. The method used in the U.S. for predicting ground-borne vibrations from high-speed railways. Noise and Vibration on High-Speed Railways Workshop, Porto, Portugal, October 2008.
- [58] HANSON, C., TOWERS, D., AND MEISTER, L. High-speed ground transportation noise and vibration impact assessment. HMMH Report 293630-4, U.S. Department of Transportation, Federal Railroad Administration, Office of Railroad Development, October 2005.
- [59] HANSON, C., TOWERS, D., AND MEISTER, L. Transit noise and vibration impact assessment. Report FTA-VA-90-1003-06, U.S. Department of Transportation, Federal Transit Administration, Office of Planning and Environment, May 2006.
- [60] HECKL, M., HAUCK, G., AND WETTSCHURECK, R. Structure-borne sound and vibration from rail traffic. *Journal of Sound and Vibration* 193, 1 (1996), 175–184.
- [61] HILDEBRAND, R. Effect of soil stabilization on audible band railway ground vibration. *Soil Dynamics and Earthquake Engineering* 24 (2004), 411–424.
- [62] HO, W., AND WONG, B. TBM groundborne noise prediction models. *Tunnelling Journal* (April/May 2010).
- [63] HOOD, R., GREER, R., BRESLIN, M., AND WILLIAMS, P. The calculation and assessment of ground-borne noise and perceptible vibration from trains in tunnels. *Journal of Sound and Vibration* 193 (1996), 215–225.

- [64] HUNT, H., AND HUSSEIN, M. Vibration from railways: can we achieve better than +/-10 dB prediction accuracy? In *14th International Congress on Sound and Vibration* (Cairns, Australia, July 2007).
- [65] INTERNATIONAL ORGANIZATION FOR STANDARDIZATION. *ISO 2631-2:1999: Mechanical vibration and shock - Evaluation of human exposure to whole-body vibration - Part 2: Vibration in buildings (1 to 80 Hz)*, 1999.
- [66] INTERNATIONAL ORGANIZATION FOR STANDARDIZATION. *ISO 14837-1:2005 Mechanical vibration - Ground-borne noise and vibration arising from rail systems - Part 1: General guidance*, 2005.
- [67] JENKINS, H., STEPHENSON, J., CLAYTON, G., MORLAND, G., AND LYON, D. The effect of track and vehicle parameters on wheel/rail vertical dynamic forces. *Railway Engineering Journal* 1, 1 (1974), 2–16.
- [68] JONES, S., AND HUNT, H. The effect of inclined soil layers on surface vibration from underground railways using the thin layer method. *ASCE Journal of Engineering Mechanics* 137, 12 (2011), 887–900.
- [69] KARL, L. *Dynamic soil properties out of SCPT and bender element tests with emphasis on material damping*. PhD thesis, Universiteit Gent, 2005.
- [70] KARL, L., AND HAEGEMAN, W. Summary of the soil tests at the testing sites: Retie, Lincent, Waremmes, Sint-Katelijne-Waver and Ghent. Report, Laboratory of Soil Mechanics, Ghent University, September 2004.
- [71] KAUSEL, E. *Fundamental solutions in elastodynamics: a compendium*. Cambridge University Press, New York, 2006.
- [72] KAUSEL, E., AND ROËSSET, J. Stiffness matrices for layered soils. *Bulletin of the Seismological Society of America* 71, 6 (1981), 1743–1761.
- [73] KAYNIA, A., MADSHUS, C., AND ZACKRISSON, P. Ground vibration from high speed trains: prediction and countermeasure. *Journal of Geotechnical and Geoenvironmental Engineering, Proceedings of the ASCE* 126, 6 (2000), 531–537.
- [74] KNAPP, C., AND CARTER, G. The generalized correlation method for estimation of time delay. *IEEE Transactions on Acoustics, Speech and Signal Processing* 24, 4 (1976), 320–327.
- [75] KNOTHE, K., AND GRASSIE, S. Modelling of railway track and vehicle/track interaction at high frequencies. *Vehicle Systems Dynamics* 22 (1993), 209–262.

- [76] KNOTHE, K., AND WU, Y. Receptance behaviour of railway track and subgrade. *Archive of Applied Mechanics* 68 (1998), 457–470.
- [77] KOGUT, J., AND DEGRANDE, G. Free field vibrations due to the passage of an IC train and a Thalys high speed train on the L2 track Brussels-Köln. Report BWM-2002-10, Department of Civil Engineering, KU Leuven, November 2002. STWW Programme Technology and Economy, Project IWT-000152.
- [78] KOGUT, J., AND DEGRANDE, G. Assessment of the dynamic parameters of the HST track L2 Brussels - Köln in Lincent using rail receptance measurements. Report BWM-2003-05, Department of Civil Engineering, KU Leuven, March 2003. STWW Programme Technology and Economy, Project IWT-000152.
- [79] KOGUT, J., AND DEGRANDE, G. Transfer functions between the HST track and the free field on the line L2 Brussels-Köln in Lincent. Report BWM-2003-03, Department of Civil Engineering, KU Leuven, January 2003. STWW Programme Technology and Economy, Project IWT-000152.
- [80] KOUROUSSIS, G., GAZETAS, G., ANASTASOPOULOS, I., CONTI, C., AND VERLINDEN, O. Discrete modelling of vertical track–soil coupling for vehicle–track dynamics. *Soil Dynamics and Earthquake Engineering* 31, 12 (2011), 1711–1723.
- [81] KOUROUSSIS, G., VERLINDEN, O., AND CONTI, C. Free field vibrations caused by high-speed lines: Measurement and time domain simulation. *Soil Dynamics and Earthquake Engineering* 31, 4 (2011), 692–702.
- [82] KOUROUSSIS, G., VERLINDEN, O., AND CONTI, C. Influence of some vehicle and track parameters on the environmental vibrations induced by railway traffic. *Vehicle Systems Dynamics* 50, 4 (2012), 619–639.
- [83] KRAMER, S. *Geotechnical earthquake engineering*. Prentice-Hall, Upper Saddle River, New Jersey, 1996.
- [84] KRYLOV, V. Calculation of the low-frequency ground vibrations from railway trains. *Applied Acoustics* 42 (1994), 199–213.
- [85] KRYLOV, V. Generation of ground vibrations by superfast trains. *Applied Acoustics* 44 (1995), 149–164.
- [86] KUPPELWIESER, H., AND ZIEGLER, A. A tool for predicting vibration and structure-born noise immissions caused by railways. *Journal of Sound and Vibration* 193 (1996), 261–267.

- [87] KURZWEIL, L. Ground-borne noise and vibration from underground rail system. *Journal of Sound and Vibration* 66, 3 (1979), 363–370.
- [88] KURZWEIL, L., AND UNGAR, E. Prediction of noise and vibration in buildings near the New York city subway. In *Proceedings of InterNoise '82* (San Fransisco, USA, 1982), pp. 213–216.
- [89] LAI, C. *Simultaneous inversion of Rayleigh phase velocity and attenuation for near-surface site characterization*. PhD thesis, Georgia Institute of Technology, 1998.
- [90] LAI, C., RIX, G., FOTI, S., AND ROMA, V. Simultaneous measurement and inversion of surface wave dispersion and attenuation curves. *Soil Dynamics and Earthquake Engineering* 22, 9-12 (2002), 923–930.
- [91] LANG, J. Results of measurements on the control of structure-borne noise from subways. In *Seventh International Congress on Acoustics* (Budapest, Hungary, 1971), pp. 421–424.
- [92] LANGDON, S., AND CHANDLER WILDE, S. N. A wavenumber independent boundary element method for an acoustic scattering problem. *SIAM Journal on Numerical Analysis* 43, 6 (2006), 2450–2477.
- [93] LIEB, M., AND SUDRET, B. A fast algorithm for soil dynamics calculations by wavelet decomposition. *Archive of Applied Mechanics* 68 (1998), 147–157.
- [94] LOMBAERT, G., AND DEGRANDE, G. Ground-borne vibration due to static and dynamic axle loads of InterCity and high speed trains. *Journal of Sound and Vibration* 319, 3-5 (2009), 1036–1066.
- [95] LOMBAERT, G., DEGRANDE, G., AND CLOUTEAU, D. The non-stationary free field response for a random moving load. *Journal of Sound and Vibration* 278 (2004), 611–635.
- [96] LOMBAERT, G., DEGRANDE, G., FRANÇOIS, S., AND THOMPSON, D. Ground-borne vibration due to railway traffic. In *Proceedings of the 11th International Workshop on Railway Noise IWRN11* (Uddevalla, Sweden, September 2013), J. Nielsen, D. Anderson, P. de Vos, P.-E. Gautier, M. Iida, J. Nelson, T. Tielkes, D. Thompson, and D. Towers, Eds., pp. 266–301.
- [97] LOMBAERT, G., DEGRANDE, G., GALVÍN, P., BONGINI, E., AND POISSON, F. A comparison of predicted and measured ground vibrations due to high speed, passenger, and freight trains. In *Proceedings of the*

- 10th International Workshop on Railway Noise IWRN10*, T. Maeda, P.-E. Gautier, C. Hanson, B. Hemsworth, J. Nelson, B. Schulte-Werning, D. Thompson, and P. de Vos, Eds., vol. 118 of *Notes on Numerical Fluid Mechanics and Multidisciplinary Design*. Springer, Nagahama, Japan, October 2010, pp. 231–238.
- [98] LOMBAERT, G., DEGRANDE, G., KOGUT, J., AND FRANÇOIS, S. The experimental validation of a numerical model for the prediction of railway induced vibrations. *Journal of Sound and Vibration* 297, 3-5 (2006), 512–535.
- [99] LOMBAERT, G., DEGRANDE, G., KOGUT, J., FRANÇOIS, S., HAEGEMAN, W., AND KARL, L. An experimental validation of a numerical model for railway induced vibrations at different levels. In *8th International Workshop on Railway Noise* (Buxton, UK, September 2004), D. Thompson and C. Jones, Eds., vol. 1, pp. 97–106.
- [100] LOMBAERT, G., FRANÇOIS, S., AND DEGRANDE, G. TRAFFIC: MATLAB toolbox for traffic induced vibrations. Report BWM-2011-12, Department of Civil Engineering, KU Leuven, March 2010.
- [101] LUCO, J., AND APSEL, R. On the Green's functions for a layered half-space. Part I. *Bulletin of the Seismological Society of America* 4 (1983), 909–929.
- [102] MADSHUS, C., BESSASON, B., AND HÅRVIK, L. Prediction model for low frequency vibration from high speed railways on soft ground. *Journal of Sound and Vibration* 193, 1 (1996), 195–203.
- [103] MADSHUS, C., AND KAYNIA, A. High-speed railway lines on soft ground: dynamic behaviour at critical train speed. *Journal of Sound and Vibration* 231, 3 (2000), 689–701.
- [104] MANNING, J., CANN, R., AND FREDBERG, J. Prediction and control of rail transit noise and vibration - a state-of-the-art assessment. Report No. UMTA-MA-06-0025-74-5, Department of Transportation, Transportation Systems Center, Cambridge, Massachusetts, April 1974.
- [105] MELKE, J. Noise and vibration from underground railway lines: proposals for a prediction procedure. *Journal of Sound and Vibration* 120 (1988), 391–406.
- [106] METRIKINE, A., AND POPP, K. Instability of vibrations of an oscillator moving along a beam on an elastic half-space. *European Journal of Mechanics, A/Solids* 18, 2 (1999), 331–349.

- [107] METRIKINE, A., AND POPP, K. Steady-state vibrations of an elastic beam on a visco-elastic layer under moving load. *Archive of Applied Mechanics* 70 (2000), 399–408.
- [108] NAZARIAN, S., AND DESAI, M. Automated surface wave method: field testing. *Journal of Geotechnical Engineering, Proceedings of the ASCE* 119, 7 (1993), 1094–1111.
- [109] NELSON, J., AND SAURENMAN, H. State-of-the-art review: prediction and control of groundborne noise and vibration from rail transit rails. Report No. UMTA-MA-06-0049-83-4, Department of Transportation, Transportation Systems Center, Cambridge, Massachusetts, December 1983.
- [110] NELSON, J., AND SAURENMAN, H. A prediction procedure for rail transportation groundborne noise and vibration. *Transportation Research Record* 1143 (1987), 26–35.
- [111] NEWLAND, D. *An introduction to random vibrations, spectral & wavelet analysis*. Longman Scientific & Technical, Essex, England, 1994.
- [112] NIELSEN, J., AND IGELAND, A. Vertical dynamic interaction between train and track-influence of wheel and rail imperfections. *Journal of Sound and Vibration* 187, 5 (1995), 825–839.
- [113] NOLLE, H. High frequency ground vibration measurements. *Shock and Vibration Bulletin* 48, 4 (1978), 95–103.
- [114] OBERLECHNER, G., METZGER, B., AND ZYWIEL, J. GPS system to boost accuracy. *International Railway Journal*, September 2000.
- [115] ORE. Question C116: Wechselwirkung zwischen Fahrzeugen und gleis, Bericht Nr. 1: Spektrale Dichte der Unregelmässigkeiten in der Gleislage. Tech. rep., Office for Research and Experiments of the International Union of Railways, Utrecht, NL, 1971.
- [116] PARK, C., MILLER, R., RYDEN, N., XIA, J., AND IVANOV, J. Combined use of active and passive surface waves. *Journal of Environmental and Engineering Geophysics* 10, 3 (2005), 323–334.
- [117] RAJARAM, S., AND SAURENMAN, H. Issues in developing accurate groundborne vibration predictions for high-speed rail projects. In *Proceedings of the 25th Conference of the Institute of Noise Control Engineering, NOISE-CON 2011* (Portland, OR, July 2011).
- [118] RAYLEIGH, J. On waves propagated along the plane surface of an elastic solid. *Proceedings of the London Mathematical Society* 17 (1887), 4–11.

- [119] RICE, S. Mathematical analysis of random noise. *Bell System Technical Journal* 24 (1945), 45–156.
- [120] RIX, G., LAI, C., AND SPANG JR., A. In situ measurement of damping ratio using surface waves. *Journal of Geotechnical and Geoenvironmental Engineering, Proceedings of the ASCE* 126, 5 (2000), 472–480.
- [121] ROBERTSON, P., CAMPANELLA, R., GILLESPIE, D., AND RICE, A. Seismic CPT to measure in situ shear wave velocity. *Journal of the Soil Mechanics and Foundation Division, Proceedings of the ASCE* 112, 8 (1986), 791–803.
- [122] SAMBRIDGE, M., AND MOSEGAARD, K. Monte Carlo methods in geophysical inverse problems. *Reviews of Geophysics* 40, 3 (2002), 1–29.
- [123] SAURENMAN, H. High speed rail ground-borne vibration test results. APTA Track, Noise and Vibration Subcommittee Meeting, Portland, OR, April 1996.
- [124] SAURENMAN, H. Historical perspective, vibration prediction in North-America. Rail Transportation Ground-Borne Noise and Vibration Prediction Workshop, TRB 85th Annual Meeting, Washington, D.C., January 2006.
- [125] SAURENMAN, H., NELSON, J., AND WILSON, G. Handbook of urban rail noise and vibration control. Report No. UMTA-MA-06-0099-82-1 DOT-TSC-UMTA-81-72, Department of Transportation, Transportation Systems Center, Cambridge, Massachusetts, February 1982.
- [126] SCHEVENELS, M. *The impact of uncertain dynamic soil characteristics on the prediction of ground vibrations*. PhD thesis, Department of Civil Engineering, KU Leuven, 2007.
- [127] SCHEVENELS, M., DEGRANDE, G., AND FRANÇOIS, S. EDT: an ElastoDynamics Toolbox for Matlab. In *Book of Abstracts of the Inaugural International Conference of the Engineering Mechanics Institute (EM08)* (Minneapolis, Minnesota, U.S.A., May 2008), p. 82.
- [128] SCHEVENELS, M., DEGRANDE, G., AND FRANÇOIS, S. EDT: Elastodynamics Toolbox for MATLAB. Version 2.2 Build 20. User’s guide BWM-2010-11, Department of Civil Engineering, KU Leuven, August 2010.
- [129] SCHEVENELS, M., DEGRANDE, G., AND LOMBAERT, G. The influence of the depth of the ground water table on free field road traffic induced vibrations. *International Journal for Numerical and Analytical Methods in Geomechanics* 28, 5 (2004), 395–419.



- [130] SCHEVENELS, M., FRANÇOIS, S., AND DEGRANDE, G. EDT: An ElastoDynamics Toolbox for MATLAB. *Computers & Geosciences* 35, 8 (2009), 1752–1754.
- [131] SCHEVENELS, M., LOMBAERT, G., AND DEGRANDE, G. Determination of the dynamic soil properties by refracted P-wave and surface wave characterization at a site in Lincent (Belgium). Report BWM-2011-17, Department of Civil Engineering, KU Leuven, September 2011.
- [132] SCHEVENELS, M., LOMBAERT, G., DEGRANDE, G., AND ARNST, M. Measurement and prediction of the soil's transfer function at a site in Lincent. Tech. Rep. BWM-2006-03, Department of Civil Engineering, KU Leuven, February 2006.
- [133] SCHEVENELS, M., LOMBAERT, G., DEGRANDE, G., AND FRANÇOIS, S. A probabilistic assessment of resolution in the SASW test and its impact on the prediction of ground vibrations. *Geophysical Journal International* 172, 1 (2008), 262–275.
- [134] SHENG, X., JONES, C., AND PETYT, M. Ground vibration generated by a harmonic load acting on a railway track. *Journal of Sound and Vibration* 225, 1 (1999), 3–28.
- [135] SHENG, X., JONES, C., AND PETYT, M. Ground vibration generated by a load moving along a railway track. *Journal of Sound and Vibration* 228, 1 (1999), 129–156.
- [136] SHENG, X., JONES, C., AND THOMPSON, D. A theoretical model for ground vibration from trains generated by vertical track irregularities. *Journal of Sound and Vibration* 272, 3-5 (2004), 937–965.
- [137] SHENG, X., JONES, C., AND THOMPSON, D. Responses of infinite periodic structures to moving or stationary harmonic loads. *Journal of Sound and Vibration* 282 (2005), 125–149.
- [138] SHINOZUKA, M., AND DEODATIS, G. Simulation of stochastic processes by spectral representation. *Applied Mechanics Reviews* 44, 4 (1991), 191–204.
- [139] SHINOZUKA, M., AND JAN, C. Digital simulation of random processes and its application. *Journal of Sound and Vibration* 25, 1 (1972), 111–128.
- [140] STICHTING BOUWRESEARCH. *SBR deel A: Schade aan gebouwen door trillingen: meet- en beoordelingsrichtlijn*, 2002.

- [141] STICHTING BOUWRESEARCH. *SBR deel B: Hinder voor personen in gebouwen door trillingen: meet- en beoordelingsrichtlijn*, 2002.
- [142] STICHTING BOUWRESEARCH. *SBR deel C: Storing aan apparatuur door trillingen: meet- en beoordelingsrichtlijn*, 2002.
- [143] TAKEMIYA, H. Simulation of track-ground vibrations due to a high-speed train: the case of X-2000 at Ledsgard. *Journal of Sound and Vibration* 261 (2003), 503–526.
- [144] THOMPSON, D. *Railway noise and vibration: mechanisms, modelling, and means of control*. Elsevier, 2009.
- [145] THOMSON, W. On the correction for shear of the differential equation for transverse vibrations of prismatic bars. *Philosophical Magazine Series 41*, 245 (1921), 744–746.
- [146] TOWERS, D. A. Evaluation of the Ground-Borne Vibration Reduction Properties of Tire Derived Aggregate Installed on the Denver RTD Light Rail System. vol. 118 of *Notes on Numerical Fluid Mechanics and Multidisciplinary Design*, pp. 283–290. 10th International Workshop on Railway Noise (IWRN 2010), Nagahama, Japan, October 2010.
- [147] UNGAR, E., AND BENDER, E. Vibrations produced in buildings by passage of subway trains - Parameter estimation for preliminary design. In *Proceedings of InterNoise '75* (Sendai, Japan, 1975).
- [148] VAN NIEKERK, J., MORGAN, J., AND COSIJN, D. Gautrain tunnels: surface vibration and ground-borne noise. *The Journal of the South African Institute of Mining and Metallurgy* 104, 4 (2004), 245–249.
- [149] VEIRMAN, N. The prediction of vibration transfer for railway induced ground vibration. Master's thesis, Department of Civil Engineering, KU Leuven, 2013.
- [150] VERBRAKEN, H., COULIER, P., LOMBAERT, G., AND DEGRANDE, G. Measurement of train passages and transfer functions at a site in Lincent. Report BWM-2012-05, Department of Civil Engineering, KU Leuven, June 2012.
- [151] VERBRAKEN, H., COULIER, P., LOMBAERT, G., AND DEGRANDE, G. Measurement of transfer functions at a site in Lincent. Report BWM-2012-07, Department of Civil Engineering, KU Leuven, July 2012.
- [152] VERBRAKEN, H., LOMBAERT, G., AND DEGRANDE, G. Verification of an empirical prediction method for railway induced vibrations by means

- of numerical simulations. *Journal of Sound and Vibration* 330, 8 (2011), 1692–1703.
- [153] VERBRAKEN, H., VEIRMAN, N., CUELLAR, V., LOMBAERT, G., AND DEGRANDE, G. The prediction of vibration transfer for railway induced ground vibration. In *Proceedings of the 11th International Workshop on Railway Noise IWRN11* (Uddevalla, Sweden, September 2013), J. Nielsen, D. Anderson, P. de Vos, P.-E. Gautier, M. Iida, J. Nelson, T. Tielkes, D. Thompson, and D. Towers, Eds., pp. 258–265.
- [154] WEI, P., XIA, H., AND CHEN, J. Validation of an empirical prediction model for train-induced ground vibrations. In *Proceedings of the 3rd International Symposium on Environmental Vibrations: Prediction, Monitoring and Evaluation* (Taipei, Taiwan, November 2007), Y. Yang and J. Yau, Eds., pp. 185–190.
- [155] WITH, C., BAHREKAZEMI, M., AND BODARE, A. Validation of an empirical model for prediction of train-induced ground vibrations. *Soil Dynamics and Earthquake Engineering* 26, 11 (2006), 983–990.
- [156] WU, T., AND THOMPSON, D. Vibration analysis of railway track with multiple wheels on the rail. *Journal of Sound and Vibration* 239, 1 (2001), 69–97.
- [157] WU, T., AND THOMPSON, D. On the parametric excitation of the wheel/track system. *Journal of Sound and Vibration* 278, 4-5 (2004), 725–747.
- [158] YOUNG, T., AND LI, C. Vertical vibration analysis of vehicle/imperfect track systems. *Vehicle Systems Dynamics* 40, 5 (2003), 329–349.
- [159] YUAN, D., AND NAZARIAN, S. Automated surface wave method: inversion technique. *Journal of Geotechnical Engineering, Proceedings of the ASCE* 119, 7 (1993), 1112–1126.
- [160] ZHAI, W., AND TRUE, H. Vehicle-track dynamics on a ramp and on the bridge: Simulation and measurements. *Vehicle Systems Dynamics* 33, Suppl. (1999), 47–58.
- [161] ZIEGLER, A. VIBRA-1-2-3: A software package for ground borne vibration and noise prediction. In *Proceedings of the Sixth European Conference on Structural Dynamics - Eurodyn 2005* (Paris, France, September 2005), C. Soize and G. Schuëller, Eds., pp. 613–618.
- [162] ZYWIEL, J., AND OBERLECHNER, G. Innovative measuring system unveiled. *International Railway Journal*, September 2001.



# Curriculum vitae

Hans Verbraeken  
° 7 January 1986, Osnabrück, Germany

## Education

*2008 – present*  
PhD in Engineering, Department of Civil Engineering, KU Leuven.

*2003 – 2008*  
MSc in Civil Engineering, KU Leuven.

*1997 – 2003*  
Secondary Education, KCST, Sint-Truiden.

## Work experience

*2009 – 2013*  
PhD fellow of the Research Foundation – Flanders (FWO),  
Department of Civil Engineering, KU Leuven.

*2008 – 2009*  
Research assistant, Department of Civil Engineering, KU Leuven.

## Publications

### International journal papers

VERBRAKEN, H., LOMBAERT, G., AND DEGRANDE, G. Experimental and numerical prediction of railway induced vibration. *Journal of Zhejiang University - Science A* 13, 11 (2012), 802–813.

VERBRAKEN, H., LOMBAERT, G., AND DEGRANDE, G. Verification of an empirical prediction method for railway induced vibrations by means of numerical simulations. *Journal of Sound and Vibration* 330, 8 (2011), 1692–1703.

### International conference papers

VERBRAKEN, H., VEIRMAN, N., CUELLAR, V., LOMBAERT, B., AND DEGRANDE, G. The prediction of vibration transfer for railway induced ground vibration. In *Proceedings of the 11th International Workshop on Railway Noise IWRN11* (Uddevalla, Sweden, September 2013), J. Nielsen, D. Anderson, P. de Vos, P.-E. Gautier, M. Iida, J. Nelson, T. T., T. D., and D. Towers, Eds., pp. 258–265.

VERBRAKEN, H., DEGRANDE, G., AND LOMBAERT, G. Experimental and numerical determination of transfer functions along railway tracks. In *Proceedings of ISMA 2012 International Conference on Noise and Vibration Engineering* (Leuven, Belgium, September 2012), P. Sas, D. Moens, and S. Jonckheere, Eds., pp. 2973–2987.

VERBRAKEN, H., FRANÇOIS, S., DEGRANDE, G., AND LOMBAERT, G. A numerical simulation of an experimental prediction method for railway induced vibration in buildings. In *Advances in Environmental Vibration. Proceedings of the 5th International Symposium on Environmental Vibration. ISEV 2011*. (Chengdu, China, October 2011), W. Zhai, H. Takemiya, G. De Roeck, and E. Tutumluer, Eds., Science Press, Beijing, China, pp. 217–223.

VERBRAKEN, H., LOMBAERT, G., AND DEGRANDE, G. Numerical and empirical prediction methods for railway induced vibrations in buildings. In *Proceedings of the 8th International Conference on Structural Dynamics EURO-DYN 2011* (Leuven, Belgium, July 2011), G. De Roeck, G. Degrande, G. Lombaert, and G. Müller, Eds., pp. 727–734. CD-ROM.

VERBRAKEN, H., DEGRANDE, G., AND LOMBAERT, G. Verification of an empirical prediction method for ground borne vibrations in buildings due to

high speed railway traffic. In *3rd International Conference on Computational Methods in Structural Dynamics and Earthquake Engineering COMPDYN* (Corfu, Greece, May 2011), M. Papadrakakis, M. Fragiadakis, and V. Plevris, Eds., pp. CD-ROM.

VERBRAKEN, H., DEGRANDE, G., AND LOMBAERT, G. A hybrid prediction method for ground-borne vibrations due to railway traffic. In *9th World Congress on Railway Research* (Lille, France, May 2011). CD-ROM.

VERBRAKEN, H., LOMBAERT, G., AND DEGRANDE, G. Hybrid predictions of environmental vibrations due to railway traffic. In *Railways and Environment* (Delft, The Netherlands, December 2010), pp. 46–48.

VERBRAKEN, H., EYSERMANS, H., DECHIEF, E., FRANÇOIS, S., LOMBAERT, G., AND DEGRANDE, G. Verification of an empirical prediction method for railway induced vibration. In *Proceedings of the 10th International Workshop on Railway Noise IWRN10*, T. Maeda, P.-E. Gautier, C. Hanson, B. Hemsworth, J. Nelson, B. Schulte-Werning, D. Thompson, and P. de Vos, Eds., vol. 118 of *Notes on Numerical Fluid Mechanics and Multidisciplinary Design*. Springer, Nagahama, Japan, October 2010, pp. 239–247.

VERBRAKEN, H., EYSERMANS, H., DECHIEF, E., FRANÇOIS, S., DEGRANDE, G., AND LOMBAERT, G. Development of a hybrid prediction method for railway induced vibration. In *Proceedings of ISMA2010 International Conference on Noise and Vibration Engineering* (Leuven, Belgium, September 2010), pp. 3559–3572.

VERBRAKEN, H., EYSERMANS, H., DECHIEF, E., FRANÇOIS, S., LOMBAERT, G., AND DEGRANDE, G. Assessment of an empirical prediction method for railway induced vibrations by numerical simulations. In *Noise in the Built Environment* (Ghent, Belgium, April 2010), D. Botteldooren, Ed., vol. 32, Pt. 3, Institute of Acoustics & Belgian Acoustical Society, pp. 609–616.

FIALA, P., VERBRAKEN, H., LOMBAERT, G., DEGRANDE, G., AND AUGUSZTINOVICZ, F. Comparative study of the efficiency of isolation measures for vibration and noise from underground railway traffic. In *Noise in the Built Environment* (Ghent, Belgium, April 2010), D. Botteldooren, Ed., vol. 32, Pt. 3, Institute of Acoustics & Belgian Acoustical Society, pp. 383–394.

VERBRAKEN, H., LOMBAERT, G., AND DEGRANDE, G. Verification and extension of an empirical prediction method for subway induced vibration with a coupled FE-BE model. In *Proceedings of 16th International Congress on Sound and Vibration* (Kraków, Poland, July 2009), M. Pawelczyk and D. Bismor, Eds. CD-ROM.

### **National conference papers**

VERBRAKEN, H., LOMBAERT, G., AND DEGRANDE, G. Experimental and numerical determination of transfer functions along railway tracks. In *Proceedings of the 9th National Congress on Theoretical and Applied Mechanics NCTAM 2012* (Brussels, Belgium, May 2012).

### **Presentations at national conferences**

VERBRAKEN, H., LOMBAERT, G., AND DEGRANDE, G. Vibrations in buildings in the mid frequency range. ABAV studiedag, Wie-doet-wat in het Belgisch akoestisch onderzoek?, February 2011.

### **Internal reports**

VERBRAKEN, H., COULIER, P., LOMBAERT, G., AND DEGRANDE, G. Measurement of free field vibration during impact tests on a pile at a site in Loon-Plage (France). Report BWM-2012-09, Department of Civil Engineering, KU Leuven, September 2012.

COULIER, P., VERBRAKEN, H., LOMBAERT, G., AND DEGRANDE, G. Determination of the dynamic soil properties by surface wave characterization at a site in Loon-Plage (France). Report BWM-2012-08, Department of Civil Engineering, KU Leuven, September 2012.

VERBRAKEN, H., COULIER, P., LOMBAERT, G., AND DEGRANDE, G. Measurement of transfer functions at a site in Lincent. Report BWM-2012-07, Department of Civil Engineering, KU Leuven, July 2012.

VERBRAKEN, H., COULIER, P., LOMBAERT, G., AND DEGRANDE, G. Measurement of train passages and transfer functions at a site in Lincent. Report BWM-2012-05, Department of Civil Engineering, KU Leuven, June 2012.

COULIER, P., VERBRAKEN, H., LOMBAERT, G., AND DEGRANDE, G. Trillingsmetingen in het postsorteercentrum te Hasselt: fase 1. Report BWM-2012-04, Department of Civil Engineering, KU Leuven, March 2012.

VERBRAKEN, H., DEGRANDE, G., AND LOMBAERT, G. Impact of mitigation measures on the track on railway induced vibration. Report BWM-2012-03, Department of Civil Engineering, KU Leuven, January 2012.



DEGRANDE, G., DE ROECK, G., LOMBAERT, G., SCHEVENELS, M., REYNDERS, E., BADSAR, S., LOURENS, E., ARNOUT, S., AND VERBRAKEN, H. A generic methodology for inverse modelling of dynamic problems in civil and environmental engineering. Report BWM-2010-01, Department of Civil Engineering, KU Leuven, January 2010. OT Project OT/05/41.

LAK, M., LOMBAERT, G., VERBRAKEN, H., AND DEGRANDE, G. Vibration measurements during the operation of a multi-head breaker on a concrete road at a site in Waarschoot. Tech. Rep. BWM-2009-14, Department of Civil Engineering, KU Leuven, August 2009.

VERBRAKEN, H., FRANÇOIS, S., AND DEGRANDE, G. Trillingsmetingen in een woning in de Wersbeekstraat in Meensel-Kiezegem. Report BWM-2008-18, Department of Civil Engineering, KU Leuven, October 2008.

FRANÇOIS, S., VERBRAKEN, H., AND DEGRANDE, G. Trillingsmetingen in een woning in de Oostereindestraat te Lummen. Report BWM-2008-17, Department of Civil Engineering, KU Leuven, October 2008.

#### **Master's thesis**

VERBRAKEN, H. Tabula Rasa: Een nieuw wegennet voor België. Master's thesis, Department of Civil Engineering, KU Leuven, June 2008. In Dutch.

